Submm Observations of Massive Star Formation in the Giant Molecular Cloud NGC 6334: Gas Kinematics with Radiative Transfer Models

Alexander Zernickel

I. Physical Institute
Faculty of Mathematics and Natural Sciences
University of Cologne
2015

Submm Observations of Massive Star Formation in the Giant Molecular Cloud NGC 6334: Gas Kinematics with Radiative Transfer Models

Inaugural-Dissertation

zur

Erlangung des Doktorgrades

der Mathematisch-Naturwissenschaftlichen Fakultät

der Universität zu Köln

vorgelegt von

Alexander Zernickel

aus Karaganda (KZ)

Köln 2015

Berichterstatter:	Prof. Dr. Peter Schilke
	Priv.-Doz. Dr. Volker Ossenkopf
Tag der mündlichen Prüfung:	07.05.2015

Abstract

Context. How massive stars (M>8 $M_\odot$) form and how they accrete gas is still an open research field, but it is known that their influence on the interstellar medium (ISM) is immense. Star formation involves the gravitational collapse of gas from scales of giant molecular clouds (GMCs) down to dense hot molecular cores (HMCs). Thus, it is important to understand the mass flows and kinematics in the ISM.
Aims. This dissertation focuses on the detailed study of the region NGC 6334, located in the Galaxy at a distance of 1.7 kpc. It is aimed to trace the gas velocities in the filamentary, massive star-forming region NGC 6334 at several scales and to explain its dynamics. For that purpose, different scales are examined from 0.01–10 pc to collect information about the density, molecular abundance, temperature and velocity, and consequently to gain insights about the physio-chemical conditions of molecular clouds. The two embedded massive protostellar clusters NGC 6334I and I(N), which are at different stages of development, were selected to determine their infall velocities and mass accretion rates.
Methods. This astronomical source was surveyed by a combination of different observatories, namely with the Submillimeter Array (SMA), the single-dish telescope Atacama Pathfinder Experiment (APEX), and the Herschel Space Observatory (HSO). It was mapped with APEX in carbon monoxide (^{13}CO and C^{18}O, J=2–1) at 220.4 GHz to study the filamentary structure and turbulent kinematics on the largest scales of 10 pc. The spectral line profiles are decomposed by Gaussian fitting and a dendrogram algorithm is applied to distinguish velocity-coherent structures and to derive statistical properties. The velocity gradient method is used to derive mass flow rates. The main filament was mapped with APEX in hydrogen cyanide (HCN) and oxomethylium (HCO+, J=3–2) at 267.6 GHz to trace the dense gas. To reproduce the position-velocity diagram (PVD), a cylindrical model with the radiative transfer code Line Modeling Engine (`LIME`) is created with a collapsing velocity field. Both clusters NGC 6334I and I(N) were observed with the interferometer SMA in HCN (J=4–3) at 354.5 GHz at the smallest scales of 0.01 pc. The combination of interferometric and multi-frequency single-dish data gives a wide range of rotational transitions, which probe the gas at different excitation conditions and optical depths. The molecule HCN and its isotopologues H^{13}CN/HC^{15}N trace radii of a HMC from 1.0–0.01 pc by a range of level energies (E_u=4–1067 K) and optical depths (τ=100–0.1). The HMCs, which have a rich line spectra, are analyzed by using 1D (`myXCLASS`) and 3D numerical radiative transfer codes (`RADMC-3D` and `LIME`) in and outside of local thermodynamic equilibrium (LTE). Multiple components and the fragmentation of the clusters are modeled with these tools. Together with the optimization package `MAGIX`, the data are compared and reproduced with synthetic maps and spectra from these models.
Results. 1. The main filament shows a velocity gradient from the end toward its center, where the most massive clumps accumulate at both ends, in accordance to predictions of a longitudinal contraction. The 3D structure is determined by taking the inclination and curvature of the filament into account, and the free-fall time is estimated to ~1 Myr; 2. The total gas mass is 2.3E5 $M_\odot$ and the average temperature 20 K. The majority of the velocity gradients are aligned with the magnetic field, which runs perpendicular to the filaments. The calculation of the average Mach numbers yields a turbulence which is super-sonic (M_S=5.7) and sub-Alfvénic (M_A=0.86). In general, the derived scaling relations are in agreement with Larson's relations. 3. The SMA observations reveal multiple bipolar molecular outflows, blue asymmetric infall profiles, rotating

cores and an ultra compact (UC) HII region in NGC 6334I which affects the surrounding gas. The average mass accretion rates are 1E-3 $M_{\odot}$/yr for the envelopes and 3E-4 $M_{\odot}$/yr for the cores, where the latter are derived from modified Bondi-Hoyle models. The orientation of the magnetic field is in NGC 6334I(N) consistent over all scales and most outflows are aligned perpendicular to it; 4. In the line surveys of the HMCs, 20 different molecules are identified with typical temperatures of 100 K. A cruel separation between the HMCs of the clusters is determined on the basis of the relative abundances.
Conclusions. The combination of single-dish with interferometric data is helpful to constrain the parameter space of a model. The envelope hinders the determination of infall velocities in HMCs via line profiles. Systematic motions as a result of gravitational attraction are difficult to find because of the turbulent nature of the ISM. The magnetic field energy in NGC 6334 is as important as the kinetic energy and regulates partly the direction of the inflowing gas and thus the geometry and collapse of the molecular clouds. NGC 6334 is heavily affected by the HII regions (produced by the OB stars), and the free-fall time and mass surface density suggest that it classifies as a starburst system.

Kurzzusammenfassung (abstract in German language)

Kontext. Im Rahmen dieser Dissertation wird die Entstehung von schweren Sternen (M>8 $M_\odot$) untersucht und wie sie Gas akkretieren. Dies ist noch immer ein offenes Forschungsfeld, aber es ist bekannt, dass sie einen immensen Einfluss auf das interstellare Medium (ISM) haben. Sternentstehung beinhaltet den gravitativen Kollaps von Gas auf Skalen von gigantischen Molekülwolken (GMCs) bis herunter zu dichten heißen Molekülkernen (HMCs). Daher ist ein Verständnis der Massenflüsse und der Kinematik im ISM äußerst wichtig.
Ziele. Der Fokus wird auf die detaillierte Studie der Region NGC 6334 gelegt, welche sich in der Galaxis bei einem Abstand von 1.7 kpc befindet. Es wird darauf gezielt, die Gasgeschwindigkeiten in der filamentartigen, massiven Sternentstehungsregion NGC 6334 auf mehreren Skalen zu verfolgen und deren Dynamik zu erklären. Zu diesem Zweck werden verschiedene Skalen von 0.01–10 pc untersucht um Informationen über die Dichte, Molekülhäufigkeit, Temperatur und Geschwindigkeit einzusammeln, und damit konsequenterweise Einsichten in die physikalisch-chemische Beschaffenheit von Molekülwolken zu gewinnen. Die zwei eingeschlossenen massiven proto-stellaren Cluster NGC 6334I und I(N), welche sich in unterschiedlichen Entwicklungsstadien befinden, wurden selektiert um deren Kollapsgeschwindigkeiten und Massenakkretionsraten zu bestimmen.
Methodik. Diese astronomische Quelle wurde durch eine Kombination von verschiedenen Observatorien beobachtet, nämlich mit dem Submillimeter Array (SMA), dem Radioteleskop Atacama Pathfinder Experiment (APEX) und dem Weltraumobservatorium Herschel (HSO). Sie wurde mit APEX in Kohlenstoffmonoxid (^{13}CO und C^{18}O, J=2–1) bei 220.4 GHz kartiert um die filamentartige Struktur und turbulente Kinematik auf den größten Skalen von 10 pc zu studieren. Die Spektrallinienprofile werden durch Gauß-Anpassungen zerlegt und ein Dendrogram Algorithmus wird angewendet um geschwindigkeits-kohärente Strukturen zu unterscheiden und statistische Eigenschaften abzuleiten. Die Geschwindigkeitsgradientenmethode wird verwendet um die Massenflussraten zu bestimmen. Das Hauptfilament wurde mit APEX in Cyanwasserstoff (HCN) und Oxomethylium (HCO$^+$, J=3–2) bei 267.6 GHz kartiert um das dichte Gas zu sondieren. Um das Positions-Geschwindigkeits-Diagramm (PVD) zu reproduzieren wird ein zylindrisches Modell mit dem Strahlungstransportprogramm Line Modeling Engine (`LIME`) erstellt mit einem kollabierenden Geschwindigkeitsfeld. Beide Cluster NGC 6334I und I(N) wurden mit dem Interferometer SMA in HCN (J=4–3) bei 354.5 GHz beobachtet auf den kleinsten Skalen von 0.01 pc. Die Kombination von multi-frequenten Daten des Interferometers und der Teleskope ergibt einen weiten Bereich von Rotationsübergängen, welche das Gas bei unterschiedlichen Anregungszuständen und optischen Tiefen erproben. Das Molekül HCN und dessen Isotopologe H^{13}CN/HC^{15}N sondieren Radien von HMCs von 1.0–0.01 pc aufgrund einer Reihe von Energielevel (E_u=4–1067 K) und optischen Tiefen (τ=100–0.1). Die HMCs, welche ein reiches Linienspektrum haben, werden mit 1D (`myXCLASS`) und 3D numerischen Strahlungstransportprogrammen (`RADMC-3D` und `LIME`) analysiert, innerhalb und außerhalb des lokalen thermodynamischen Gleichgewichtes (LTE). Mehrere Komponenten und die Fragmentierung des Clusters werden mit diesen Werkzeugen modelliert. Zusammen mit dem Optimierungspaket `MAGIX` werden die Daten mit den synthetischen Karten und Spektren der Modelle verglichen und reproduziert.
Resultate. 1. Das Hauptfilament zeigt einen Geschwindigkeitsgradienten von den Enden in Richtung Zentrum, wo sich an beiden Enden die massivsten Akkumulationen befinden, in Über-

einstimmung mit Vorhersagen einer longitudinalen Kontraktion. Die 3D Struktur wird bestimmt durch die Berücksichtigung der Inklination und Elliptizität, und die freie Fallzeit wird auf $\sim$1 Myr geschätzt; 2. Die totale Gasmasse ist 2.3E5 $M_{\odot}$ und die durchschnittliche Temperatur 20 K. Die Mehrheit der Geschwindigkeitsgradienten ist mit dem Magnetfeld orientiert, welches senkrecht zu den Filamenten verläuft. Die Berechnung der durchschnittlichen Machzahlen ergibt eine Turbulenz, welche super-sonisch ($M_{\rm S}$=5.7) und sub-Alfvén ($M_{\rm A}$=0.86) ist. Allgemein sind die abgeleiteten Skalenrelationen in Übereinstimmung mit Larsons Relationen. 3. Die SMA Beobachtungen zeigen mehrere bipolare molekulare Ausflüsse, blau-verschobene asymmetrische Spektrallinienprofile, rotierende Kerne und eine ultrakompakte (UC) HII Region in NGC 6334I, welche das sich umgebende Gas beeinflusst. Durchschnittliche Massenakkretionsraten von 1E-3 $M_{\odot}$/yr für die Hüllen und 3E4 $M_{\odot}$/yr für die Kerne werden abgeleitet, wobei letzteres durch modifizierte Bondi-Hoyle Modelle berechnet wird. Die Orientierung des Magnetfelds ist in NGC 6334I(N) konsistent über alle Skalen, und die meisten Ausflüsse sind senkrecht dazu ausgerichtet; 4. In den Liniendurchmusterungen der HMCs werden 20 verschiedene Moleküle identifiziert mit typischen Temperaturen von 100 K. Eine grobe Separierung der HMCs der Cluster ist feststellbar anhand der relativen Häufigkeiten.

Schlussfolgerung. Die Kombination von Interferometer- mit Teleskop-Daten ist hilfreich um den Parameterraum eines Modells einzuschränken. Die Hülle verhindert die Bestimmung der Kollapsgeschwindigkeiten aus den Linienprofilen. Systematischen Bewegungen als Folge von Akkretion oder gravitativer Anziehung sind schwierig zu finden aufgrund der turbulenten Natur des ISM. Die Energie des Magnetfelds in NGC 6334 ist so bedeutsam wie die kinetische Energie und reguliert teilweise die Richtung des einfallenden Gases und somit die Geometrie und den Kollaps der Molekülwolken. NGC 6334 ist stark beeinflusst von den HII Regionen (produziert von OB Sternen), und die freie Fallzeit und hohe Massenoberflächendichte weisen darauf hin, dass es als ein Sternenausbruchsystem klassifiziert werden kann.

Contents

Appendix

1. Introduction

1.1. Motivation and outline

Astrophysics is about the nature of stars (derived from the Greek language, astron=star and physice=science of nature), which includes their birth, evolution and death. The overall context of this thesis is the question of how massive stars form and what determines their final mass. From several theoretic and observational point of views, it is established that they form and evolve in a different way than low-mass stars. Because these massive protostars are embedded in dense clouds and clustered environments, it is attempted to answer the question by following the gas dynamics from the largest to the smallest spatial scales by several orders of magnitude from 1E-2 pc to 1E2 pc. The goal is to collect information about the global mass flows from the filaments to the clusters, and within the clusters onto the embedded cluster members where the protostars reside. The different scales are probed by the usage of several molecular line tracers, mainly CO and HCN, to span a range in the gas density from n=1E3–1E7 1/cm^3. Therefore, this work focuses on the gas kinematics of dense clouds and studies one particular massive star-forming region in detail, instead of making conclusions about a statistical sample of different regions. One hypothesis is that it should be able to observe the accretion rates of HMCs with modern telescopes on several scales in the velocity maps, because they must be supplied by inflowing gas streams to maintain these high rates for their life timescales of approximately 0.1 Myr. If the gas mass reservoir is pre-assmbled or constantly replenished and newly distributed is an open question in the theory of massive star formation, and high-resolution observations of two massive protostellar clusters are used to verify these scenarios.

Out of the several divisions in astrophysics, this thesis is classified more into the fields of astronomical observations and astrophysical analyzes, and less into technical or theoretical aspects (e.g., by computer simulations). The thesis is structured as follows: Chap. 3–6 present the analysis of new data (obtained from 2010–2013) from different telescopes of the astronomical source NGC 6334, supported with public data from large surveys. In general, the chapters are ordered from the large to the small scale observations of this region, and can be read independently as they do not build on one another.

- Chap. 1 summarizes the current knowledge of the ISM, of (massive) star formation and introduces the source NGC 6334. Different theories are presented for the explanation of the formation of GMCs and massive protostars, which are tested by the observations and models in the following chapters.

- Chap. 2 elaborates on the experimental methods and tools which are used in submm astrophysics to clarify how this knowledge is obtained in practice. It therefore comprises and repeats the fundamentals of this specific area of astronomy, on which the following chapters rely and build on. For a more detailed review about the topics in this chap. (especially on more technical aspects), see Wilson et al. (2009). The methods used for the analysis of the data are specified in the respective chapters 3–6.

- Chap. 3 presents HCN/HCO$^+$ (J=3–2) observations with APEX of the dense gas of the main filament of NGC 6334, which has a total length of 12 pc. It is based on the published paper Zernickel et al. (2013), and includes an additional section and further explanations. The PVD is compared with analytical descriptions of collapsing filaments and is reproduced by a radiative transfer model.

- Chap. 4 describes NGC 6334 on the largest scales of 60 pc by ^{13}CO (J=2–1) observations with APEX. This molecular line transition traces the less dense gas (n=1E3–1E5 1/cm^3) and therefore allows probing the subfilaments surrounding the main filament. A velocity gradient method and structure function is applied to characterize the velocity field and turbulence. The main results are obtained from statistical methods, among others by the usage of a dendrogram algorithm, and the different energy contributions are derived.
- Chap. 5 presents the smallest scales (0.01–1 pc) of the two selected massive protostellar clusters NGC 6334I and NGC 6334I(N), which were observed with SMA, APEX and HSO. The molecule HCN and its isotopologues are used to trace the most dense gas of HMCs (n=1E7 1/cm^3), and the several kinematic components (infall, outflow, rotation) are investigated by using 3D radiative transfer models. A connection to the larger scales is made in terms of the geometry and the mass accretion rate.
- Chap. 6 is a successor of chap. 5 and consists of molecular line surveys of different HMCs within NGC 6334I and I(N), and their astrochemical properties are compared among each other.
- Chap. 7 presents the conclusion and gives an outlook for possible future studies.

A list of abbreviations (acronyms and molecules) and astrophysical units, which are used in the following throughout this work, are listed in the appendix A and B. Some numbers are presented in the scientific E notation, where aEb indicates $a \times 10^b$. Computer codes and programs are marked in the `typewriter` font, whereas all variables are typeset in *italics*. The language follows the standard conventions of American English. All figures in chap. 1–2 are taken from references, whereas all the figures presented in chap. 3–7 are original.

1.2. The ISM

A brief overview of the ISM is given and its connection to star formation is discussed. Several aspects of the physics and chemistry of the ISM are reviewed by Tielens (2005), Kwok (2007), and Klessen and Glover (2014). These reviews are taken as a reference for the remaining section. What makes the study of the ISM complex is the fact that there are interplays of several physical mechanism: gravitation, thermodynamics, turbulence, magnetism, etc. In addition, it is necessary to understand the microscopic scales (on levels of atoms and molecules) to understand the macroscopic scales (on parsec). Because NGC 6334 is a source in the Milky Way Galaxy and massive star formation can only be studied in detail locally, the remaining focus lies on Galactic star formation. For a review about extragalactic studies, see Kennicutt and Evans (2012). An important relationship that connects the local and extragalactic scales is the Kennicutt-Schmidt law, eq. 1.1, which was derived from observations of star formation in several galaxies. It states that the star formation rate surface density $\Sigma_{\rm SFR}$ is proportional to the gas surface density $\Sigma_{\rm gas}$ as

$$\Sigma_{\rm SFR} = (2.5 \pm 0.7)\text{E-4} \left(\frac{\Sigma_{\rm gas}}{\rm M_\odot/pc^2}\right)^{1.4\pm0.15} \times {\rm M_\odot/yr/kpc^2}\ . \tag{1.1}$$

This relation is valid on very large scales of Mpc and is based on statistical averages, but it fails for individual GMCs. Out of all values, high density regimes are considered to be present when Σ_{gas}>100–300 M$_\odot$/pc^2, which are then called starbursts (galaxies).

The total mass of the ISM in the Galaxy is about 1E10 M$_\odot$ or 1% of the total mass in the Galaxy, which has 1E11 stars (Stahler and Palla, 2005). The ISM consists mainly of primordial gas, which elemental constituents are composed of about 70% hydrogen (H), 28% Helium (He) and the rest are heavier elements called metals. Besides of H and the chemically inert He, the most abundant metals are carbon (C), nitrogen (N) and oxygen (O). The different phases of the ISM can be distinguished by the chemical states of matter of hydrogen (or carbon): ionized (HII), neutral (HI) or molecular (H_2). In the case of carbon, these are CII, CI or CO. In general, the neutral phase is distinguished into a cold neutral medium (CNM) at temperatures of T=100 K and into the warm neutral medium (WNM) at T=1E4 K, because these two phases are stable under certain pressures. The ionization energy of H is 13.6 eV, and similar values are found for C (11.3 eV), N (14.5 eV) and O (13.6 eV). The dissociation energy of H_2 is 4.5 eV, and of CO 11.9 eV. The H-to-H_2 transition occurs at a visual extinction of A_V=0.1–0.2, which corresponds to a hydrogen column density of N(H)=2E20 1/cm^2. The dissociation of molecules in molecular clouds is protected by a mechanism called self-shielding for H_2 and by interstellar dust. At the boundaries of molecular clouds, this mechanism shields the molecular gas from the interstellar radiation field (ISRF), which originates from different sources at different wavelengths. When H_2 absorbs a UV photon, an effect called UV pumping leads to an excitation of H_2 into a higher vibrational state and will not lead directly to a photodissociation. At higher densities, this excessive energy of H_2 is released by collisions with other particles in the gas. Dust is heated by UV photons via the photoelectric effect. In the UV range (6–13.6 eV), the energy density is often expressed in units of the Habing field G_0=5.3E-14 erg/cm^3. If molecular clouds are exposed to UV photons (6–10 eV), a so-called photon dominated or photo dissociated region (PDR) develops with a layered structure. Below T = 100 K, CO and the fine structure lines of [CII], [CI] and [OI] are the most efficient cooling lines in molecular clouds.

The average galactic conversion factor from CO-to-H_2, called X_{CO} factor (eq. 1.2), relates the integrated CO line intensities to molecular column densities. According to Dame et al. (2001), this is

$$X_{CO} = N(H_2)/W_{CO} = (1.8 \pm 0.3)\text{E20 } 1/(\text{cm}^2\text{ K km/s}) . \qquad (1.2)$$

But as pointed out above, CO forms at higher A_V than H_2 and misses the content of H_2 at the surface of the molecular cloud, which mass is comparable to the molecular one (mass fraction of 50–100%, Grenier et al. 2005). This gas is called "dark gas" (invisible in CO and HI) and can be inferred by [CII], [CI] or gamma rays through interaction of H_2 with cosmic rays (CR). Cosmic rays or particles consist mainly of energetic protons and He nuclei, with energy ranges from E=100 MeV–1 TeV and an overall energy distribution of $N(E) \propto E^{-3}$ (Blasi, 2014). The origin of the accelerated particles at the highest energies is mostly unknown. Fig. 1.1 illustrates that two constituent of the ISM in the Galactic plane at different wavelengths, dust in the optical window seen in extinction and molecular gas emission from CO at submm wavelengths, are well associated with each other.

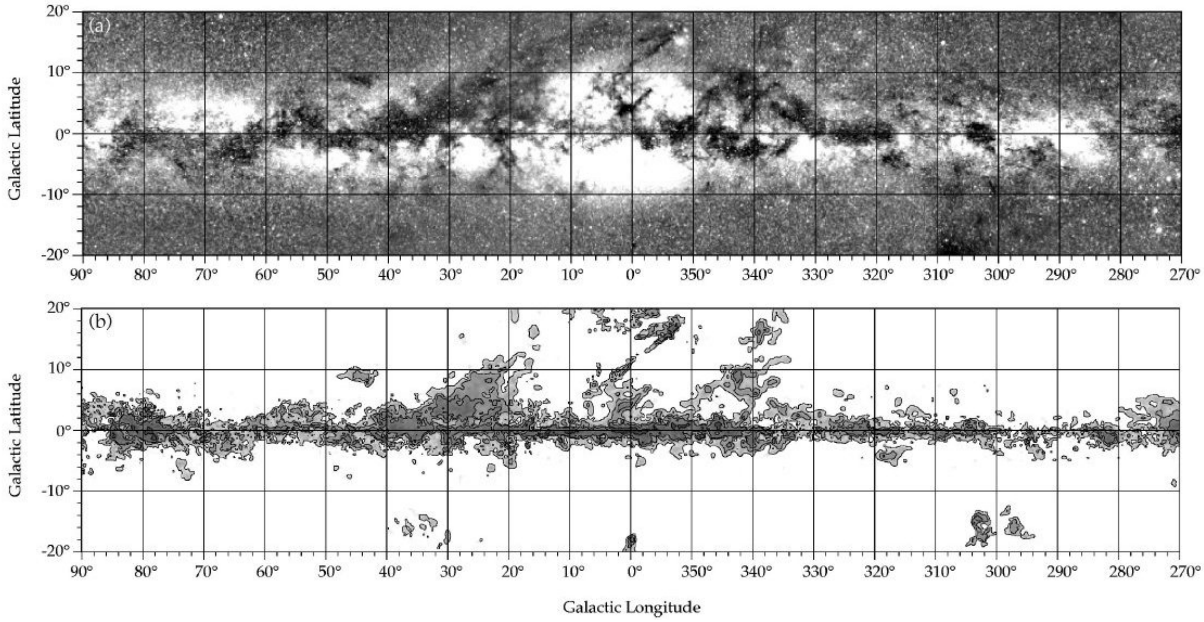

Figure 1.1.: The Galactic plane, as viewed from earth in the optical window (top) and in the submm window (bottom) by molecular gas. Adapted from Dame et al. (2001).

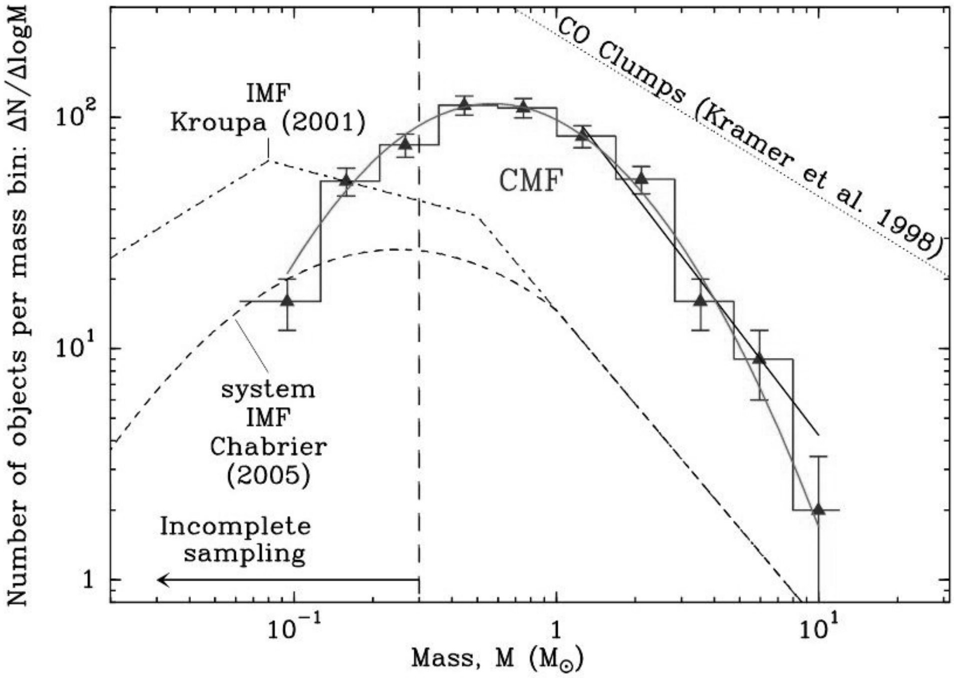

Figure 1.2.: The IMF according to Kroupa and Chabrier, together with the CMF in the Aquila region and clump mass function. Adapted from André et al. (2010).

The initial mass function (IMF), eq. 1.3 and shown in fig. 1.2, is a histogram of the stellar masses at birth, namely the number N of stars per mass interval dM. Salpeter (1955) found for stars with $M \geq 1$ M$_\odot$ the relation

$$\xi(M) = \mathrm{d}N/\mathrm{d}M \propto \mathrm{d}M^{-\alpha_\mathrm{S}}\,, \tag{1.3}$$

where the slope is constant and has a value of $\alpha_\mathrm{S} = 2.35$. In logarithmic scales, the IMF is $\xi[\log(M)] \propto \mathrm{d}M^{-x}$ with $x = \alpha_\mathrm{S} - 1$. The IMF is a cornerstone for the understanding of the stellar population and evolution in the universe, although its universality is debated. Several parameterizations exist for the IMF over all mass ranges, where the Kroupa IMF (Kroupa, 2001) and Chabrier IMF (Chabrier, 2003) are the most common ones. The Chabrier IMF includes a theoretical description of its origin, where the IMF is approximated by a log-normal function for $M \leq 1$ M$_\odot$ and for $M \geq$1 M$_\odot$ by the Salpeter slope. The mean mass is around M_c = 0.2 M$_\odot$ with a variance of logarithmic mass of 0.6. Observational constraints in the determination of the IMF are set at the higher end because massive stars become too rare, and at the lower end because substellar objects (such as brown dwarfs) become too faint. One consequence of the IMF is that out of all new born stars, only about 2% of them will have masses of $M \geq 8$ M$_\odot$. Similarly to the stages prior to the stellar birth, the core mass function (CMF) can be described at the higher mass end by a slope $\alpha_\mathrm{CMF} \approx \alpha_\mathrm{S}$. The resemblance and similar slopes between the IMF and CMF, where the CMF is shifted on the axis to higher masses, thus makes it likely that the properties of the IMF are developed in the star formation process, where an efficiency factor ε accounts for the shift and the fact that not all cores form stars. A survey of molecular clouds on bigger scales revealed that the clump mass function also has a negative constant slope, which is flatter and in the range α_cloud = 1.5–2.0 (Kramer et al., 1998).

1.2.1. Interstellar dust

For a review about the properties of interstellar dust, see Draine (2003). Historically, the existence of dust grains was inferred from a frequency dependent absorption of light against luminous sources. The so-called "reddening" (similar to phenomena in the earth's atmosphere) must be caused by small particles with sizes a at sub-micrometer scales a ≤1E7 m. More smaller grains exist than bigger grains, because the size distribution scales as $N(a) \propto a^{-3.5}$. Their total mass is usually approximately 1% of the gas mass in the ISM, i.e., the gas-to-dust mass ratio is 100. Interstellar dust mainly consists of silicates, graphites and PAHs (polycyclic aromatic hydrocarbons) with an irregular structure. One evidence for this is that the silicon monoxide (SiO) abundance is enhanced in shocked regions, such as molecular outflows, which is explained by the destruction of dust grains (Schilke et al., 1997). As these elements are only produced in the late stages of evolved stars, the origin of dust is located in the ejections of stellar winds and in the remnants of supernovae. Stars at the asymptotic giant branch at the end of their lifetime eject carbon and silicates to the ISM. It is possible that some compounds of dust produce the unknown features of the diffuse interstellar bands, which are present in absorption from the UV to the IR.

The interactions with the ISM have at least three important consequences: First, the dust emission is responsible for most of the emission in the IR by absorbing the stellar radiation energy in the VIS. They are thus important coolants at higher densities. Secondly, they interact with the interstellar magnetic field which can be deduced from polarization measurements.

The photons are scattered by the non-spherical spinning dust grains, which are aligned with their long axis perpendicular to the magnetic field through "radiative torque" (Lazarian, 2007). Consequently, the thermal radiation is polarized linearly and perpendicular to the magnetic field orientation. Thirdly, they play an important role in astrochemistry, because the dust grain mantles serve as a surface where ices can form, such as CO/H_2O, and molecules such as H_2.

1.2.2. Astrochemistry

A review about the chemical evolution in star-forming regions is given by van Dishoeck and Blake (1998). The fact that interstellar chemistry (i.e., the formation of molecular bonds) must happen in space was found by the detection of interstellar molecules. Astrochemistry tries to understand and predict via models the formation, abundance, transformation, and destruction of molecules in interstellar space. One distinguishes between reactions in the gas phase and on grain surfaces. Relative abundances of ionized molecules such as H_3^+, HCO^+, N_2H^+ can be used to derive the cosmic ray ionization rate, which is in the order of ξ_{H_2}=4E-16 1/s in the diffuse gas (Indriolo and McCall, 2012). As the temperatures in cold regions are very low (10 K), many (endothermic) reactions of neutrals are hindered in the gas phase because of an activation barrier. Molecular ions play an important role for the reactions via cosmic ray ionization such as $H_2 + CR \longrightarrow H_3^+$. N_2H^+ is for example produced via $H_3^+ + N_2 \longrightarrow N_2H^+ + H_2$. The most abundant molecule in the ISM after H_2 is CO. The formation in the gas phase follows via the reaction type dissociative recombination

$$\mathrm{HCO^+ + e^- \longrightarrow CO + H}\,, \tag{1.4}$$

whereas destruction is followed by the charge exchange

$$\mathrm{CO + H_3^+ \longrightarrow HCO^+ + H_2}\,. \tag{1.5}$$

Another reaction via other intermediates such as OH^+ or OH, or CH and CH_2, follows via the neutral-neutral reactions

$$\mathrm{C + OH \longrightarrow CO + H} \tag{1.6}$$
$$\mathrm{CH + O \longrightarrow CO + H}\,. \tag{1.7}$$

The formation of a complex organic molecule (COM), for example of methanol (CH_3OH), can be explained by the consequent hydrogenation of solid CO on grain mantles:

$$\mathrm{H + CO \longrightarrow HCO + H \longrightarrow H_2CO + H \longrightarrow H_3CO + H \longrightarrow H_3COH}\,. \tag{1.8}$$

CH_3OH acts as parent for the formation of other COMs (Choudhury et al., 2015). As the formation/destruction of one chemical species often depends on many others (and several channels compete with each other), chemical networks are build up for the purpose of modeling. The time evolution of the molecular abundances and their ratios could be used as a chemical clock to determine the age of cores. In the cold (T=20 K) dense center of pre-stellar cores, gas molecules such as CO or H_2O can absorb onto dust grains and freeze out onto their surface, thus creating icy grain mantles. This is visible in the depletion of the abundance of some molecules (e.g., CO or N_2H^+) in the gas phase in these pre-stellar regions. At later stages when a HMC develops and the temperature increases, the ice evaporates at about T=100 K for solid H_2O. This leads to a desorption of atoms and molecules into the gas phase and eventually to a rich gas phase chemistry, which is evident from the line-rich spectra of HMCs (chap. 6) and is accompanied by a chemical stratification.

1.2.3. Turbulence

By studying the properties of molecular clouds, Larson (1981) found universal scaling relationships between the velocity dispersion σ, size L and mass M or density n. The so-called three Larson's laws are :

$$(1) \qquad \sigma\ (\mathrm{km/s}) = 1.1\ L(\mathrm{pc})^{0.38} \qquad (1.9)$$

$$(2) \qquad \sigma\ (\mathrm{km/s}) = 0.42\ M(\mathrm{M}_\odot)^{0.2} \qquad (1.10)$$

$$(3) \qquad n(\mathrm{H}_2)\ (1/\mathrm{cm}^3) = 3400\ L(\mathrm{pc})^{-1.1}. \qquad (1.11)$$

The constant slope over a large variety of scales is understood to originate from the self-similar structure of the interstellar turbulence (Kritsuk et al., 2013). Turbulence is a property of fluids, which are part of hydrodynamics and described by the Navier-Stokes equation. When flows are no longer laminar, changes occur when the advection term is stronger than the dissipation term. The source for turbulence are inhomogeneities in the mean flow, which produce velocity gradients and consequently instabilities. In the ISM, examples for these sources are temperature inversions or shocks. This state is thus far from a thermodynamic equilibrium.

The definition of the Reynolds number is $Re = vL/\eta$, where v is the mean velocity, L the characteristic scale and η the kinematic viscosity. This number can be regarded as the ratio of the advection over the dissipation term. When $Re \gg 1$, a fluid becomes turbulent. The first indications for turbulence in the ISM were the large line widths and large numbers of Re>1E6, and thus many molecular clouds are super-sonic. The turbulence is thought to be driven on galactic scales by supernovae, thermal instabilities, converging flows and shear motions, because otherwise it would decay too fast compared to the crossing/dynamical timescales of GMCs. The dissipation timescales are about the same as the crossing timescale, therefore the turbulence would dissipate to fast if it is not replenished. A question remains what kind of driving sources maintain it in the Galaxy. Two forcing modes are possible, compressible modes (div $F \neq 0$) and solenoidal modes (rot $F \neq 0$), where a natural mixing of these two is often assumed in the ISM with a ratio of 0.5 (Federrath and Klessen, 2012). The formation of molecular clouds can be explained by a converging/colliding flow model (Hennebelle et al., 2008), in which flows from lower density gas collide and produce an enhancement of dense gas. Once formed, they accrete more mass from the diffuse gas. The sources of these flows and their driving mechanism could be caused by gravitationally instabilities or shears from the rotating galactic disk.

The kinetic energy power spectrum in dependence of wavenumbers $k = 2\pi/L$ at scales L for isotropic turbulence is

$$P_v(k)k^2\mathrm{d}k \propto \dot{e}^{2/3}k^{-\beta}\mathrm{d}k\,, \qquad (1.12)$$

where β=5/3 was calculated by Kolmogorov (1941) for incompressible fluids and $\beta = 2$ is obtained for compressible fluids (the so-called Burgers turbulence, see Bec and Khanin, 2007). The energy dissipation rate is denoted by $\dot{e}$. Thus, the largest energy is present at the smallest k, and the kinetic energy cascades down from the largest scales to smaller and smaller scales by creating eddies and vortices, and is dissipated at the microlevel into heat. Because the slope in eq. 1.12 is independent of the scale, this behavior is called scale-free or self-similar. Observationally, the so-called structure function is an important tool to characterize the slopes α and β. Its definition for the order p is

$$\xi(v, L) = \langle [v(r + L) - v(r)]^p \rangle , \tag{1.13}$$

where the velocity differences are calculated between a position r in dependence of the lag L, the brackets denote the average, and the mean velocity is normalized to $\langle v \rangle = 0$. The structure function of first and second order are connected via the relation $\xi_1 = \xi_2/2$. The first structure function of order p=1 corresponds to a line width-size relation and can be thus compared with Larson's first relation given in eq. 1.9. While Larson found $\alpha_1 = 0.38$, the Kolmogorov case predicts $\alpha_1 = 0.33$ and Burgers case predicts $\alpha_1 = 0.5$, which is often found in the ISM. The Fourier Transform of this autocorrelation function in eq. 1.13 of order p=2 is related to the kinetic energy power spectrum $P_v(k)$ in eq. 1.12 with the slope β by $\beta = \alpha_2 + 1$.

Turbulence in interaction with gravity is thought to be the dominant process in star formation and results in a gravo-turbulent paradigm (Klessen and Glover, 2014). Turbulence can have a positive or negative feedback, i.e., it can trigger or hinder star formation. On large scales it counteracts gravity, but on local scales it produces transient density enhancements, which can become gravitationally unstable for a short time to start the collapse. Turbulence likely controls the star formation rate and shape of the IMF. In this framework, the IMF results from an interplay between self-gravity and turbulence of the molecular gas in the ISM. The interplay between stochastic processes lead to the log-normal shape (according to the central limit theory) of the IMF for lower masses, while the scale-free behavior of the energy cascade of turbulence leads to the Salpeter slope for higher masses. Furthermore, the density and column density probability distribution function (PDF) derived from observations of molecular clouds have a log-normal shape together with a power law at the highest densities, which is due to self-gravity and collapse (Federrath and Klessen, 2012).

1.3. Star formation

1.3.1. Criteria and conditions of star formation

For a review about the theory of star formation, see McKee and Ostriker (2007), whereas the review given by Zinnecker and Yorke (2007) focuses on the special role of massive star formation. The terms "massive" and "high-mass" are used equivalently. The process of star formation is presented here with a focus on massive stars. In the context of the ISM, star formation undergoes a cyclic process: the condensations in molecular clouds form stars, which at the end of their lifetime loose mass via stellar winds (observed as planetary nebulae or Wolf-Rayet star) or via supernovae and replenish the ISM back with matter. Hydrogen and He are transformed into heavier elements through nuclear fusion in the core of stars. The ISM is therefore enriched by higher atomic numbers in the periodic system of elements for each generation or population of new stars. In detail, not all the mass is transferred back into the ISM. On the one hand, this is because of a low star formation efficiency. On the other side, low-mass stars and brown dwarfs have extreme long life times on the main sequence (>10 Gyr), and the corpses of stars (white dwarfs, neutron stars, black holes) remain and are not recycled.

It was noted on galactic and extragalactic scales that star formation is associated with molecular gas, with temperatures in the order of 1E1 K and densities above 1E2 1/cm^3. The lifetimes of protostars are approximately 0.1–0.2 Myr and for GMCs 10 Myr. GMCs are transient and bound objects, and based on Larson's relation one can estimate a dissipation timescale of $t_D = L/\sigma$. For typical values of L=100 pc and σ=10 km/s, this leads to t_D=9.8 Myr. GMCs have typical masses of 1E4–1E6 $\mathrm{M}_\odot$ and sizes of 10–100 pc and are best to study massive stars, because GMCs are often influenced by newly born OB stars. The star formation efficiency $\varepsilon = M_*/(M_* + M_\mathrm{cloud})$ is defined as the fraction of formed stellar masses M_* out of the total cloud mass M_cloud. This efficiency is generally low with 1–10%, but can reach up to 30% in GMCs (Murray, 2011). The low efficiency is explained by the turbulent properties of the ISM and by feedback from massive stars. In the Galaxy, the star formation rate is 1–2 $\mathrm{M}_\odot$/yr.

Assuming a virial equilibrium of a cloud, the equation $2\langle E_\mathrm{kin}\rangle = -\langle E_\mathrm{V}\rangle$ holds, where E_V is the potential energy and brackets denote the time average. This can for example be used to estimate the mass of a star cluster. The virial parameter is then defined as the ratio $\alpha_\mathrm{vir} = E_\mathrm{kin}/E_\mathrm{V}$. The critical threshold where a cloud is bound and self-gravitating is at $\alpha_\mathrm{crit} \leq 2$. In more general terms, a GMC under long-term conditions requires for stability the virial equilibrium to be

$$0 = 2E_\mathrm{kin} + 2E_\mathrm{T} + E_\mathrm{mag} + E_\mathrm{V}, \tag{1.14}$$

where E_T is the thermal energy and E_mag the magnetic energy.

The general criterion for star formation is that the gravitational energy E_grav dominates over all other terms in the energy balance equation 1.14, such as the kinetic energy E_kin. Jeans (1902) made a stability analysis of the necessary conditions to set collapse in a spherical cloud. This leads to a formula for certain thresholds, the Jeans mass M_J and Jeans length λ_J, whereas by neglecting all counteracting forces one obtains the free-fall time τ_ff:

$$M_\mathrm{J} = \sqrt{\frac{3}{4\pi\rho}} \left(\frac{5\mathrm{k_B}T}{\mathrm{G}m}\right)^{3/2} \;;\quad \lambda_\mathrm{J} = \sqrt{\frac{15\mathrm{k_B}T}{4\pi\mathrm{G}m\rho}} \;;\quad \tau_\mathrm{ff} = \sqrt{\frac{3\pi}{32\mathrm{G}\rho}} \,. \tag{1.15}$$

The mass of the clouds is denoted by m, $\mathrm{k_B}$ is the Boltzmann constant, G is the gravitational constant, and ρ is the mass density. The equations 1.15 thus illustrate that a decrease in the temperature T and an increase of the density ρ supports and leads to star formation in the initial stages. Furthermore, small instabilities lead to an isolated collapse and fragmentation of a cloud into multiple smaller cores. The collapse of the core begins from the center toward the outside, which is known as inside-out collapse (Shu et al., 1987). This is the transition from the pre-stellar to protostellar core. While at lower opacities the contraction and collapse evolve isothermal through radiation, the radiation gets later trapped at higher optical depths when the density increases and the core heats up. The core is then in a hydrostatic equilibrium, where the thermal pressure balances the gravitational pressure and accretion occurs only at the surface (Masunaga and Inutsuka, 2000). The angular momentum has to be conserved during the accretion process, which lead to a rotating disk and later on to a protoplanetary disk around the protostar. The pre-main sequence phase ends with the beginning of nuclear fusion of ^{1}H , the definition for the birth of a star or stellar object.

One distinguishes between a pre-stellar core, with no signs of stellar activity, and a protostellar core where the luminosity is due to the newborn star. For low-mass stars, different phases are characterized by the spectral energy distribution (SED) and its slope, which lead to the classification of a young stellar object (YSO) into Class 0, I, II, and III (Lada, 1987; André and Montmerle, 1994).

1.3.2. Massive star formation

For massive stars, this approach and classification is not applicable anymore, as they are embedded in such high densities that the SED is not sensitive to their evolutionary state. The difference between low-mass and high-mass star formation is that the Kelvin-Helmholtz timescale $t_{\mathrm{KH}} = \mathrm{G}M^2/(RL)$ is much shorter than the accretion timescale $t_{\mathrm{ac}} = M/\dot{M}$ with higher masses. The radius of a star is here R and its luminosity L. For low-mass star, the relation $t_{\mathrm{ac}} < t_{\mathrm{KH}}$ holds, while for high-mass stars the opposite is valid, $t_{\mathrm{ac}} \gg t_{\mathrm{KH}}$. The equivalence $t_{\mathrm{ac}} = t_{\mathrm{KH}}$ is approximately reached at M=8 $\mathrm{M}_\odot$ according to stellar models. This means that low-mass stars have completed their accretion before reaching the zero age main sequence (ZAMS), whereas massive protostars accrete gas also during their lifetimes on the ZAMS. A natural limit of the upper mass is given by the Eddington luminosity, when the radiation pressure balances the gravitation and the star is no longer in hydrostatic equilibrium, which is at about 150 $\mathrm{M}_\odot$. Hosokawa and Omukai (2009) studied the evolution of massive protostars with high accretion rates of >1E-4 $\mathrm{M}_\odot$/yr and derive an upper mass limit at the main sequence of 250 $\mathrm{M}_\odot$. These high rates are expected to be similar in the formation processes of the first star in the early, metal-poor universe. The extreme radiation pressure can be relaxed by non-spherical outflows along the polar axes. Massive stars above the Chandrasekhar limit of 1.4 $\mathrm{M}_\odot$ end as neutron stars or black holes, and they are responsible for the enrichment of the ISM by heavier elements than iron when they explode as a supernova type II.

Fig. 1.3 illustrates the evolution of massive stars and their typical observational features. Massive stars are formed in clusters at the condensation points of a GMC or an infrared dark cloud (IRDC), where they collapse under self-gravity and increase in mass by further accretion (ii). Such an object is also referred as High Mass Protostellar Object (HMPO). The HMC phase is characterized by a high temperature, rich chemistry and molecular outflows (iii). HMCs have main characteristics of T>100 K, r<0.1 pc, M=10–1000 $\mathrm{M}_\odot$ and L>1E4 $\mathrm{L}_\odot$ (Kurtz et al., 2000). The Lyman photons (E=hν>13.6 eV) start to ionize the surrounding gas and lead to the formation of an HII region (classified by the size as hyper-, ultra- or compact) (IV). The last stage (V) is the end of the formation, when an OB cluster/association is created which has dispersed most of the surrounding gas of the envelope. The total timescale for the formation process is about 1–2E5 yr. Molinari et al. (2008) suggested to use the L/M ratio to distinguish their evolutionary stages. From chemical models of a sample of 59 massive star-forming regions at different evolutionary stages, Gerner (2014) derives average lifetimes of 1E4 yr for an IRDC, 6E4 yr for a HMPO, 4E4 yr for a HMC and 1E4 yr for an UCHII region. It should be noted that in the sketch of fig. 1.3 the single protostars evolve simultaneously, while in nature a mixing between the stages is observed, such as an UCHII regions near a HMC or protostellar core. UCHII regions are observed in different morphologies, which is explained by simulations of Peters et al. (2010) as fluctuating and observing effects. A further observational feature of massive star-forming regions are masers detected at radio wavelengths, e.g., $\mathrm{CH_3OH}$ maser

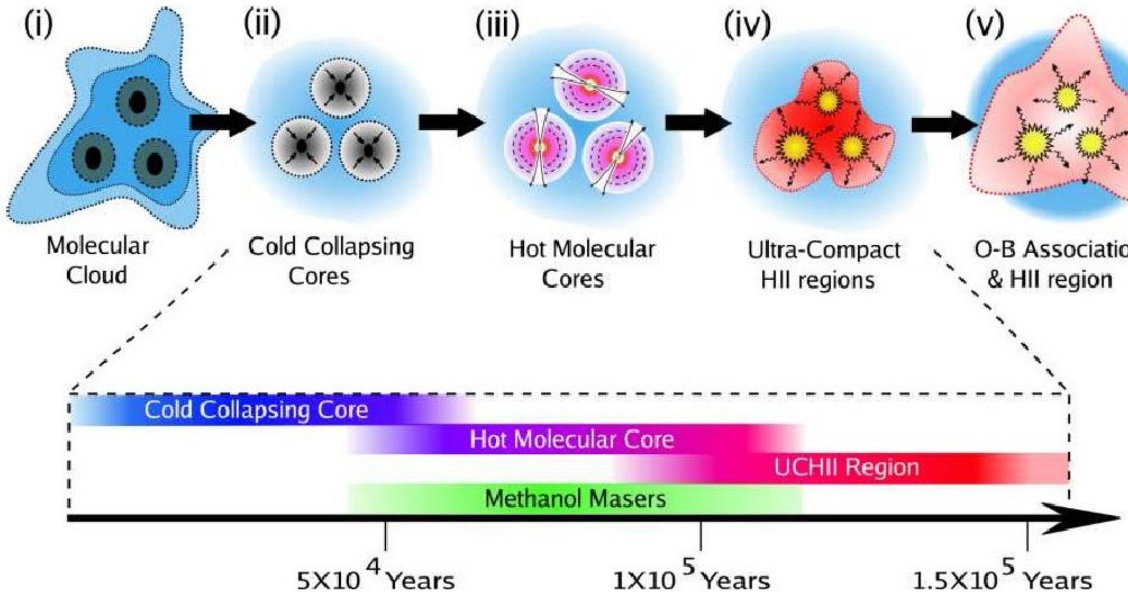

Figure 1.3.: Evolution of massive stars at different stages. A time axis is given below. Adapted from Purcell (2006).

at 6.7 GHz and 44 GHz (Cyganowski et al., 2009). They are associated with UCHII regions, circumstellar disks or outflows and are either collisionally (Class I) or radiatively excited (Class II) to maintain a population inversion.

OB-type stars are very luminous, their luminosity L scales as $L \propto M^{3.5}$ for $M < 20\ \mathrm{M}_\odot$ and scales linearly for very massive stars. Using Einstein's equation $E = Mc^2$, the life time t scales as $t \propto M/L \propto M^{-2.5}$. Thus, massive stars are short-living and their nuclear fusion reactions are very efficient. Their feedback through molecular outflows, HII regions and supernovae to the ISM is very important. They could either trigger star formation by shock compression on nearby clouds, or stop it by disrupting the molecular gas. Furthermore, the feedback can be responsible for the driving of the turbulence and the low star formation efficiency, as mentioned above.

The full understanding of the formation of massive stars is still a challenge (Tan et al., 2014). Observational complications come from the fact that they mostly form in binaries or clustered environments and are deeply embedded in their natal clumps. Furthermore, they are rare according to the IMF and because of their short life time, and many sources have large distances of many kpc. Here, the fragmentations of molecular clouds or clumps are denoted as dense cores, where the former has typical sizes of r =0.1–1 pc and masses of M=1E2–1E3 $\mathrm{M}_\odot$ and the latter r=1E2–1E3 au and M = 1–10 $\mathrm{M}_\odot$. Clumps are therefore the progenitor of a stellar cluster, while cores are the birth places of single stars or a multiple system (such as binaries). Theoretically, it is relatively unknown how these stars gather their mass and what limits the upper mass. Two main theories have been proposed for the formation of massive stars:

- The final mass of the star is pre-assembled in the core (monolithic collapse, McKee and Tan, 2003). This turbulent core model is similar to low-mass star formation with scaled up parameters. It expects high accretion rates of 1E-4–1E-3 $\mathrm{M}_\odot$/yr, which can be achieved through non-spherical infall through disks (Kuiper et al., 2010). In combination with bipolar jets/outflows, this circumvents the large radiation pressure barrier.

- Protostars grow in mass depending on their position in the clump (competitive accretion, Bonnell et al., 2006). The most massive core accretes more mass from the gas reservoir in the gravitational potential wall and wins over lower mass stars. This explains naturally the highly clustered structure of OB associations and the mass segregation (where the most massive stars are found in the center). Furthermore, these simulations lead to a stellar mass distribution in agreement with the IMF.

The merging and coalescence model (Bonnell and Bate, 2002), where massive stars are formed by the encounter or collision of lower mass stars, is assumed to occur only in rare events. Although these scenarios appear to be distinct and the question arises which of them dominates, it is imaginable that intermediate scenarios occur.

1.3.3. The filamentary structure of the ISM

With the sensitivity of the HSO, the evidence for the importance of filaments in the ISM was established, which are present universally in all molecular clouds (Molinari et al., 2010; André et al., 2010). The non-observance of filaments previously can be explained by the lack of resolution and sensitivity. Furthermore, the clump finding algorithms tended to decompose the clouds into separate cores, whereas newer algorithms take into account the hierarchical structure of GMCs. For the sources in the Gould Belt survey, it was shown that the average widths of the filaments are similar in a narrow range, namely 0.1 pc (Arzoumanian et al., 2011). The filament's profile is well fitted by a Plummer-like function with a flatter exponent of p=2.4. One explanation for the observed width is that this corresponds to a stability point in the turbulent scenario if the sound speed is c_s=0.2 km/s, which is typically observed in the ISM.

In this new paradigm of star formation, filaments form first in the ISM as a result of magnetohydrodynamic (MHD) turbulence (or by shocks or convergent flows). In the densest filaments ($n \geq$2E4 1/cm^3), pre-stellar cores form within filaments because of gravitationally instabilities above a certain threshold (150 $\mathrm{M}_\odot/\mathrm{pc}^2$ or A_V=8). Elongated structures perpendicular to the main filament, called subfilaments or striations, are found to accrete onto it (Schneider et al., 2010). The formation of filaments is a natural outcome of the interplay of gravo-turbulence, where for example sheets collapse to cylindrical structures (Burkert and Hartmann, 2004) and their formation is enhanced by magnetic fields. As is pointed out by Gómez and Vázquez-Semadeni (2014), filaments accrete gas from their environment and transmit it to the clumps within them. The collapse proceeds along the shortest axes in the filament. This picture is furthermore similar at extragalactic scales, where the cosmic web is made out of a network of filaments, where the knots correspond to galaxies but the main gravitational mass is assumed to be made out of dark matter.

A velocity analysis of the filaments in the 10 pc-long complex L1495/B213 in Taurus revealed that they consist of subfilaments, which are distinguished by their mean velocity and have small velocity separations of <1 km/s (Hacar et al., 2013). They are grouped similar to fibers in a rope or bundles. Some of them are fertile, i.e., they include protostellar cores, but most are infertile and stable against collapse. Some properties of an infinite isothermal gas cylinder were initially calculated by Ostriker (1964), such as the critical mass per line M_crit. Larson (1985) and Nagasawa (1987) calculated the fragmentation length λ_f for an infinite isothermal gas cylinder for the case if the radius $\mathcal{R}$ is bigger than the scale height, $\mathcal{R} \gg H$ and p=4. The equations are:

$$M_{\rm crit} = 2c_{\rm s}^2/{\rm G} \tag{1.16}$$

$$\lambda_{\rm f} = 22.4H \quad \text{where} \quad H = c_{\rm s}/\sqrt{4\pi {\rm G}\rho}. \tag{1.17}$$

Following the analysis from Jackson et al. (2010), the sound speed $c_{\rm s}$ should be replaced by the velocity dispersion σ in eq. 1.16 if the turbulent pressure is higher than the thermal pressure.

An attempt is being made to understand the role of the magnetic field in the formation of filaments. For a sample of GMCs, Crutcher (2012) used a Bayesian analysis to deduce the magnetic field strength $B_{\rm z}$ in z-direction by

$$B_{\rm z}(n) = \begin{cases} B_0 & \text{if } n < n_0 \\ B_0(n/n_0)^\alpha & \text{if } n > n_0\,, \end{cases} \tag{1.18}$$

where median values of B_0 = 10 μG, n_0=300 1/cm^3 and α=0.65 are obtained. Most often, the magnetic field energy is too weak to support the gravitational collapse. This is expressed by the mass to magnetic flux ratio $\lambda = M/M_\Phi$, where $\lambda > 1$ is defined as supercritical. In terms of the column density, this can be expressed as

$$\lambda = 7.6\text{E-21}\ N({\rm H_2})(1/{\rm cm}^2)/B(\mu{\rm G})\ . \tag{1.19}$$

Observations indicate that the orientations of magnetic fields follow a bimodal distribution with the orientation of filaments, which are either parallel or perpendicular to them (Li et al., 2013). They could channel the sub-Alfvénic turbulence to form filaments aligned with them. Mechanism to get rid of strong magnetic fields, which would otherwise prevent the collapse, are known as ambipolar diffusion (a drift between charged and neutral particles) or magnetic braking. Magnetorotational instabilities help to move the angular momentum outside and gas mass inside.

1.4. Review of the NGC 6334 complex

NGC 6334 is a massive star-forming region and listed as no. 6334 in the New General Catalogue of Nebulae and Clusters of Stars (NGC). It is located at the central equatorial coordinates of α(J2000):17$^{\rm h}$20$^{\rm m}$36$^{\rm s}$, δ(J2000):-35°51′0″, or in Galactic coordinates at l=351.33° and b=0.66°. It lies thus slightly above the Galactic plane in the southern hemisphere, -9° west of the Galactic center. Fig. 1.4 presents the appearance of NGC 6334 at different wavelengths, which stretches to some 10 pc. Observations of NGC 6334 in the VIS show that the main filament, which runs parallel to the Galactic plane, is seen in absorption. The filament thus lies on the front side toward the observer and is illuminated by HII regions in the background. Because it radiates in the VIS and Hα at 656.3 nm, it is classified as a diffuse emission nebula. About 270 publications have been published with the focus on NGC 6334, whereas papers related to it reaches over 1000. It is thus attempted to give only an overview over the most important articles and aspects of this source. A detail discussion of relevant parts, and details about sources embedded in this region such as the dense clumps NGC 6334I and I(N), are discussed in the corresponding chapters.

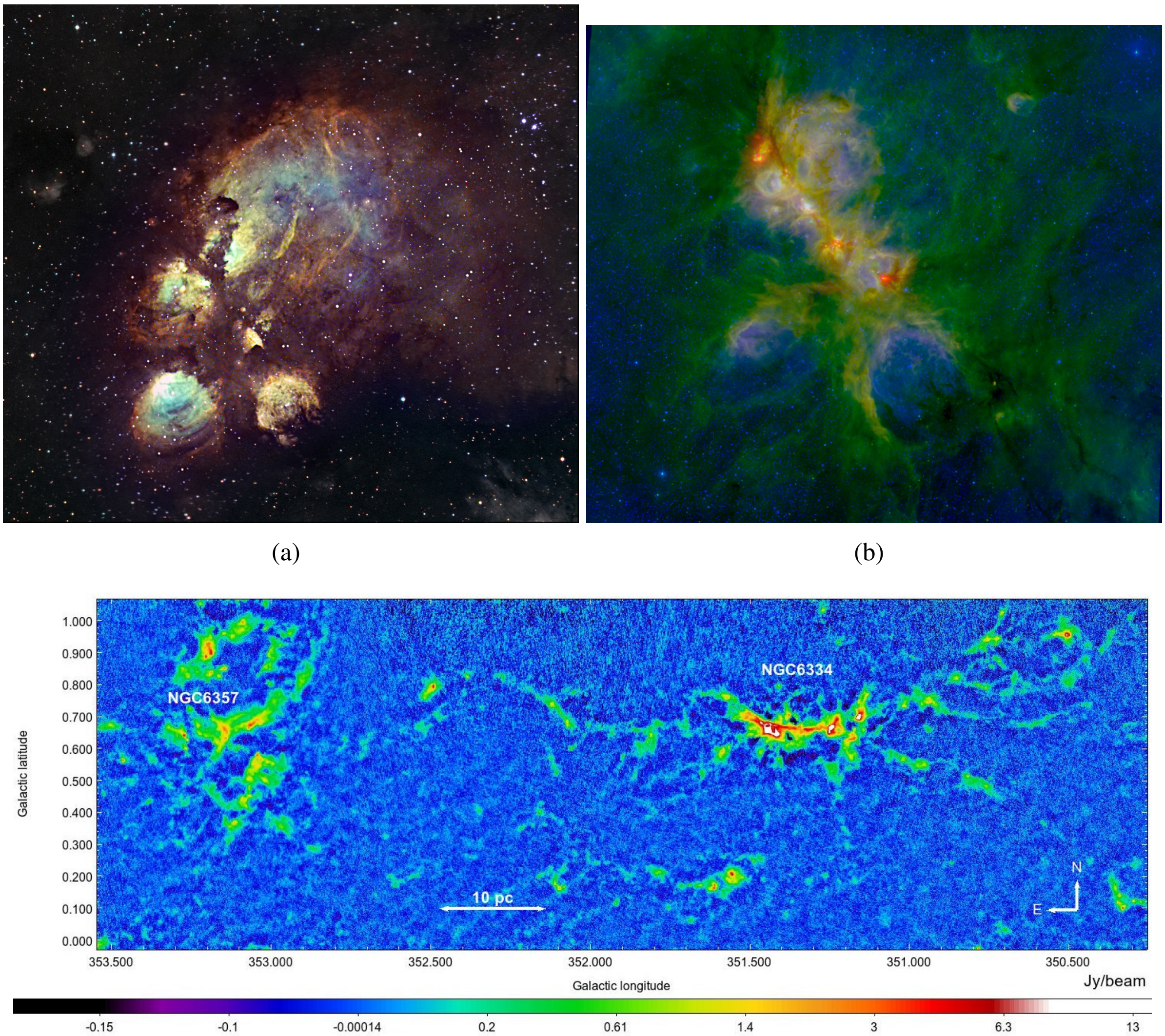

(a) (b)

(c)

Figure 1.4.: The star-forming region NGC 6334 at different wavelengths. (a) VIS color composite image (credit: M. Caligiuri, Uniform resource locator (URL): `http://www.mcaligiuri.net/NGC6334_nb.html`). (b) IR composite image, adapted from Willis et al. (2013). (c) Submm dust continuum emission from the APEX Telescope Large Area Survey of the Galaxy (ATLASGAL, Schuller et al., 2009). (a) and (b) are given in equatorial and (c) in Galactic coordinates.

The distance was determined by Neckel (1978) to 1.7 kpc and confirmed by Russeil et al. (2012). It is thus part of the Carina-Sagittarius arm of the Galaxy. Recently, the distance to the clump I(N) is reported to be (1.35 ± 0.1) kpc (Wu et al., 2014) and ($1.26^{+0.3}_{-0.2}$) kpc (Chibueze et al., 2014) from trigonometric parallax observations of CH_3OH and H_2O maser, respectively. As this deviates from the previous derived photometric distance of (1.7 ± 0.3) kpc mentioned above, and from the kinematic distance of 1.7 kpc (Wu et al., 2014), it was decided to use in this work the more commonly adopted value of 1.7 kpc in the literature for consistency with other works.

NGC 6334 has been explored at multiple wavelengths from the radio to X-ray bands in molecular, atomic and ionized gas (Persi and Tapia, 2010): at radio bands for example by Rodriguez et al. (1982) and Jackson and Kraemer (1999); at submm wavelengths in molecular lines by Dickel et al. (1977) and Kraemer and Jackson (1999) in CO; in other molecular tracers by Russeil et al. (2010); in dust continuum by Muñoz et al. (2007) and Matthews et al. (2008); at THz frequencies in [CII] by Boreiko and Betz (1995), which revealed contributions from PDRs, ionized and colder gas; in [OI] and [CII] by (Kraemer et al., 2000); in the IR by Loughran et al. (1986) and Willis et al. (2013), where the total luminosity of the FIR-sources I–V was determined to be 1.7E6 $L_\odot$ and the total mass is a few 1E5 $M_\odot$; in the UBVR bands by Russeil et al. (2012); and in X-rays by Feigelson et al. (2009), who estimate the total stellar population to 2–3E4 pre-main sequence stars.

The magnetic field strength was studied by Sarma et al. (2000) with Zeeman observations of OH and HI, where values in the order of $B = 200\ \mu$G are found for the dense clumps. Especially for source A (or IV), the velocities are super-sonic (M_S=2.9) and sub-Alfvénic (M_A=0.3), and the magnetic field energy is as important as the kinetic energy. The polarimetry measurements of Li et al. (2006) show that the mean magnetic field orientation in NGC 6334 is perpendicular to the Galactic plane, in contrast to other GMCs. Similarly, the magnetic energy density is comparable with the turbulent energy density.

Recently, NGC 6334 was observed with the HSO as part of the program Herschel imaging survey of OB Young Stellar objects (HOBYS, Tigé, 2014; Russeil et al., 2013). Focusing on the most dense cores, where a threshold of 40 $M_\odot$ is applied, most of them are found in the dense ridge or main filament. A total number of 46 cores are counted, and all dense cores are placed in filaments. The average values are r=0.08 pc, n =6E5 1/cm^3, m=104 $M_\odot$ and L=5.73E3 $L_\odot$. With an average temperature of T=23.5 K they are warmer than the lower dense cores. According to the temperature and density distribution in NGC 6334, Russeil et al. (2013, fig. 3) divide this region into 4 sub-regions: the center with the so-called main ridge, a cold region to the east, a filamentary region to the west, and a quiet region to the northwest.

The nearby large HII region NGC 6357 (2° east) is a GMC in a much more evolved stage, where most of the molecular gas is disrupted, and the embedded open OB cluster Pismis 24 contains very massive stars (Cappa et al., 2011). It is found that NGC 6357 and NGC 6334 have about the same distance, the same mean velocity of -4 km/s and are connected by a filament. Thus it is assumed that they have formed together out of a larger complex (Russeil et al., 2010, 2012).

2. Basics of molecular and submm astrophysics

2.1. Molecular spectroscopy

Molecules can be excited in different ways, and energy levels exist for rotational, vibrational, electronic and nuclear excitations. Like for atoms, at lower energies there are energy separations in the case of fine structure (which is among others due to the spin-orbit coupling of electrons) and hyperfine structure (by interactions between the quadrupole moment of the nucleus and the gradient of the electric field). There are additionally internal degrees of freedom modes, such as torsional (CH_3OH), inversion (NH_3) transitions or ℓ-type doubling (HCN). Because ^{14}N has a non-zero nuclear spin, HCN shows a hyper-fine splitting. According to the Born-Oppenheimer approximation, the energetic terms in the Hamiltonian operator can be decoupled because of mass differences (between the electrons and nuclei) and energetic differences. The typical wavenumbers $\tilde{\nu}$ for rotational transitions are 1 cm^{-1}, for vibrational transitions 1E3 cm^{-1}, and for electronic excitations >1E4 cm^{-1}. One wavenumber corresponds to a frequency of $\nu \approx 30$ GHz or to a thermal energy of $E/k_B = 1.4$ K.

The rotational transitions of molecules can be derived if they are treated as rotors, where a classification into five categories is made dependent on their moment of inertia (linear, spherical, prolate symmetric, oblate symmetric and asymmetric top). At submm wavelengths and temperatures of 10–100 K, most molecules are only rotationally excited. The energy levels of a linear molecule, approximated to first order by a rigid rotor, and its energy separations ΔE are given by eq. 2.1 and 2.2:

$$E(J) = \mathrm{h}^2/(8\pi^2 I)J(J+1) = \mathrm{h}BJ(J+1) \tag{2.1}$$

$$\Delta E(J) = \mathrm{h}\Delta\nu = \mathrm{h}2BJ \quad \text{for} \;\; \Delta J = \pm 1 \; . \tag{2.2}$$

The moment of inertia is I, J is the rotational quantum number (with a degeneracy of $g_J = 2J+1$), B is the rotational constant, and h is the Planck constant. The larger I gets for more complex molecules, the smaller B and therefore the density of spectral lines per frequency band increases. The rotational constant is for example for the molecule $^{12}C^{16}O$ B=57.636 GHz. The atomic mass number for the main isotopologue is omitted in the following, i.e., $^{12}C^{16}O \mathrel{\widehat{=}} CO$. The transition probability p is proportional to the transition dipole moment M:

$$p \propto |M|^2 \, , \quad \text{where} \quad M = \langle \Psi(J) | \hat{\mu} | \Psi(J-1) \rangle \; . \tag{2.3}$$

The allowed selection rule for dipole transitions is $\Delta J = \pm 1$. The electric dipole moment is for example for CO μ=0.1 D (1 Debye = 3.33564E-30 Cm), for HCN μ=3 D, and for HCO^+ μ=3.9 D (see the Cologne Database for Molecular Spectroscopy (CDMS) for references). The most abundant molecule in the ISM, molecular hydrogen, is difficult to observe because of a missing permanent electric dipole moment and a high excitation level. This is the reason why CO is used to trace the gas contents of molecular gas, as mentioned in sect.1.2.

Big databases of rotational and vibrational spectra of molecules, related to astronomy, are collected in the CDMS (Müller et al., 2005) and JPL catalog (jet propulsion laboratory, Pickett et al., 1998). Both catalogs are being incorporated into the Virtual Atomic and Molecular Data Centre (VAMDC, Rixon et al., 2011). Because spectral lines in the ISM can only be identified if the chemical species is measured in the laboratory, the unambiguous detection of new species depends on the availability of new measurements in molecular spectroscopy. As of 11.2014, more than 180 molecules have been detected in the ISM or circumstellar shells [1].

2.2. Radiative transfer

Almost all information in astronomy is inferred from electromagnetic radiation. Thus, the understanding of the propagation and change of light in a medium is fundamental to understand the matter in it. The differential change of the specific intensity dI ($[I]$=W/(m^2 Hz sr)) at a frequency ν in a medium along the path ds is governed by the emission coefficient ϵ and absorption coefficient κ. The equation of transfer is referred as

$$\mathrm{d}I_\nu = \epsilon_\nu \mathrm{d}s - I_\nu \kappa_\nu \mathrm{d}s \quad \text{or} \quad \mathrm{d}I_\nu / \mathrm{d}\tau = -I_\nu + S_\nu \,, \tag{2.4}$$

where the optical depth is defined as $\mathrm{d}\tau = \kappa_\nu \mathrm{d}s$ and the source function as $S_\nu = \epsilon_\nu / \kappa_\nu$. The solution of this differential equation is complicated by the fact that it is a recursive problem, where S and I have to be known at once and depend on each other. A so-called gray body is a frequency independent source function. The formal solution between τ_1 and τ_2 is given by:

$$I_\nu(\tau_1) = I_\nu(\tau_2) \exp[-(\tau_2 - \tau_1)] + \int_{\tau_1}^{\tau_2} \mathrm{d}t S_\nu \exp[-(t - \tau_1)] \,. \tag{2.5}$$

With the assumption of a constant source function, eq. 2.5 is solved to give

$$I = I_0 \exp(-\tau) + S[1 - \exp(-\tau)] \tag{2.6}$$

$$I_{\mathrm{on}} - I_{\mathrm{off}} : T_\nu = [J(T_{\mathrm{ex}}) - J(T_{\mathrm{bg}})][1 - \exp(-\tau)] \tag{2.7}$$

$$\text{where} \quad J(T) = \frac{\mathrm{h}\nu}{\mathrm{k_B}} \frac{1}{\exp[\mathrm{h}\nu/(\mathrm{k_B}T)] - 1} \,. \tag{2.8}$$

The eq. 2.7 is the so-called detection equation, where the line emission on the source I_{on} is subtracted from another position on the sky which is free of line emission in the ideal case I_{off}. This on-off observation is done for calibration purposes and is further discussed in sect. 2.3. The intensity is conventionally given in brightness temperature $J(T)$ in radio/submm astronomy. If no other background sources are present, $J(T_{\mathrm{bg}})$ corresponds to the cosmic microwave background of 2.7 K. If the source function is a black body and the Rayleigh-Jeans approximation

$$I = 2\nu^2 \mathrm{k_B}/\mathrm{c}^2 \times T \tag{2.9}$$

holds, then the brightness temperature equals the radiation temperature, $T_{\mathrm{B}} = T_{\mathrm{R}}$. The speed of light is denoted as c. The antenna temperature is the measured temperature at the telescope including the beam dilution for unresolved sources, i.e., $T_{\mathrm{A}} = \eta T_{\mathrm{B}}$. The beam filling factor is $\eta = \theta^2/(\theta^2 + \theta_B^2)$, where θ is the source size and θ_{B} the beam size. By using the Rayleigh-Jeans approximation, the flux density or intensity I can be converted from units of Jy/beam into brightness temperature T_{B} in units of Kelvin by taking the beam size θ_{B} of the telescope into

---

[1] URL: `http://www.astro.uni-koeln.de/cdms/molecules`

account:

$$T_{\rm B}({\rm K}) = 1.22{\rm E}6 \cdot F({\rm Jy})/[\nu({\rm GHz}) \cdot \theta_{\rm B}('')]^2\,. \tag{2.10}$$

Two limiting cases occur in eq. 2.7 in dependence of the optical depth τ. In the optically thin limit $\tau \ll 1$, $T \propto \tau \propto N$ and the measurement is sensitive to the column density N. In the optically thick limit $\tau \gg 1$, $T = J(T_{\rm ex})$ and the brightness temperature equals the excitation temperature, but the column density or abundance is undetermined because only the surface of the emitting region is visible.

2.2.1. Line emission

Under the conditions of LTE, every population of a level n_i is given by the Boltzmann distribution in eq. 2.11:

$$n_i = \frac{N}{Z(T)} g_i \exp[-E_i/({\rm k_B}T_{\rm ex})] \quad \left(Z = \sum_j g_j \exp[-E_j/({\rm k_B}T)]\right), \tag{2.11}$$

where Z is the partition function and N is the total number of particles. $T_{\rm ex}$ equals the kinetic temperature $T_{\rm kin}$ for high densities if collisions dominate the excitation of energy levels. If on the other hand the radiative excitation dominates, then $T_{\rm ex}$ equals the radiation temperature $T_{\rm R}$. In general, the question is which excitation mechanism dominates in eq. 2.14. The optical depth is related to the upper state column density $N_{\rm u}$ of a chemical species by

$$\tau(\nu) = \frac{{\rm c}^3}{8\pi\nu^3} A\, N_{\rm u}\, (1 - \exp[-{\rm h}\nu/({\rm k_B}T_{\rm ex})])\, \phi(\nu)\,, \tag{2.12}$$

where A is the Einstein coefficient for spontaneous emission, and $\phi(\nu)$ is the normalized line profile function (e.g., a Gaussian) in units of $1/\Delta\nu$.

Several approximate solutions exist to solve eq. 2.4 for line emission, involving simplifications such as the escape probability solution or the Large Velocity Gradient (LVG) method, also called as Sobolev approximation (Sobolev, 1957). If $\Delta v_{\rm th}$ is the thermal line width and $\mathrm{d}v/\mathrm{d}r$ the velocity gradient, this approximation is justified if the Sobolev length $l_{\rm S} = \Delta v_{\rm th}/(\mathrm{d}v/\mathrm{d}r)$ is smaller than the interaction length, which means that photons from different regions are not interacting anymore with others as a result of a Doppler velocity shift. For molecular clouds, this method is a valid approximation in the line tracer of ^{13}CO (Ossenkopf, 2002).

Full non-LTE conditions can be solved only numerically and iteratively, where again different methods and codes exist, see van Zadelhoff et al. (2002) for an overview. In non-LTE conditions, the statistical equilibrium equation must be solved. If the population distribution is unchanged in a steady state, the incoming rates R_{kj} must balance the outgoing rates in eq. 2.13. Considering a two-level system (l for the lower and u for the upper state), the statistical equilibrium equation (eq. 2.14) balances the radiative and collisional excitation and de-excitation of the population n:

$$\sum_j n_j R_{jk} = \sum_k n_k R_{kj} \tag{2.13}$$

$$n_{\rm l} n_{\rm c} \gamma_{\rm lu} + n_{\rm l} B_{\rm lu} J_{\rm ul} = n_{\rm u} n_{\rm c} \gamma_{\rm ul} + n_{\rm u} B_{\rm ul} J_{\rm ul} + n_{\rm u} A_{\rm ul}\,. \tag{2.14}$$

A and B are the Einstein coefficients, n_c is the collision partner (H_2 or He) and γ_{ul} the collisional rate coefficient. Collision rates are either computed quantum-chemically, or are measured from reaction rates in the laboratory which is difficult at very low temperatures. A collection of collision rates for the most common molecules are listed in the Leiden Atomic and Molecular Database (LAMDA, Schöier et al., 2005).

Examples of radiative transfer codes are RATRAN (Hogerheijde and van der Tak, 2000) in 1D, and `RADMC-3D`[2] and `LIME` in 3D (Brinch and Hogerheijde, 2010). `LIME` is furthermore incorporated in the ARTIST program (Adaptable Radiative Transfer Innovations for Submillimeter Telescopes; Padovani et al., 2011). `myXCLASS`[3] is an 1D LTE code, which makes use of the line catalogs with entries for many species (>1000) and is now interfaced with the `CASA` (Common Astronomy Software Applications) package.

`LIME` uses the accelerated lambda iteration method (ALI, Rybicki and Hummer, 1991) in combination with a Monte-Carlo method for the photon propagation (accelerated Monte-Carlo). Basically, the radiation field is split into a local and external field by

$$J_\nu^{k+1} = \Lambda_{\rm ext}[S_\nu(J_\nu^k)] + \Lambda_{\rm loc}[S_\nu(J_\nu^{k+1})]\,, \tag{2.15}$$

and the equations are solved for the part that come inside and outside of a cell separately for the current iteration k. Because the local lambda operator $\Lambda_{\rm loc}$ is a di- or triagonal matrix, the inversion of this matrix and this algorithm is much faster. In the first step, the source function is often assumed to be the LTE solution. The intensity J is then calculated at every point as a function of τ. This is then substituted back into the eq. 2.4 and repeated until convergence is achieved.

The usefulness of molecular or atomic line tracers depends on the physio-chemical conditions which one wants to study. The critical density is defined as

$$n_{\rm cr} = A/\langle v\sigma\rangle\,, \tag{2.16}$$

where v is the mean velocity and σ the cross section. The denominator is thus the collision rate coefficient γ (in units of cm^3/s). If the density is higher than $n_{\rm cr}$ of a transition, the populations are excited enough to be in LTE and thermalized. If the density is too low, the populations are only subthermal excited and can be out of equilibrium. For example, the values for line tracers used in this work (together with the upper energy level E_u) are

- $n_{\rm cr}$=6.7E3 1/cm^3, E_u=16.6 K for CO (J=2–1),
- $n_{\rm cr}$=4.2E6 1/cm^3, E_u=26 K for HCO$^+$ (J=3–2),
- and $n_{\rm cr}$=1.5E8 1/cm^3, E_u=43 K for HCN (J=4–3).

The values are taken from Tielens (2005). Thus, only a combination of several line transitions will probe all regions of a molecular cloud.

---

[2] URL: `http://www.ita.uni-heidelberg.de/~dullemond/software/radmc-3d/`

[3] URL: `https://www.astro.uni-koeln.de/projects/schilke/myXCLASSInterface`

2.2.2. Continuum emission

The continuum SED provides important information about an astronomical source. In the submm regime, the dust continuum emission is often modeled by a modified black body, which in the optically thin case τ<1 gives

$$I = \Omega\ B(T)\ \tau_\mathrm{d} = \Omega\ B(T)\ \tau_0\ (\nu/\nu_0)^\beta \tag{2.17}$$

$$\tau_\mathrm{d} = N(\mathrm{H}_2)\ (\kappa_\mathrm{d}/\rho_\mathrm{d})\ (\rho_\mathrm{d}/\rho_\mathrm{gas})\ m_\mathrm{g} \tag{2.18}$$

$$B(\nu,T) = \frac{2\mathrm{h}\nu^3}{\mathrm{c}^2}\frac{1}{\exp[\mathrm{h}\nu/(\mathrm{k_B}T)]-1}\ . \tag{2.19}$$

Ω is the source solid angle, τ_d the dust optical depth, and κ_d is the dust opacity (in units of cm^2/g). The third factor in eq. 2.18 is the dust-to-gas mass ratio R_d, and m_g is the gas mass per H_2 molecule. The gas mass per particle in a molecular cloud is computed to 2.7 $\mathrm{m_h}$, with the condition that the composition of the ISM is 73% H, 25% He and 2% metals. The dust emissivity index β is usually in the range 1–2. $B(\nu,T)$ in eq. 2.19 is the Planck function. By knowing or fitting the dust temperature from the SED, the total dust or gas mass of a cloud is calculated by

$$M = S_\nu D^2/(\kappa_\mathrm{d} R_\mathrm{d} B(T))\ , \tag{2.20}$$

where S_ν is the integrated flux density $S_\nu = \int I_\nu\ \mathrm{d}\Omega$ (integrated over the source size) and D the distance. The optical depth is related to the visual extinction by $A_\mathrm{V} = 1.086\tau$, and the average galactic conversion factor from N(H) to extinction is N(H)/A_V=1–2E21 1/(cm^2 mag). The dust temperature in `RADMC-3D` is calculated after the recipe by Bjorkman and Wood (2001). A star is placed at a position r with a luminosity L, and in thermal equilibrium the dust heating and cooling rates of dust particles are balanced in each cell by Monte Carlo sampling the grid via sending photons from the star in each direction. The star is assumed to be a black body with a radius R and an effective surface temperature of T_eff. Given the luminosity, T_eff is calculated via

$$L = 4\pi R^2 \sigma T_\mathrm{eff}, \tag{2.21}$$

where σ is the Stefan-Boltzmann constant.

In the case of an UCHII region, the ionized gas radiates by free-free emission from electrons. The free-free opacity is given by

$$\tau_\mathrm{ff} \propto \nu^{-2.1}\ T_\mathrm{e}^{-1.35} \int n_\mathrm{e}^2\ \mathrm{d}s, \tag{2.22}$$

where T_e is the electron temperature, n_e is the electron density and $\int n_\mathrm{e}^2\ \mathrm{d}s$ is known as the emission measure along the line-of-sight (LOS). The SED is then flat or declining with $S_\nu \propto \nu^{-0.1}$ in the optically thin case (typically at submm ranges), and scales like $S_\nu \propto \nu^2$ in the optically thick case at lower frequencies. Thus, radio continuum observations at cm wavelengths are suited to study this ionized medium. Furthermore, the dust is heated in the vicinity of an UCHII region, which can be seen by the PAH emission in the IR at 8 μm (see sect.5.3.4). The radius R_s of an HII region is related to the ionizing flux S (number of Lyman photons above 13.6 eV per second) by the so-called Strömgren sphere in eq. 2.23, which is calculated by balancing the ionization and recombination rates of H. In a homogenous medium, this is

$$4/3 \times \pi R_s^3 n_e^2 \alpha = S, \tag{2.23}$$

where $\alpha(T_e)$ is the recombination coefficient and n_e is equal to the number of protons n_p if the HII region is fully ionized.

2.3. Submm telescopes

The submm wavelengths lie between the microwave/radiowave and far infrared regime of the electromagnetic spectrum. These wavelengths are sensitive and best suited for studying star formation, because the typical continuum temperature of 10–30 K peaks in the FIR (according to Wien's displacement law $T\lambda_{\max}$=2.9 mm K), and the molecules are excited such that their rotational lines fall in this window, as mentioned above. Furthermore, the information in spectral line profiles allows studying the kinematic properties of molecular clouds, and the extinction by dust grains declines with decreasing frequency, as mentioned in sect. 2.2.2. Most of the submm telescopes operate with receiver bands in the frequency range 100–1000 GHz (or equivalently at wavelengths of 3–0.3 mm and photon energies of 4.8–48 K). A challenging problem at these frequencies is the earth's atmosphere with its telluric absorption lines, because water (H_2O) and oxygen (O_2 and O_3) have some absorption bands in this window. The water vapor (measured in PWV) decreases with increasing height above the sea level. Therefore, the precipitable water vapor (PWV) in the atmosphere effects the transmission and noise, see fig. 2.1. One expensive solution to circumvent this issue is to move above the atmosphere, by either using balloons, planes or satellites in space. For example with the HSO, it was possible to detect and study the important molecule H_2O in protoplanetary disks.

Fig. 2.2 comprises the three telescopes used in this work. APEX is a 12m single-dish (Güsten et al., 2006), located at the Llano de Chajnantor Observatory at an altitude of 5100 m in the Atacama desert in Chile. SMA (Ho et al., 2004) is an interferometer which consists of 8 × 6 m telescopes, located at the volcano Mauna Kea at an altitude of 4080 m on Hawaii. The HSO uses a 3.5 m single-dish (Pilbratt et al., 2010), which was during its operating time (2009-2013) parked in the Lagrange point L2 outside of the earth's orbit.

2.3.1. Single-dishes

In the following, the APEX telescope is used as a prototype for most antennas in the submm range. The common submm single-dishes are parabolic antennas with a secondary reflector. They are alt-azimuth mounted Cassegrain-Nasmyth systems, which focuses the collected signal into the receiver cabins. For dust continuum observations, which need no coherent detection, bolometer cameras are used by absorbing the photon energies. Furthermore, by implementing a polarizing device in front of them, sensitive polarization measurements are possible of magnetic fields. For spectroscopic observations, heterodyne receivers are used, which are made mostly of Superconductor-Insulator-Superconductor (SIS) mixers and cooled down to liquid helium temperatures of 4 K. The input signal in voltages is calibrated to temperatures by the chopper wheel method by measuring hot/cold loads and the sky. The main lobe of the power beam pattern (the Fourier Transform of the aperture) can be approximated by a Gaussian function

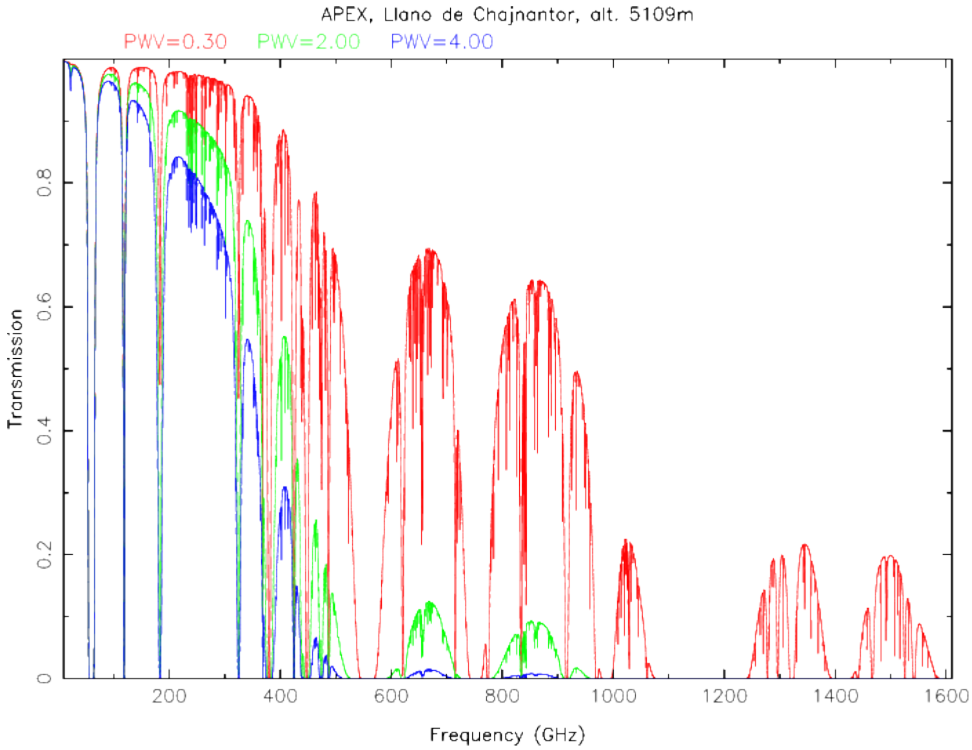

Figure 2.1.: Atmospheric transmission at the site of APEX in dependence of frequency for different PWV. Reference: APEX transmission calculator, Juan Pardo.

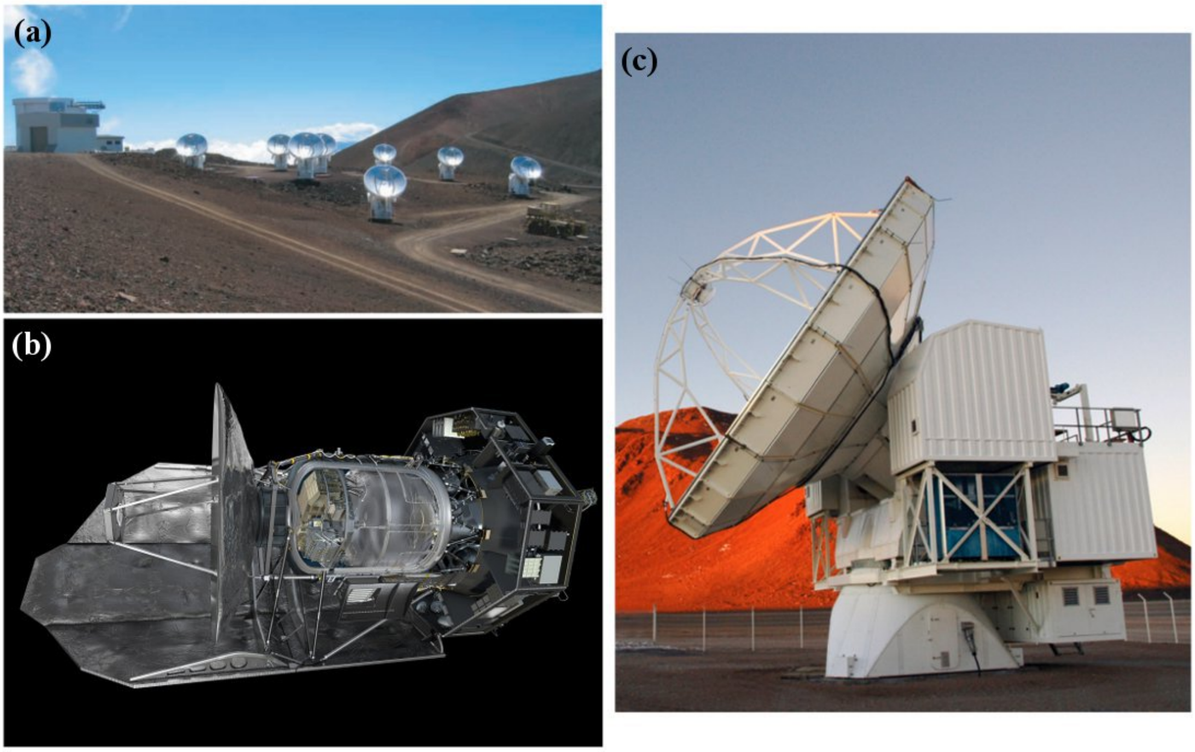

Figure 2.2.: Submm observatories used in this work. (a) SMA (Ho et al., 2004), (b) computer model of HSO (Pilbratt et al., 2010), (c) APEX (Güsten et al., 2006).

with a beam size θ_B, whereas the secondary maxima are referred as side-lobes. The angular resolution δx of a single-dish with a diameter D at a wavelength λ is after the Rayleigh criterion

$$\delta x = 1.22\ \lambda / D\ . \tag{2.24}$$

The system noise temperature T_{sys} consists of the receiver and antenna temperature and limits the signal-to-noise ratio (SNR) for possible significant detections. The radiometer equation gives an estimation on the noise temperature ΔT in a channel width $\Delta\nu$ after an integration time t by

$$\Delta T = \frac{T_{\text{sys}} K}{\sqrt{\Delta\nu \times t}}\ . \tag{2.25}$$

K is a factor which depends on the observing mode. Receiver instabilities lead to drifts for too long integration times such that the stability is limited by the Allan variance. In addition with the changing atmospheric conditions, it is sometimes better to split the observations in N parts, where the noise temperature scales then as $\Delta T \propto 1/\sqrt{N}$. The pointing and focus is checked regularly on point-like sources (typically planets). Additionally for interferometers, a gain, flux and passband calibrator must be observed, which are typically strong point-like sources such as quasars. Depended on the atmospheric conditions, a calibration should be executed every 10 minutes. To have good baselines, the reference positions should be observed after several minutes depended on the instrument's stability and atmospheric conditions. The off or reference position should be free of line emission and is subtracted from the on-source position to remove the sky contribution and instrumental effects.

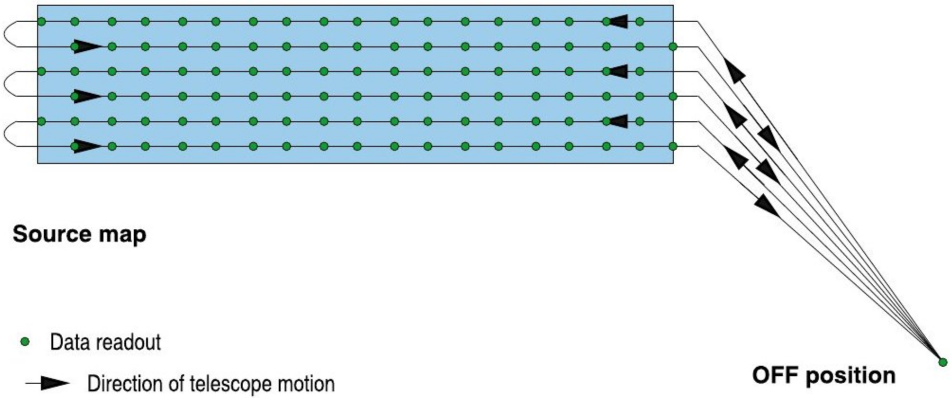

Figure 2.3.: Sketch of an OTF observation. The region of interest is colored in blue, and the scan is alternated in the horizontal direction after one row. Adapted from Ossenkopf (2009).

Different observing modes exist dependent on the scientific goal, such as single pointing on a point-like source, or scanning a large map. For mapping a large area of a sky, the on-the-fly (OTF) mapping is an efficient method (Mangum et al., 2007). The telescope is slewed continuously along one direction and the spectra are stored at a constant period in the order of 1 Hz, see fig. 2.3. This method allows observing several on positions in a row after one off position. The spacing difference between the on positions should be less than the beam size to avoid gaps and a loss of spatial information. From the Nyquist sampling theorem, it is proved that the sampling must be at least in steps of $\theta = \lambda/(2D)$ to recover the full spatial frequency information without losses. The observing time is then roughly given by

$$t = t_{\mathrm{on}} + t_{\mathrm{off}} = t_{\mathrm{on}}(N + \sqrt{N}) \times M\,, \tag{2.26}$$

where N is the number of rows, M the number of columns and it is observed along the row axis. Additionally, an overhead of typically a factor of 0.5 (depended on the telescope facility and experience of the user) is added for the setup to get the estimated total observing time, which is requested in proposals. To avoid possible stripes and artifacts by sampling only in one direction, additional scans in the orthogonal direction can be added, which is called "basket-weaving". After obtaining the calibrated data, the spectra are reduced in several steps which include combining, checking for inconsistencies and spikes, and removing the baseline. From experience, even a little smoothing of the spectral channels by averaging over 2 or 3 channels usually results in a good improvement. The spectra are then gridded to a raster (typically by half or third of the beam size) and convolved with a Gaussian of the beam size to obtain the final map $T(x, y)$ or spectral data cube $T(x, y, v)$. The antenna temperature T_{A} is converted to the main beam temperature T_{mb} by taking the forward efficiency F_{eff} and beam efficiency B_{eff} of the antenna into account:

$$T_{\mathrm{mb}} = F_{\mathrm{eff}}/B_{\mathrm{eff}}\; T_{\mathrm{A}}\,. \tag{2.27}$$

These steps were applied for all APEX observations, chap. 3–5, which were done in the OTF mode.

2.3.2. Astronomical radio interferometers

Because the maximum diameter D_{max} of a single-dish is limited because of technical reasons to $D_{\mathrm{max}} \leq 100$ m, another approach is pursued to increase the angular resolution. To achieve a higher resolution, astronomical interferometers are used, which measure the amplitude and phase differences by several antennas. They consist of an array of single-dish telescopes, which correlate the incoming signal. At the end, the so-called aperture synthesis tries to resemble the same observations with a large single-dish, with the disadvantage of a smaller collecting area and an incomplete sampling of the brightness distribution. For simplicity, in the following a monochromatic array of two elements is described in one dimension. Given a two element interferometer with length separation L, phase delay θ and phase difference $\psi = 2\pi L \sin(\theta)/\lambda$, the measured electric field radiation becomes

$$E = E_1 \exp(-i\psi/2) + E_2 \exp(+i\psi/2) \tag{2.28}$$
$$= 2E_0 \cos(\psi/2) \quad \text{for} \quad E_1 = E_2\,. \tag{2.29}$$

The power is then

$$P(\theta) = |E^2| = 4E_0^2 \cos^2(\psi/2) \propto [1 + \cos(\psi)], \tag{2.30}$$

and gives therefore an interference pattern. Consequently, by using Fourier optics, the visibility function in eq. 2.31 is defined as the Fourier transform of the surface brightness distribution I:

$$V(k) = |V(k)| \exp(i2\pi k\theta) = \int \mathrm{d}\theta\; I(\theta) \exp(i2\pi k\theta)\,, \tag{2.31}$$

where $k = L/\lambda$ is the wavenumber. The incoming electromagnetic waves must be coherent to perform interference, but astronomical sources emit usually non-coherent radiation. The van Cittert-Zernike theorem states that for long distances (as always given in astronomy), the observed brightness distribution of a source on the sky is the complex visibility function $V(k)$ as measured by an interferometer. In 2D space, the Fourier transform pairs of the coordinates in the (x,y)-plane are referred as (u,v). A single measurement gives two symmetric points in the uv-plane at one time. As the earth rotates, the phase changes while tracking the source, which results in more measured points. Thus, the true visibility function $V(k)$ is only sampled by the sampling function of the interferometer,

$$V'(k) = S(k) * V(k)\ . \tag{2.32}$$

The Fourier transform of the sampling function $S(k)$ gives the dirty beam or point spread function (PSF) D. Therefore, a good uv-sampling is preferred, which is achieved by using various baselines and non-uniform array spacings. The number of baselines increases with the number of antennas N by $N(N-1)/2$. The image I is deduced by Fourier transforming the sampled visibilities $V'(k)$. The resulting image is referred as dirty map F:

$$F = D \otimes (P \times I) + N\ , \tag{2.33}$$

where P is the power pattern of the single-dish (primary beam), which is together with I, convolved with D, and N is the noise distribution. This image is improved by a deconvolution algorithm such as the CLEAN algorithm (Högbom, 1974). This improvement consists of decomposing the image by a collection of the dirty beam and its side-lobes, and at last replacing the dirty beam by a clean beam, i.e., a Gaussian function which results in a synthetic beam. Since non-observed areas in the uv-plane will result in negative lobes or features in the image, a good uv-coverage for $V'(k)$ is necessary for a good image quality or fidelity.

Because interferometer are sensitive only to small scales, they resolve out large scales or slowly continuous changing emission, which can be the major component of flux in molecular clouds. Up to a certain radius in the uv space (where large uv-radii correspond to small spatial scales), the inner most part is not sampled at all. This issue is solved by conducting additional observations. This means either by changing the antenna configuration with smaller baselines (short-spacing), or by using single-dish observations at the same frequencies (zero-spacing, as single-dishes completely fill the uv-plane up to their diameter D), see for example fig. 5.4(c). For the Atacama Large Millimeter/submillimeter Array (ALMA, Brown et al., 2004), this common issue was considered by installing an additional antenna set, the Atacama Compact Array (ACA), at the same infrastructure which operates simultaneously. ALMA consists of 66 antennas: 50×12 m, 4×12 m and 12×7 m, where the latter two are reserved for short-spacing. The large number of antennas guarantees a good uv-coverage in short times.

In comparison to single-dishes, the concept of wide-field imaging with interferometers is called mosaicing or OTF mosaicing. The angular resolution of an interferometer is given by replacing D in eq. 2.24 with the longest baseline $L : \delta x = \lambda/(2L)$. The field of view is determined by the primary beam. The noise in the radiometer equation 2.25 decreases with the number of antennas N as $\Delta S \propto 1/(A \times N)$, where A is the effective antenna aperture.

2.4. Kinematics and infall motions

The velocity information from spectral lines is used to examine the gas dynamics in the ISM. According to the Doppler effect of electromagnetic waves, a velocity difference between a receiver and sender will result in a frequency shift of the spectral line. To relate from frequency to velocity scale, the eq. 2.34 is used:

$$\frac{\Delta\nu}{\nu_0} = \frac{\nu_0 - \nu}{\nu_0} = \frac{v_{\mathrm{LSR}}}{\mathrm{c}} \,. \tag{2.34}$$

ν is the observed frequency, ν_0 is the laboratory rest frequency and v_{LSR} is the radial source velocity relative to the local standard of rest (LSR), i.e., relative to the barycenter of the solar system by accounting for the standard solar motion (v_{S}=20 km/s). The definition is such that an increase in frequency is assigned to a decrease in velocity. This change in frequency is called red- or blueshift, based on the behavior in the VIS. For instance, a source velocity of 10 km/s at 220 GHz results in a frequency shift of 7.3 MHz. The frequency resolution of most spectrometers (acousto-optical, autocorrelation, Fourier-Transform) achieves today 1–0.01 MHz, which corresponds at 100 GHz to a velocity resolution of 3–0.03 km/s. According to the radiometer equation 2.25, the narrower the band the less flux is received, which increases the noise and thus the integration time. Therefore, a compromise between the SNR and the frequency resolution must be achieved for spectral line observations. A good spectral resolution is desirable to get the line profile shape, to separate blended lines, and to distinguish several dynamic velocity components (e.g., rotation, expansion, infall collapse, outflows).

The gas in the ISM is due to the low density approximated well by the ideal gas law in eq. 2.35, from which the sound speed c_{s} is derived under adiabatic conditions by

$$PV = N\mathrm{k_B}T \tag{2.35}$$

$$c_{\mathrm{s}} = \sqrt{\gamma \mathrm{k_B} T/m} \,. \tag{2.36}$$

P is the pressure, V the volume, and γ the adiabatic index.

Different mechanism are responsible for the line width. Among others, these are the natural broadening, the thermal Doppler broadening, and the optical depth broadening. The Doppler broadening is due to the random motion of particles at a gas temperature T, where the velocities are distributed according to the Maxwell-Boltzmann distribution in equilibrium, and the line profile has a Gaussian shape. It is commonly found in molecular clouds that the line broadening is dominated by random motions in the LOS as a result of turbulence v_{turb}, and is larger than the Doppler line width. The total line width in velocity space is then

$$\Delta v = \sqrt{\frac{2\mathrm{k_B}T}{m} + v_{\mathrm{turb}}^2} \,. \tag{2.37}$$

Fig. 2.4(a) is a sketch of an infall profile of a collapsing cloud. The colder envelope produces a self-absorption dip in the center of the line profile, whereas the blueshifted peak comes from the background relative to the observer. Because the infall velocity increases toward the center, different shells emanate at different positions in the spectrum. Owing to optical depth effects, the blue peak is higher than the red peak. Note that in nature, high-velocity wings stem also from molecular outflows. A similar, but reversed effect from variable stars is known as a P Cygni profile. A necessary condition for the detection of an infall profile is an optically thick line (where the optically thin line should arise at the self-absorption dip), and a radial temperature and velocity gradient in the cloud. Fig. 2.4(b) presents models of an infalling or rotating cloud and the corresponding PVD. The geometry of the cloud effects the PVD, and it can be difficult to distinguish between infall or rotation motions only in real observations with an unknown inclination angle. These difficulties occur because only the z-component v_z of the velocity vector $\vec{v}$ is measured with spectral lines.

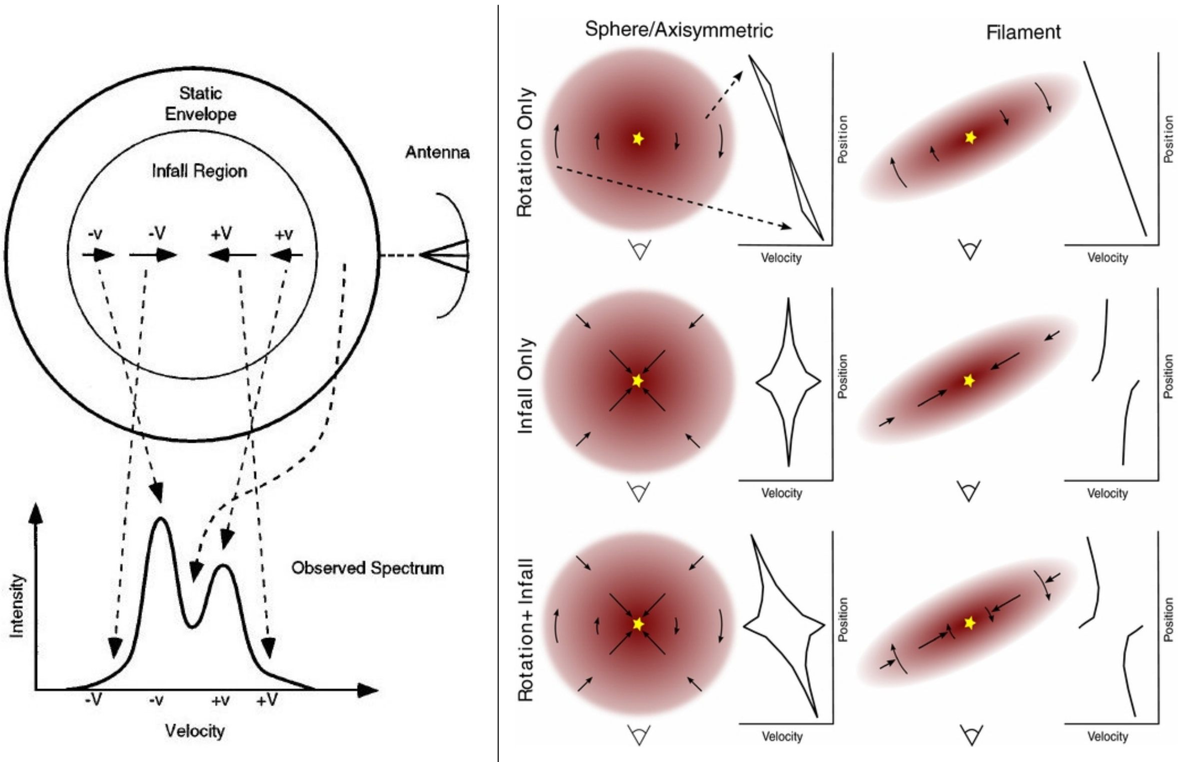

(a) (b)

Figure 2.4.: Sketches of different kinematic features in the ISM. (a) An infall profile of a collapsing cloud, adapted from Evans (1999). (b) PVDs for cases of infall and rotation for different cloud geometries, adapted from Tobin et al. (2012).

3. The global velocity field of the filament in NGC 6334

3.1. Introduction

Recent observations with the HSO have shown the importance of filaments in star formation, as cores and clusters are embedded in or along filamentary structures, sect.1.3.3. In the case of massive star formation, it is necessary to maintain a high gas accretion rate, and filamentary flows are one method of achieving this (Myers, 2012). Recent simulations have highlighted the importance of large scale collapse motions in massive star formation regions (e.g., Bonnell et al., 2006; Smith et al., 2009). In this picture, cores and clusters accrete gas from filaments that serve as mass reservoirs. Filaments may evolve from the gravitational collapse of sheets that are created by interstellar shocks, collisions of bubbles driven by supernovae, or stellar winds (Burkert and Hartmann, 2004). Determining the velocity fields of filaments, their density, and temperature distribution are crucial to test the validity of these models. To accomplish this, large scale observations must be linked with high-spatial resolution maps on cluster scales.

Fig. 3.1 presents the dust continuum emission taken from ATLASGAL at 870 μm/345 GHz. The position angle of the filament is about PA=35°. For practical reasons, it is presented here in Galactic coordinates, where the filament is nearly parallel to the longitude axis. Its total length is about 12 pc, the average full width at half maximum (FWHM) is 0.3 pc, and the average flux is 2–3 Jy/beam and raises up to 5 Jy/beam in the vicinity of source I and I(N). The FIR sources, labeled by Roman numerals in the FIR (see Kraemer and Jackson, 1999), correspond to sites of massive star formation, ranging from 200–2000 $M_\odot$. They represent features such as HII regions, HMCs, masers, and molecular outflows. The sources are at different evolutionary stages, ranging from the cold dense core I(N) to the HMC I, and to the diffuse HII region III in the center. This may be indicative of sequential star formation, e.g., triggered by a spiral density wave. However, other observations have revealed a more complex structure (Rodriguez et al., 1982). The gaps between the sources II and III and IV and V originate from disrupted, ionized gas of HII regions. The white contours in fig. 3.1 depict the Hα emission ($n = 3 \rightarrow 2$ at λ=656.3 nm, where n is the main principal quantum number of the hydrogen atom) in this region from the AAO/UKST Hα survey (Parker et al., 2005), and the position of the gaps correspond to the emission of Hα.

3.2. Observations and data Reduction

Observations were made in July 2012 in a total time of 2 h with APEX to map the region displayed in fig. 3.1, which has an extension of 29.4′×13.8′. The APEX-2 SHeFI receiver and the XFFTS backend (Klein et al., 2012) were used, a digital Fast Fourier Transform Spectrometer, to measure the HCO$^+$ J=3–2 (267.557 GHz) and HCN J=3–2 (265.886 GHz) transitions. The receiver provides 32 768 channels in a bandwidth of 2.5 GHz and a maximum velocity resolution of 0.085 km/s. The region was observed in the OTF mode with position switching and sampled with half-beam spacing and a dump time of 1 s. Pointing and focus were checked regularly on Saturn. The average value of the system temperature was 170 K and of the PWV 1.5 mm. The calibration uncertainty is estimated to ~10%. The beam width (FWHM) at 267.6 GHz is

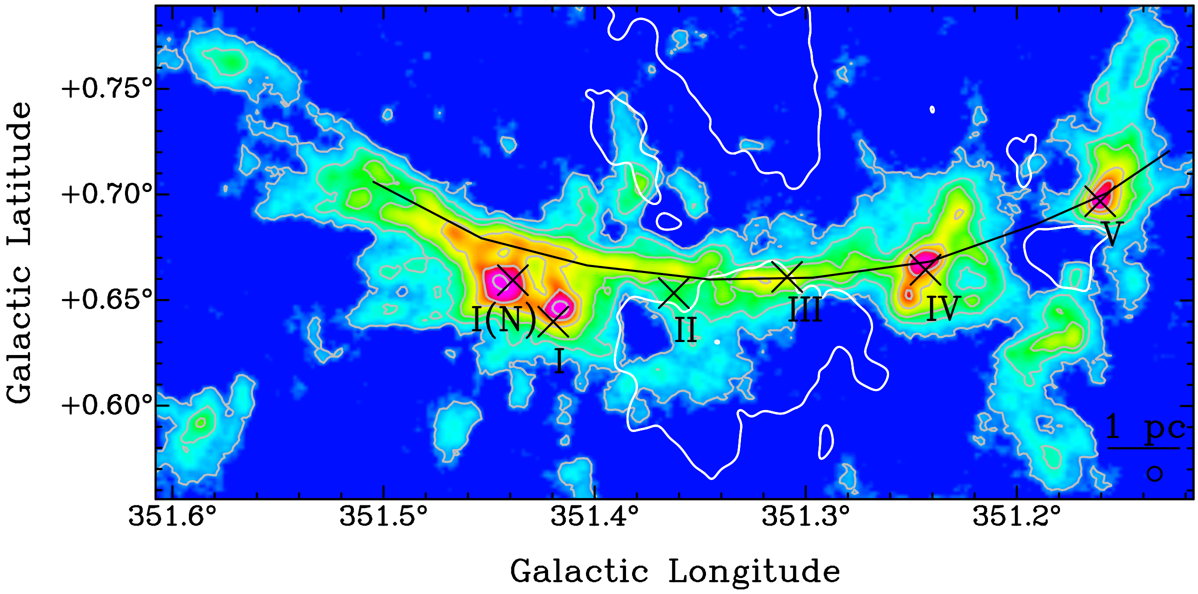

Figure 3.1.: ATLASGAL map of NGC 6334. The continuum levels in gray are set at 0.3 (3σ), 1, 2, 5, 10, and 30 Jy/beam. The black line marks the main filament, black crosses denote FIR sources (Kraemer and Jackson, 1999), and the beam width at 266 GHz is indicated in the lower-right corner. Overlaid in white contours (at 90% of the maximum intensity) is the $H\alpha$ emission (Parker et al., 2005).

θ_B=23.5″. The data was reduced with the Grenoble Image and Line Data Analysis Software (`GILDAS`[1]) within `CLASS`, baseline-subtracted, convolved with a Gaussian of 1/3 beam width and gridded to a map with a pixel size of $\theta_B/2$=11.75″. The spectra were converted to main-beam temperature using a main beam efficiency of η_{mb}=0.75 (F. Wyrowski, private communication) and Hanning smoothed to a velocity resolution of 0.51 km/s to achieve an rms of 0.31 K. The maps and PVD were created with the software Multichannel Image Reconstruction, Image Analysis and Display (`MIRIAD`, Sault et al., 1995) and visualized with the toolkit `Karma` (Gooch, 1996).

HCO^+ is a good tracer of dense molecular gas and well suited to examine the kinematics of infalling clumps or outflows (Rolffs, 2011). To check that the optically thick spectral lines of HCO^+ do not consist of several, superimposed kinematic components, the maps were compared to complementary maps of the optically thin isotopologue $H^{13}CO^+$ (J=1–0) and other molecules from the survey Millimetre Astronomy Legacy Team 90 GHz (MALT90, Foster et al., 2011). Only two small regions show two components in optically thin lines, the first at l=351.42°, b=0.66° and the second at l=351.51°, b=0.7°. The first one is due to the different radial velocity between source I and the filament; the second one can be explained by the superposition of multiple structures which also appear as a bifurcation in the dust emission maps of Matthews et al. (2008). Thus, the main velocity structure is not distorted by other kinematic components. In this chapter, only the radial velocities of HCO^+ are discussed without reference to local spectroscopic features of the clumps.

---

[1] `URL:http://www.iram.fr/IRAMFR/GILDAS`

3.3. Results

3.3.1. Velocity field

The first three moment maps of a spectral data cube are defined by eq. 3.1:

$$M_0 = \sum_c I_c; \quad M_1 = \left(\sum_c I_c v_c\right) / M_0; \quad M_2 = \sqrt{\sum_c (I_c (v_c - M_1)^2) / M_0}. \tag{3.1}$$

Per pixel, the zeroth moment M_0 is the intensity map integrated over velocity channels c (with a width of Δv) in units of K km/s. M_1 is the first moment or the centroid velocity map, and M_2 is the second moment and quantifies the velocity dispersion. Thus, if the spectrum consists of one single line with a Gaussian shape, M_0 gives the area, M_1 the mean and M_2 the standard deviation. Fig. 3.2 shows the first moment map in HCO$^+$. The highest redshifted velocity of +2 km/s occurs in the center at the position of source II. There is a velocity gradient toward both ends with the highest blueshifted velocity of −7 km/s at source I and V. It is noted that the radial velocity increases again for l>351.46°. Perpendicular to the main filament, two subfilaments exhibit longitudinal gradients at l = 351.2° and l = 351.38°. The velocity gradient at the position of source IV, which is tilted relative to the main filament and marked by double arrows, was explained by Kraemer et al. (1997) as the rotation of a molecular disk around IV.

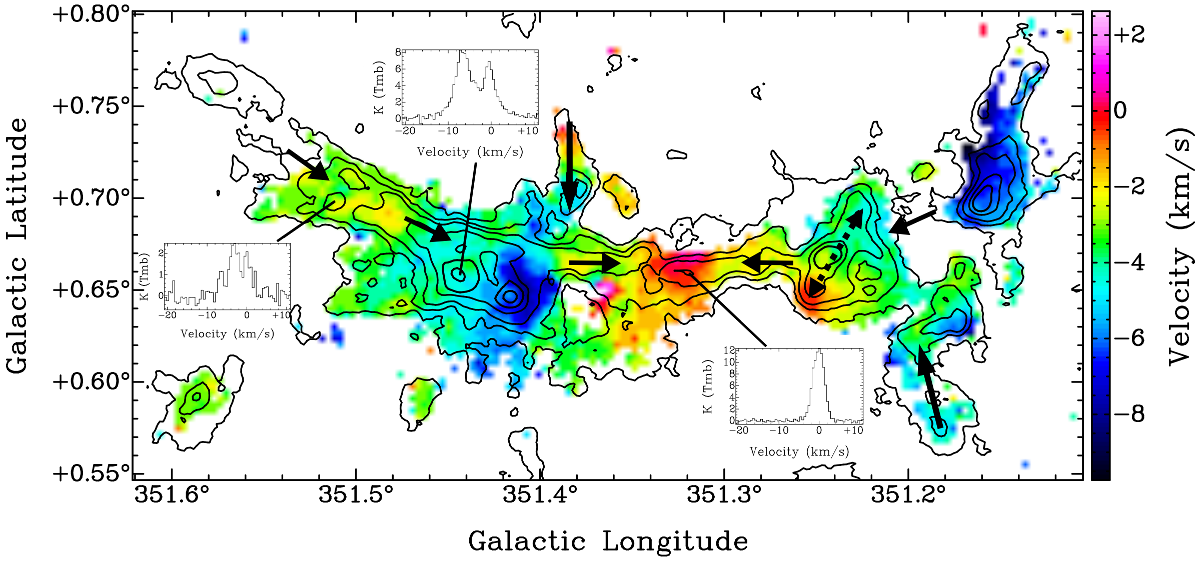

Figure 3.2.: First moment map of the HCO$^+$ J=3–2 transition of NGC 6334. Emission below 3σ = 0.93 K is discarded. Overlaid in black contours is the continuum emission from fig. 3.1. The black arrows denote the gas flow direction in the scenario of a longitudinal contracting filament. Spectra from selected regions are depicted by lines.

The PVD of NGC 6334 is presented in fig. 3.3. It is created by reordering the axis from the spectral cube from xyv to xvy and by integrating over the Galactic latitude axis. The velocity gradient in the center is about 1 km/s/arcmin or 2 km/s/pc. Small deviations from the general trend are recognized at the position of the sources I, I(N), IV, and V. These deviations originate from outflows that cause the line profiles to have larger wings and that account for the smallest Doppler velocities below −7 km/s. The asymmetric double-peak profile of sources I(N) and I, apart from the filament, arises from self-absorption and infall motions (sect. 2.4) and cause a slight blueshift in the radial velocity of the first moment map. The typical line width (FWHM), deduced from the diazenylium (N_2H^+) and cyanoacetylene (HC_3N) emission lines in the MALT90 data, is Δv=1.0–2.0 km/s in the filament and increases to Δv =3–4 km/s in the dense clumps. These values are in agreement with the line widths reported in Russeil et al. (2010).

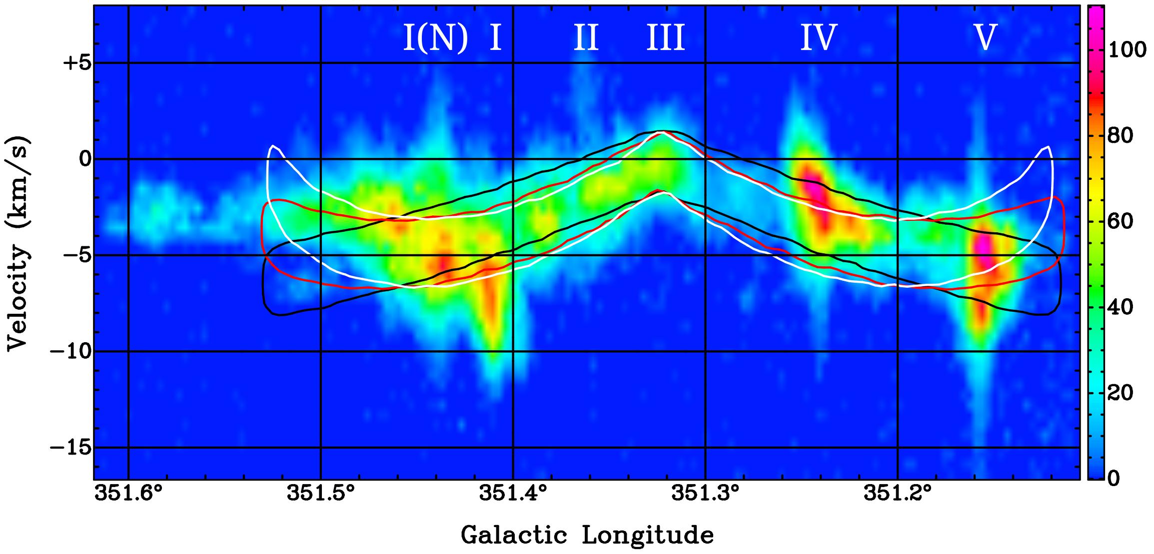

Figure 3.3.: PVD in $HCO^+(J$=3–2) of NGC 6334 with a cutoff at $3\sigma = 0.93$ K. The position of the FIR sources are labeled above. Overlaid in contours are the PVDs of the three best-fit models of sect. 3.3.3. The contours are set at 50% of the integrated emission, which corresponds to the average velocity width of 3.5 km/s of the filament in this figure. The model in white assumes an initial velocity of zero at the edges, and the model in red that the filament has already contracted from 7 to 6 pc (both at $i = 45°$). The model in black contours is defined with a constant velocity of v=10 km/s and $i = 68°$.

3.3.2. Analytical model

Burkert and Hartmann (2004) derive the gravitational acceleration in finite sheets and filaments. They assume a uniform, self-gravitating cylindrical cloud with a constant volume density $\rho = M/(\pi\mathcal{R}^2 2L)$, where M is the total mass, $2L$ is the total length, $\mathcal{R}$ is the radius, and l is the distance from the center on the longer axis. The aspect ratio is defined as $A = L/\mathcal{R}$. Neglecting all pressure supporting forces against the gravity (e.g., rotation, turbulence, magnetic fields), the cloud will collapse along the longer axis starting from the ends and moving toward the center. The assumption is that the radius $\mathcal{R}$ remains relatively constant and that gravitation dominates on the large scales (pc). The acceleration a at position l is

$$a(l) = -2\pi \mathrm{G}\rho \left[2l - \sqrt{\mathcal{R}^2 + (L+l)^2} + \sqrt{\mathcal{R}^2 + (L-l)^2} \right] . \tag{3.2}$$

The acceleration has the highest value at the end of the filament, which leads to a pile up and to an enhanced concentration of the gas at the periphery. In elongated elliptical sheets, the mass concentrates at the focal points. Based on this, and under the assumption that the density remains constant, Toalá et al. (2012) derive the radial velocity of the filament, after it has contracted from L to l, to

$$\begin{aligned} v(l) = \sqrt{4\pi \mathrm{G}\rho} \Bigg[&(L-l)(L+l+\mathcal{R}) - \frac{L}{2}\sqrt{\mathcal{R}^2 + 4L^2} \\ &+ \frac{l}{2}\sqrt{\mathcal{R}^2 + 4l^2} - \frac{\mathcal{R}^2}{4} \ln \left| \frac{\sqrt{\mathcal{R}^2 + 4L^2} + 2L}{\sqrt{\mathcal{R}^2 + 4l^2} + 2l} \right| \Bigg]^{1/2} . \end{aligned} \tag{3.3}$$

The larger the aspect ratio, the smaller the rise and value of the final velocity. They also calculate the free-fall time for filaments and sheets. Whereas in the spherical case the free-fall time only depends on the density, for filaments and sheets there is an additional dependence of the geometry, characterized by the aspect ratio A. In conclusion, the free-fall time for filaments τ_{ff} is longer than in the spherical case τ_{s},

$$\tau_{\mathrm{ff}} = \sqrt{\frac{32A}{3\pi^2}} \times \tau_{\mathrm{s}} = \sqrt{\frac{32A}{3\pi^2}} \times \sqrt{\frac{3\pi}{32\mathrm{G}\rho}} . \tag{3.4}$$

3.3.3. Application to NGC 6334

We aim to take the velocities predicted from eq. 3.3 and to compare them with the observations of NGC 6334. Although eq. 3.3 is not applicable for every position l of the filament at one point in time, it is a good approximation for cases with high aspect ratios where the value of the radial velocity increases only slightly during the collapse. Furthermore, only the longitudinal velocity is considered and it is assumed that the radius $\mathcal{R}$ stays constant. As the shape of the filament is not a regular cylinder but is curved elliptically, a generalized conic section is used via the implicit function

$$\sqrt{x^2 + y^2} = (l + e * x) , \tag{3.5}$$

where l is the semi-latus rectum and e the eccentricity. The latus rectum is the line segment through the focus and is perpendicular to the major axis a. The eccentricity of an ellipse is defined as

$$e = \sqrt{1 - (b/a)^2} , \tag{3.6}$$

where b is the minor axis. It is assumed that the direction of the velocity v is determined by the shape of the filament. Then the velocity direction field is gained from the derivative of eq. 3.5

and normalized to unit vectors

$$\vec{v} = \begin{pmatrix} x & , & y \end{pmatrix} = \left(\frac{y}{\sqrt{y^2+((l+e*x)*e-x)^2}} \quad , \quad \frac{(l+e*x)*e-x}{\sqrt{y^2+((l+e*x)*e-x)^2}} \right). \tag{3.7}$$

The total mass of NGC 6334, within the observed region, is estimated to M=16.7E3–23.1E3 $M_\odot$ (Matthews et al., 2008; Muñoz et al., 2007), where half of this is contained in the seven most massive clumps. Eliminating I, I(N), and the other sources that do not lie on the filament and given the uncertainties, it is assumed that the filament's mass is $M \approx$1E4 $M_\odot$. A slightly larger radius of $\mathcal{R}$=0.2 pc is adopted for the analytical model because the observed density profile follows a Plummer-like function and does not vanish at the observed radius of 0.15 pc. Matthews et al. (2008) derive average dust temperatures of 25 K and higher average gas temperatures of 50 K in the filament. The average hydrogen column density is $N(H_2)$=5E22 1/cm^2 (Matthews et al., 2008), resulting in a density of $n(H_2)$=5E4 1/cm^3. Using the density formula in sect. 3.3.2, the analytical model has an average density of n=1E5 1/cm^3, twice as large as the observed density because the massive clumps are included. The value of v obtained from eq. 3.3 is then about 10–20 km/s.

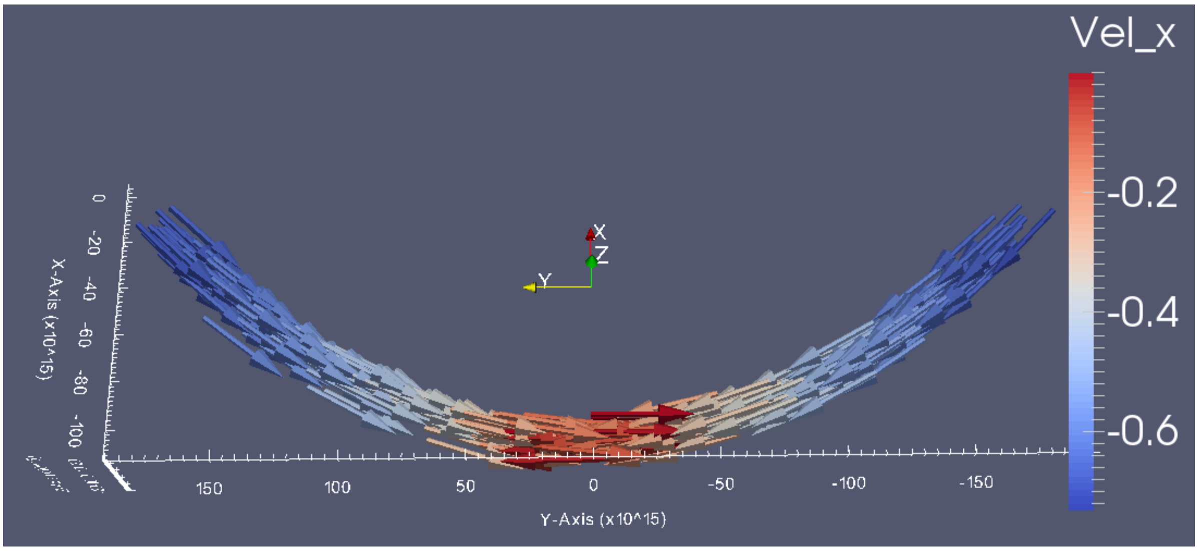

Figure 3.4.: 3D visualization of the model, where arrows denote the velocity direction and the normalized magnitude denote the x-component in the LOS of the observation.

Using the geometry and analytical velocity field above, a model of the filament is created with the 3D radiative transfer code `LIME` and synthetic HCO^+ (J=3–2) observations are produced, see fig. 3.4. The collision rates are taken from Flower (1999). The parameters in the `LIME` code match the values of NGC 6334, with a constant gas temperature of 50 K, a constant density of n=1E4 1/cm^3, a radius of 0.2 pc, a line width of 1.7 km/s, and a fractional abundance of $X(HCO^+)$=2E-9. The HCO^+ abundance in NGC 6334 lies in the range of 5E-10 to 5E-9, which is found in other star-forming regions (Godard et al., 2010). The resulting spectral cubes are convolved with the APEX beam size, rotated by the angle PA and i, where PA is the fixed position angle and i the inclination, and the same reduction steps are applied as for the data to obtain the PVD. An inclination of 0° corresponds to a face-on view. Because the radial velocity is nonzero along the line of sight, it is clear that $i > 0°$. A parameter study of the free parameters

e and i shows that small eccentricities are a poor match to the figures 3.1 and 3.3. Consequently, if this model is true, the filament cannot be circular. On the other hand, values of $e > 1.5$ result in a straight shape. The values that best fit both the dust continuum map and the PVD are $e \approx 0.9$ and $i \approx 45°$ (see the contours in fig. 3.3). The white model corresponds to the actual observed size with a half-length of L=6 pc. The red model presumes that the initial conditions were L=7 pc, so that the filament has contracted by 1 pc at the edges, which would take a time of 4E5 yr. The black model assumes a constant velocity value of v=10 km/s throughout the cylinder and a higher inclination of i=68°. The red model shows the best fit to the data. The white model underestimates the radial velocity at the edges, meaning that the observed filament must have been already contracted. On the other hand, the black model overpredicts the radial velocity at the edges, illustrating that the velocity magnitude is not constant.

3.3.4. Density profile and fragmentation length scale

NGC 6334 could represent a later evolutionary stage of a filamentary IRDC (Jackson et al., 2010). To look for a possible, characteristic fragmentation length scale for the cores in NGC 6334, the first 17 cores with the highest peak intensity and highest mass are selected from table 4 of Muñoz et al. (2007) and the projected distances between the next neighbors are calculated. These condensations are visible in fig. 3.1 and include the most massive cores I–V. On the basis of the expected inclination and curvature, the observed fragmentation length should decrease only slightly by 10% at the filament's end. The median and median absolute deviation of the distances is $\lambda_\mathrm{m} = (1.9 \pm 0.5)'$ or $\lambda_\mathrm{m} = (0.94 \pm 0.25)$ pc.

The typical line widths in the filament of $\Delta v = 2.355\sigma$=1.0–2.0 km/s are larger than what would be expected from Doppler broadening, and turbulent pressure or systematic motions are dominant. Accordingly to equation 1.17, the predicted fragmentation length is in the range λ_F=0.8–1.5 pc. Measuring the scale height H directly is hindered by the limited resolution of the APEX observations, because the beam size is equivalent to the filament's radius of ≈0.15 pc. To increase the resolution, a high-resolution dust emission map of NGC 6334 is taken from the SHARC-II (Submillimeter High Angular Resolution Camera II) 350 μm bolometer array at the CSO (Caltech Submillimeter Observatory), see fig. 1 of Vaillancourt (2011). The angular resolution is 8.5″, the pixel size is 1.62″, and the intensities are uncalibrated and in arbitrary units. This map is used to find a best fit to the profile by following the method in Arzoumanian et al. (2011) and assuming isothermal conditions. According to eq. 2.20, the flux density is proportional to the column density or mass. In the APEX dust continuum map, the average intensity is 3 Jy/beam. Assuming T=50 K and a dust opacity of $\kappa = 1$ cm^2/g, the column density is $N(H_2)$=4.7E22 1/cm^2, in good agreement with the value from Matthews et al. (2008). The profile is often modeled by a Plummer-like function with parameter p and radius R:

$$\Sigma_p(r) = \frac{\Sigma_c \rho_c R}{[1 + (r/R)^2]^{(p-1)/2}} \tag{3.8}$$

For the HSO observations, the average value obtained is p=2.4, whereas p=4 would correspond to an infinite isothermal cylinder (Ostriker, 1964) and p=5 to a Plummer function. Fig. 3.5 presents the average profile in the central region between the clumps I and II. The profile is symmetric above the FWHM and has extended emission at lower values on one side. This is caused probably by the nearby HII region at clump II, which piles up the gas and results in this asymmetry at lower intensities. The fitting range is thus restricted to ±15″ from the mean value. The results by using eq. 3.8 are $R = (14 \pm 2)''$, or $R = (0.11 \pm 0.02)$ pc, and $p = 3.1 \pm 0.5$. The relation to the scale height is $R = 2H$, which gives H=0.06 pc and results in $\lambda = (1.3 \pm 0.2)$ pc, which is close the observed median value λ_{m} mentioned above. The width of the profile is fitted in the central region by a Gaussian function and gives FWHM=(0.206±0.002) pc. This is approximately twice as large as the values of FWHM=0.1 pc observed in the HSO Gould Belt survey. A possible explanation for the deviations are the higher temperatures in NGC 6334.

The origin or driving force of the turbulence might be the gravitational infall, and the question of the impact of the global collapse to the fragmentation and star formation is pointed out by Pon et al. (2011). Unlike spheres or disks, fragmentation occurs easily in filaments because the timescale for local collapse of small density perturbations is shorter than the global collapse timescale. This explains the appearance of cores and density enhancements in the filament, before the global infall has finished.

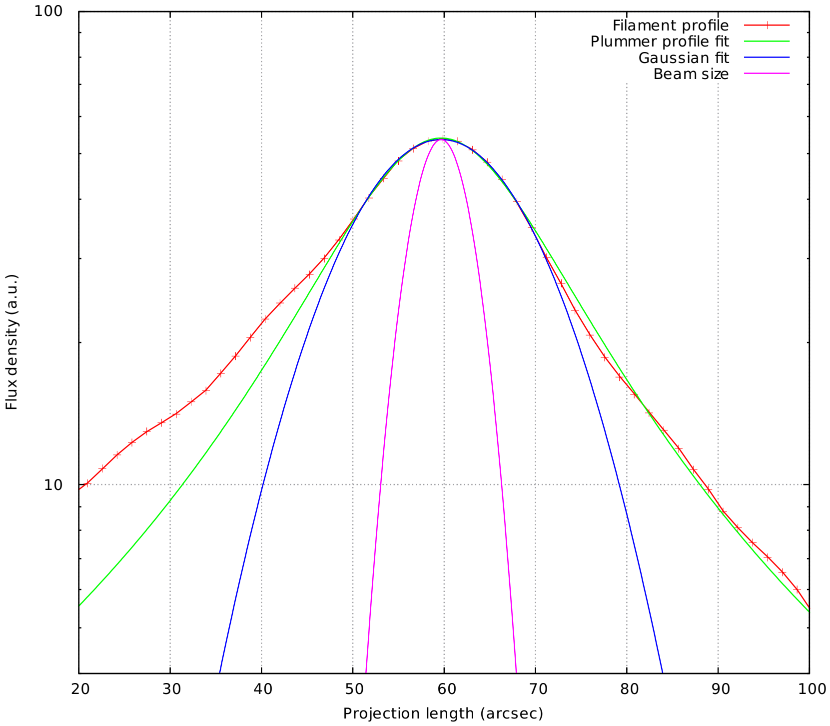

Figure 3.5.: Average intensity profile of the main filament of NGC 6334, taken from the SHARC-II dust continuum observations with CSO. The best fits are used to derive the radius and scale height.

3.4. Discussion

A PVD of NGC 6334 was presented by Batchelor et al. (1984) in HCO$^+$ (1–0) and by Kraemer and Jackson (1999) from carbon monosulphide (CS) and CO observations. Both analyzes suggested a collapse or an expansion. Based on the FIR sources which lie mostly on the major axis of this elliptical cloud, Dickel et al. (1977) presented a spherical model of a global collapse.

The new observations reveal the filamentary and subfilamentary structure in dust and molecular emission and a coherent velocity field. The symmetric shape in fig. 3.3, and the fact that the highest blueshifted emission stems from the region with the highest density (1.7E5 1/cm^3 in source V and 1.2E6 1/cm^3 in source I, Russeil et al. 2010), agrees with the predictions in sect. 3.3.2, where the gas accumulates at the filament's edges. The emission at l>351.46° that causes the slightly unsymmetrical shape in fig. 3.3 can be explained by later infall from ambient gas and the presence of multiple components as mentioned in sect. 3.2. It is noted that the dense region at source I and I(N) formed out of the major axis is a deviation to the idealized model of sect. 3.3.2. This deviation can be explained by a non-uniform density distribution and cloud geometry at the beginning of the collapse, as is shown by Burkert and Hartmann (2004) for irregular cloud boundaries. The HCN spectra indicate that this region is collapsing and thus may have decoupled from the rest of the filament.

There are two other possible explanations for the velocity field. First, the whole filament could be collapsing toward a focal point above the filament's center away from the observer, see for example fig. 11 of Burkert and Hartmann (2004). However, this would lead to the highest densities in the center, as opposed to the observations. Moreover, a gravitational focal center could not be assigned to any visible source. Secondly, there is an uncertainty about the direction of the velocity when a gradient is observed. Excluding rotational effects, one expects a flow toward the largest center of mass. As the sources I, I(N), and IV have the highest mass, this could mean that the central part of the filament is moving toward it. The observed high stellar activity in this region has already disrupted some gas and may be complicating the gas motions. Bright sources could even reverse the velocity gradients. However, an expansion motion, caused by stellar winds or shocks, would need strong excitation sources near the center of the filament, but the stellar clusters and OB stars are inhomogeneously distributed throughout (Feigelson et al., 2009). In conclusion, while the local gas motions may be affected by feedback, the global velocity structure over 12 pc suggests a large-scale collapse scenario. The geometry with the bended shape in center could be formed as a result of the HII regions in the background. Recent observations of the IRDC SDC13 indicate also the presence of a longitudinal collapsing filament (Peretto et al., 2014).

The observed aspect ratio of NGC 6334 is A=6 pc/0.15 pc=40. From eq. 3.4 and using a mean density of n=5E4 1/cm^3, a free-fall time of $\tau_{\rm ff}$=1.0 Myr is derived. As no additional supportive forces were considered, this value should be considered as a lower limit. The resulting free-fall time is one magnitude longer than the lifetimes of massive protostars in NGC 6334 of 1E4–1E5 yr (Russeil et al., 2010), which means that these protostars may evolve while the filament is contracting. The constant density approach of Toalá et al. (2012) is used here, but they also discuss another approach where the total mass is conserved and ρ is variable. This second approach overestimates the gravitational attraction during the collapse, and it is estimated that the actual timescale lies between these two cases. While Toalá et al. (2012) are sensitive to the collapse dynamics at the edge of a cylinder, Pon et al. (2012) probe the timescale of the interior of a cylinder and find a linear dependence of the free-fall time on A, $\tau \sim 0.82A\tau_{\rm s}$. This homologous collapse assumes that the total mass is conserved and would result in τ=5.0 Myr for NGC 6334. However, the edge-driven collapse (sect. 3.3.2) becomes more dominant than the homologous collapse in elongated filaments with large aspect ratios ($A \gg 1$). As this is the case in NGC 6334, the edge-driven scenario with a lower free-fall time of 1 Myr will be more likely.

4. Large scale ^{13}CO observations of NGC 6334 with APEX

4.1. Introduction

Following the studies of chap. 3, ^{13}CO (J=2–1, E_u $\approx$15.9 K) and C^{18}O (2–1) maps were obtained of the whole filamentary structure of NGC 6334 over 60 pc to study the velocity field and mass flows along the sub-filaments and striations. While HCN traces the dense gas, CO is more abundant and traces in addition the lower density gas, because of its lower critical density. CO is often used for observations of molecular clouds, but as it becomes quickly optically thick, the isotopologues of CO are used instead or are added to the CO observations. Furthermore, the J=2–1 transition of ^{13}CO and C^{18}O are separated only by 0.8 GHz, which makes it feasible to observe them simultaneously within one receiver band. The goal of these observations is to see how filaments accrete the gas from the diffuse gas, and to build a connection between the main filament and its surrounding region. In contrast to previous continuum observations with the HSO (sect. 1.4), the velocity information allows characterizing the kinematic structure and turbulence in this region.

4.2. Observations and data reduction

Observations were conducted from 23.–28.7.2013 with APEX. For technical reasons, the whole map was divided into 17 subfields. An OTF mapping was performed in one scanning direction for each subfield (along the Galactic longitude) with an observing time of about 1 h per subfield. To decrease the slewing time of the single-dish to the offset position, the map was divided into two parts (east and west) with a nearby offset position for each part. The SHeFI receiver (Vassilev et al., 2008) in band 1 was used to observe both lines simultaneously, ^{13}CO(2–1) at 220.398677 GHz and C^{18}O(2–1) at 219.560357 GHz. Combined with the backend XFFTS, this provides a bandwidth of 2×2.5 GHz with an overlap of 1 GHz, so the spectral range is in the end 216.8–220.8 GHz. The spectral resolution is 88.5 kHz, which corresponds to a velocity resolution of 0.12 km/s at 220 GHz. The average PWV was around 3–4 mm and the system temperatures varied between 100–200 K. The data reduction was done with `GILDAS`. The spectra were smoothed to a velocity resolution of 0.3 km/s to give a final average rms of 0.35 K for ^{13}CO and 0.45 K for C^{18}O, which varies by ±0.1 K for different submaps because of changing weather conditions during the observing week. The ^{13}CO data were gridded to the same angular resolution as C^{18}O to make the further comparison and analysis between these two molecules easier. The final resolution is 30.2$''$ (pixel size=14.3$''$), and the final size of the cube $T = T(x, y, v)$ is 561 × 175 × 226 channels. Complementary data are used from the Galactic survey of the CO (J=1–0) transition by Dame et al. (2001) at an angular resolution of 8.5$'$, and from the Southern Galactic Plane Survey (SGPS) in HI (McClure-Griffiths et al., 2005) at a resolution of 2$'$.

Fig. 4.1 presents the average spectra of the whole map in ^{13}CO and C^{18}O. The emission at -100 km/s stems most likely from the 3 kpc spiral arm, and the emission at -40 km/s is another background cloud according to Kraemer and Jackson (1999). The absorption features at -141,

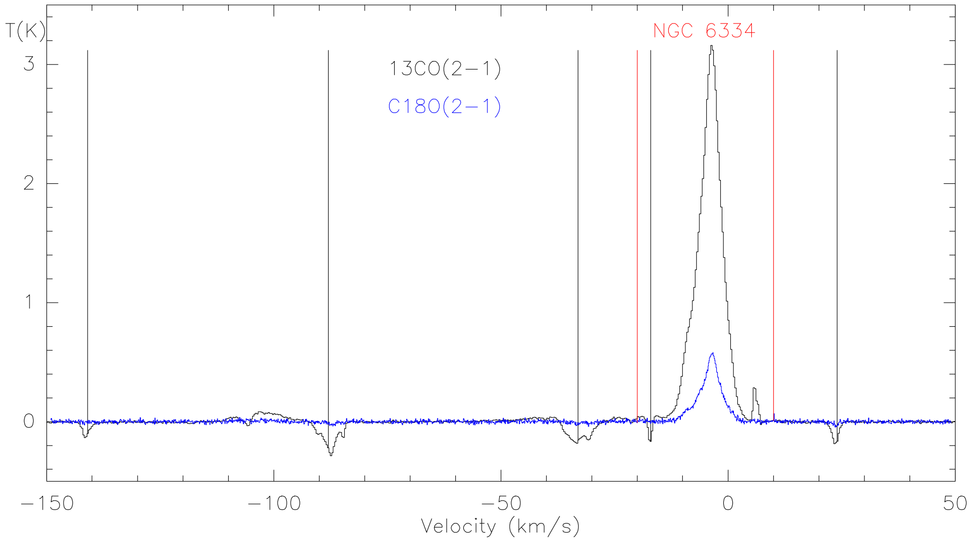

Figure 4.1.: Average spectra of the ^{13}CO and C^{18}O data. Black lines denote background clouds, and the red vertical lines denote the range used for the further analysis.

−88, −33, −17 and +24 km/s mainly origin from fore- or background clouds at these velocities, which contaminated the offset position and are therefore seen dominantly in absorption over the whole map at these velocity channels on average. All these components are accompanied by emission features at some regions in the map and differ in intensity, which can be distinguished by the two different offset positions. In addition, as mentioned above, the submaps were observed under different weather conditions and therefore some scans contribute more noise than other. The emission at −4 km/s is associated with NGC 6334, and the possible nature of the feature at +6 km/s is discussed in sect. 4.4.4. For the further analysis, the velocity range is limited to [−20, +10] km/s which is associated with gas of NGC 6334.

4.3. Methods and results

4.3.1. Moment maps

Fig. 4.2 demonstrates the first three moment maps in ^{13}CO. The bulk of the integrated emission comes from the main filament, while additional peaks are found further away at l=352.5° and l=350.5°. The velocity field reveals no systematic motions on small scales, but a large velocity gradient along the Galactic plane from blueshifted velocities at l=350.5° to redshifted velocities at l=352.1°, spanning a range of 12 km/s. Additionally, concentrating on the range l=[350.5°, 351°], a gradient along the Galactic latitude b is visible. A velocity dipole is often found in GMCs and is associated to a large scale rotation. The velocity dispersion map has the highest values of σ = 3 km/s in the central, most dense region, but also at some regions away from it. These higher values in the region further away are caused by several velocity components in the LOS.

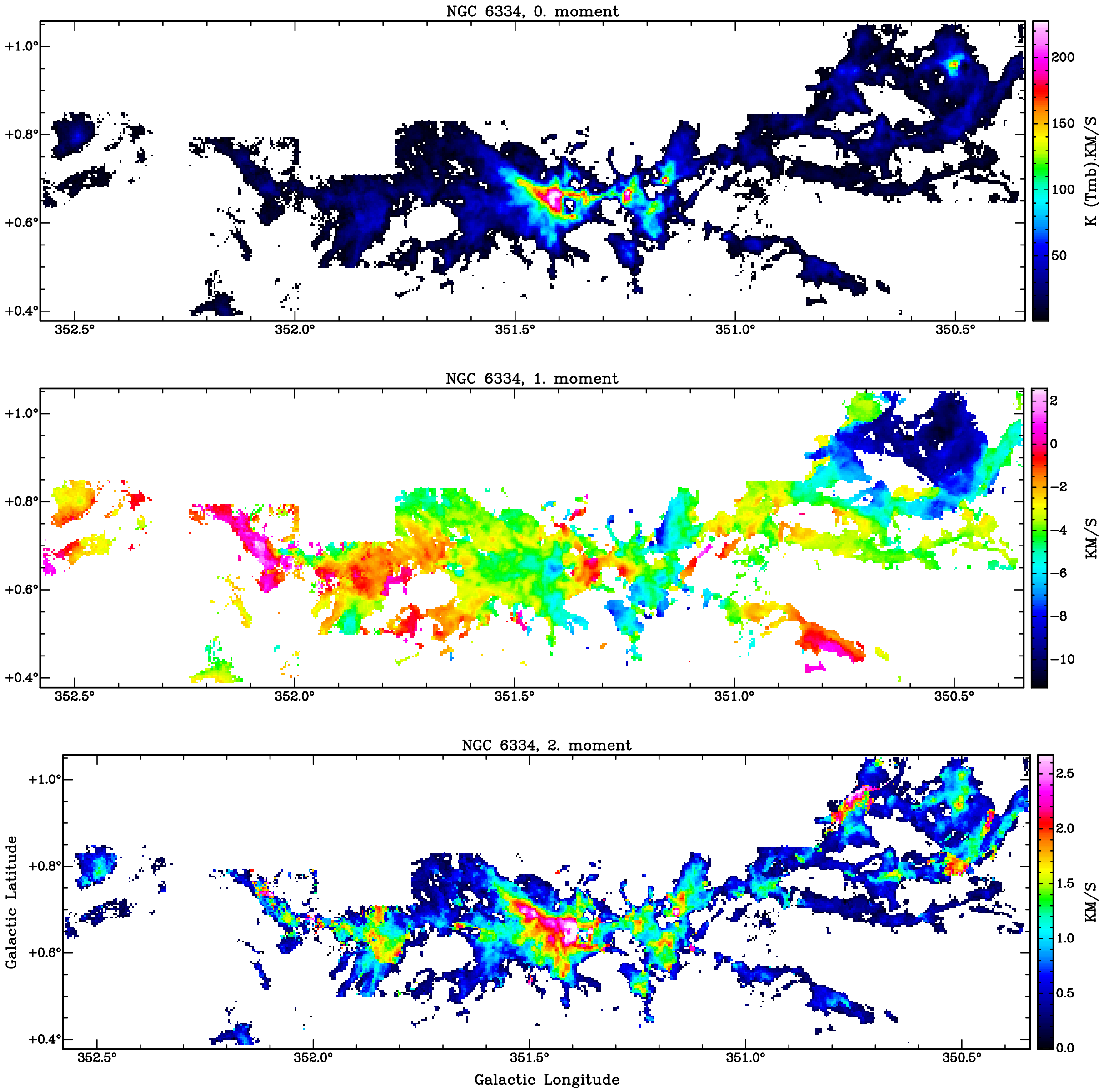

Figure 4.2.: First three moment maps (from top to bottom) of NGC 6334 in ^{13}CO (J=2–1). The lower threshold is set at 5 K in each case.

Fig. 4.3(a) shows the PVD of NGC 6334 from ^{13}CO embedded in a larger picture from the CO (1–0) survey by Dame et al. (2001). Both are integrated along the Galactic latitude. The details of the emission are much better resolved without loosing too much emission from the diffuse gas. Only the weak velocity feature at +6 km/s is more prominent in the CO (1–0) emission, because CO has a higher abundance than ^{13}CO and this cloud is more optically thin than the others. Additionally, many diffuse clouds between [−10, −20] km/s show a brighter emission in CO.

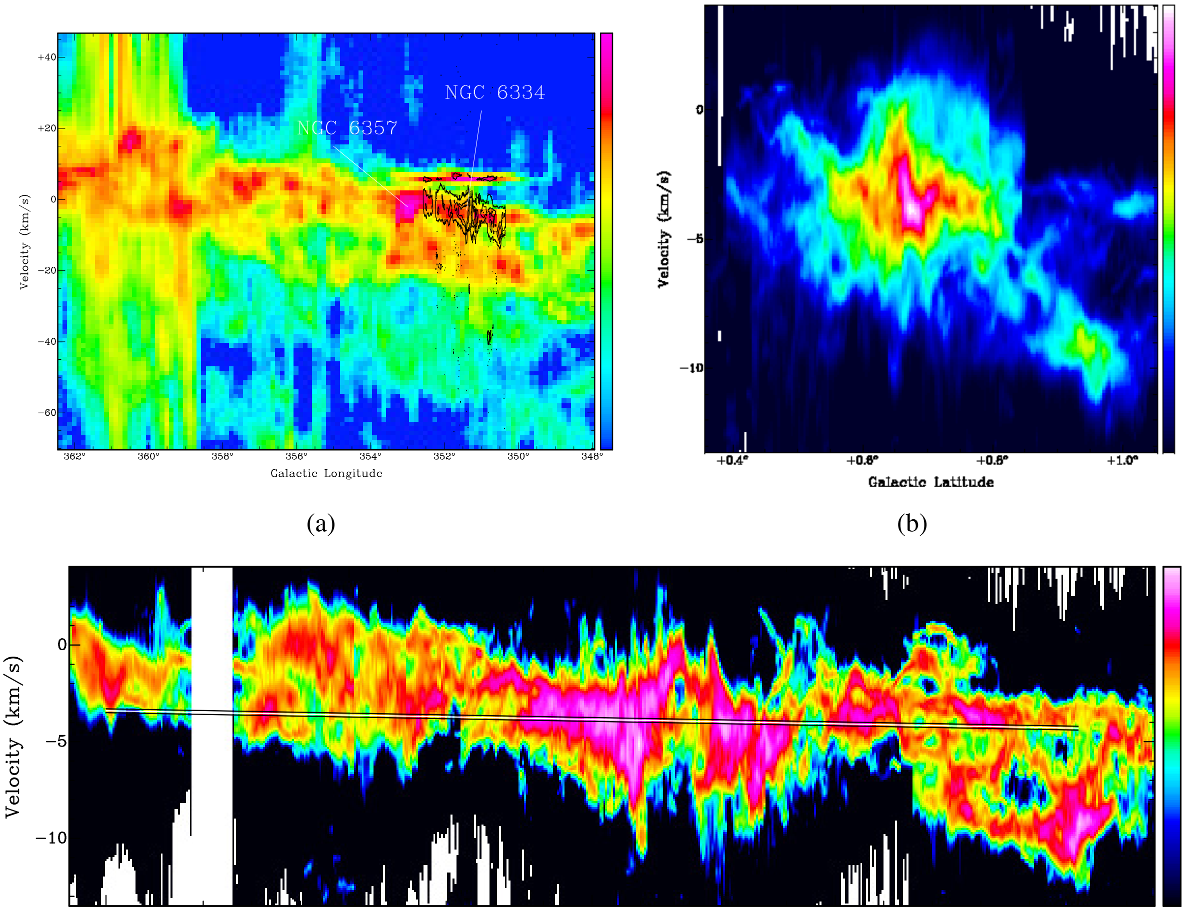

(a)

(b)

(c)

Figure 4.3.: PVDs of NGC 6334 in ^{13}CO (J=2–1). All color scales are logarithmically proportional to the intensity. (a) Overlaid in black contours on the CO survey by Dame et al. (2001). (b) PVD in the Galactic latitude direction (integrated over the longitude) and (c) in the Galactic longitude direction (integrated over the latitude). The white line in (c) denotes the expected velocity gradient from the Carina-Sagittarius arm.

The slight gradient is due to the so-called "Galactic molecular ring" from the rotation of the spiral arms. Because NGC 6334, together with NGC 6357, is part of the Carina-Sagittarius spiral arm, the velocity gradient could be impregnated by the rotation feature of this arm. The gradient dv/dl in this part of the molecular ring is approximated by the value Ω_1=0.45 km/s/deg. (or 0.015 km/s/pc at a distance of 1.7 kpc), which is derived from the spiral arm model of the Galaxy by Vallée (2008) in the galactic quadrant IV. It is noted that in this quadrant at longitudes of 350°, the Carina-Sagittarius arm and the Norma-Cygnus arm overlap in the velocity range [0,−20] km/s, and it is therefore difficult to assign a cloud to one of these arms at these position in the PVD from observations alone. However, the velocity gradient is flatter in the Carina-Sagittarius arm than in the Norma-Cygnus arm. Fig. 4.3(b) and (c) show the PVD along both Galactic coordinates. These plots do not show the reduced data from sect. 4.2, but correspond to the Gaussian fits described in sect. 4.3.2. The velocity dispersion from these fits for each component was hereby divided by a factor of three. The reduction of the line width improves the visibility of the mean velocity of each component, which would otherwise be smeared out by the large line widths. The marked line in fig. 4.3(c) indicates that this gradient from the spiral arm is to low and can not explain the overall gradient seen in NGC 6334. By averaging the radial velocity for each longitude, weighted by the intensity, a gradient is obtained of Ω_2=(2.5±1) km/s/deg., or (0.084±3) km/s/pc. Therefore, subtracting the spiral arm gradient from the velocity field does not change it significantly. As mentioned before, this gradient or velocity dipole is regarded as a large scale rotation, and the rotational energy, together with other energy terms, is discussed in sect. 4.5. Several velocity components exist in the LOS for the most redshifted and blueshifted part in NGC 6334, which could introduce artificial rotation or gradient features for an observer. By taking into account the bulk of the emission and by averaging over the largest scales of this GMC, the gradient in NGC 6334 is proven to exist.

4.3.2. Gaussian fitting

An analysis based only on the moment maps and data with noise could be misleading in some aspects. First, the mean velocity is deviated by non-Gaussian line profiles and multiple components in the LOS. Secondly, a lower threshold must be chosen, typically 3–5 times the rms, to subtract the noise, which will discard especially weak components under this threshold.

By following the analysis of Hacar et al. (2013) and Henshaw et al. (2014), it was therefore attempted to decompose the spectral information by Gaussian fitting. The task `gaufit` from `MIRIAD` was used to fit an arbitrary number of Gaussian components to each pixel in the spectral line cube, which uses the Levenberg-Marquardt algorithm for local optimization. First, the fits can be done fully automatically with an assumption for the upper limit of Gaussian components and an automatic finding of the best initial parameters. To reduce the number of bad fits, the initial estimates can be given by the user. By the assumption that the line profiles change only slightly from pixel to pixel, the fits for a pixel row are improved by using the fits from the pixels in the previous row. Finally, each 4 neighboring pixels in ^{13}CO and C^{18}O were checked block-wise manually for consistency and improved for bad fits, e.g., in the cases of high nose or low SNR. In the case of an optically thick self-absorbed ^{13}CO line, the comparison with the C^{18}O line therefore helps to decide how many line components are probably present.

The uncertainties for the intensities were used as mentioned in sect. 4.2. Because the spectral line width is resolved by typically 10 channels, the centroid velocity is determined more precisely by a fit (Δv=0.03 km/s) than from the velocity channel resolution of Δv=0.3 km/s. For each component, the amplitude, radial velocity and FWHM, their errors and the residuals are derived. The relation between the FWHM and dispersion or standard-deviation of a Gaussian is FWHM=$\sqrt{8\ln(2)}\sigma \approx 2.355\sigma$. The integral Σ is computed from the amplitude A and line width by $\Sigma = \sqrt{2\pi} A\sigma \approx 1.064\ A$ FWHM. The maximum number of components in one LOS are five for ^{13}CO and three for C^{18}O, see fig. 4.4 for an example.

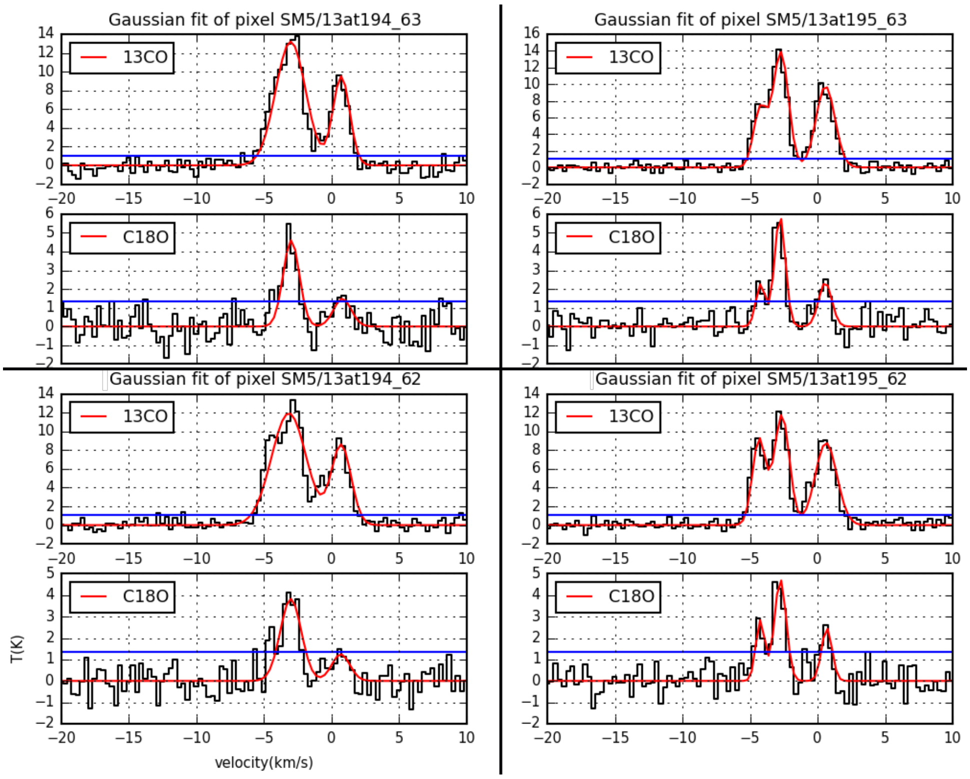

Figure 4.4.: Example of Gaussian fits at l=3518°, b=0.61°, where multiple components are visible. The blue line denotes the 3σ level.

4.3.3. Physical parameters and errors

Carlhoff (2014) presented observations and studies of the GMC W43 in ^{13}CO and C^{18}O with the Institut de Radioastronomie Millimétrique (IRAM) 30m telescope. The steps presented in Carlhoff (2014) are followed to calculate the temperatures, column densities and masses of the observational data. The error calculations are taken partly as presented by Furuya et al. (2014), assuming a Gaussian error propagation and an independence between the errors of the ^{13}CO and C^{18}O data. For example, a 3σ detection in C^{18}O can correspond to an error of 50% in R and consequently up to 100% in $\Delta\tau$.

The opacity of τ of ^{13}CO can be derived from the detection equation 2.7 by using the ratio of the intensity to an isotopologue:

$$R = \frac{I(^{13}\mathrm{CO})}{I(\mathrm{C}^{18}\mathrm{O})} = \frac{1 - \exp(-\tau_{13\mathrm{CO}})}{1 - \exp(-\tau_{\mathrm{C18O}})} = \frac{1 - \exp(-\tau)}{1 - \exp(-\tau/r)} \tag{4.1}$$

$$\Delta\tau^2 = \left[\left(\frac{\partial R}{\partial I(^{13}\mathrm{CO})} \Delta I(^{13}\mathrm{CO}) \right)^2 + \left(\frac{\partial R}{\partial I(\mathrm{C}^{18}\mathrm{O})} \Delta I(\mathrm{C}^{18}\mathrm{O}) \right)^2 \right] \left(\frac{\partial R}{\partial \tau} \right)^{-2} . \tag{4.2}$$

r is the isotopologue ratio. In NGC 6334, the ratio is calculated from the abundance of the isotopes by

$$r = [^{13}\mathrm{CO}]/[^{12}\mathrm{CO}] \times [^{12}\mathrm{CO}]/[\mathrm{C}^{18}\mathrm{O}] = 1/60 \times 500 = 8.\overline{3}\ . \tag{4.3}$$

Because eq. 4.1 cannot be solved analytically for τ, it is solved numerically. Although the relation in eq. 4.1 holds for every spectral channel, for simplicity it is assumed that the emission of ^{13}CO and C^{18}O traces the same region and the velocity differences are marginal, such that only the peak center or amplitude A of each component is taken. In the case of multiple components in ^{13}CO and C^{18}O, the components are sorted and assigned to each other such that the difference in their mean velocity is minimal. Furthermore, constraints are set up for the result of τ for low SNR to avoid unphysical results (R<1) or extreme values as a result of too high uncertainties. A high value of R is due to a weak detection of C^{18}O, whereas a low value of R is due to high opacities. Fig. 4.5 shows the ratio R in dependence of the optical depth τ as given by eq. 4.1. The curve gets flat in the limit $\tau \rightarrow 0$ and $\tau \rightarrow \infty$, and therefore R is not sensitive anymore for a precise derivation of τ. The mean uncertainty in R is $\delta R = \pm 0.3$. Thus a threshold is set at an upper limit of R=8.0 (corresponding to τ=0.09) and to a lower limit of R=1.3 (τ=12.2). Each ratio which exceeds or falls below these limits is replaced by the aforementioned opacities. This effects about 3% of the total number of 23E3 spectra.

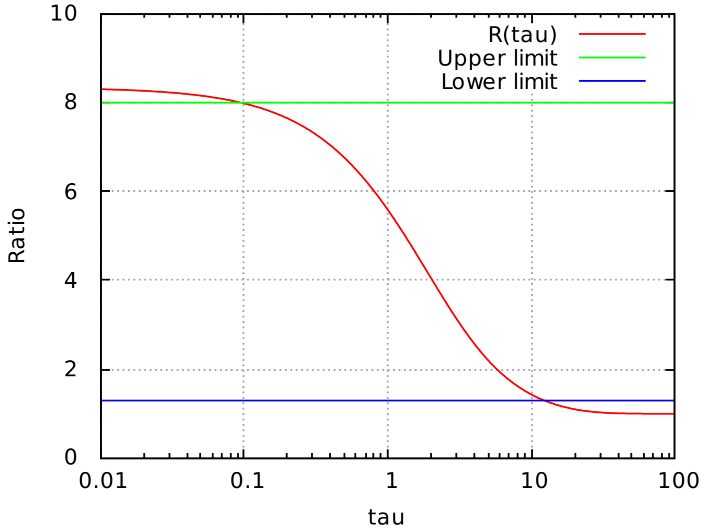

Figure 4.5.: The intensity ratio R in dependence of the opticl depth τ according to eq.4.1. The upper and lower limits are marked by horizontal lines.

By assuming LTE, the excitation temperature can be derived from the amplitude of the ^{12}CO line, which is always optically thick and therefore the temperature at the τ=1 surface would be measured. Because ^{12}CO observations are not available yet, the detection equation 2.7 is used to solve for T_{ex}:

$$T_{\mathrm{ex}} = \frac{Tc}{\ln(\left[\left(\frac{T_{\mathrm{p}}\,\eta}{1-\exp(-\tau)} + J(T_{\mathrm{bg}})\right)/Tc\right]^{-1} + 1)}\ , \tag{4.4}$$

where $Tc = \mathrm{h}\nu(^{13}\mathrm{CO})/\mathrm{k_B}$ and the error is $\Delta T_{\mathrm{ex}} = \Delta T_{\mathrm{ex}}(\Delta T_{\mathrm{p}}, \Delta\tau)$. T_{p} is the peak temperature or amplitude of the spectral line.

According to Wilson et al. (2009), the ^{13}CO column density $N(^{13}\mathrm{CO})$ and consequently H_2 column density $N(\mathrm{H_2})$ is calculated as:

$$N(^{13}\mathrm{CO}) = 1.5\mathrm{E}14 \times I(^{13}\mathrm{CO}) \times \frac{\tau}{1-\exp(-\tau)} \times \frac{\exp(T_{c1}/T_{\mathrm{ex}})}{1-\exp(-T_{c2}/T_{\mathrm{ex}})}, \tag{4.5}$$

where $T_{c1} = \mathrm{h}\nu(^{13}\mathrm{CO}(1-0))/\mathrm{k_B} \approx 5.3$ K and $T_{c2} = \mathrm{h}\nu(^{13}\mathrm{CO}(2-1))/\mathrm{k_B} \approx 10.6$ K. The last two factors in eq. 4.5 are the opacity and temperature correction, and $I(^{13}\mathrm{CO})$ is the integrated line intensity. The error of $\Delta N(^{13}\mathrm{CO})$ depends on $\Delta I(^{13}\mathrm{CO}), \Delta T_{\mathrm{ex}}$, and $\Delta\tau$. By assuming a standard CO/H_2 abundance ratio of 1E-4 in the Galaxy, the H_2 column density is calculated by

$$N(\mathrm{H_2}) = N(^{13}\mathrm{CO}) \times 60 \times 1\mathrm{E}4\ . \tag{4.6}$$

Finally, provided that m_{g} is the mass per particle, D is the distance and α is the angular extent of a pixel, the mass per pixel is

$$M_{\mathrm{p}} = N(\mathrm{H_2}) \times m_{\mathrm{g}} D^2 \alpha^2\ . \tag{4.7}$$

In NGC 6334, the following values are applied: $m_{\mathrm{g}} = 2.7\ \mathrm{m_h}$, D=(1.7±0.3) kpc and $\alpha = 14.3''$.

The sonic Mach number M_{S} is defined as the ratio of the velocity dispersion over the speed of sound:

$$M_{\mathrm{S}} = \frac{\sigma}{c_{\mathrm{s}}} = \frac{\sqrt{3}\sigma_{\mathrm{1D}}}{\sqrt{\mathrm{k_B} T / m_{\mathrm{H_2}}}}. \tag{4.8}$$

The one-dimensional dispersion is related by $\sqrt{3}\sigma_{\mathrm{1D}} = \sigma_{\mathrm{3D}}$ to the 3D dispersion for isotropic turbulence. The magnetic field B is calculated via the Chandrasekhar-Fermi method (Chandrasekhar and Fermi, 1953) by means of the polarization dispersion $\Delta\phi$. In cgs units, the magnetic flux unit is given in Gauss, where 1 G=1E-4 Tesla. By knowing B, the Alfvénic speed v_{A} and Alfvénic Mach number M_{A} are calculated by

$$B = \frac{\sigma}{\Delta\phi}\sqrt{\frac{4}{3}\pi\rho}; \quad v_{\mathrm{A}} = \frac{B}{\sqrt{4\pi\rho}}; \quad M_{\mathrm{A}} = \frac{\sigma}{v_{\mathrm{A}}}. \tag{4.9}$$

4.3.4. Velocity gradients

Some general trends about the velocity of the gas, such as systematic or random motions, can be obtained from calculating velocity gradients and movements on the velocity field map. If molecular gas in the geometry of a filament or cylinder is gravitational accelerated onto a massive clump, a velocity gradient is expected to occur in the velocity map with a decreasing or increasing velocity shift along the path. Free-fall accretion onto filaments can lead to elongated clouds, so-called striations or fans, which are formed by tidal forces (Heitsch, 2013). Fig. 4.6(a) depicts all velocity gradients with a size ≥ 1 pc by filtering them out from the velocity map in fig. 4.2. For simplicity, the orientations are limited to a multiple of 45° and only monotonically in- or decreasing velocities are selected. These regions are selected by numbers where a convergence of the flows onto dense clouds is visible . A gravitational collapse would also be visible along the LOS by a blueshifted asymmetric infall profile. Only the clumps no. 4, 5 (corresponding to NGC 6334I(N)) and 6 show this characteristic profile, which is hampered by the fact that ^{13}CO is only marginal optically thick ($\tau \sim 1$). By extending the velocity map from chap. 3, more flows are detected perpendicular to the main filament, of which two are marked by arrows in fig. 4.6(a). This is a further confirmation for an edge-driven collapse of the filament toward the clumps NGC 6334I and I(N).

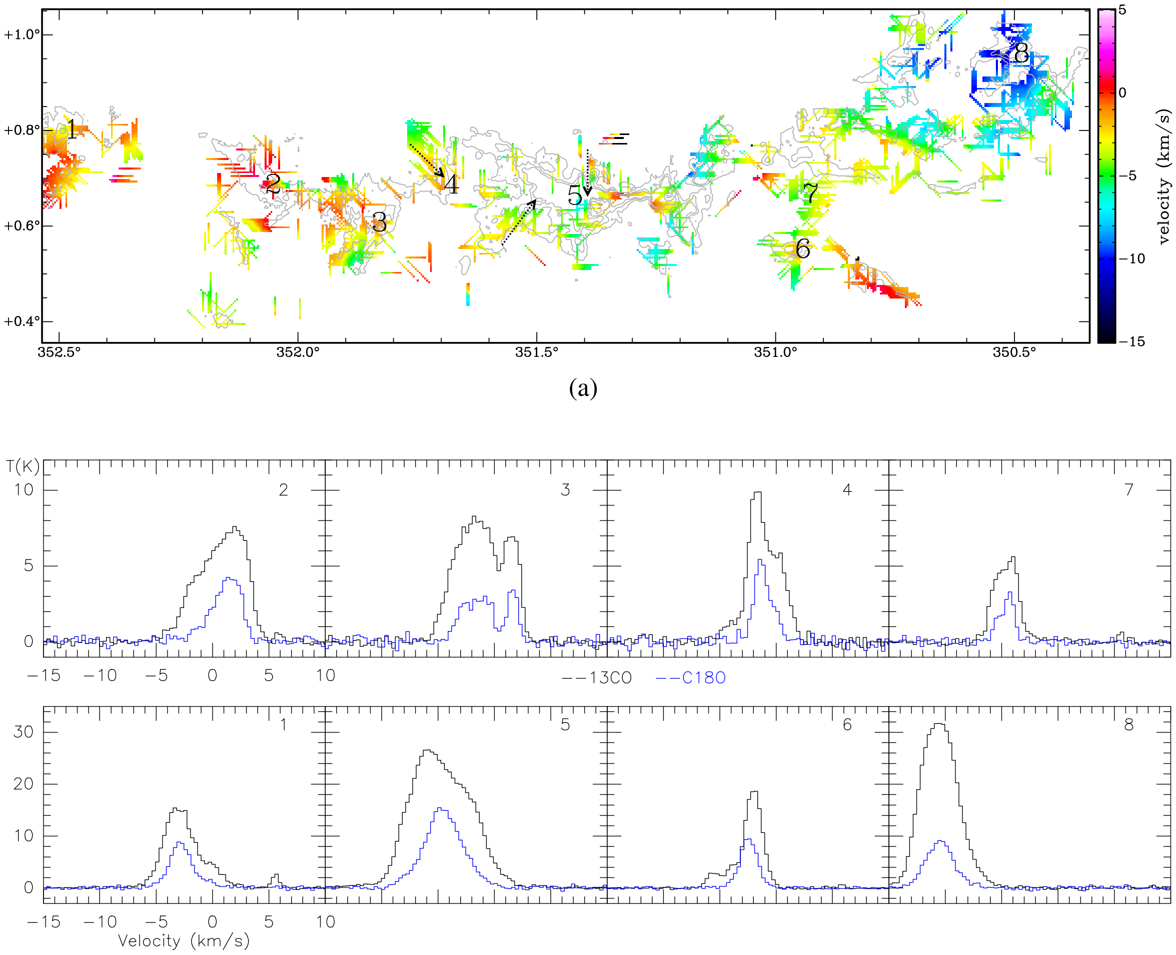

(a)

(b)

Figure 4.6.: (a) Velocity gradients in NGC 6334, overlaid in gray contours with the integrated intensity of C^{18}O. The spectra of selected regions are shown in (b).

The region no. 3 at l=351.9° has two velocity components in ^{13}CO and C^{18}O, which seem to merge into each other in the velocity channel map in fig. 4.7(b). The magnification of the velocity map in fig. 4.7(a) exhibits a gradient above and below the most dense clump in the center. While the peak of emission in the center has a mean velocity of 0 km/s, the upper and lower gas have a continuous gradient to lower mean velocities of −6 km/s. This can be interpreted as accretion flows or converging flows from the diffuse gas to the gravitational center. As this region is very cold and young with no signs of star formation, the opposite case of a possible outflow motion is excluded.

An initial attempt to calculate velocity gradients of an array was using the `NumPy` package and second order central differences. Because this algorithm calculates the differences from

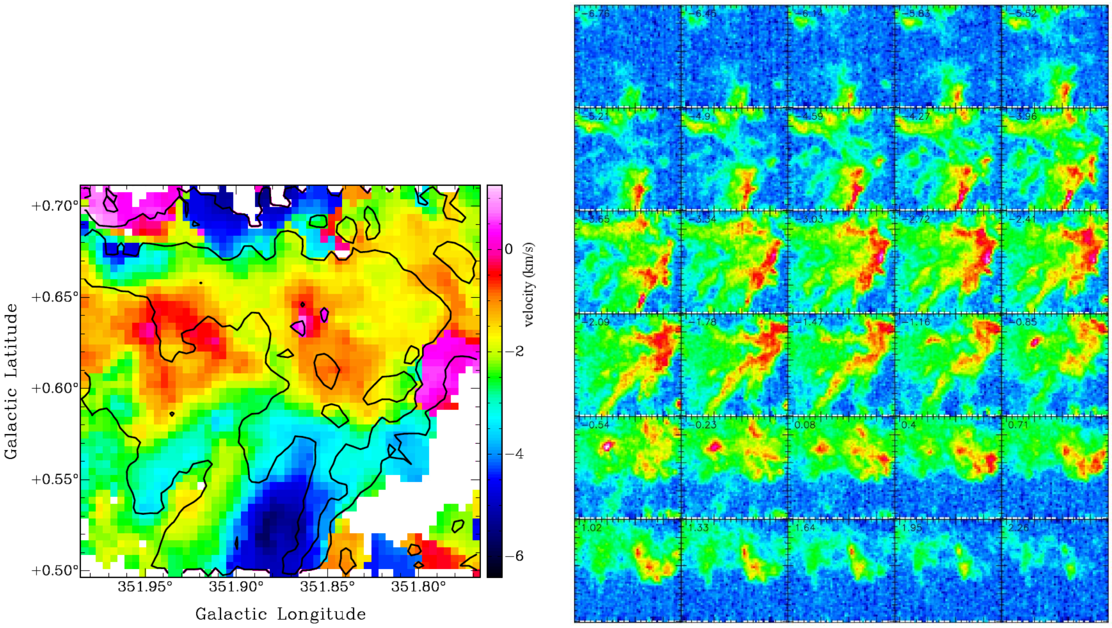

(a)

(b)

Figure 4.7.: (a) Velocity field of one submap in NGC 6334 with indications for accretion. Overlaid in black contours is the integrated ^{13}CO emission. (b) Corresponding velocity channel maps in the range [−6.8, +2.3] km/s in steps of +0.3 km/s.

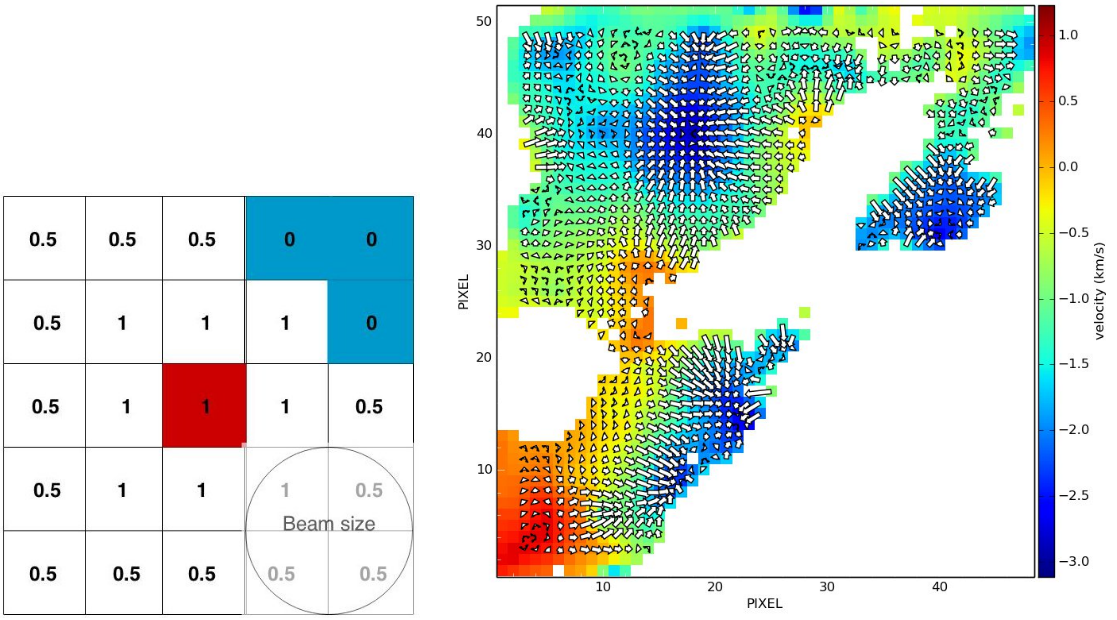

0.5	0.5	0.5	0	0
0.5	1	1	1	0
0.5	1	1	1	0.5
0.5	1	1	1	0.5
0.5	0.5	0.5	0.5	0.5

(a)

(b)

Figure 4.8.: Sketch of the velocity gradient method. (a) Sketch of the kernel and its weighting values. The central pixel is marked in red and missing values in blue. (b) Example of the method applied to the submap at l=352.5°. The arrow length is proportional to the magnitude.

direct neighboring pixels, it produces the gradients only on the smallest scales. Another method to calculate and fit velocity gradients was presented initially by Goodman et al. (1993) (for a recent application see Henshaw et al., 2014). The basic idea is to fit a linear function, a plane of a certain size, to the velocity field. In the context of image analysis, this can be regarded as running a kernel over an image. The equations are

$$\vec{v}(x,y) = c_0 + c_1 \times x + c_2 \times y; \quad |\vec{v}| = \sqrt{c_1^2 + c_2^2}; \quad \phi = \arctan(c_2/c_1). \tag{4.10}$$

One obtains the velocity gradient vector $\vec{v}$, its magnitude $|\vec{v}|$ and its direction ϕ. Although scripts of this procedure exist in `IDL`, the method was rewritten in `Python` by using libraries from `Astropy` (Robitaille et al., 2013). The plane size was chosen to 5×5 pixels, where additional a weighting in the fitting for each pixel is defined such that the outer more distant pixels are weighted less and pixels with no information, typically at the boundaries, are neglected. The bigger plane size of ca. 2.5×beam size is thus more robust against small scale fluctuations than the initial method mentioned above. See fig. 4.8 for an illustration and exemplary application. If the line width-size relation follows the proportionality $\mathrm{d}v = \sigma \propto L^{0.5}$, then the velocity gradient should decrease with increasing distance L by $\mathrm{d}v/\mathrm{d}L \propto L^{-0.5}$.

In context of vector analysis, this method is applied to a scalar field F (the velocity map) and outputs a vector field. The second derivation gives the scalar divergence field. A rotation or whirl cannot be obtained by this method because rot(grad F)=0. However, if for example a molecular disk is observed edge-on, the velocity map gives an almost linear velocity gradient if it is not resolved well. If the true motion follows a Keplerian rotation, the characteristic PVD would resemble fig. 2.4(b). On a first view it is thus not distinguishable if a systematic motion is due to a linear movement or a rotation, and there is an ambiguity about the flow direction (from red to blue velocities or the other way). The velocity gradients, which are shown here, are defined to point to the negative or blueshifted velocities, but in general they should be considered in dependence of the environment of the molecular cloud, e.g., if a gravitational center is present (fig. 4.7).

According to Kirk et al. (2013), filamentary accretion flows can be derived from the formula

$$\dot{M} = (M/L \times v_{\|}) / \tan(\alpha), \tag{4.11}$$

where $v_{\|}$ is the velocity gradient (in km/s) parallel to the filament, M/L is the mass per line density and α the inclination angle of the filament. The mass per line density is obtained from the kernel by summing up the mass and diving the length of 5 pixels or 0.55 pc. In general, the mass accretion rate is deduced for geometric objects by using the fact that $\mathrm{d}V/\mathrm{d}r = A$ by

$$\dot{M} = \frac{\mathrm{d}M}{\mathrm{d}r}\frac{\mathrm{d}r}{\mathrm{d}t} = A\rho v = A\frac{M}{V}v = \begin{cases} 3(M/R)v & \text{for spheres} \\ (M/L)v & \text{for cylinders .} \end{cases} \tag{4.12}$$

Due to projection effects in dependence of the angle α, the rate $\dot{M}' = \dot{M}/\tan(\alpha)$ is observed for cylinders. For $\alpha \approx 45°$, as derived in chap. 3, this correction simplifies to $\tan(\alpha) = 1$.

4.3.5. Dendrogram

Several algorithms were developed to find velocity-coherent structures in data cubes of molecular clouds. Initially developed for cosmic scales, `DisPerSE` (Discrete Persistent Structures Extractor) identifies filamentary structures, e.g., as demonstrated by Panopoulou et al. (2014). The codes `getsources` and `getfilaments` are used for identifying cores and filaments on maps obtained with the HSO (André et al., 2010). The code Friends-In-Velocity (FIVE, Hacar et al., 2013) is based on the friends-of-friends algorithm. Algorithms for characterizing the turbulent properties of molecular clouds are the Delta-variance method (Ossenkopf et al., 2008) or the principal component analysis (PCA, Brunt and Heyer, 2002).

The hierarchical clustering algorithm `astrodendro`[1] is used here (written in `Python`), which makes use of the hierarchical structure of the ISM. Applications of it for different molecular clouds are presented, among others, by Rosolowsky et al. (2008), Goodman et al. (2009), and Storm et al. (2014). It disentangles overlapping astronomical sources by using the full position-position-velocity (PPV) information of data cubes. After the run, the intensity values are replaced by the structure number (idx) in each voxel, which makes further analysis and visualization easier, see fig. 4.9. A voxel is the 3D equivalent to a pixel and represents a data point in the PPV cube. In this terminology, a tree-like structure is build up where the trunk is the lowest structure (with the largest scales, corresponding to the total GMC), which subdivides into branches and leaves to higher numbered structures (corresponding to the smallest scales, i.e., cores and clumps). The level number or segmentation height of a structure is counted from the trunk. At the moment, only a binary tree structure is included, which means that for each new structure a new branch is invented. This leads in some cases to "ghost branches", which are almost identical to the previous branch and therefore not a new real structure.

The outcome of the dendrogram analysis depends on three main parameters, which are set by the user: the threshold, the min-delta and the min-pixel parameter. The threshold parameter neglects all pixels below this threshold (typically 3σ) because of noise, while the min-delta parameter accounts for the substructure threshold and determines the degree of segmentation. That means, neighboring pixels need a difference of at least x Kelvin to account as an independent structure, otherwise they are merged together. The min-pixel parameter is the minimum number of pixels a structure should have to avoid spikes, which could be chosen by a multiple of the beam size. To find a overall coherent structure for the whole data cube of NGC 6334, the missing part at l=352.3° was interpolated linearly between the two adjacent maps. The synthetic data cube from sect. 4.3.2 is used to include fainter structures. Although this cube has no noise, a threshold of 0.1 K was used which is the typical order of magnitude of the real noise. While the values for the min-pixel parameter seem to have no effect on the data cube, the min-delta parameter is the most crucial one. The algorithm was run for two parameter sets: one with min-delta=10 K, which finds the 43 most important structures; the other one with min-delta=2 K, which results in ca. 700 structures and is used to get better statistics in sect. 4.4.1.

---

[1] URL: `http://www.dendrograms.org/`

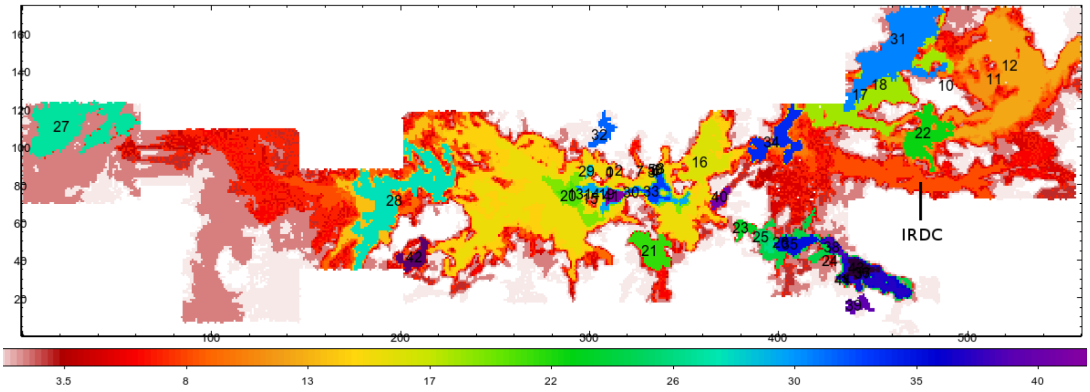

(a) PP projection for min-delta=10 K

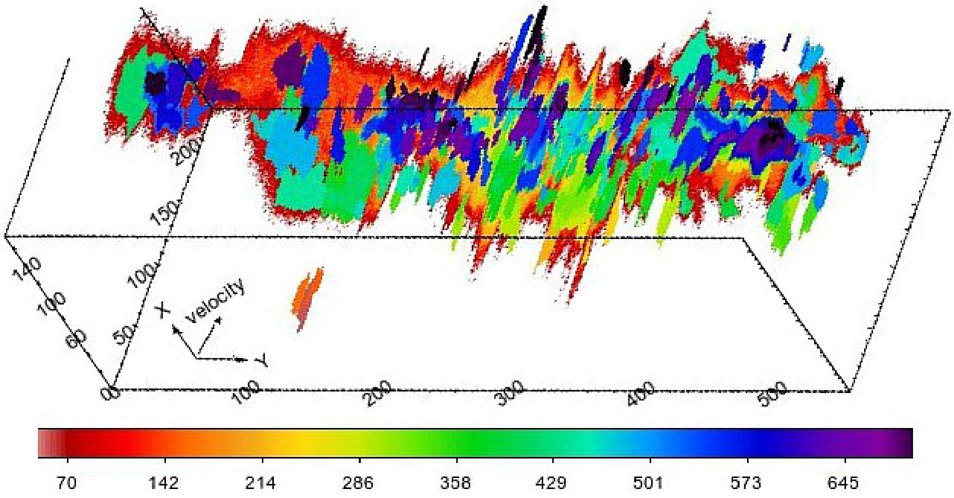

(b) PPV ray tracing for min-delta=2 K

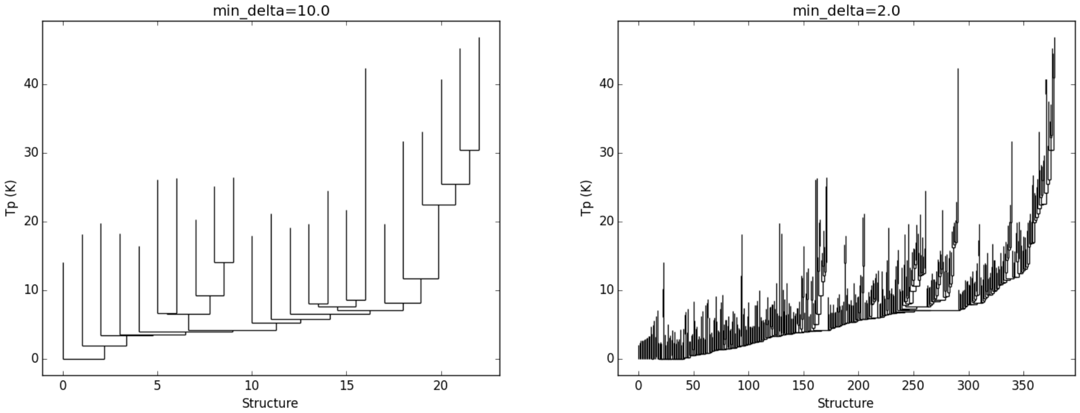

(c) Dendrogram for min-delta=10 K (d) Dendrogram for min-delta=2 K

Figure 4.9.: Dendrogram results for NGC 6334 (see table 4.1 for the structure idx).

4.4. Physical Properties

The median value of the ^{13}CO/C^{18}O intensity ratio R is 5.2 and $\Delta R/R$ =20 %, τ=1.2 (±60%) and T=20 K (±18%). The median column density is $\langle N(\mathrm{H}_2)\rangle$=1.3E22 1/cm^2 (±33%). The results from the calculations of the temperature and column density are shown in fig. 4.10(a,b). Because of several velocity components in the LOS, there are different ways to project them on a 2D map. In the case of the temperature map in fig. 4.10(a), the average temperature is calculated, weighted by the intensity. The average gas temperature is T=20 K, and ranges from 10 K outside to 50 K at the main filament, where the HII regions are present. The good association of the temperature increase with the Hα emission thus means that the molecular gas temperature is increased by the HII regions in their vicinities as a result of UV radiation by young OB stars. The column density map in fig. 4.10(b) is calculated from the sum of the components. It shows a variation from 21–23.5 $\log_{10}(N(\mathrm{H}_2)/\mathrm{cm}^2)$, where the highest values are found in the main filament. In general, it is proportional to the integrated ^{13}CO emission. The total mass is 1.5E5 M$_\odot$, which counts only the emission found in C^{18}O.

The mass derived from ^{13}CO is higher, because there is emission detected in the more outer regions where the C^{18}O is too weak. The total mass from the ^{13}CO emission is given in sect. 4.4.1. The mean Mach number in NGC 6334 is M_S = 5.7 (derived from C^{18}O), and thus the gas motions are super-sonic, as was anticipated from the line widths. Fig. 4.10(c) presents the derived mass accretion rates by using the mass map, the results from the velocity gradient method and eq. 4.12 for cylinders/filaments with an inclination angle of 45°. The mass accretion rates range from 1E-3 to 1E-7 M$_\odot$/yr, where the highest values are found near the cores in the main filament, as they have the most mass. In the vicinity of the cluster I and I(N), the maximum rate reaches 1–2E-3 M$_\odot$/yr, which is related to the smaller scale observations in chap. 5 for a spherical geometry.

The 2D Histogram of the velocity gradients, fig. 4.11(a), shows that the peak magnitude is around 1 km/s/pc. This is one order of magnitude higher than the general velocity gradient of 0.084 km/s/pc on the largest scales in NGC 6334 discussed in sect. 4.3.1. The direction or position angle is preferentially at +75° and -70°. A degree of 0 corresponds to an east–west alignment, and ±90° to an north–south alignment on the image. Thus, more gradients are oriented perpendicular to the Galactic plane. They are probably connected to and channeled by the magnetic field, which is also oriented perpendicular to the filaments. The histogram of the mass accretion rates (fig. 4.10(c)) is presented in fig. 4.11(b). It can be approximated by a log-normal PDF, which is defined as

$$f(x,\mu,\sigma) = \frac{1}{x\sqrt{2\pi\sigma^2}} \exp\left[-(\ln(x)-\mu)^2/(2\sigma^2)\right]. \tag{4.13}$$

The variable is x, μ is the mean and σ the standard deviation, and $f(x)$ is equivalent to the normal distribution $f(x')$ by changing the variable to $x' = \ln(x)$. The data were binned into 100 bins in log scale, and the fit was restricted to $x > -5.3$ because lower values show an excess. The mean is $\mu = -4.74$ or 1.8E-5 M$_\odot$/yr.

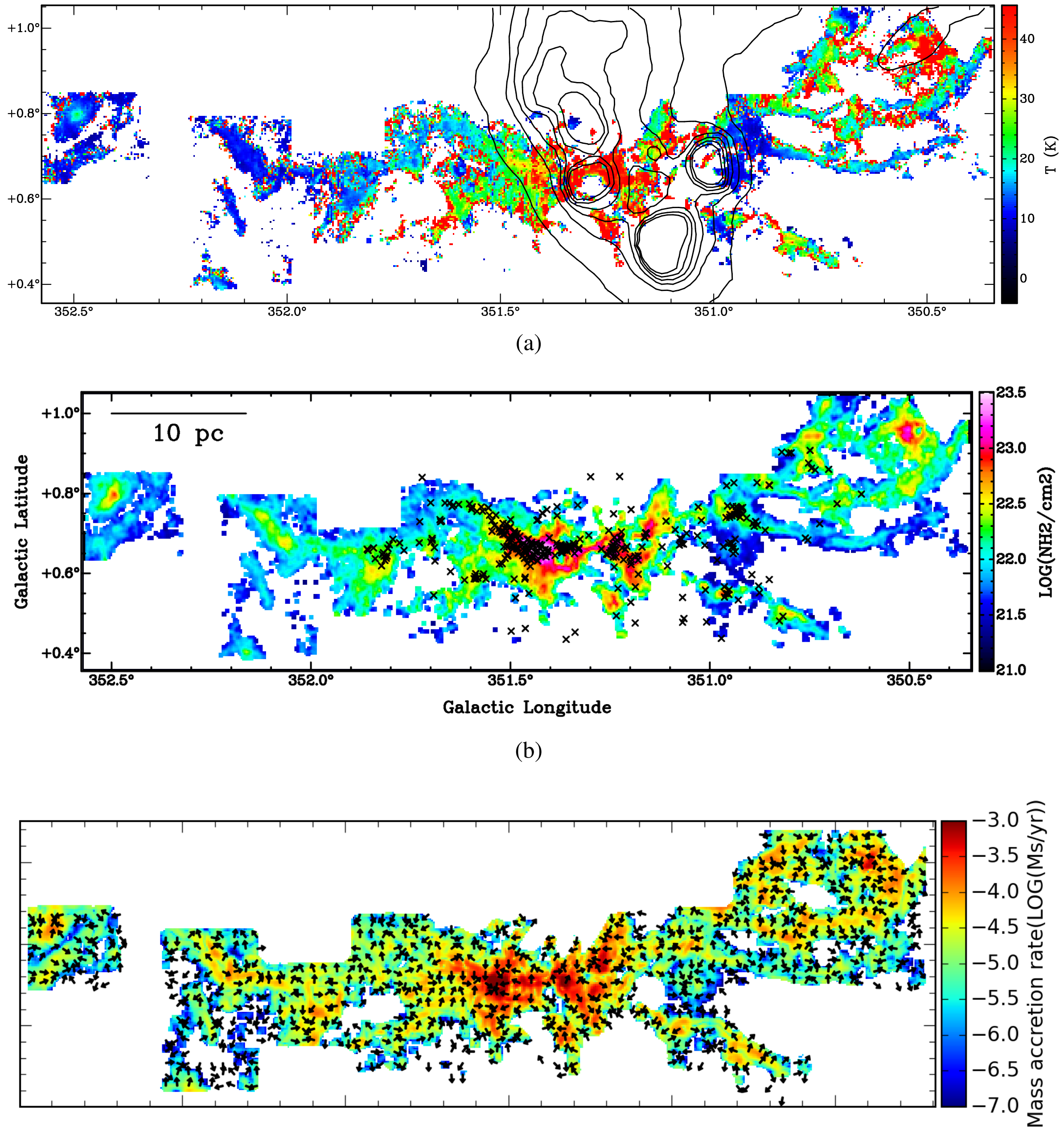

(a)

(b)

(c)

Figure 4.10.: (a) Excitation temperature map of NGC 6334, overlaid with Hα emission in black contours. (b) Molecular hydrogen column density map in logarithmic scales, where the position of Class I YSO from Willis et al. (2013) are marked by crosses. (c) Mass accretion rates, overlaid with a selection of arrows obtained from the velocity gradient method.

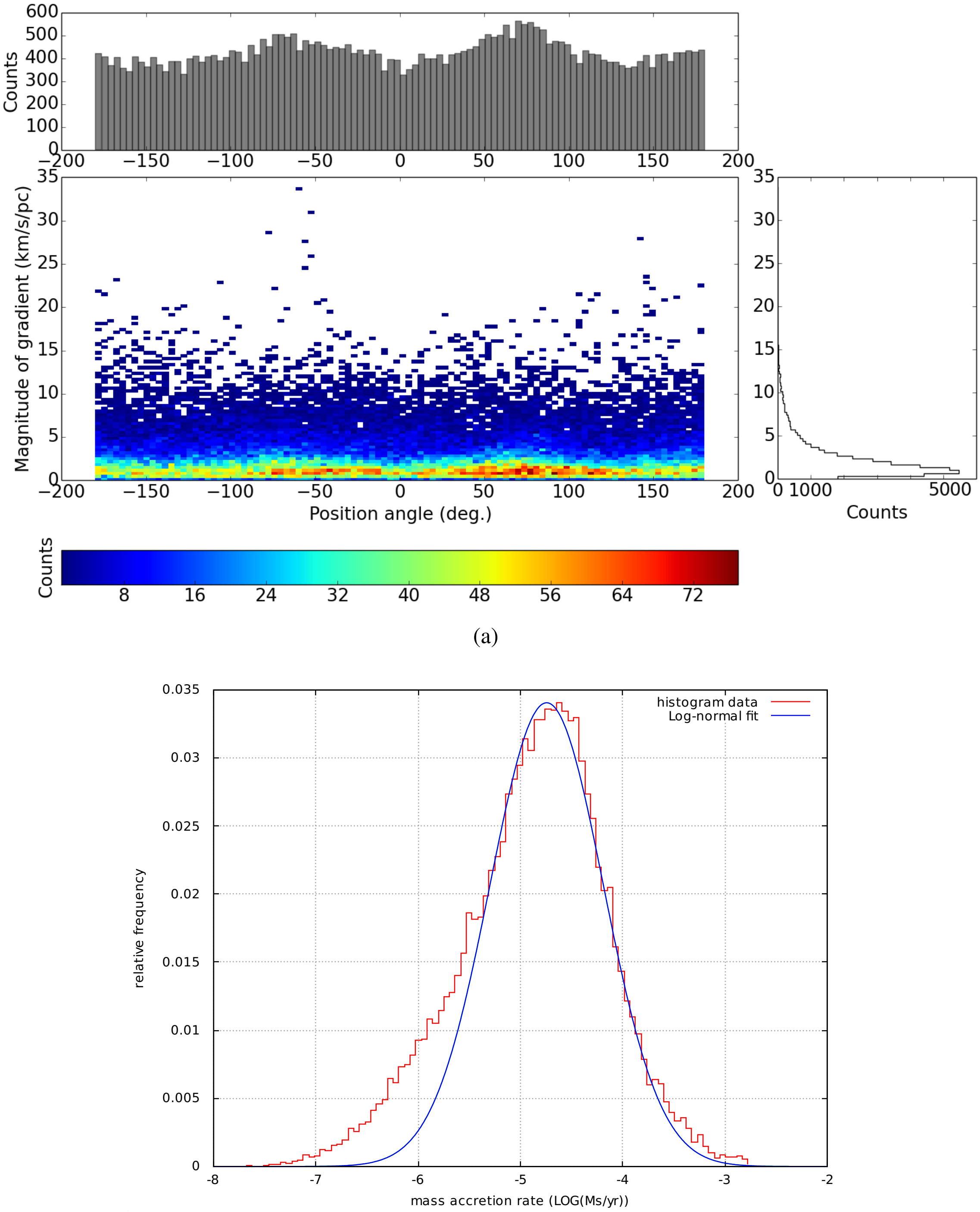

(a)

(b)

Figure 4.11.: (a) 2D histogram of all gradients in NGC 6334 obtained from the velocity gradient method. (b) Histogram of the mass accretion rates. The best log-normal fit is shown with values of A=0.047, $\mu = -4.74$, and σ=0.55.

A catalog of YSO was obtained from Willis et al. (2013). Because the earliest stages of star formation are studied here, only the Class I YSO are selected, which are depicted by crosses in fig. 4.10(b). The direct correlation between the position of a YSO and the column density is shown in fig. 4.12. For each pixel, the number of YSO is counted within a search radius of 3×beam size. The number of YSO or probability increases with the column density. However, there is a drop at approximately 23.2 $\log_{10}(N(\mathrm{H}_2)/\mathrm{cm}^2)$ concerning the maximum number and, on the average plot, a dip at this value, and the number seems to remain constant for the highest densities. This value is, in other units, similar to a column density of about 1 g/cm^2, which is theoretically predicted as the threshold for massive star formation by Krumholz and McKee (2008). This would explain that the fractionation does not increase anymore at this value, and the mass is accumulated by massive stars instead of several low mass stars. Some more properties about the mass of these YSO would be beneficial, but do not exist at the moment. Another possible effect resulting for the decline could be the extinction, so that the YSO are not visible in the IR at these very high column densities and are not counted properly, e.g., if they are located behind the cloud in the LOS.

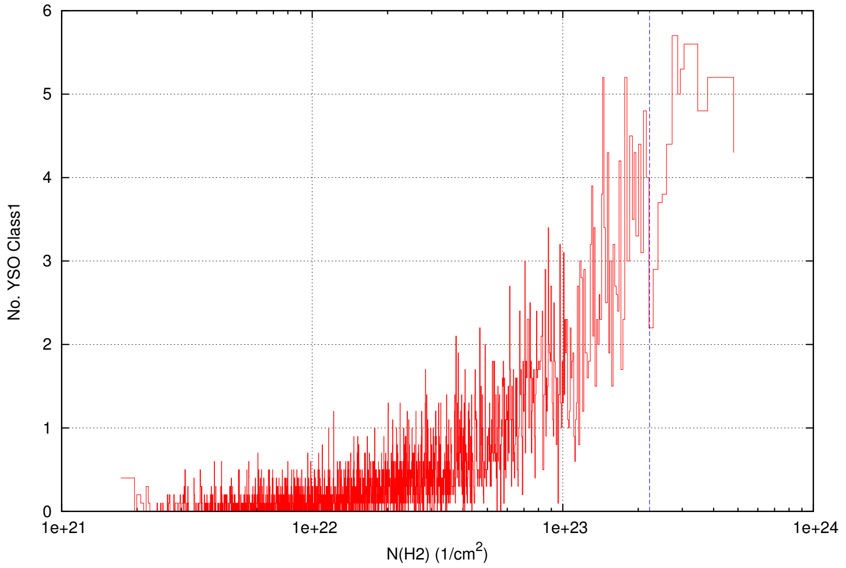

Figure 4.12.: Correlation between the hydrogen column density and average number of YSO Class I (averaged by 10 neighboring bins). The blue vertical line marks a column density of ≈1 g/cm^2.

4.4.1. Results from the dendrogram algorithm

Table 4.1 summarizes the outcome for the run with min-delta=10 K and includes statistics for each structure. The six subfigures of fig. 4.13 represent the correlation and scaling relations of these values. The area in the PP projection is derived from elliptical fits, and the velocity center (v_c) and velocity dispersion (σ) are calculated from the first and second moment in the velocity space. The exact area A is obtained by adding all the pixels, and because the fitted area is always lower than the exact one, the ratio of the fitted area over the exact area is called filling factor and takes the values ≤ 1.

Table 4.1.: Dendrogram results for each structure in NGC 6334 with min-delta=10 K

idx	leaf	x|y (pixel)	RA (degr)	Dec (degr)	Flux (K km/s)	Mass ($M_\odot$)	*A* (exact) ($arcs^2$)	*r*(maj) (arcs)	*r*(min) (arcs)	PA (degr)	v_c (km/s)	σ (km/s)	$\alpha_{\rm vir}$
0	0	312.3 | 86.4	260.1090	-35.8210	9.13E+6	2.34E+5	9.01E+6	1956.2	401.7	-173.4	-4.07	2.93	1.56
1	0	312.2 | 86.5	260.1088	-35.8209	9.12E+6	2.34E+5	8.80E+6	1956.1	400.8	-173.4	-4.07	2.92	1.52
2	0	316.9 | 87.4	260.0921	-35.8340	7.83E+6	2.01E+5	7.29E+6	1890.5	383.7	-173.2	-4.11	2.80	1.40
3	0	334.4 | 86.6	260.0461	-35.8926	6.25E+6	1.60E+5	5.24E+6	1607.0	332.2	-170.4	-4.34	2.75	1.42
4	0	336.2 | 86.7	260.0408	-35.8987	5.93E+6	1.52E+5	4.80E+6	1574.8	323.7	-169.8	-4.39	2.73	1.38
5	0	334.2 | 88.0	260.0412	-35.8892	5.62E+6	1.44E+5	4.40E+6	1568.6	284.2	-168.8	-4.48	2.71	1.40
6	0	336.4 | 87.7	260.0361	-35.8967	4.94E+6	1.27E+5	3.69E+6	1497.4	269.2	-167.7	-4.57	2.64	1.35
7	0	328.1 | 87.1	260.0618	-35.8711	6.41E+6	1.65E+5	5.48E+6	1705.1	357.9	-172.3	-4.29	2.75	1.35
8	0	339.0 | 88.3	260.0265	-35.9038	4.47E+6	1.15E+5	3.20E+6	1446.1	242.5	-166.7	-4.63	2.59	1.33
9	0	338.0 | 88.1	260.0302	-35.9013	4.04E+6	1.04E+5	2.68E+6	1395.7	229.7	-165.8	-4.67	2.58	1.28
10	0	489.7 | 132.3	259.4229	-36.2940	8.49E+5	2.18E+4	9.16E+5	611.5	220.5	-163.7	-7.25	2.50	3.00
11	0	515.6 | 136.0	259.3344	-36.3697	4.98E+5	1.28E+4	4.92E+5	352.0	180.5	-137.9	-7.99	2.25	3.24
12	1	523.5 | 142.9	259.2838	-36.3793	3.43E+5	8.82E+3	2.98E+5	207.2	162.1	89.5	-8.70	1.83	2.59
13	0	294.0 | 74.8	260.2068	-35.7880	2.93E+6	7.52E+4	1.55E+6	635.6	188.2	-176.5	-3.94	2.04	1.05
14	0	302.6 | 74.9	260.1826	-35.8157	2.51E+6	6.43E+4	1.09E+6	503.8	179.1	-175.7	-4.08	2.01	0.96
15	0	301.9 | 72.6	260.1938	-35.8188	1.64E+6	4.20E+4	6.23E+5	401.6	137.1	178.5	-3.94	1.97	1.03
16	1	359.5 | 91.8	259.9549	-35.9628	1.61E+5	4.13E+3	8.94E+4	111.8	58.5	65.1	-5.79	1.47	2.44
17	0	444.5 | 127.6	259.5704	-36.1579	2.73E+5	7.02E+3	3.40E+5	438.9	109.3	-148.5	-6.10	2.42	5.43
18	1	454.4 | 132.9	259.5211	-36.1780	2.08E+5	5.35E+3	2.53E+5	280.6	108.7	-141.5	-6.81	1.99	4.52
19	0	310.3 | 75.0	260.1604	-35.8407	4.84E+5	1.24E+4	1.52E+5	296.9	68.0	-179.9	-3.70	2.10	1.60
20	1	290.1 | 74.2	260.2202	-35.7764	8.05E+4	2.07E+3	1.94E+4	36.6	33.5	115.1	-6.48	1.24	1.73
21	1	333.2 | 44.9	260.2175	-35.9838	7.81E+4	2.01E+3	5.48E+4	75.7	46.1	129.9	-6.00	1.34	3.47
22	1	477.7 | 107.5	259.5572	-36.3120	5.85E+4	1.50E+3	8.10E+4	110.9	67.8	59.5	-5.34	1.45	5.50
23	1	381.4 | 57.1	260.0328	-36.1133	8.19E+3	2.10E+2	1.35E+4	38.6	30.7	178.1	-5.74	0.92	6.64
24	0	428.5 | 39.7	259.9706	-36.3067	1.60E+5	4.12E+3	2.19E+5	349.9	57.6	159.6	-1.77	1.50	3.53
25	1	391.7 | 52.1	260.0240	-36.1583	1.24E+4	3.17E+2	1.31E+4	32.0	21.8	133.6	-4.42	0.80	4.20
26	0	402.6 | 49.5	260.0040	-36.1999	4.29E+4	1.10E+3	4.72E+4	117.4	32.3	169.8	-2.91	1.19	4.17

Table 4.1 – Continued from previous page

idx	leaf	x|y (pixel)	RA (degr)	Dec (degr)	Flux (K km/s)	Mass ($M_\odot$)	A (exact) (arcs^2)	r(maj) (arcs)	r(min) (arcs)	PA (degr)	v_c (km/s)	σ (km/s)	α_{vir}
27	1	22.1 | 110.8	260.8147	-34.8166	1.22E+5	3.13E+3	2.01E+5	171.4	86.8	-170.5	-1.86	1.15	2.92
28	1	198.2 | 71.4	260.4875	-35.4823	1.19E+5	3.05E+3	2.20E+5	269.2	113.8	-140.2	-2.25	1.16	2.32
29	1	299.8 | 86.8	260.1422	-35.7794	7.84E+3	2.01E+2	3.89E+3	26.5	9.9	70.9	-4.56	0.86	3.69
30	0	323.3 | 75.8	260.1208	-35.8813	2.10E+5	5.39E+3	7.30E+4	211.3	46.9	-179.4	-2.45	1.43	1.16
31	1	464.6 | 156.9	259.3953	-36.1560	7.87E+4	2.02E+3	2.32E+5	204.2	81.0	52.5	-3.48	0.68	1.74
32	1	306.5 | 106.3	260.0451	-35.7570	1.21E+4	3.11E+2	2.35E+4	62.4	30.4	61.2	-1.37	1.65	19.8
33	1	334.1 | 76.6	260.0873	-35.9144	6.32E+4	1.62E+3	2.31E+4	56.1	40.8	-149.2	-2.84	1.28	2.04
34	1	397.6 | 102.3	259.8051	-36.0630	4.34E+4	1.11E+3	6.52E+4	115.9	65.1	-143.3	-2.78	0.82	1.90
35	1	407.3 | 48.4	259.9953	-36.2174	2.95E+4	7.57E+2	3.19E+4	64.7	28.9	-174.0	-2.27	0.61	1.54
36	0	445.3 | 33.7	259.9475	-36.3749	7.95E+4	2.04E+3	9.96E+4	152.5	52.3	151.0	-0.87	0.88	1.80
37	0	446.0 | 33.0	259.9483	-36.3789	5.36E+4	1.38E+3	6.77E+4	116.9	46.5	159.2	-0.79	0.80	1.81
38	1	429.5 | 47.2	259.9374	-36.2927	4.80E+3	1.23E+2	1.12E+4	56.3	15.8	136.5	-1.60	0.46	2.75
39	1	441.3 | 16.1	260.0300	-36.4020	3.55E+3	9.12E+1	1.82E+4	56.3	24.8	-172.2	0.60	0.36	2.87
40	1	370.2 | 73.4	259.9989	-36.0395	9.36E+3	2.40E+2	1.23E+4	50.1	14.5	55.2	-1.24	0.73	4.23
41	1	312.7 | 74.1	260.1576	-35.8504	3.42E+4	8.78E+2	1.31E+4	38.2	23.0	-166.0	-0.85	0.73	1.13
42	1	208.6 | 41.6	260.5785	-35.5834	9.67E+3	2.48E+2	2.70E+4	71.6	40.1	-136.6	-0.79	0.59	2.97
43	1	442.7 | 35.9	259.9460	-36.3615	1.86E+4	4.78E+2	2.23E+4	55.2	32.2	173.3	-0.90	0.50	1.16
44	1	435.5 | 29.5	259.9919	-36.3524	6.61E+2	1.70E+1	1.43E+3	21.1	5.1	110.7	-0.93	0.22	1.66

Columns denote: (1) structure id, (2) leaf(1) or branch (0), (3) pixel coordinates, (4) right ascension (J2000), (5) declination (J2000), (6) flux, (7) mass, (8) exact area, (9) major axis of fitted ellipse, (10) minor axis of fitted ellipse, (11) position angle (counter-clockwise from the x-axis) , (12) mean velocity, (13) velocity dispersion, and (14) virial parameter. The effective radius is computed from $r = \sqrt{r_{\mathrm{maj}}\, r_{\mathrm{min}}}$ and the area from the ellipse by $A = \pi r^2$.

Most structures are not spherical, but the major axis r(maj) is about a factor 3–4 larger than the minor axis r(min), which is due to the filamentary structure of the clouds and clumps. The position angles (PA) are preferentially grouped along the Galactic plane (±180°), which is also evident from the moment maps. The integrated flux is defined as

$$F = \sum_i T_i \Delta\alpha_x \Delta\alpha_y \Delta v \quad ([\mathrm{F}] = \mathrm{K\ km/s\ sr}), \tag{4.14}$$

where the last three factors are the PPV or voxel unit. By following Rosolowsky et al. (2008), the total mass can be calculated by using the X_{CO} factor and the luminosity $L = FD^2$ in eq. 4.15:

$$M_{\mathrm{Lum}} = X_{\mathrm{CO}}[2\mathrm{E}20\ 1/(\mathrm{cm}^2\ \mathrm{K\ km/s})] \times 4.4 \times L_{\mathrm{CO}}(\mathrm{K\ km/s\ pc}^2) := 4.4 X_2 L_{\mathrm{CO}}. \tag{4.15}$$

X_2 is a correction factor which accounts for other X factors, either by local differences in the Galaxy or by using an isotopologue instead of CO. In NGC 6334, a standard $X(^{13}\mathrm{CO})$ factor of 9.22E20 1/(cm^2 K km/s) is derived, which gives X_2=4.61. This constant conversion factor assumes that the temperature and opacity are constant in eq. 4.5.

The three scaling relations in fig. 4.13 show that the slopes are in general agreement with the slopes by Larson (1981). The clump mass function is obtained from the statistics of the structures with a run of min-delta=2 K, see fig. 4.13(e), which results in a total number of 700 structures. Only the leafs of the dendrogram are counted and branches are excluded. The lower end is limited by the SNR of the observations. The variance for each bin is calculated from the binomial distribution as Var=$n\,p(1-p)$ or Var=$N_k(1 - N_k/N)$, where N_k is the frequency in a bin and N the total number. The histogram can be fitted by a power law with a slope $\alpha_{\log} = (-0.86{\pm}0.05)$ in logarithmic scale or $\alpha_{\mathrm{lin}} = (-1.7 \pm 0.1)$ in linear scales. This value is in agreement with the ranges given by Kramer et al. (1998) in general, who found values for CO clumps of α_{lin}=1.6–1.8. And it agrees with the slope of $\alpha_{\log} = (-0.88{\pm}0.13)$ given by Muñoz et al. (2007) particular in NGC 6334 for a two-temperature clump ensemble (17 K and 34 K).

An application of dendrograms to synthetic data cubes from MHD simulations is presented by Burkhart et al. (2013). They demonstrate that different properties of turbulence (sub-/super-sonic, sub-/super-Alfvénic, self-gravity) result in different statistical moments and hierarchical structures in the dendrogram. Therefore, this method qualifies to characterize basic turbulent features of a molecular cloud. The definition of the sonic Mach number M_{S} and Alfvénic Mach number M_{A} are given in sect. 4.3.3. These simulations were run for different ranges of M_{S} (0.5–8.8) and M_{A} (0.5–1.8). A diagram of the total number of structures versus the min-delta parameter shows that lower magnetizations with $M_{\mathrm{A}} = 2.0$ decline faster than higher magnetizations with $M_{\mathrm{A}} = 0.7$ for super-sonic Mach numbers of $M_{\mathrm{S}} \approx 3$ and $M_{\mathrm{S}} \approx 7$ (Burkhart et al., 2013, fig. 4). This method is compared with the results for NGC 6334 in fig. 4.13(f) with a slope of (-2.04 ± 0.06) for a range min-delta>0.4. The average sonic Mach number in NGC 6334 is $\overline{M_{\mathrm{S}}}$=5.7, which is near the value of $M_{\mathrm{S}} = 7.2$, $M_{\mathrm{A}} = 2.0$ with a slope of -1.67 in Burkhart et al. (2013). Then again the slope found in NGC 6334 matches best with a slope of -2.2 for $M_{\mathrm{S}} = 2.7$, $M_{\mathrm{A}} = 0.7$ in Burkhart et al. (2013). Due to the limited number of simulations, the comparison therefore shows that M_{A} in NGC 6334 lies most likely in the trans-Alfvénic domain ($M_{\mathrm{A}} \approx 1$). The reason for setting a fitting range is that the data follow a flatter slope at lower min-delta parameter. Fig. 4.13(f) shows in addition that for min-delta=10 K, the total number of structures and levels does not change as much as for lower values.

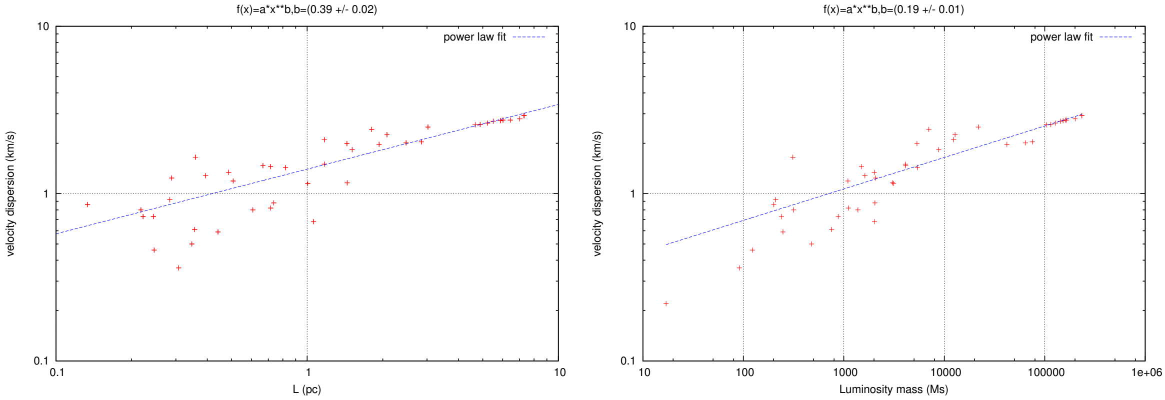

(a) Larson's first relation (b) Larson's second relation

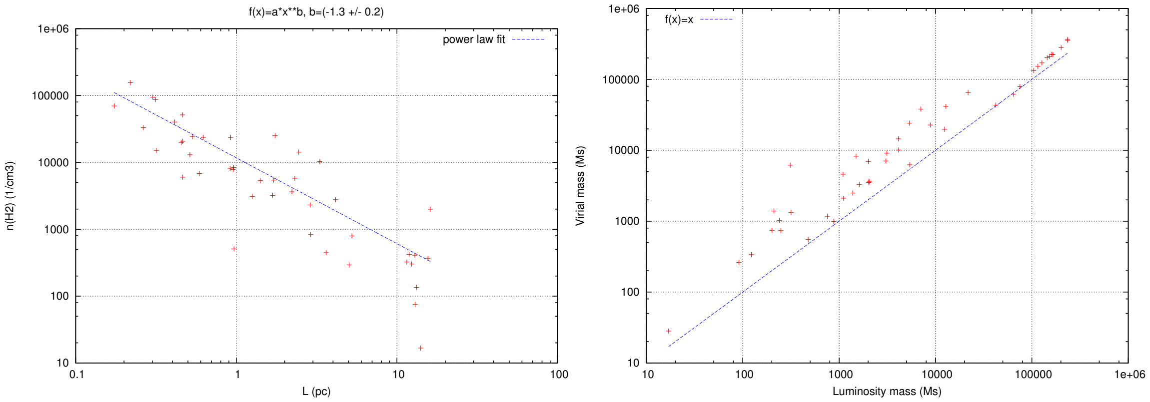

(c) Larson's third relation (d) Virial parameters

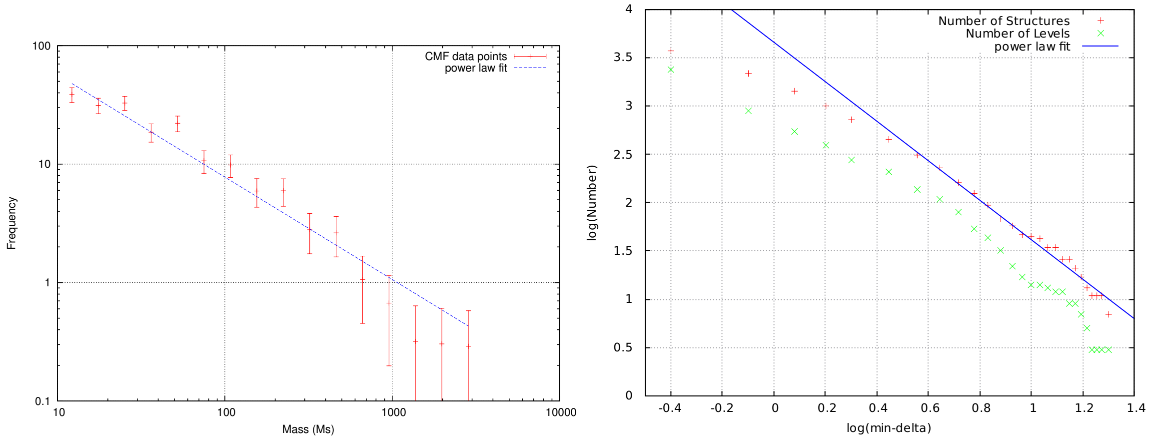

(e) Clump mass function (f) Structure depth

Figure 4.13.: Several scaling relations derived from the dendrogram statistics. The slopes are given in the subfigs. (a),(b) and (c) above. The line in (d) marks $\alpha_{\rm vir}$=1. The slope in (e) is (-0.86 ± 0.05) and in (f) (-2.04 ± 0.06).

The virial parameter $\alpha_{\rm vir}$ is calculated from the eq.

$$\alpha_{\rm vir} = \frac{5\eta\sigma^2 r}{M_{\rm Lum} G}, \tag{4.16}$$

where η=1.91 and r is the radius of the cloud (Rosolowsky et al., 2008). Because this radius is obtained from the fitted area, but the mass fluxes $M_{\rm Lum}$ are obtained from the exact area, the mass is scaled down by the filling factor. The lowest values of $\alpha_{\rm vir}$ (where a gravitationally bound clump has $\alpha_{\rm vir} < 2$) are found among others in the protoclusters NGC 6334I and I(N), whereas the highest value is found at structure no. 32. This is in agreement with the general trend found by Kauffmann et al. (2013), where low virial parameters are particularly found for high-mass star-forming clumps. Fig. 4.13(d) and the histogram in fig. 4.14 demonstrate that NGC 6334 as a whole is gravitationally bound and that most structures are below $\alpha_{\rm vir} = 2$. For comparison, the virial parameters of the GMC W43 are also shown, which peak at $\alpha_{\rm vir}$ =2.75. Although the line widths are similar between both GMCs, the ratio r/M in eq. 4.16 for the same mass M of a cloud is higher in W43 than NGC 6334, which means that the gas is less dense in W43 because the density scales as $\propto M/r^3$.

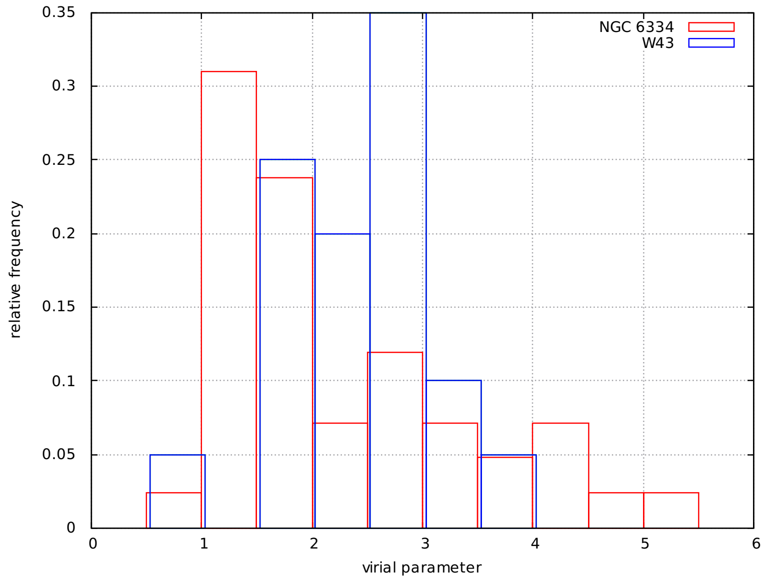

Figure 4.14.: Histogram of virial parameters of clouds in NGC 6334, compared with W43 (Carlhoff, 2014, table 5.2).

4.4.2. Column density PDF

As discussed in sect.1.2.3, the column density PDF is a diagnostic tool in the theory of gravo-turbulent star formation. Fig. 4.15 presents this PDF of NGC 6334 obtained from ^{13}CO, which is made in similar ways as described in Russeil et al. (2013). Its shape can be described by a log-normal form at lower column densities and a power law at the highest densities. The lower value of 1E21 1/cm^2 is probably not only because of the sensitivity of the observations, but also because the CII-to-CO transition occurs at an extinction of $A_V = 1$, which corresponds to about

2E21 1/cm^2. In general, it has some similar and some different properties in comparison with the column density PDF of the HSO dust continuum map (Russeil et al., 2013, fig. 4). Both PDFs peak about the same point, which is $\eta = \ln(N/\langle N\rangle) = -(0.60\pm0.02)$ (or 0.74E22 1/cm^2), and the deviation point lies at approximately η=0.6 or 2.4E22 1/cm^2. The median column density ($\eta = 0$) is $\langle N\rangle$=1.34E22 1/cm^2. But there are two main differences: the width of the log-normal function from molecular gas is twice as wide, namely $\sigma = (0.76 \pm 0.01)$, and the slope of the power law is flatter, namely $s = (-1.41 \pm 0.04)$. According to Federrath and Klessen (2013), the slope is related to the radial profile exponent of the density distributions, $\rho(r) = \rho_0(r/r_0)^{-\alpha}$, where $\alpha = -2/s + 1 = 2.4$ in the case of NGC 6334. This high value of $\alpha>2.1$, in agreement with the value $\alpha = 2.37$ found by Russeil et al. (2013) for the main filament of NGC 6334, points to an accelerated collapse with some external pressure mechanism.

A similar result with a flatter slope is reported by Carlhoff (2014) in W43, when comparing the PDF from molecular lines with the HSO PDF. The reason for the different properties of the PDF derived from molecules and dust continuum is unknown. But it is known that both tracers have drawbacks and can get into problematic ranges, namely optically thickness in the case of molecular lines and dust and the confusion or contamination of several clouds in the LOS in the case of using dust continuum emission (Schneider et al., 2015). The different methods to derive the PDF needs to be further investigated, e.g., by using a simulation of a turbulent star-forming molecular cloud and then simulated observations of it in different tracers.

According to Federrath and Klessen (2012), the width of the log-normal function is related to the sonic Mach number by $\sigma^2 = \ln(1 + b^2\, M_S^2)$, where b is a parameter which describes the driving force mode of the turbulence. In NGC 6334, a value of b=0.16 is derived, so that the forcing mode would point more to a solenoidal (b=1/3) than compressive (b=1) one. However, it is noted that this analytical formula for the width σ is only applicable without magnetic field forces and in the super-Alfvénic regime (for large Alfvénic Mach numbers), but fails for the description of sub-Alfvénic motions. Since the motions in NGC 6334 are sub-Alfvénic, as explained further below, the forcing mode remains uncertain.

4.4.3. Properties of the turbulence

Larson's first relation can be directly compared with the first order structure function as defined in eq. 1.13. For this purpose the velocity map is used. Because this map was gridded to 2 pixels per beam size, it is binned here by 2 pixels in x and y direction to avoid linear correlations, which come from comparing similar or the same values in the LOS. The structure function of first (p=1) and second order ($p = 2$) are presented in fig. 4.16. The slope is constant up to a distance of 4 pc, whereas for larger distances the slope flattens and becomes non-homogenous. This behavior suggests that the driving scale is larger than 10 pc. Another possibility for the breakdown of the power law are systematic motions, such as gravitational collapse on larger scales or the rotation of NGC 6334 on 30 pc scales as discussed in sect. 4.3.1. If the whole range of values is used for the fitting, the slopes are α_1=0.38 and α_2=0.76, whereas restricting the range to [0,4] pc results in α_1=(0.483±0.006) and α_2=(0.79±0.01). Thus, α_1 is in agreement with the Larson slope in eq. 1.9 and the value obtained from the dendrogram analysis if all scales are used. As mentioned in sect. 1.2.3, the slope β of the kinetic energy power spectrum $P_v(k)$ is connected to α_2 by $\beta = \alpha_2 + 1$. This results therefore in β=1.79 in NGC 6334 and lies between the Kolmologorov slope of β=1.67 and Burgers slope of $\beta = 2.0$. It is noted that β=1.8 is

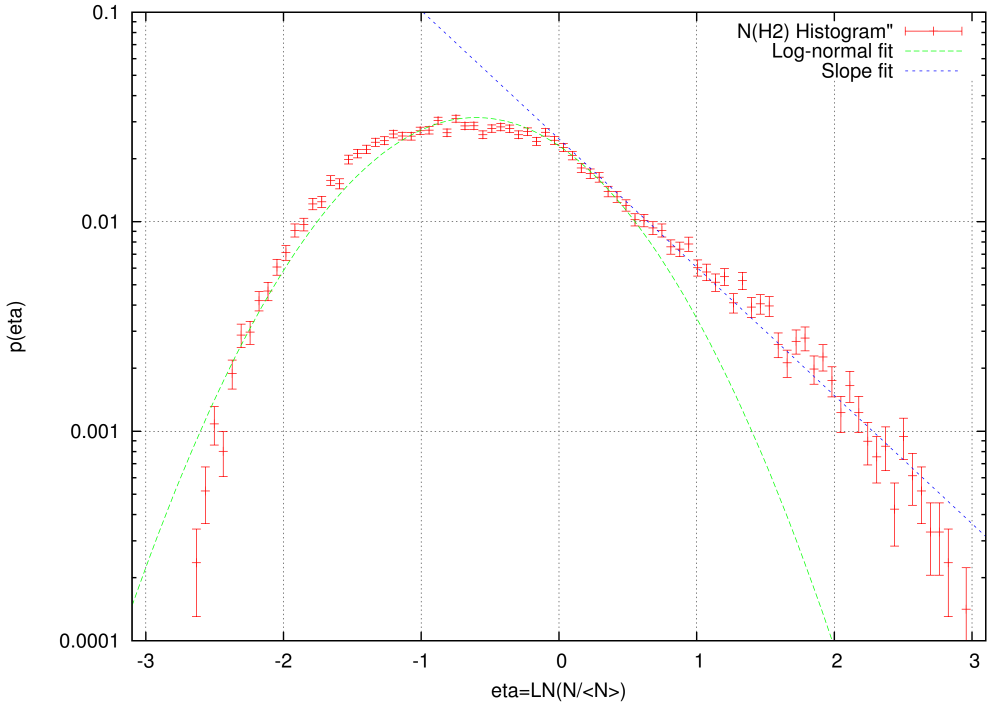

Figure 4.15.: The column density PDF of NGC 6334 derived from the ^{13}CO observations. The best fits are shown to a log-normal shape at low densities and to a power law at high densities.

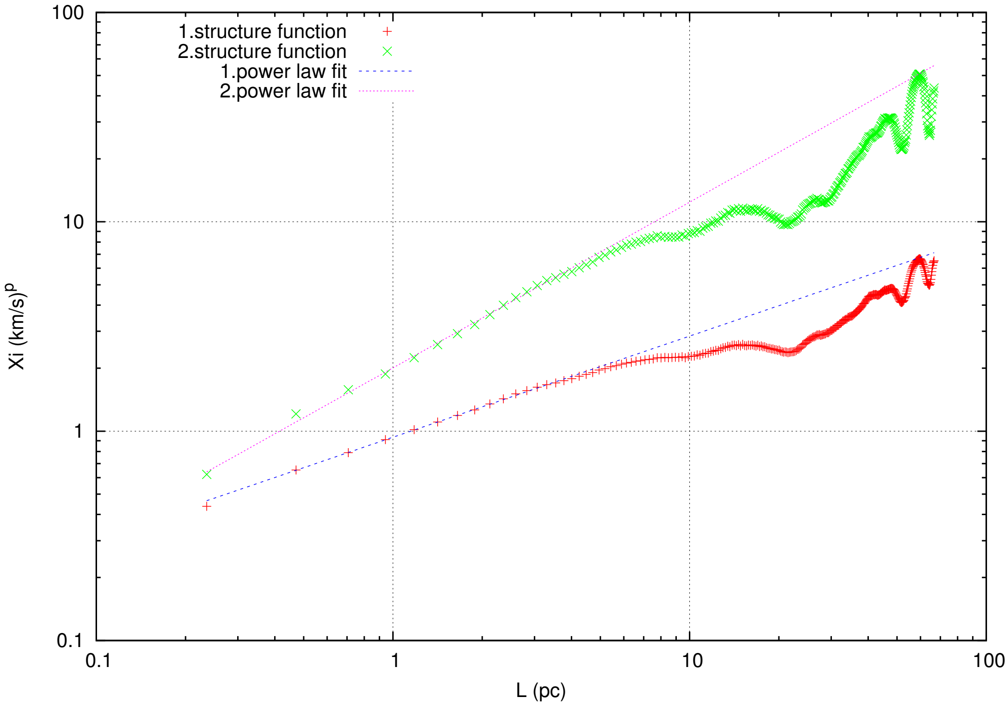

Figure 4.16.: The structure function of first and second order in NGC 6334.

comparable to intermediate values found in MHD simulations and observations by Padoan and Nordlund (2002), which results from a line width-size relation with α_1=0.4. Furthermore, this scaling is able to explain the Salpeter slope of the IMF by turbulent fragmentation (Padoan and Nordlund, 2002; Kritsuk et al., 2013). Compared to the results of Russeil et al. (2013), which use the Delta-variance method and find values of $\beta = 2 \pm 0.2$ in the center and β=1.7 for the filaments, the value derived above is an intermediate one. The structure range in their method is chosen to 1–6 pc in the center, and similarly for the other subregions.

By assuming a universality of the line width-size relationship for all molecular clouds in the Galaxy, Brunt and Kerton (2002) suggest estimating the distance to GMCs from the equations

$$l = l_0 \delta v^{\kappa} \quad L_0/(f l_0) = D \quad L_{\text{ref}} = L_0 \delta v_{\text{ref}}^{\kappa}. \tag{4.17}$$

l is the angular spatial scale in pixel units, δv the velocity scale in km/s, L is the physical scale in pc, D is the Distance, f is a conversion factor and κ is $1/\alpha_1$. The calibration based on the principal component analysis of a sample of clouds with embedded HII regions leads to the normalization parameters $L_0 = (1.1 \pm 0.33)$ pc at δv_{ref}=1 km/s, with an uncertainty of 30% in the distance. They also notice that there is a large scatter in κ for individual clouds, and the values above are mean values with the smallest measurable scales of motion. Applying this method and eq. 4.17 to NGC 6334 (by using the inverse structure function), l_0 is 4.7 ± 0.1 and $\kappa = 2.15$ in the range [0:4] pc as used above, where the pixel scale is 28.6″. This leads to a distance of $D = (1.69 \pm 0.51)$ pc, which is in agreement with the one refereed to in sect. 1.4 despite the larger uncertainty.

4.4.4. The emission feature at +6 km/s

The velocity component at +6 km/s in the ^{13}CO data is very weak and has a very narrow line width of only 1–2 channels. The HI kinematics is briefly discussed from the SGPS. The HI spectrum in fig. 4.17(b) has two absorption peaks: one at −4 km/s and the other one at +7km/s. According to the spiral arm models of Vallée (2008) in the 4th. Galactic quadrant, this velocity could be associated with the far side of the Carina-Sagittarius arm or of the Scutum-Crux arm. Roman-Duval et al. (2009) explain that the kinematic distance ambiguity can be resolved by using HI and ^{13}CO data: the near kinematic distance cloud is expected to have the HI line in self-absorption at the velocity coincident with the ^{13}CO line emission, whereas the far kinematic distance cloud should have no HI self-absorption. Therefore, both absorption lines in fig. 4.17(b) must come from the near distance of the Carina-Sagittarius arm. Zernickel et al. (2012) reported furthermore the detection of a velocity component between 6–8 km/s toward the HMC NGC 6334I in the lines of CI, CII, CH$^+$, CH and HF. All these lines have a narrow line width, low abundances and were explained as contributions from foreground clouds in the LOS. The dip at negative velocities is associated with the molecular gas of NGC 6334, whereas the dip at positive velocities could be associated with the HII regions. Spectral resolved Hα observations from the HII regions by Tigé (2014) show indeed that there are two velocity components, one at −4 km/s and another at +8km/s. The velocity map of this +6 km/s component in fig. 4.17(a) demonstrates that (a) the emission is located closely to the HII region on the projected map, and (b) that there is a velocity gradient away from the HII regions. In this scenario, the gradient originates from an expansion motion of the HII regions which move the gas away.

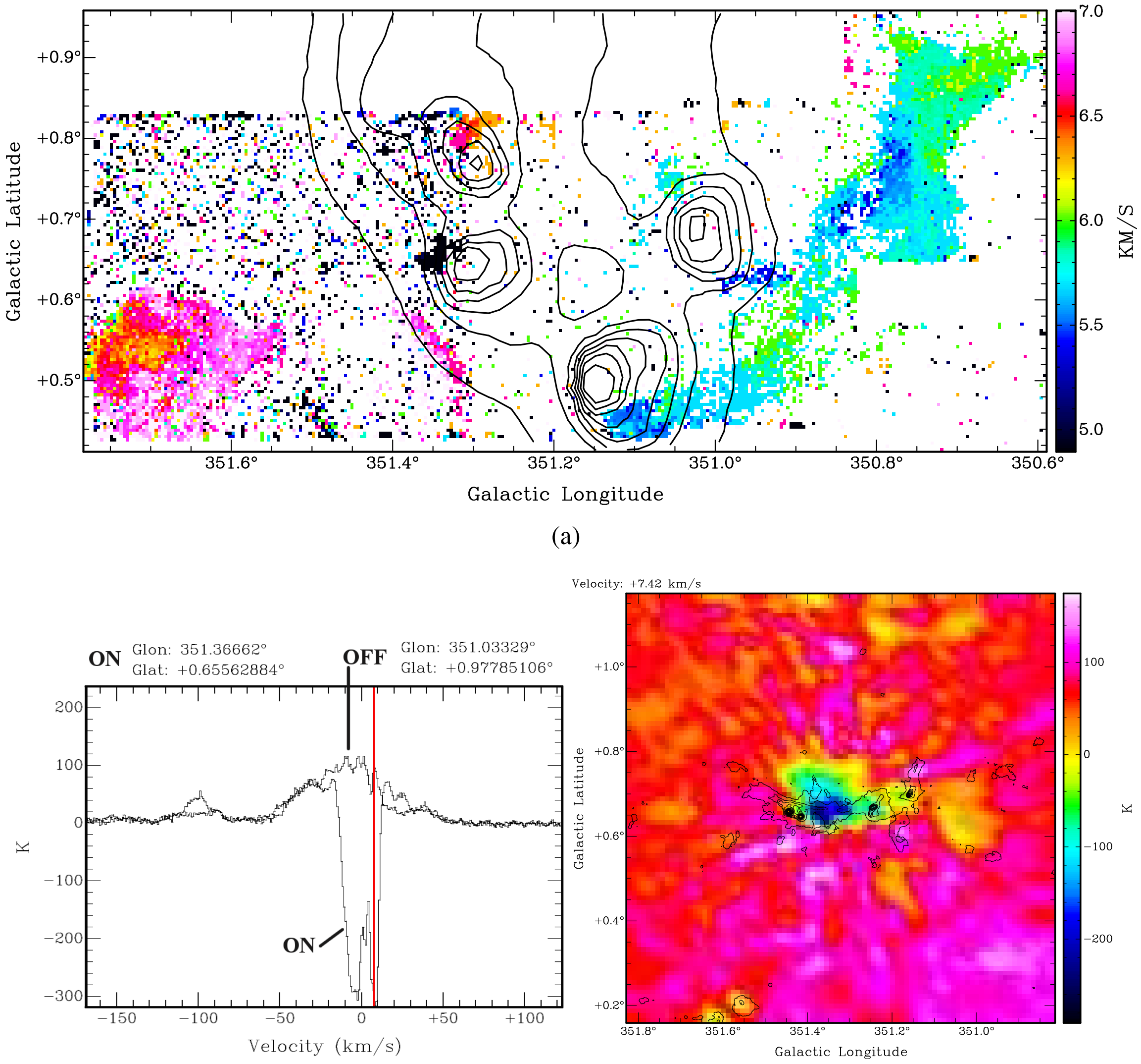

(a)

(b)

(c)

Figure 4.17.: (a) Velocity map of the +6 km/s emission feature in the narrow range [5,6] km/s, overlaid with Hα emission in black contours. (b) HI spectra at the on and off position of NGC 6334, and (c) corresponding HI intensity map at the velocity channel 7.4 km/s (marked as red line in (b)).

4.4.5. An IRDC in detail

A remarkable filament is found at the coordinates l=350.6° and b=0.7°. It has a velocity and spatial coherent structure, and is seen in absorption in the images of the Galactic Legacy Infrared Mid-Plane Survey Extraordinaire (GLIMPSE, Churchwell et al., 2009), and therefore classifies as an IRDC, see the close-up in fig. 4.18(a). As mentioned in chap. 3, these are the signposts of early (massive) star formation. It has length of about 13 pc and a total mass of 1.6E3 $M_\odot$. To derive several properties of this IRDC, a segmented polygon is defined along it and cuts are made parallel and perpendicular to it. From these cuts, the average value is calculated along the axis. Fig. 4.18(b) presents these mean values for cuts along and across the filament. The vertical mass distribution follows the expectation of a centrally condensed cylinder with a radial decreasing density profile, whereas the horizontal mass distribution is not homogenous distributed, but mass is accumulated in the center and at both ends. The temperature varies between 15–30 K, and the line width is on average σ=1.65 km/s in both directions. The velocity gradient along the short axis could be regarded either as a rotation, or as a collapsing feature assuming that gas is accreted in a planar geometry and the inclination angle is 45°. The radial velocities along the long axis indicates also a gradient toward the blueshifted center of −4.2 km/s and is similar to the PVD observed in chap. 3. The outlier at 460 pix. is due to an arm which connects this IRDC to the other sub-filaments further north. The velocity gradient method reveals also that the gradient (i.e., the highest decrease from a certain pixel) is preferentially perpendicular to the long axis of the filament.

By using the eq. 1.16 with an average temperature of T=20 K, the critical mass is derived as M_{crit}= 28.7 $M_\odot$/pc. For line widths caused by turbulence, c_s is replaced by the average dispersion σ and thus gives a virial mass per unit length of 257.2 $M_\odot$/pc. Because the gas mass line density is 123 $M_\odot$/pc, this filament is stable against collapse on average. However, as the mass along it varies significantly, several segments could become unstable such as the middle part and the end points. The deconvolved mean width of the filament from profiles (see sect. 3.3.4) derived from the ^{13}CO emission is about 0.53 pc (deconvolved 0.47 pc), but the profile is only marginally resolved because the beam size is 0.25 pc. However, this width is similar to the width of 0.4 pc which was found for the ^{13}CO filaments in the Taurus molecular cloud at a much higher resolution (Panopoulou et al., 2014), as the distance to Taurus is 140 pc.

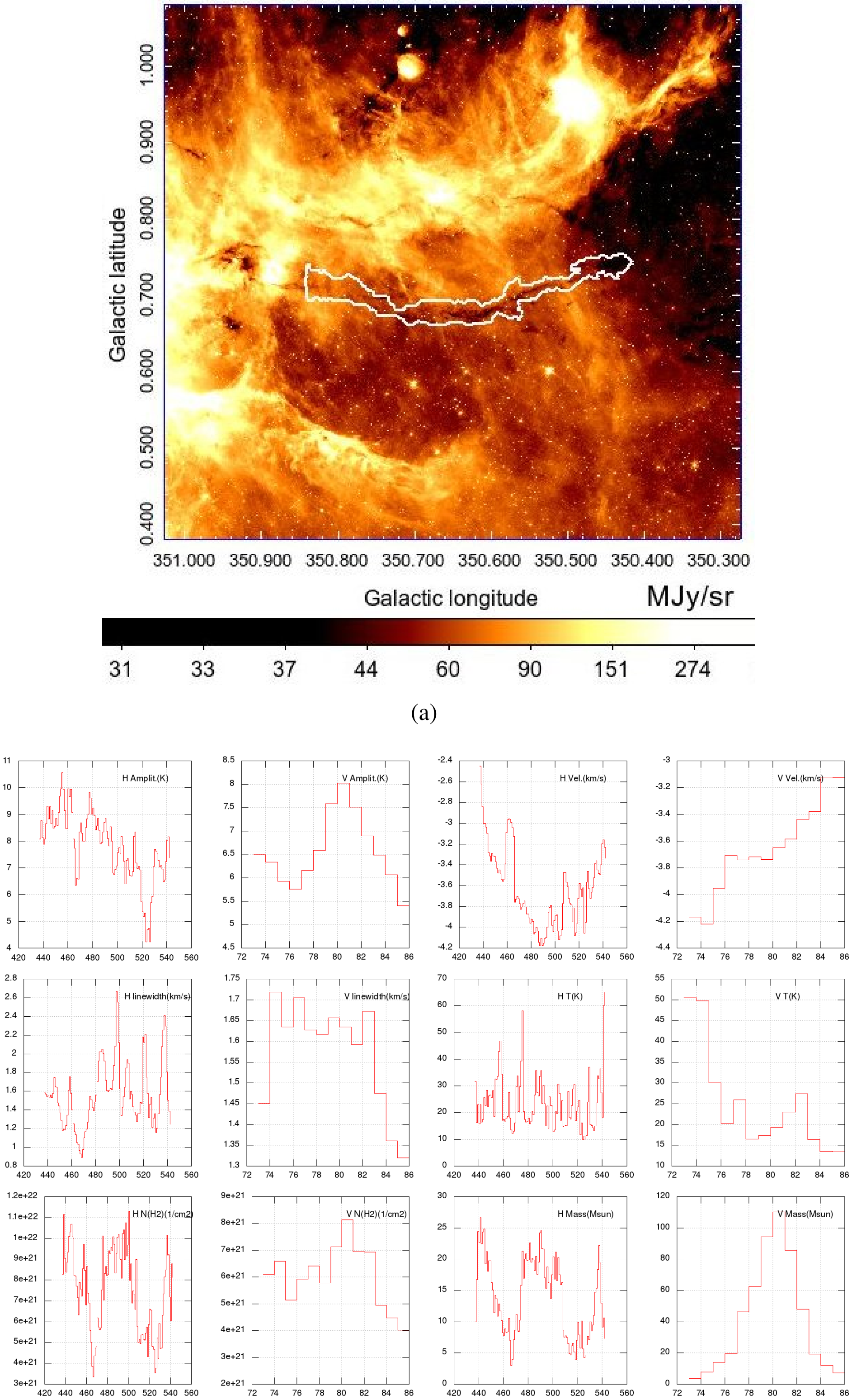

(a)

(b)

Figure 4.18.: (a) GLIMPSE image at 8 μm of the IRDC, marked by white contours at 1 K km/s of the ^{13}CO emission. (b) Physical properties derived from cuts. H stands for parallel, V for perpendicular cuts, where the x-axis is in units of pixel.

4.5. Discussion

The analysis of the kinematic features in this chap. are summarized by differentiating three different velocity scales:

1. globally on 10–100 pc scales because of the rotation of the Galaxy and GMCs,
2. on local scales 1–10 pc because of systematic flows or motions, e.g., collapse, accretion, rotation, expansion,
3. and on the smallest scales $\leq$ 1 pc because of microturbulence which seems to be random.

The last point comes also from the fact that the protostars in the star-forming clumps are not resolved with a single-dish. As is demonstrated in chap. 5, the kinematics on scales <1 pc consist of several components such as transversal motion, infall, outflow and rotation. The reason that no fibers are found, such as in the studies by Hacar et al. (2013), could be either a result of the much larger line widths (which are typically for massive star-forming regions) or the lower spatial resolution.

The magnetic field strength in NGC 6334 is derived as follows: Novak et al. (2009) derive a mean polarization dispersion of $\Delta\phi$=28°. From sect. 4.4.1, the average density is $\rho = 2.5E3$ 1/cm^3, which results in an average value of B=62.5 μG for the whole cloud when using equation 4.9. This result is in general agreement with the typical values found in GMCs (Crutcher, 2012). It would predict, by applying the mean column density in NGC 6334, a strength of B_z=40 μG. The median column density is $N(\mathrm{H_2})$=1.3E22 1/cm^2 in NGC 6334, and by using eq. 1.19 the critical flux ratio is calculated as $\lambda = 1.6$. This means that this GMC is supercritical in general. The average Alfvénic Mach number is $M_A = 0.86$ and thus this region is sub-Alfvénic, as was indicated by the dendrogram analysis and from previous studies of dense cores, sect. 1.4.

After deriving the basic properties of NGC 6334, the energy terms in eq. 1.14 are calculated. The gravitational energy is E_G, the kinetic or turbulent energy is E_kin, the thermal energy E_T, and the magnetic field is E_mag. A spherical geometry is approximated by an effective radius of $R = \sqrt{16.1 \times 3.3} = 7.3$ pc, and mean values are used for the velocity dispersion (σ=1.4 km/s) and temperature (T=20 K). The number of degrees of freedom for $\mathrm{H_2}$ is taken to be only three for the translation, because the temperatures are too low to induce excitation for rotation or vibration. The angular velocity Ω is derived from the average velocity gradient in NGC 6334 mentioned in sect. 4.3.1. The energies are:

$$E_\mathrm{G} = -3\mathrm{G}M^2/(5R) = 3.7\mathrm{E}43\ \mathrm{J} \tag{4.18}$$

$$E_\mathrm{kin} = 1/2\ M\sigma^2 = 5.5\mathrm{E}41\ \mathrm{J} \qquad E_\mathrm{mag} = B^2/6\ R^3 = 7.5\mathrm{E}41\ \mathrm{J} \tag{4.19}$$

$$E_T = 3/2\ N\mathrm{k_B}T = 4\mathrm{E}40\ \mathrm{J} \qquad E_\mathrm{rot} = 1/5\ MR^2\Omega^2 = 3.5\mathrm{E}40\ \mathrm{J}. \tag{4.20}$$

By looking at the orders of magnitude, the statement is $E_\mathrm{G} > E_\mathrm{mag} \approx E_\mathrm{kin} > E_T \approx E_\mathrm{rot}$. The magnetic and turbulent energy are thus of equal importance. This rough approximation therefore demonstrates that the gravitational energy is dominant and the whole region must undergo a collapse in the future. A destiny similar to NGC 6357 will be expected most likely, where most of the gas will be disrupted at the end. How much of the gas will end in stars will remain open, but the star formation efficiency in GMCs is often enhanced (Murray, 2011).

As mentioned in sect. 4.3.1, the angular velocity in NGC 6334 is higher by the factor Ω_2/Ω_1=5.6 compared to the expected rotation by the Galactic spiral arm. If one assumes that the whole GMC undergoes gravitational contraction, but the angular momentum L and the mass M in the inertia of moment I is conserved, than the following relation holds:

$$L = \text{const.} \Rightarrow I_1\Omega_1 = I_2\Omega_2 \Rightarrow \frac{R_1}{R_2} = \sqrt{\frac{\Omega_2}{\Omega_1}}. \tag{4.21}$$

Thus, if the present diameter is taken with a size of 1.5° or $D_2 = 2R_2 = 44.5$ pc, this region could initially have formed out of a larger GMC with a diameter of $D_2 = \sqrt{5.6} \times 2R_2$=105 pc. Therefore, the acceleration in the angular rotation of NGC 6334 can be explained by a collapse along its main axis by about a factor of two.

In sect. 4.4.1, the mass is calculated based on the ^{13}CO luminosity to 2.3E5 $M_\odot$. According to eq. 4.7, the uncertainty in the mass scales with the uncertainty in the distance as $\Delta M/M = 2\Delta D/D$, which is therefore $\Delta M/M$=35% in the case of NGC 6334. Russeil et al. (2013) derive a total mass of 3.8E5 $M_\odot$, which is about twice as high. One explanation for the deviation is that the map from the HSO is bigger and the instruments on board have a higher sensitivity of detecting lower dense gas and dust. Given the uncertainties of both methods, the ^{13}CO abundance and the assumptions on the grain properties, this is still in agreement within a factor of two. The reported values are in better agreement with the total mass of 2.2E5 $M_\odot$ derived from extinction maps by Willis et al. (2013). The gas mass surface density is calculated as 382 $M_\odot$/pc^2, and thus it classifies as a starburst region (Willis et al., 2013), similarly to Orion and W43.

Inoue and Fukui (2013) propose that GMCs with a high star formation activity, such as NGC 6334, NGC 6357, or W43, are formed by cloud-cloud collisions. This mechanism is able to explain a rapid formation in <1 Myr with high mass accretion rates, resulting in a top heavy CMF. Their MHD simulations of a shock-induced formation produce filamentary clouds which are threaded perpendicular by the magnetic field, in agreement with the observations in NGC 6334.

5. Kinematics of the massive protostellar clusters NGC 6334I and I(N)

5.1. Introduction

Liu et al. (2011, 2013) studied massive protostellar clusters and derived mass accretion rates by detecting infall motions toward multiple sources and using optically thick spectral lines of the rotational transitions of HCN (J=3–2 or J=4–3). The derived rates are 4.3E-3 $M_\odot$/yr in the core G9.62+0.19E and 1–2E-2 $M_\odot$/yr in the clump G10.6-0.4. In general, they find better agreements with the competitive accretion model, because of a mass segregation found in the cluster and high velocity differences between the cores. Similarly, Wang et al. (2013) found in the massive star-forming region W3 IRS5 accretion rates in the order of 1E-4 $M_\odot$/yr. In the series "Line Profiles of Cores within Clusters I-III", Chira et al. (2014) have examined spectral line profiles of different tracers of cores within filaments. Based on these simulations, the transition HCN (4–3) has been proven to be suited best for the detection of infall signatures.

The two clusters NGC 6334I and NGC 6334I(N) (abbreviated I and IN hereafter) are part of the massive star-forming region NGC 6334 (sect. 1.4). They are embedded in the northeast end of the main filament and are separated by 2′ on the sky, which corresponds to 1 pc at a distance of 1.7 kpc. Both have been studied extensively in molecular line emission, e.g., in ammonia (NH_3) (Kuiper et al., 1995; Caproni et al., 2000), as well as in dust continuum emission (Gezari, 1982; Sandell, 2000). Megeath and Tieftrunk (1999) reported the first detection of a large scale outflow in IN, together with shock-excited nebulae traced by H_2 knots. Although often referred to as a twin-core system, the two clusters are in fact at different evolutionary stages, with IN being significantly younger (Beuther et al., 2007). Sandell (2000) derived from submm continuum observations average temperatures, masses, and luminosities of

- 30 K, 400 $M_\odot$, 1.7E4 $L_\odot$ for IN,
- and 100 K, 200 $M_\odot$, 2.6E5 $L_\odot$ for I.

The angular size (FWHM) is ≈10″ for both clusters. The total mass of the surrounding region of IN is ≈ 2700 $M_\odot$, in agreement with NH_3 observations by Kuiper et al. (1995). Tapia et al. (1996) report the detection of a young stellar cluster (93 sources with mainly spectral types earlier than B4) in I within a size of 0.6 pc, yielding to a stellar density of 1200 1/pc^3.

I and IN were studied interferometrically by Hunter et al. (2006, 2014), Brogan et al. (2009) and Beuther et al. (2005, 2007, 2008). Observations with SMA revealed that the two sources fragment at least into four cores in the case of I and seven cores in the case of IN (labeled by SMA1, SMA2, etc. in descending order of intensity). Recent higher-angular resolution observations with SMA and the Very Large Array (VLA) increased the number of associated protocluster members in IN to 25 (Hunter et al., 2014). Out of all cores, ISMA1,ISMA2, and INSMA1 are clearly classified as HMCs with signposts of massive protostars: they are accompanied by molecular outflows, masers, and an UCHII region.

Spherically symmetric 1D models have not been able to reproduce the complex internal structure of high-mass star-forming regions (Rolffs, 2011). Thus, several efforts have been made for the development of 3D radiative transfer codes, as reviewed for dust radiative transfer codes by Steinacker et al. (2013). In this chapter, the physical structure of the protoclusters is analyzed by employing these codes to derive the kinematics and mass accretions rates.

5.2. Observations and data reduction

5.2.1. Interferometric observations

A proposal was written to conduct observations of these two sources with SMA (principal investigator: A. Schmiedeke, co-investigators: S.-L. Qin, P. Schilke, A. Zernickel et al.), based on a previous proposal to observe both clusters with ALMA in Cycle 0 (principal investigator: M. Emprechtinger). The observations of the clusters I and IN were carried out with the SMA in the compact configuration in a track sharing mode. The details are summarized in table 5.1 and the uv-coverage is presented in fig. 5.1. The SMA data are publicly available under the project code "2012A-S074" in the SMA data archives. Although two configurations were proposed for, the compact and extended, only the compact configuration was observed. They consisted of single pointings centered on ISMA3 and INSMA4 for the source I and IN, respectively. The total observing time was 6.4 h, with an on source time of 1.9 h and 1.6 h for I and IN. The local oscillator of the single receiver was centered at 350 GHz, which results in a frequency coverage from 342–346 and 354–358 GHz with a small gap of 40 MHz at 344 and 356 GHz. The correlator configuration was set with a uniform spectral resolution across the band. The spectra were recorded in double sideband mode and the frequency ranges were selected such that they cover the HCN(4–3) line and its isotopologues H^{13}CN(4–3) and HC^{15}N(4–3).

The `MIRIAD` package was used for the calibration and imaging, which was done by S.-L. Qin and his scripts. Where necessary, new images were created based on these scripts to enhance the resolution for modeling purposes. The line and continuum emission were separated by selecting line-free channels, where the line emission data is baseline subtracted and the continuum data is gained from the average of all line-free channels. The uv-data were imaged with uniform weighting and deconvolved with the CLEAN algorithm down to the theoretical noise limit. For the HCN (4–3) transition, the SMA and single-dish data from APEX (see sect. 5.2.2) were combined by using the task `mosmem`, which uses the zero-spacing information to make a joint deconvolution (see fig. 5.4). However, it was noticed that different algorithms and parameter settings for the combination and merging procedure produce diverging results. Because the result and uncertainty of the absolute flux density of the combined datasets remain unsure, the modeling is still done on these two datasets separately.

5.2.2. Single-dish observations

To overcome the problem of missing flux from interferometric observations, additional data were obtained from APEX with the same frequency setup as for SMA. While the SMA is sensitive to scales of 0.01–0.1 pc, the single-dish data are able to probe larger scales from 0.1–1 pc. The northern region of NGC 6334 was observed with APEX as a part of an observing program to map the large-scale filament (chap. 3). The FLASH receiver was used with a main beam efficiency of 0.73 (Güsten et al., 2006). The map covers a field of 3.5′×4.4′ (including both clusters I and IN, see fig. 5.7) and was obtained in the OTF mode. The data reduction was performed in the same way as described in chap. 3. Compared with previous observations of the

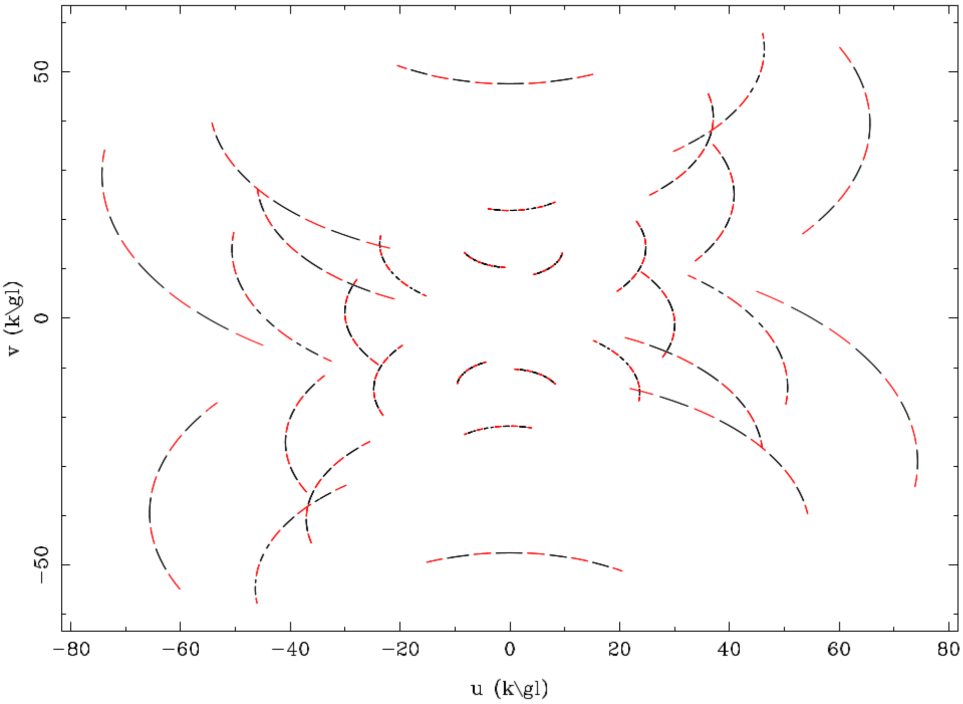

Figure 5.1.: UV-coverage of the SMA observations at 357 GHz. Black tracks correspond to observations of IN and red tracks to the ones of I. The units are in kilolambda (kλ).

Table 5.1.: Parameters of the SMA observation of NGC 6334I and I(N)

Project code	2012A-S074
Observing date	2012 Jul 02
Max. baseline	70 m
Phase center:	
I: RA, Decl. (J2000)	$17^h20^m53.44^s$, $-35°47'02.2''$
IN: RA, Decl. (J2000)	$17^h20^m54.63^s$, $-35°45'08.5''$
Primary beam (HPBW)	$36''$
Synthesized beam	$2.84''\times1.57''$ at 356.7 GHz
Position angle	-11°
LO frequency	350 GHz
Bandwidth	2×4 GHz
Spectral / velocity resolution	0.81 MHz / 0.7 km/s
Gain calibrator	QSO1924-292, NRAO530
Bandpass calibrator	3C279
Flux calibrator	Titan
Average system temperature	216 K
rms continuum I/IN	38 / 15 mJy/beam
rms lines I/IN	193 / 130 mJy/beam
conversion factor at 357 GHz	2.16 K/(Jy/beam)

Table 5.2.: Summary of all observations and lines of HCN used in this study of I and IN

Telescope	HCN transition	Frequency (GHz)	Beam size (″)	Δv (km/s)	rms (K)
MOPRA	J=1–0	88.632	39	0.1	0.2
APEX	J=3–2;4–3	265.886;354.505	24;18	0.5	0.3;0.2
SMA	J=4–3	354.505	2.9×1.6	0.7	0.3
HSO	J=6–5. . .13–12	531.72. . .1151.45	41. . .19	0.6. . .0.3	0.02. . .0.37

same source I by Rolffs (2011) (sect. 5.7.1), the deviations in the peak intensities from the data are less than 10%, which is commonly taken as the calibration uncertainty.

The sources I and IN are also targets of the HSO key project Chemical HErschel Surveys of Star forming regions (CHESS, Ceccarelli et al., 2010). To give a better estimate of the derived parameters in the models, complemented data are used from single-pointing observations at the higher-energy rotational transitions of HCN with the Heterodyne Instrument for the Far Infrared (HIFI, de Graauw et al., 2010) on board of the HSO. The full molecular line survey spans a range from 480–1910 GHz for the source I and is presented in Zernickel et al. (2012). Additional data from the source IN in the HIFI bands 2a/2b (626–801 GHz, see chap. 6) are available and were reduced following the procedure described in Zernickel et al. (2012). The HIFI bands 2 of IN were reduced by M. Emprechtinger (co-author of Zernickel et al., 2012) with the Herschel Interactive Processing Environment (`HIPE`) version 8 and rechecked by R. Higgins with a newer version. The possibility of line contamination from the offset positions was checked and is significant only in the most intense transition of CO and ^{13}CO. The HIFI data can be obtained from the Herschel Science Archive. These single-pointing observations were centered at the coordinates α(J2000)=17$^{\mathrm{h}}$20$^{\mathrm{m}}$53.3$^{\mathrm{s}}$, δ(J2000)=−35°46′58.5″ toward source I, and at α=17$^{\mathrm{h}}$20$^{\mathrm{m}}$55.2$^{\mathrm{s}}$, δ=−35°45′03.9″ toward source IN. Additional spectral cubes of HCN (1–0) of the sources were taken from the MALT90 survey (a beam efficiency of 0.49 was adopted to convert to main-beam temperatures). A summary of all observations is given in table 5.2, where Δv is the velocity resolution.

5.3. Observational results

5.3.1. Continuum emission

The dust continuum map of both clusters is presented in fig. 5.2, and basic parameters from the SMA continuum and line observations are listed in table 5.3. The full spectra at the peak position of each core are shown in fig. 6.1 of chap. 6. In the dust continuum maps, three fragmentation in I and four in IN are detected. These cores in the clusters are label as NGC 6334I SMAX, where X denotes the core number and the numbers are usually arranged by the flux density of the core. In comparison to continuum observations of these two sources at 222 GHz (Hunter et al., 2006), ISMA3 is not resolved but merged with ISMA1, INSMA2 and INSMA3 are blended, and INSMA5 and INSMA7 are too weak to be detected.

In source I, ISMA3 is a known cometary UCHII region excited by a B2 star of 3.3E3 $L_{\odot}$ (De Buizer et al., 2002), derived from mid-infrared fluxes. The Strömgren radius of 0.02–0.03 pc (eq. 2.23) in radio continuum observations is in agreement with such an exciting star

Table 5.3.: Observed parameters of the cores in NGC 6334I and I(N) at 350 GHz

Core	I_{peak} (Jy/beam)	S_ν (Jy)	Line flux (K km/s)	L/C ratio^a	v^b_{LSR} (km/s)	Δv^b (km/s)
ISMA1	5.0(1)	6.0(4)	6236	0.20	−4.6(0.4)	4.4(0.2)
ISMA2	1.9(1)	3.3(3)	6422	0.55	−7.9(0.1)	3.0(0.2)
ISMA3	0.9(1)	1.5(4)	0	-	-	
ISMA4	0.9(1)	0.8(2)	0	-	-	
INSMA1	1.69(5)	2.4(1)	691	0.06	−2.0(0.5)	4.7(0.5)
INSMA2	0.58(2)	1.04(8)	640	0.21	−4.4(0.5)	3.6(0.4)
INSMA3^c	0.58(2)	1.04(8)	-	-	-	-
INSMA4	0.23(3)	0.31(7)	240	0.08	−3.1(0.4)	4.9(0.6)
INSMA5^c	0.26(4)	0.3(1)	0	0	-	-
INSMA6	0.52(3)	0.55(6)	673	0.15	−1.6(0.1)	2.1(0.1)

Values and uncertainties are derived from multi-component 2D Gaussian fits in `MIRIAD`. (a): Ratio of line flux to continuum emission. (b): The radial velocities v_{LSR} and line widths Δv are taken from chap. 6. (c): blended with other cores.

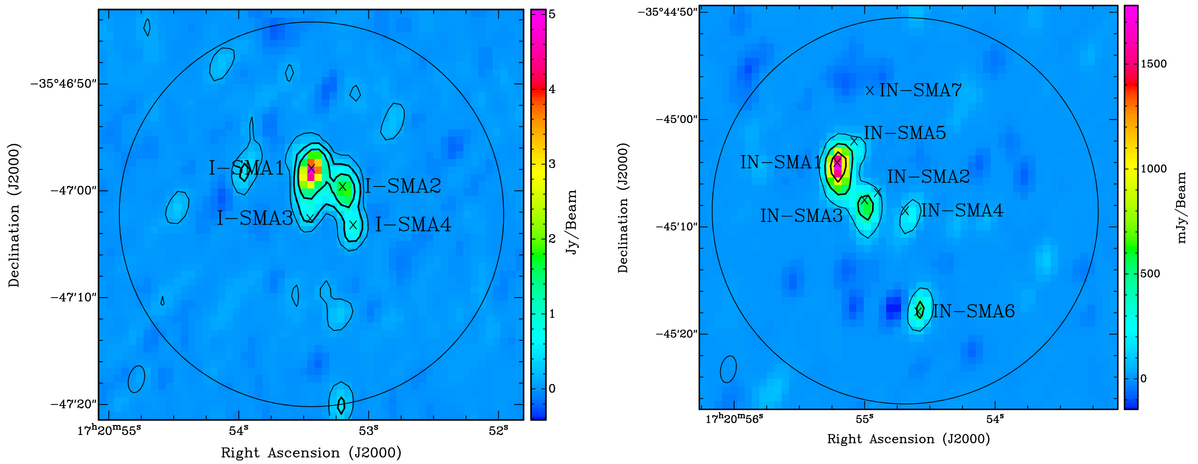

(a) NGC 6334I

(b) NGC 6334I(N)

Figure 5.2.: SMA dust continuum emission maps of I and IN at 350 GHz. Contours in black are set at 0.1, 0.4, and 1.0 Jy/beam. Crosses mark the peak intensity position of the cores detected by Hunter et al. (2006), where the name of the cores are denoted next to the crosses. The outer circle denotes the primary beam and the synthesized beam is shown in the bottom left corner.

(de Pree et al., 1995), where an electron density of 3.8E4 1/cm^3 is found. It has the weakest intensity relative to the nearby cores because of the flat SED of the free-free emission at this high frequency. The condensation ISMA4 has dust but no clear line emission on its own, and the line detection is hindered by the residual line emission of ISMA2 and confusion with the blueshifted part of an outflow (see sect. 5.3.5). In IN, the core INSMA3 is brighter than INSMA2 at 0.86 mm, which is in contrast to the observations in Hunter et al. (2006) at 1.3 mm. But INSMA2 is blended with INSMA3 in the data, which applies also for INSMA5 with INSMA1.

5.3.2. Line emission

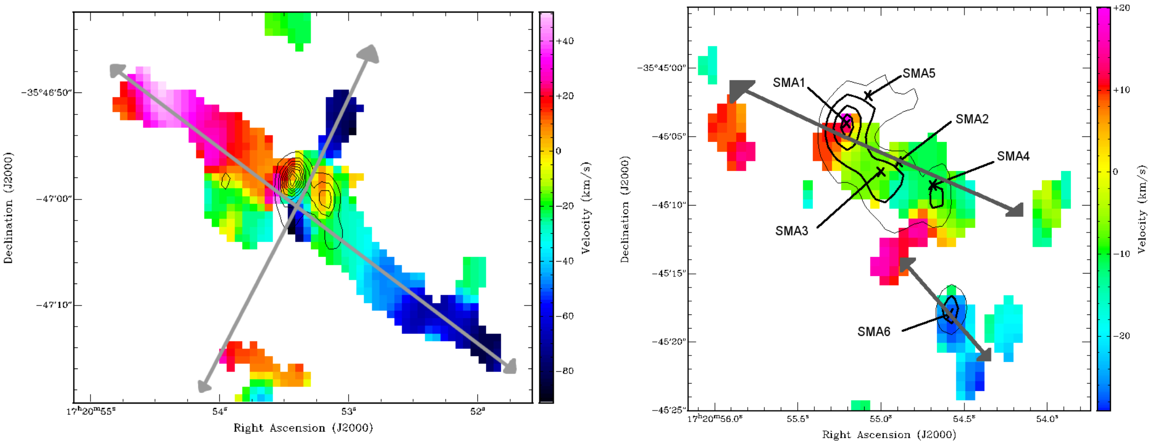

(a) NGC 6334I (b) NGC 6334I(N)

Figure 5.3.: SMA first moment maps of (a) source I in CO(3–2), and (b) source IN in HCN(4–3). Overlaid in black contours is the continuum emission, and bipolar molecular outflows are marked by gray arrows.

The optically thick lines of HCN (4–3) have an inverse P Cygni profile in the APEX and SMA spectra of the clusters I and IN, see fig. 5.15 and 5.17. If other possibilities are excluded, this profile is an indication for a collapsing molecular cloud (sect. 2.4). An exception of this is ISMA1 that has a red-shifted asymmetric profile and would correspond to an expansion motion. The optically thin lines of HC^{15}N, centered at the velocity of the absorption dip, confirm that this double peak is not produced by multiple components. The broad line wings of the spectral lines toward some cores stem from molecular outflows. Furthermore, vibrationally excited lines of HCN (J=4–3, v_2 = 1, E_u=1067 K) are found in ISMA1, ISMA2, and INSMA1. The velocity map of the sources in CO and HCN is shown in fig. 5.3. Multiple outflows and different radial velocities of the cores are evident. The outflow stemming from INSMA1 and INSMA6 are reported in Brogan et al. (2009), whereas here the first time the blue lobe of an outflow (outflowI2) is detected between ISMA1 and ISMA2 in the northwest direction. The velocity of outflowI1 (powered by INSMA1) is increasing with increasing distance from its origin, which is denoted as a "Hubble law" velocity relation.

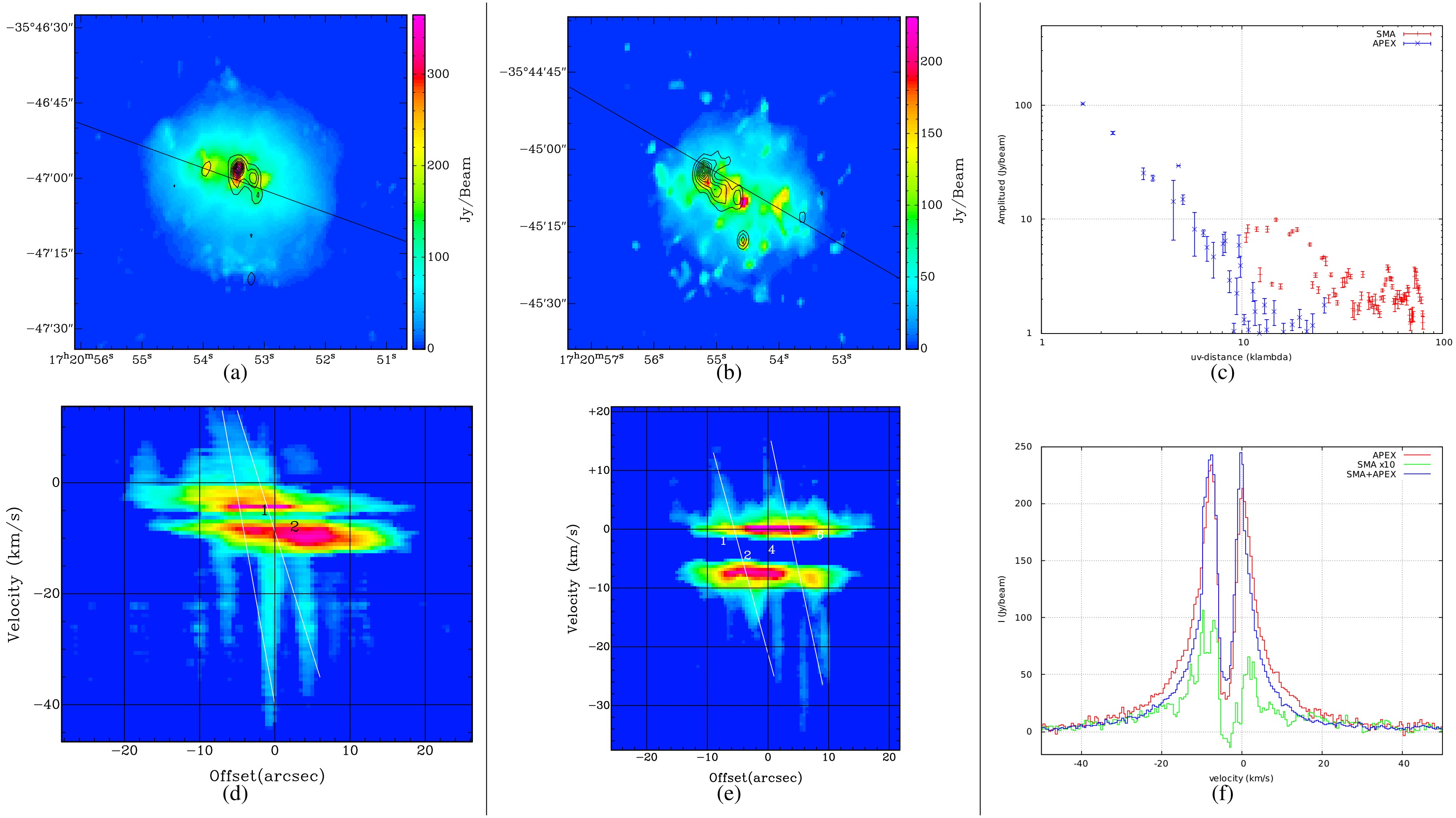

Figure 5.4.: (a) HCN(4–3) 0th moment map of the combined datasets (SMA+APEX) for source I and the corresponding PVD (d), and similar for source IN in (b) and (e). Black contours denote the dust continuum and the black line the cuts for the PVDs, in which the position of the cores are denoted by numbers and the two molecular outflows by white lines. Subfig. (c) shows the amplitude versus uv-distance in IN and (f) the resulting spectra taken from the central position.

Fig. 5.4 presents the combined maps of HCN(4–3) from SMA and APEX. The amplitude flux density versus uv-distance plot in fig. 5.4(c) for source IN demonstrates that there is a mismatch in the absolute flux calibration between 10–20 kλ, so that to recover the flux density of the APEX emission it is multiplied by a factor 1.8 in the `mosmem` routine. The resulting spectrum for source IN, taken from the central position, is shown in fig. 5.4(f) (all at the same angular resolution). The emission at the high velocities in the profile wings is not recovered to a full amount in the combined map, and the SMA flux density is on average only 5% of the single-dish flux density and most of the large scale emission is resolved out, as expected from an interferometer for observations of a HMC embedded in a GMC. The black line in fig. 5.4(a) and 5.4(b) denotes the direction in which the PVD are made by rotating the cube by 20° in source I and 30° in source IN and integrating all the emission perpendicular of this line. Because of the self-absorption, the integrated emission is no longer centered at the peak position of each core. As can be seen from the PVD, the self-absorption from the envelope contaminates the emission at the radial velocities of the cores. Thus any possible self-absorption profiles of the cores are hindered by the overall clump profile. In addition, the relative velocity difference between the core and the clump can lead to a blue- or redshifted asymmetric line profile in the spectrum of a core, even if no infall or expansion motions are present for this core.

5.3.3. Indications for rotating disks

Similar to the formation of low-mass stars, high-mass stars likely accrete gas through a protostellar disk or torus. High excitation lines of optically thin tracers should be used to trace the innermost part of the HMC. Fig. 5.5(a) shows the velocity map in HC_3N (J=39–38) of I and fig. 5.5(b) in HCN (4–3, $v_2 = 1$) of INSMA1. All the three cores ISMA1, ISMA2, and INSMA1 have velocity gradients of $\approx$2 km/s over a size of 2″ , which are almost perpendicular to the outflow axis. This suggests that they trace a rotating disk or toroidal structure. The current observations lack of angular and spectral resolution to properly study the origin of the velocity gradients and presumably a Keplerian rotation. However, the recent observations by Hunter et al. (2014) confirm that INSMA1 is a candidate for a massive disk. Furthermore, while the rotation axes of ISMA1 and ISMA2 are parallel, the rotation direction is opposite. Recent observations of the massive cores in G35.20-0.74N with ALMA revealed a similar configuration with two nearby cores showing opposite directions of rotation (Sánchez-Monge et al., 2013a). Studies of the direction of the magnetic field on scales of sub-arcsec could corroborate these indications of circumstellar disks around massive stars.

In addition to submm rotational lines, high-angular resolution observations of masers at radio frequencies can also be used to derive kinematics of high-mass star-forming regions. Norris et al. (1998) proposed that many methanol masers with velocity gradients stem from circumstellar disks. The source NGC 6334I was studied among them under the name "G351.42+0.64" (other names used in the literature are "IRAS 17175-3544" and "NGC 6334F"). From observations of 12.2 GHz methanol masers toward I, they find indeed two emission sources (corresponding to ISMA2 and ISMA3) with opposed velocity gradients, and derive Keplerian masses of 9 $M_\odot$ and 2 $M_\odot$ for the UCHII region ISMA3 and ISMA2, respectively. From VLBI measurements of OH masers toward ISMA3, Zheng (1989) reported a velocity gradient of 6–10 km/s/arcsec over a linear size of 334 au and derived a Keplerian mass of 10–25 $M_\odot$.

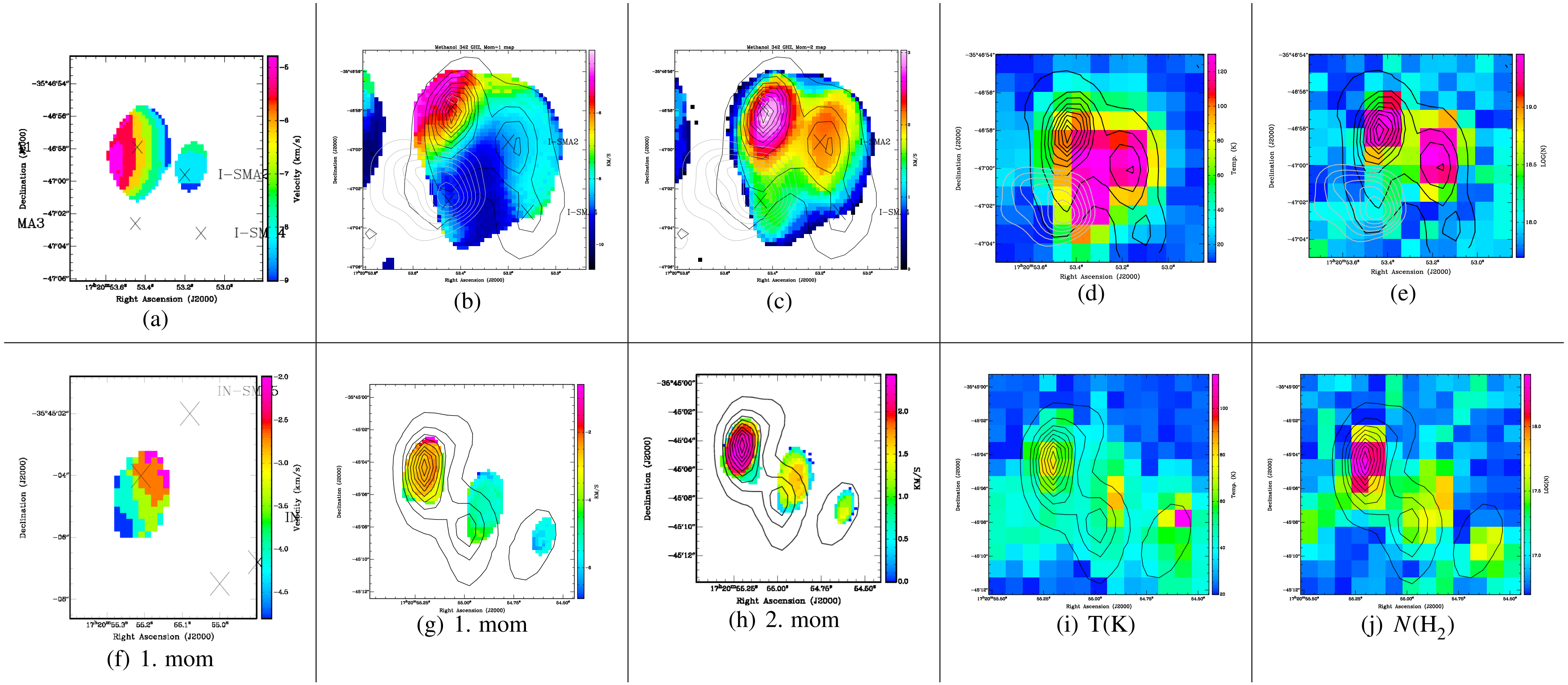

(a) (b) (c) (d) (e)

(f) 1. mom (g) 1. mom (h) 2. mom (i) T(K) (j) $N(H_2)$

Figure 5.5.: Line emission maps of I (top) and IN (bottom). Shown are from left to right: velocity map of HC_3N(39–38) in I and of HCN(4–3), $v_2 = 1$ in IN; first and second moment map of CH_3OH(13(0,13)–12(1,12)); and the temperature and column density map. The last two are derived from fits to all CH_3OH transitions with `myXCLASS`. Overlaid in black contours is the dust continuum emission and in gray contours the continuum at 3 mm from Beuther et al. (2008).

5.3.4. The influence of the UCHII region.

Three-color images in the NIR from GLIMPSE, performed by an Infrared Array Camera on board the Spitzer Space Telescope, toward the source I reveal that the cometary UCHII region ISMA3 formed a half-circular ring of hot dust in the northwest direction, whereas in the southeast direction the morphology is dominated by its champagne-like flow, fig 5.6. The structure of HMCs can be derived from tracers such as methyl cyanide (CH_3CN) or methanol. The impact of the UCHII region on the molecular gas could be thus seen in the temperature and velocity field of these tracers. The transition CH_3OH ($J_{K_aK_c} = 13_{0,13} - 12_{1,12}$, E_l=194 K) at 355.603 GHz is used as a tracer, where the results are shown in fig. 5.5. The temperature and column density maps were derived by fitting all detected lines of CH_3OH on a pixel by pixel basis with `myXCLASS` in LTE. The free-free emission of the UCHII region is dominating the continuum emission at 3 mm (Beuther et al., 2008). The methanol emission extends up to ISMA3, where the line width decreases at this position relative to the cores ISMA1 and ISMA2. The gas temperature reaches a value above 100 K. The velocity field reveals a blueshifted emission at −9 km/s at the peak of ISMA3. Thus, the impact of the UCHII region in the northwest direction onto the remaining, surrounding gas is seen in the lines of methanol and produces a cavity. In this cavity, the gas temperature is increased because of the heating and the gas velocity is blueshifted because of the pressure by ≈3 km/s relative to the clump velocity. Further implications on the infall velocity field are discussed in sect. 5.7.1.

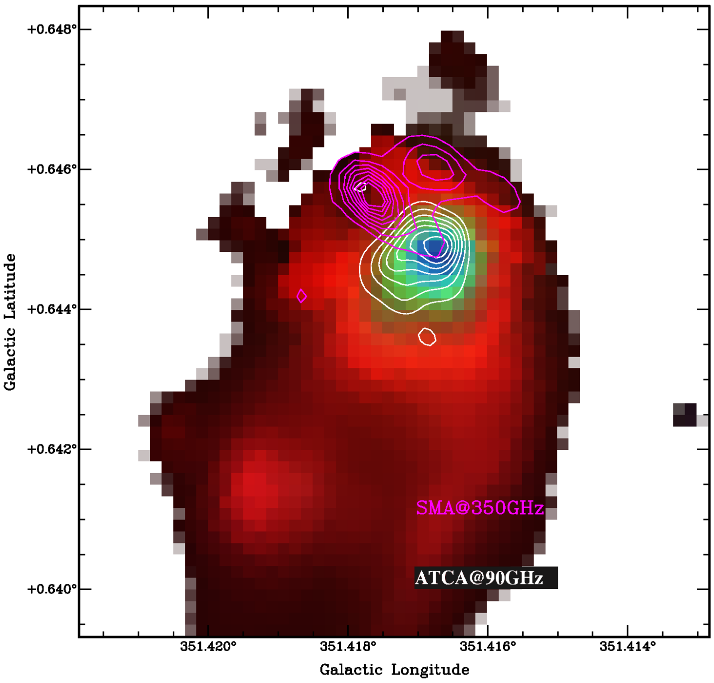

Figure 5.6.: Three-color GLIMPSE image (blue: 3.6 μm; green: 4.5 μm; red: 8 μm) of NGC 6334I, showing the UCHII region ISMA3. Observations with SMA at 350 GHz, and with the Australia Telescope Compact Array (ATCA; from Beuther et al. 2008) at 90 GHz, are overlaid in magenta and white contours, respectively .

5.3.5. Outflows in the northern region of NGC 6334

Fig. 5.7 presents the APEX observations of the northern region of NGC 6334 toward I and IN in the emission of HCN (4–3) and CO (3–2) (compare also with fig. 3 in McCutcheon et al., 2000). Fig. 5.7(a) shows particularly the high velocity gas in CO (3–2) in the range $[-100, +100]$ km/s, which depicts the outflow motions. The detection of three new outflows is reported here (the orientation axis are denoted by white lines in fig. 5.7), that can all be associated with the already known submm condensations SM2, SM5, and I(NW) (Sandell, 2000). The extended emission, which is only seen at blueshifted velocities without a redshifted counterpart, is associated with the HII region NGC 6334E.

The distribution of the position angles of the detected outflows in the northern region is not random: five out of the seven outflows have a preferential direction in the northeast–southwest direction. According to Houde et al. (2002), the orientation of the magnetic field B (the angle between the line of sight and B) can be derived from line observations by calculating the line width ratio of HCO^+ over HCN. As ionized molecules such as HCO^+ are charged, they are coupled closer to the magnetic field and their gas flow should deviate from the one of neutral molecules. Fig. 5.7(b) shows the line width ratio HCO^+/HCN of the northern region of NGC 6334, which was calculated from the second moment maps to obtain the velocity dispersion σ. Qualitatively, a general trend is found of a decreasing ratio in the northwest to southeast direction, which means that B is perpendicular to the main filament. This orientation is confirmed by the direction of B in the plane of the sky derived from dust polarimetric observations of NGC 6334 (Dotson et al., 2010). Thus, the homogenous magnetic field in this region could explain the preferential alignment of the outflows on large scales and the similar morphology of I and IN. As interferometric observations suffer from missing flux, this method of deriving the orientation of B is less reliable than polarimetric measurements for studying B at core scales.

Studies of B at core scales of star-forming regions revealed statistically that the orientation can change remarkably compared to the large scale B-field (Hull et al., 2014), where outflows are randomly aligned, but preferentially perpendicular to small-scale B-fields at a low polarization percentage. Recently, SMA dust polarization measurements (Zhang et al., 2014) of a sample of massive star-forming regions revealed that the B-field at core scales and the morphology tends to be parallel or perpendicular to the large scale B-field and thus is important for the collapse and fragmentation of clumps. Both sources I and IN are aligned within 45° of the large scale B-field, where in IN the polarization percentage is high (10%) and the orientation is almost parallel to the large scale B-field (see figs. 1d,1e, Zhang et al., 2014).

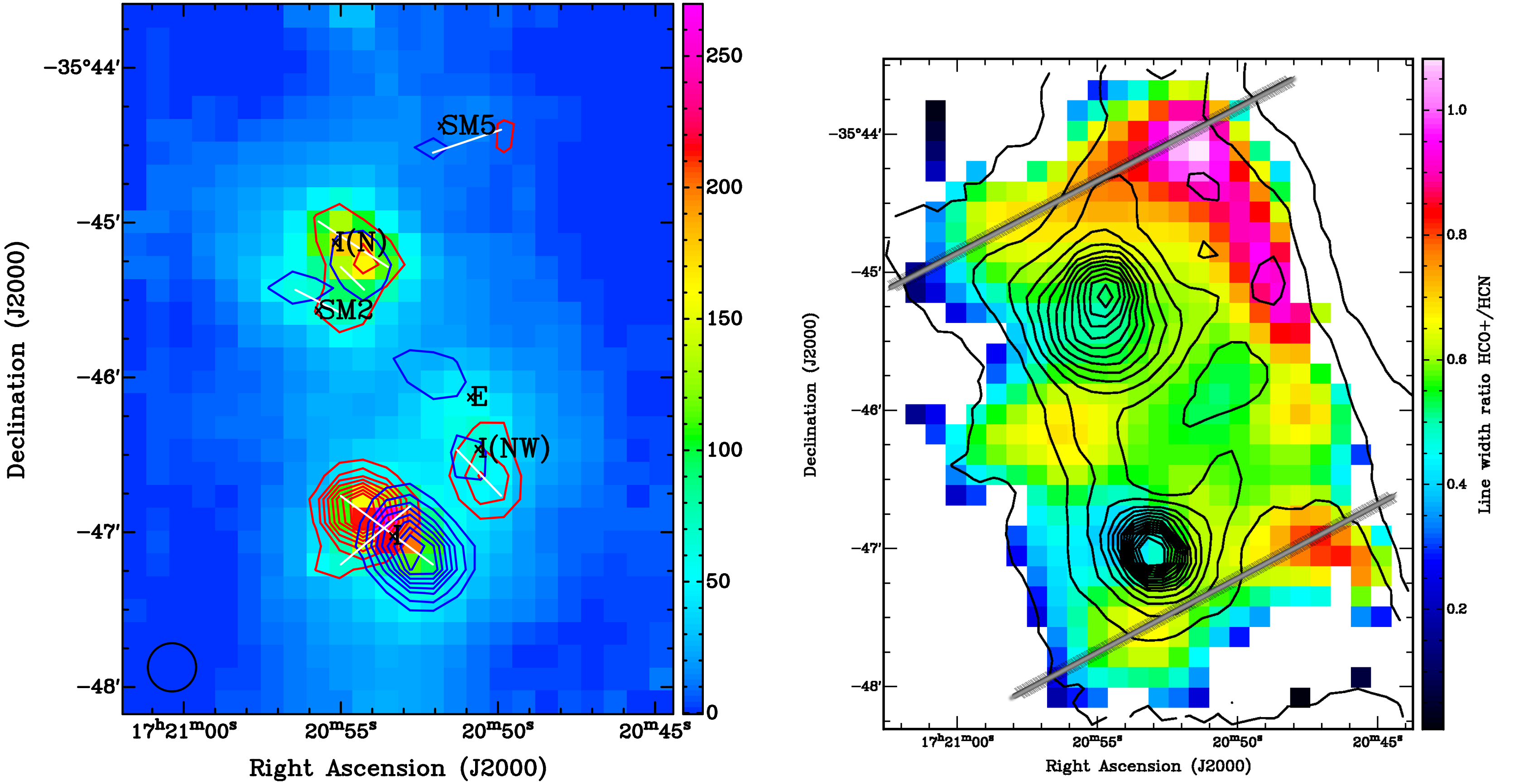

(a)

(b)

Figure 5.7.: (a) 0th moment map in HCN(4–3) of NGC 6334 north. Blue and red contours show the integrated intensity in CO(3–2) in the velocity ranges [−14.8,−100] km/s and [+4.7,+100] km/s. Blue contours are set from 15 to 90% of the max. at 701 K×km/s in steps of 10%, and red contours from 11 to 90% of the max. at 480 K×km/s in steps of 10%. The position of submm cores and the HII region NGC 6334E are denoted by a cross (Sandell, 2000). The orientation of the seven outflows are marked by white lines, and the beam size is shown in the lower left corner. (b) Line width ratio of HCO+(4–3)/HCN(4–3) in NGC 6334 north. The gray lines depict the orientation of the magnetic field. The map is smoothed to a resolution of 35″ to reduce the noise. Overlaid in black contours is the continuum from ATLASGAL from 6 to 90% of the max. at 57 Jy/beam in steps of 5%.

5.4. Modeling procedure

Fig. 5.8 is a schematic diagram of the main codes used in this chap. for modeling and producing synthetic spectra and maps. The model is set up in `RADMC-3D` that calculates the dust temperature and dust continuum maps. The non-LTE calculation of the molecule populations for each level is achieved with `LIME` by importing the physical parameters $n, T, X, v = (v_x, v_y, v_z), \Delta v$ at each cell position from `RADMC-3D` to `LIME`. Both codes use a right-handed coordinate system where the z-axis is pointing toward the observer. The raytracer produces spectral line cubes, that are then post-processed with `MIRIAD` to be "observed" with a telescope. This means that for single-dish telescopes the maps are convolved with a Gaussian according to the beam size of the telescope. In the case of interferometers such as SMA, the maps of the models are Fourier transformed, folded with the uv-coverage of the observations and then inverted and CLEANed in the same way as the observational data. To compare the observations with the models reliably, it is necessary that the model is much better sampled than the angular resolution of the observation, i.e., the relation should be pixel size $\ll$ beam size. After the convolution, the spectra are taken from the center of the source, and this way the information only changes marginally and smooth between adjacent pixels.

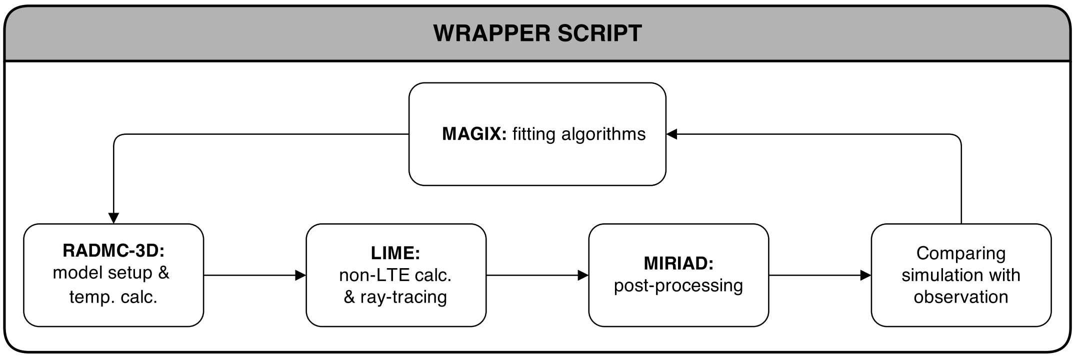

Figure 5.8.: Flowchart of the modeling routine and software codes. The codes are connected via `Python` scripts.

Models should be as simple as possible to not overstretch the number of parameters. For the purpose of exploring the parameter space and quantifying the goodness of different models, the optimization package Modeling and Analysis Generic Interface for eXternal numerical codes (`MAGIX`, Möller et al., 2013) is called after one run and local and global optimizing algorithms find the best values for the intensity and shapes of the spectral lines. The codes were connected initially via `Python` through a wrapper script written by A. Schmiedeke (private communication), based on scripts by R. Rolffs (Rolffs, 2011). `RADMC-3D` is written in `Fortran 90` and `LIME` in the programming language `C`. The scripts were reprogrammed, extended and modified in many parts where necessary: the connection to `MAGIX`; the parallelization of the post-processing for many molecules; the plotting and comparison; removing bugs; and modifications and extensions inside `LIME` and `RADMC-3D` for specific applications to NGC 6334.

5.4.1. Density structure

Resolved observations of massive dense cores in the dust continuum have shown that the radial density distribution is non-Gaussian and has more emission at larger radii (Rolffs, 2011). The density profile can be approximated well by a Plummer function, which is used for the cores, according to

$$n(r) = n_{\max} \times \left(1 + 0.31951(r/R)^2\right)^{-5/2}, \tag{5.1}$$

where $n_{\max}$ is the maximum density in the center, and R is the half-width half-maximum radius. The column density through the center is derived by integrating over the radius by $N(H_2)$=2.3588 × $R \times n_{\max}$. The total volume is

$$V = 4\pi \int_0^\infty \frac{n(r)}{n_{\max}} r^2 dr = 23.1935 \times R^3, \tag{5.2}$$

from which the total mass of the core is derived by $M_{\mathrm{tot}} = V\rho$, where ρ is the mass density. A mass per particle of 2.7 m_{h} is adopted and a gas-to-dust mass ratio of 100. For several objects, the densities are summed up by the contribution of each core at the radius r. To give a smooth transition between different values of the parameters $X, v, \Delta v$ of each core, a scalar field is created by the weight of the density of each core i that can be refined furthermore by a factor. This means for example by an abundance factor $AF(i)$ for the general relative abundance X of a species:

$$X(r) = X \times W(r), \quad W(r) = \frac{\sum_i [n(r,i) \times AF(i)]}{\sum_i n(r,i)}. \tag{5.3}$$

5.4.2. Temperature field

The calculation of the dust temperature is described in sect. 2.2.2. The gas kinetic temperature is assumed to be equal to the dust temperature in the cores and clumps, so that $T_{\mathrm{dust}} = T_{\mathrm{gas}}$, which is a good approximation for high densities (≥1E5 1/cm^3) and non-shocked gas. Exceptions from this procedure are outflows and HII regions, where the temperature is set manually.

5.4.3. Molecular abundances

The relative abundance in observations of a molecule m is defined as the ratio of the column density to the molecular hydrogen column density $X_{\mathrm{m}} = N_{\mathrm{m}}/N(H_2)$. Likewise, in the model this is the ratio over the densities $X_{\mathrm{m}} = n_{\mathrm{m}}/n(H_2)$. The abundances are described by a step function $X(T)$ with a jump temperature T_{jump}. T_{jump} is fixed at 50 K, which is the typical evaporation temperature of CO on ice mantles on dust grains. The global value for X can be furthermore adjusted by an abundance factor (AF) for each core or outflow. Based on the level populations it is possible to estimate the radius from where the main emission of a transition originates, see fig. 5.14. The vertical line marks the radius at which τ=1. For optically thick lines, this radius is higher than the radius of the maximum of the relative population.

5.4.4. Velocity field

The infall velocity is derived from an effective free-fall velocity v_{inf} and the rotation is modeled by Keplerian rotation v_{r}:

$$v_{\mathrm{inf}} = \sqrt{2GM_{\mathrm{ff}}/r} \quad ; \quad v_{\mathrm{r}} = \sqrt{GM_{\mathrm{rot}}/r}. \tag{5.4}$$

The free parameters in both cases is the effective mass M_{ff} or M_{rot}. Because both equations 5.4 are similar apart from $\sqrt{2}$, they can be interpolated by a parameter α following the equations (3) and (4) in Brinch et al. (2007). Intermediate values of α would then correspond to spiraling inward motions of the gas. The line width Δv for each cell is a number that mimics the microturbulence, such that the observed spectral line width is reproduced.

Bipolar molecular outflows are set up in a bicone geometry with a height/length of h, a half-opening angle OA, an inclination angle IA and a position angle PA. The physical model that best describes the observations is of the type of the wide-angle wind models (Arce et al., 2007), where the velocity corresponds to $v_{\mathrm{outflow}} = v_{\mathrm{max}}/h$. As the velocity increases linear with distance, this is called a Hubble-like structure . The density and temperature is constant inside the cones.

5.4.5. Convergence

The resolution of the models is set up with a minimum cell size of 50 au and a computation border radius of 0.5 pc. The model therefore spans a range over three orders of magnitude in space. A regular grid is utilized with an oct-tree adaptive mesh refinement (AMR) in `RADMC-3D` to build up an efficient grid according to the geometry of the model. The grid is refined according to the change in the density profile with user defined parameters.

The number of cells is >2E6 in `RADMC-3D` and >2E5 in `LIME`, which is sufficient for minimizing the variation in the line intensities and profiles. `LIME` uses an unstructured Voronoi grid that builds up randomly in such a way that the line length between the random point distribution is continuously increasing with higher density. The weighting of the points follows the relation $w = (n(r)/n_{\mathrm{max}})^{0.2}$, where n_{max} is a user-defined reference value set to 2E7 1/cm^3 in the models. Because `RADMC-3D` and `LIME` use different grid structures, there is no one-to-one mapping between the cells (see Camps et al. (2013) for a comparison), and the cell information is taken from the nearest neighbor found in the regular grid. Therefore, the resolution should be chosen such that both codes give the same results on conditions of LTE. Because `LIME` needs a given density structure to create the Delaunay grid, the density parameters and functions are exported 1:1 into `LIME` from `RADMC-3D`. After building up the grid, all other parameters are taken from `RADMC-3D`. Both `RADMC-3D` and `LIME` are capable to output the grid and stored parameters for each cell into the VTK format, which can be visualized in 3D by `ParaView`.

The number of cells, grid points and iterations affect the precision of the model and the derivation of the level populations. An increase of these values results in an increase of computation time. Thus, a criterion for convergence was chosen at a median SNR of the populations of S/N>1000 and a minimum S/N ratio of S/N>100, which is achieved after 20 iterations in general (the S/N ratio is defined after eq. (15) in Brinch and Hogerheijde, 2010). The extensive computation time can be decreased by using parallel processing in `LIME`.

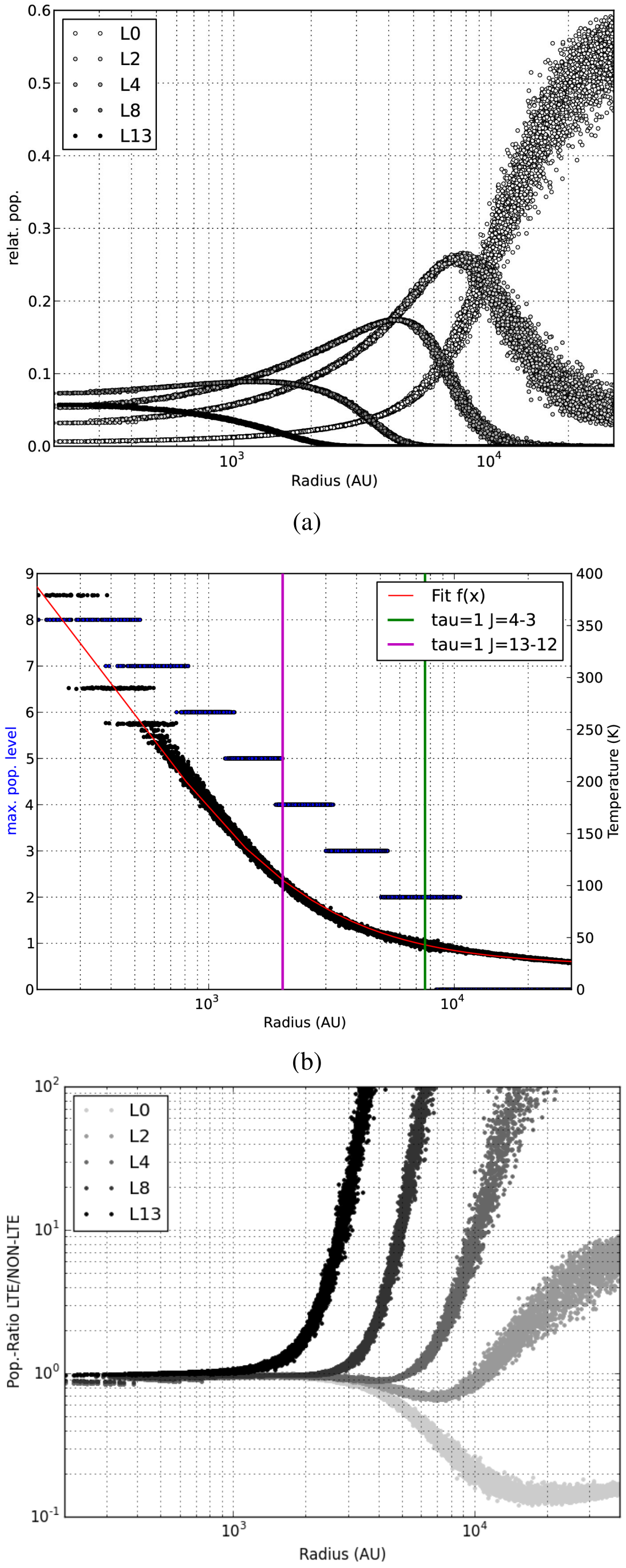

(a)

(b)

(c)

Figure 5.9.: Level populations in a toy model. (a) Relative populations of HCN (X=3E-8) for different energy levels. (b) Most populated level and τ=1 radii for selected transitions. (c) LTE/non-LTE ratio of the HCN population from (a).

Fig. 5.9 illustrates different properties of a model of a HMC, which is used as a toy model. The parameters are set with typical values for a HMC of L=1E4 $L_\odot$, $n_{\max}$=2E7 1/cm^3 and R=1500 au. The most populated level in fig. 5.9(b) increases with the temperature (depicted by black points). The temperature profile can be fitted by the function $f(x) = a*(x+b)^c + d$, where the exponent is $c = -1.22(1)$. Fig. 5.9(c) demonstrates that the difference in the populations for HCN levels in LTE/non-LTE decreases with increasing density, and all selected levels approach LTE for R$\leq$1E3 au.

5.5. Model setup and optimization for I and IN

It is aimed to model the observed spectra, which are shown in figs. 5.15 and 5.17, and to derive physical parameters of the sources. For this purpose the 3D radiative transfer code `LIME` is used, which is capable of calculating level populations in non-LTE conditions. The simulated spectral data cubes are then compared with the observational data. The procedure for modeling a specific astrophysical source is done in two successive major steps. First, the distribution of the molecular hydrogen densities and dust temperature is constrained based on the dust continuum observations, which sets the basic framework of the model. Second, the molecular line emission is simulated by supplying the distribution of the fractional abundance and the velocity field. Special conditions such as shocked gas from outflows and HII regions are taken into account.

5.5.1. Dust continuum

Based on the observations here and previously, the model for I and IN is set up consistent with values derived from the literature (Sandell, 2000; Hunter et al., 2006; Brogan et al., 2009). The molecular hydrogen densities in the cores are typically $n(\mathrm{H_2})$>1E7 1/cm^3. Almost all cores are internally heated in the model, except of INSMA3 and INSMA5 because of confusion with INSMA2 and INSMA1. The sizes (FWHM) of the cores range from 1–2E3 au, but it is noted that the cores are probably not resolved in the data and may have additional sub-structure, as is proven for INSMA1 by Hunter et al. (2014). The dust opacities are taken from Ossenkopf and Henning (1994), where the tables are taken from coagulated dust particles at densities of n=1E6 1/cm^3 without ice mantles (MRN6) for source I, and of coagulated dust particles at n=1E7 1/cm^3 with thin ice mantles (thin7) in the case of IN. The dust opacity at λ=1.3 mm is κ=1.993 cm^2/g for MRN6 and κ=1.052 cm^2/g for thin7. The different values were set to take the distinctive evolutionary stage of both sources into account. The luminosities for the different cores are set manually with an upper limit of 3E4 $L_\odot$ for a single star, because higher values would be sufficient to develop an HII region (Choudhury et al., 2015). The luminosities in the model are total luminosities, because a distinction is not possible from observations between the accretion luminosity and the interior luminosity of the star.

The external code `mcluster` (Küpper et al., 2011) is employed to implement the young star cluster around I (Tapia et al., 1996). The important input parameters are the total mass of the cluster and the Plummer density radius. The stars are drawn according to the IMF and are assumed to be at the ZAMS. Together with the single-star evolution routine (Hurley et al., 2000) the luminosity of each star is derived. After subtracting the luminosity of the protostars in ISMA1–4, the remaining luminosity is 2.0E5 $L_\odot$ in I. The following parameters are chosen to build up the approximately 90 stars and a stellar density field of 1200 1/pc^3: a mass of 500 $M_\odot$, a Plummer profile with a radius of 0.3 pc, and a Kroupa IMF with a lower limit of 3 $M_\odot$ and an upper limit of 15 $M_\odot$. By decreasing the lower mass limit the total number of stars increases, but not the total luminosity, because most of it (as it is the case for the total mass) is contained in the massive OB stars. Therefore, the total luminosity of 2.6E5 $L_\odot$ originates from the embedded star cluster and not from the protostars. In IN, the total luminosity is dominated by INSMA1. In the model, a luminosity of >1E4 $L_\odot$ is needed to obtain temperatures high enough to model emission of HCN (J=4–3, $v_2 = 1$). The SEDs of both clusters are shown in fig. 5.10.

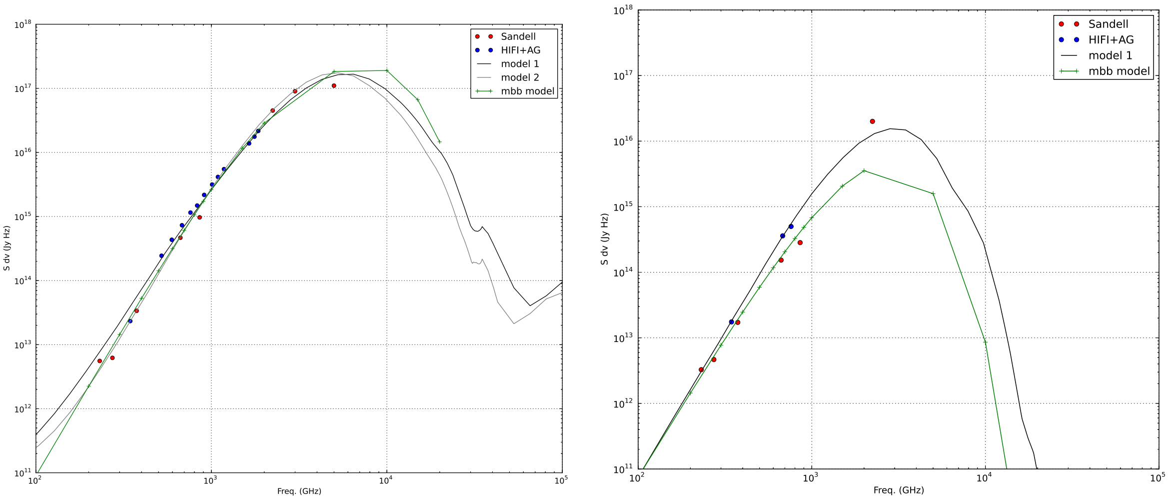

(a) (b)

Figure 5.10.: The SED of I (a) and I(N) (b). Measured points (taken from the observation and Sandell, 2000, fig. 3) are overlaid with fits from a modified black body (green, with T_{I}=90 K, T_{IN}=30 K) and the SED of the radiative transfer model (black).

5.5.2. Molecular lines

Various effects of different model parameters (infall velocity, rotation, line width, opacity, beam size, etc.) on the line profiles are described in Ward-Thompson and Buckley (2001), and apply qualitatively also to the procedures presented here. The collision rates for HCN, CS and CO are taken from the LAMDA. Dumouchel et al. (2010) and Sarrasin et al. (2010) calculated the collision rates of HCN with He, and these rates are then approximately scaled with a constant factor of 1.363 to represent collisions with H_2 owing to its reduced mass. The hyperfine structure of HCN is not taken into account, but as pointed out by Sarrasin et al. (2010), it is assumed that the rates are proportional to the degeneracy of the final hyperfine state, which is 3:5:1 for HCN (1–0). Because of the large line widths, only the ground transition HCN (1–0) shows hyper-fine splitting. Thus, the table is changed such that it includes only the hyperfine splitting of HCN (1–0). The same collision rates for the isotopologues $H^{13}CN$ and $HC^{15}N$ are used as for HCN. This approximation is valid because the mass difference between them is less than 4%. Vibrationally excited HCN lines are good tracers of the most inner part of protostars (Veach et al., 2013). Since no collision rates are available for $v_2 \neq 0$, these transitions are modeled in LTE. This is adequate because these levels are probably radiatively excited by the warm dust continuum and not by collisions (Rolffs, 2011).

The fractional abundances are set constant in a given temperature range, because the abundance of molecules change mostly at evaporation temperatures of 50–100 K (Garrod et al., 2008). By using a fixed jump temperature of $T_{\text{jump}} = 50$ K, two abundances are derived for the ranges above and below T_{jump}. The abundances of the molecules HCN and CS, whose emission is generally optically thick, are estimated from their isotopologues by using certain isotopologue ratios. The adopted isotopologue ratios in NGC 6334 (D=1.7 kpc and assuming a Galactic distance dependent ratio) are $[^{12}\text{C}]/[^{13}\text{C}]$=60, $[^{32}\text{S}]/[^{34}\text{S}]$=23, $[^{14}\text{N}]/[^{15}\text{N}]$=300, and $[^{16}\text{O}]/[^{18}\text{O}]$=500. Because of possible degeneracies and interdependencies, it was not attempted to fit all model parameters (>100) simultaneously. The most crucial parameters were determined in the following order:

1. global abundance and global line width,
2. local abundance factor and line width factor of each core,
3. radial and infall/expansion velocities of each core,
4. abundance, temperature, line width and outflow velocities of each outflow.

The dataset consists of the transitions of HCN given in table 5.2, and similarly frequency ranges are gathered from transitions of CS and CO. While the main tracer is HCN, transitions of CS and CO are used complementary to constrain the parameters and corroborate the significance of the models. The abundances of HCN and CS were first derived independently, whereas for determining the velocity field, HCN and CS data are used simultaneously (and CO in the case of source I). The relative abundance of CO is thereby set to a constant value of 1E-4 with no temperature dependence. Blended lines were excluded from the fitting procedure, as this is the case for example for HCN(11–10) at 974.487 GHz, which is affected by absorption of NH(1–0).

In general, the values are adjusted manually to give the best fit. For the modeling of spectral lines, the parameter space is explored by using `MAGIX` to minimize the χ^2 value, as defined in eq. 5.5. The summed difference between the observed data y_i over n data points and the model $y(x_i|a_0 \ldots a_{M-1})$ with M parameters a is

$$\chi^2 = \sum_{i=0}^{n-1} \frac{(y_i - y(x_i|a_0 \ldots a_{M-1}))^2}{\sigma_i^2} \, . \tag{5.5}$$

The error for y_i is σ_i. Because the χ^2 can fluctuate a lot, a global swarm algorithm was used, such as the bees or genetic algorithm, to find possible multiple minima and explore the landscape, see for example fig. 5.11. The SMA spectra were converted from units of Jy/beam to Kelvin to have the same units and an equal weighting with the single-dish data. No error σ_i for the channels was used.

Fig. 5.12(a) presents the dust and temperature distribution of the model of source I versus the radius. The peaks correspond to the position of the cores, and the constant values are set for the outflows. Fig. 5.12(b) demonstrates that the kinematics can be distinguished on three spatial scales:

1. (Keplerian) rotation for radii r<1E4 au,
2. outflow motions for r<5E4 au (sub-pc scales),
3. and infall motions for r<1E5 au or at pc scales.

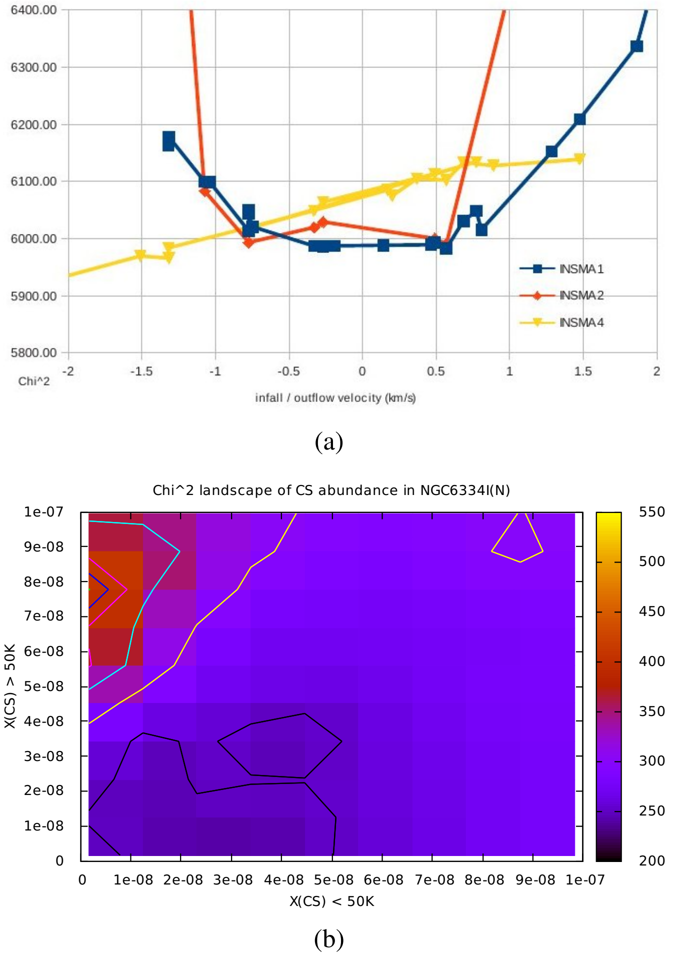

(a)

(b)

Figure 5.11.: χ^2 landscape of (a) infall/outflow velocities of cores in IN, and (b) of the CS abundance in IN below and above the jump temperature of 50 K.

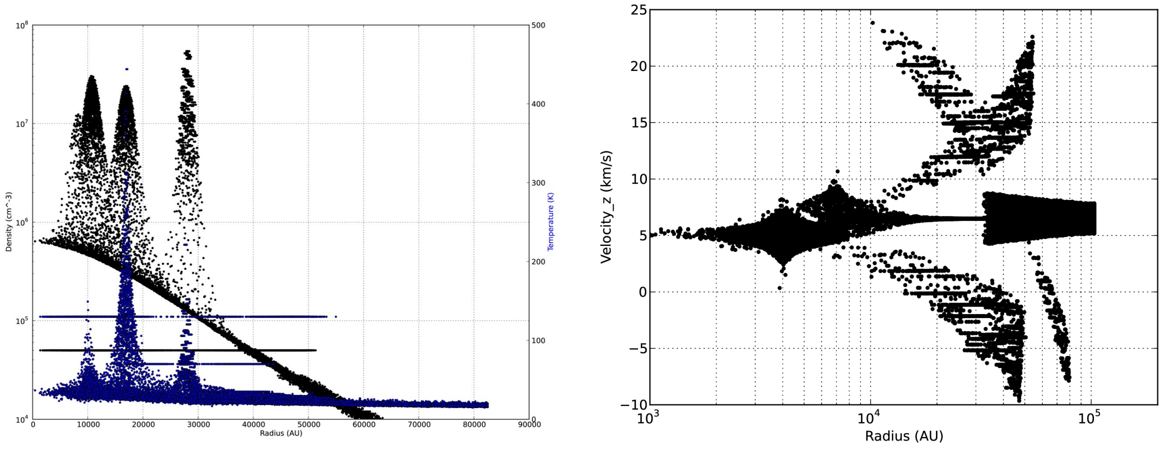

(a)

(b)

Figure 5.12.: Model parameters in NGC 6334I and I(N). (a) Molecular hydrogen density $n(r)$ and temperature of the model of IN in dependence of the radius. (b) The z-component of the velocity vector of the model of I versus radius.

5.5.3. Mass accretion and outflow rates

By obtaining the infall velocity $v_{\rm inf}$ of the clump and knowing the gas density, the present kinematic mass accretion rate is derived from the eq.

$$\frac{\mathrm{d}M_{\rm K}}{\mathrm{d}t} = \frac{\mathrm{d}M}{\mathrm{d}R} \times \frac{\mathrm{d}R}{\mathrm{d}t} = 4\pi\rho R^2 \times v_{\rm inf}, \tag{5.6}$$

where ρ is the mass density at the radius R. Similarly, the mass entrainment rate of outflows is derived (assuming a bicone geometry) from the eq.

$$\dot{M}_{\rm outfl} = 2/3\pi\rho s^2 \times v_{\rm max}, \tag{5.7}$$

where s is the radius and the 2 accounts for both lobes. The height/length h of a cone is connected to the radius by $s = \tan(OA) \times h$, where OA is the half-opening angle. Because the infall velocity of the cores in the clusters cannot be measured directly, three modified Bondi-Hoyle type (Bondi and Hoyle, 1944) accretion models are used to estimate the mass accretion rates of the cores. Following the competitive accretion model of Bonnell et al. (2001), the accretion rate in embedded clusters is

$$\dot{M} \approx \pi\overline{\rho}R_{\rm acc}^2 v\,, \tag{5.8}$$

where $\overline{\rho}$ is the mean density of the cloud and the accretion radius $R_{\rm acc}$ can be either the Bondi-Hoyle radius $R_{\rm BH}$ or the tidal-lobe radius $R_{\rm tid}$:

$$R_{\rm BH} = \frac{2\mathrm{G}m_*}{v_{\rm rel}^2 + c_{\rm s}^2} \quad ; \quad R_{\rm tid} = 0.5r_*\left(\frac{m_*}{M_{\rm enc}}\right)^{1/3}. \tag{5.9}$$

The relative velocity is $v_{\rm rel}$, the stellar mass is m_*, and $M_{\rm enc}$ is the mass enclosed within the cluster at the star's position r_*. The actual accretion radius is expected to be the smaller one of the two. The velocity v in eq. 5.8 is then $v = (v_{\rm rel}^2 + c_{\rm s}^2)^{0.5}$ for the Bondi-Hoyle type and $v = v_{\rm rel}$ for the competitive accretion type. Another approach takes the turbulence into account. Krumholz et al. (2005) suggests to use the velocity dispersion σ as a zeroth-order estimate for the accretion rates:

$$\dot{M}_{\rm T} \approx 4\pi\overline{\rho}\,(\mathrm{G}m_*)^2 \,/\, \left(\sqrt{3}\sigma\right)^3. \tag{5.10}$$

The 1D velocity dispersion σ is derived from the line width of methanol (see Liu et al., 2013):

$$\sigma = \sqrt{\sigma_{\rm NT}^2 + c_{\rm s}^2} \quad \text{and} \quad \sigma_{\rm NT} = \sqrt{\sigma_{\rm CH_3OH}^2 - \mathrm{k_B}T/m_{\rm CH_3OH}}. \tag{5.11}$$

An average temperature of $T = 100$ K is taken for the HMCs, which results in $c_{\rm s}$=0.553 km/s. The radial velocity of the clump is −6.5km/s in I and −2.2 km/s in IN, from which the relative velocities are derived toward the cores. The line widths are taken from table 5.3 and not from the microturbulent line widths from the model. To estimate $R_{\rm tid}$, the radius of the star r_* from the center of the cluster is calculated by assuming that the z-position is $r_z = (r_x + r_y)/2$. The center of the cluster is measured by fitting a Gaussian to the dust continuum observations of NGC 6334 with SCUBA (Submillimetre Common User Bolometer Array, (Di Francesco et al., 2008)) on JCMT at 450 μm. The center coordinates are α=17^{h}20^{m}53.3^{s}, δ=−35°47′4.8″ for the source I and α=17^{h}20^{m}55.1^{s}, δ=−35°45′13.3″ for the source IN.

5.6. Model results

Table 5.4 lists the results of the most important parameters of the model, and fig. 5.13 is a 3D visualization of the model of IN as seen by an observer. The velocity parameters, crucial to derive the kinematics of the protoclusters, are listed in table 5.5. Figs. 5.15, 5.16 and 5.17 show the simulated spectra on top of the observed spectra in different tracers.

As discussed in sect. 5.3, the absorption dip is mainly produced by the surrounding clump or envelope, in which the cores are embedded. The asymmetric line profiles of the cores can be thus produced just by the radial velocity difference between the clump and the cores. Furthermore, depending on the position of the core in the cluster, the core can be affected by the blue or red lobe of an outflow in the line of sight. The asymmetric line emission distribution of the outflow wings can thus lead to pseudo infall profiles, too. Because of the self-absorption of the clump in the line profiles, it is not possible to derive core specific infall or expansion motions, because the spectrum and χ^2-value does not change significantly. However, the upper and lower value of the velocities (assuming a constant value independent of the radius) can be limited to $\approx \pm 1$ km/s from the model. The rotation of the HMCs can be reproduced by a Keplerian rotation with an effective Keplerian mass of ≈ 8 M$_\odot$ that is smaller than the stellar or gas mass. Because the inclination angle is unknown, but depends on the observed Keplerian mass by $M_{\rm rot}/\sin(i)^2$, this lower mass could be explained by a lower inclination angle of 27–31° instead of the assumed value of i=45° taken from the orientation of the accompanied molecular outflows. The infall motion is modeled by a free-fall velocity and an effective mass. While for IN this infall motion extends all the way to the center, for source I this predicted asymmetry in the higher-frequency lines of HCN and CS would be stronger than observed. Thus a new parameter $r_{\rm a}$ is introduced, which is the factor of the clump's radius at which the infall motion stops. By inspecting the observed CO ladder from $J_{\rm u}$=3–16 it is evident that the blue asymmetry is no longer present for the transition J=10–9. From the optically thick CO emission, which is more sensitive to trace the outer parts, this radius is determined as $r_{\rm a} = 2.0$. This derived radius of 34E3 au is comparable to the radius 20E3 au at which the optical depth $\tau = 1$ for CO (10–9), which is derived from the model (fig. 5.14). In contrast to Larson's line width-size relationship, a decrease of the line width with decreasing radius is not matching the observations. The envelope of IN (IN$_{\rm clump}$) has a similar or smaller line width by a factor 0.8–1 compared to the cores and the velocity dispersion is slightly increasing with density.

The 3D modeling allows studying the effect of the third spatial axis z on observations. Because of differences in the optical depth of gas layers in the line of sight and the development of absorption features, it is possible to determine whether an object is in the foreground or in the background. However, the z values given in table 5.4 should be regarded with caution, as they have a larger uncertainty than the x and y values, which are derived from the position in the plane of the sky. The HCN (4–3) emission of ISMA2 is almost completely self-absorbed by outflowI1 and is thus in the background, whereas ISMA4 is in the foreground. OutflowI2 was set behind ISMA1 and ISMA2, which would otherwise influence the emission of these cores in the LOS. In IN, INSMA2 and INSMA4 are influenced by outflowIN1 in the line wings, but not self-absorbed and thus in the foreground. Less absorption can be achieved for the core INSMA6 by placing it outside of $\mathrm{IN}_{\mathrm{clump}}$ and in the foreground. The 3D geometry of both clusters is therefore such that cores in the southwest are in the foreground and cores in the northeast are farther away relative to the observer. By comparing this geometry with the result of the bended main filament derived in chap. 3, a consistent geometry is found. This leads to the conclusion that the elongated structure of the clusters is impregnated by the filament.

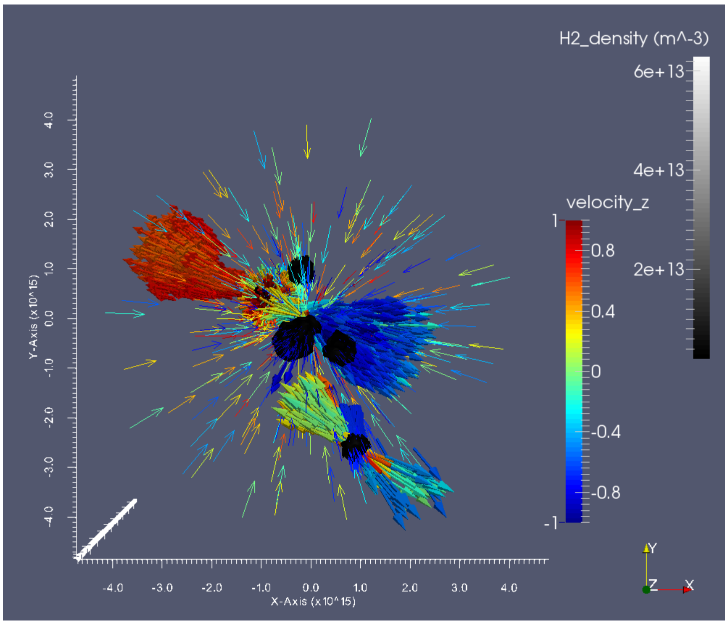

Figure 5.13.: 3D visualization of the model of IN. The dense center of the cores are marked in black, and the outflow and infall motions by arrows. The magnitude of the velocity vector $\vec{v}$ is normalized and the v_z-component is shown.

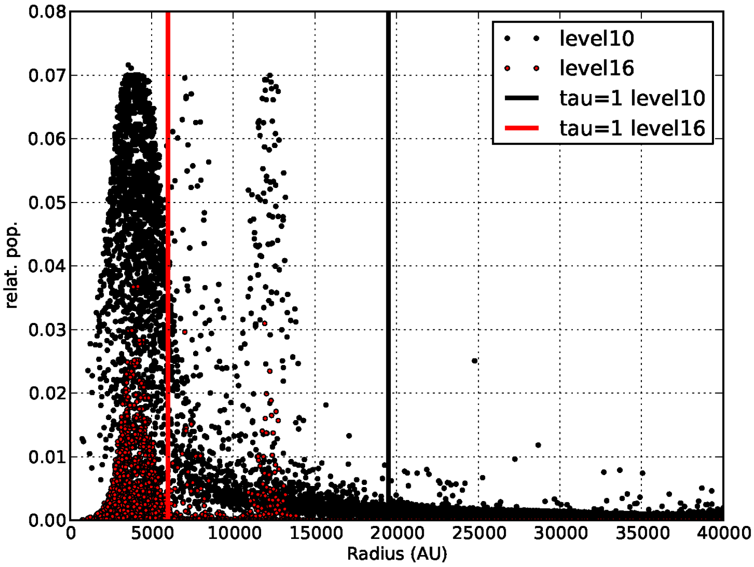

Figure 5.14.: Relative populations of CO for level 10 and 16 in the model of NGC 6334I. The vertical lines mark the τ=1 surface in the LOS.

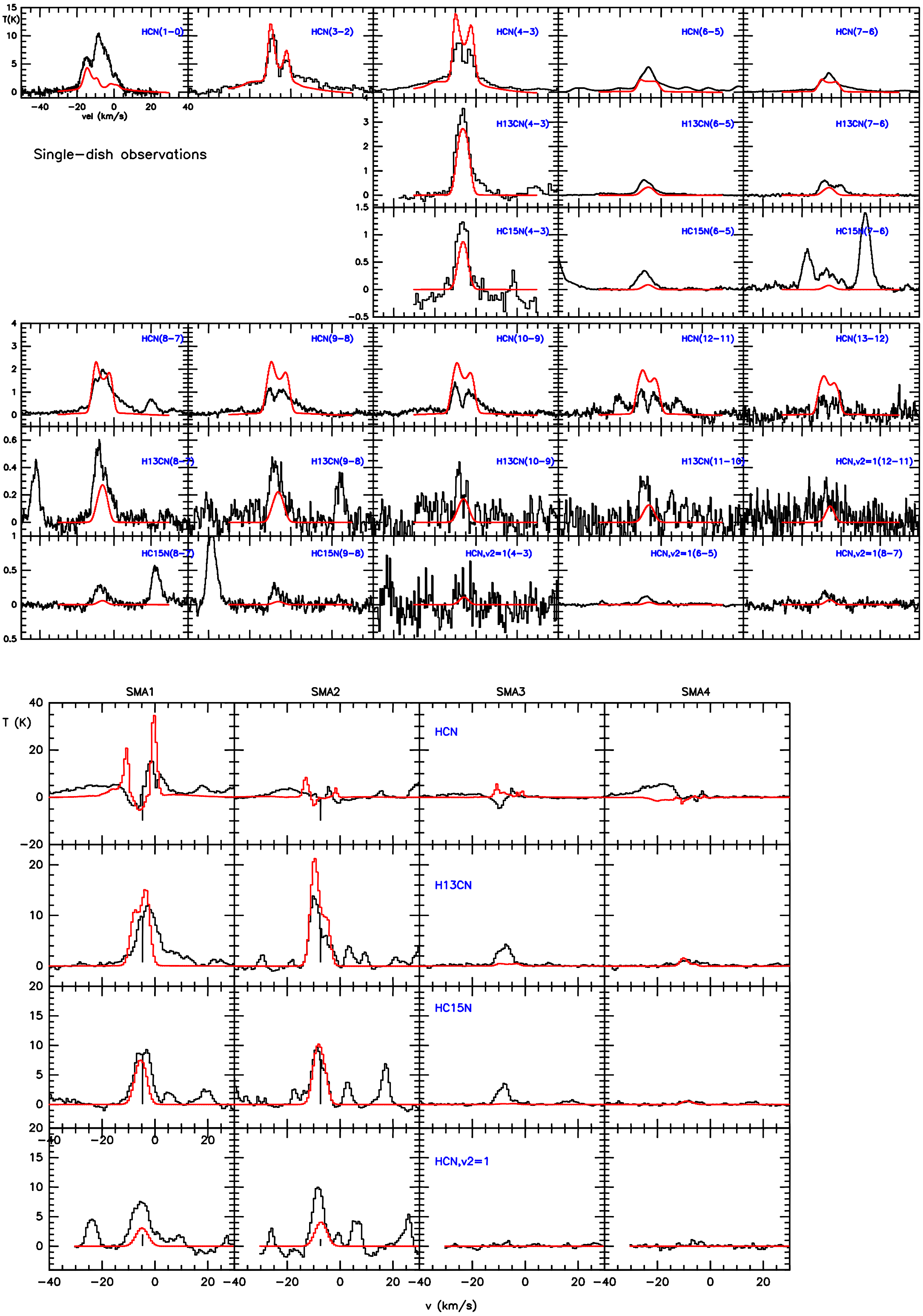

Figure 5.15.: NGC 6334I: Simulated spectra (red) overlaid with single-dish and interferometric observations (black). The velocity ranges are [−50,40] km/s in HCN. The highest-frequency transitions are smoothed in this figure, and vertical lines in the SMA spectra denote the central radial velocity of a core.

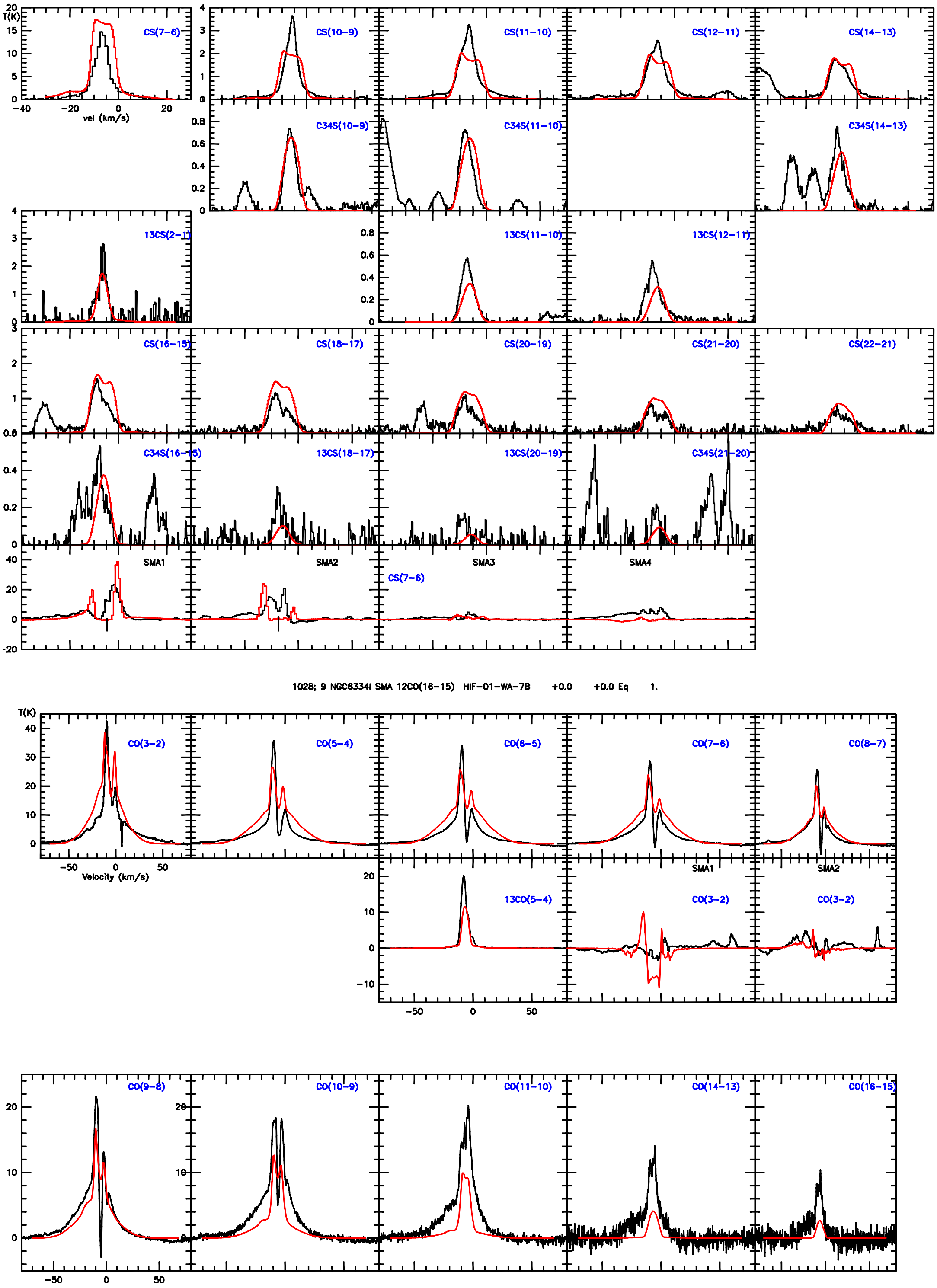

Figure 5.16.: NGC 6334I: Simulated spectra (red) overlaid with single-dish and interferometric observations (black). The velocity ranges are [−40,30] km/s in CS and [−80,80] km/s in CO. The highest-frequency transitions are smoothed in this figure, and vertical lines in the SMA spectra denote the central radial velocity of a core.

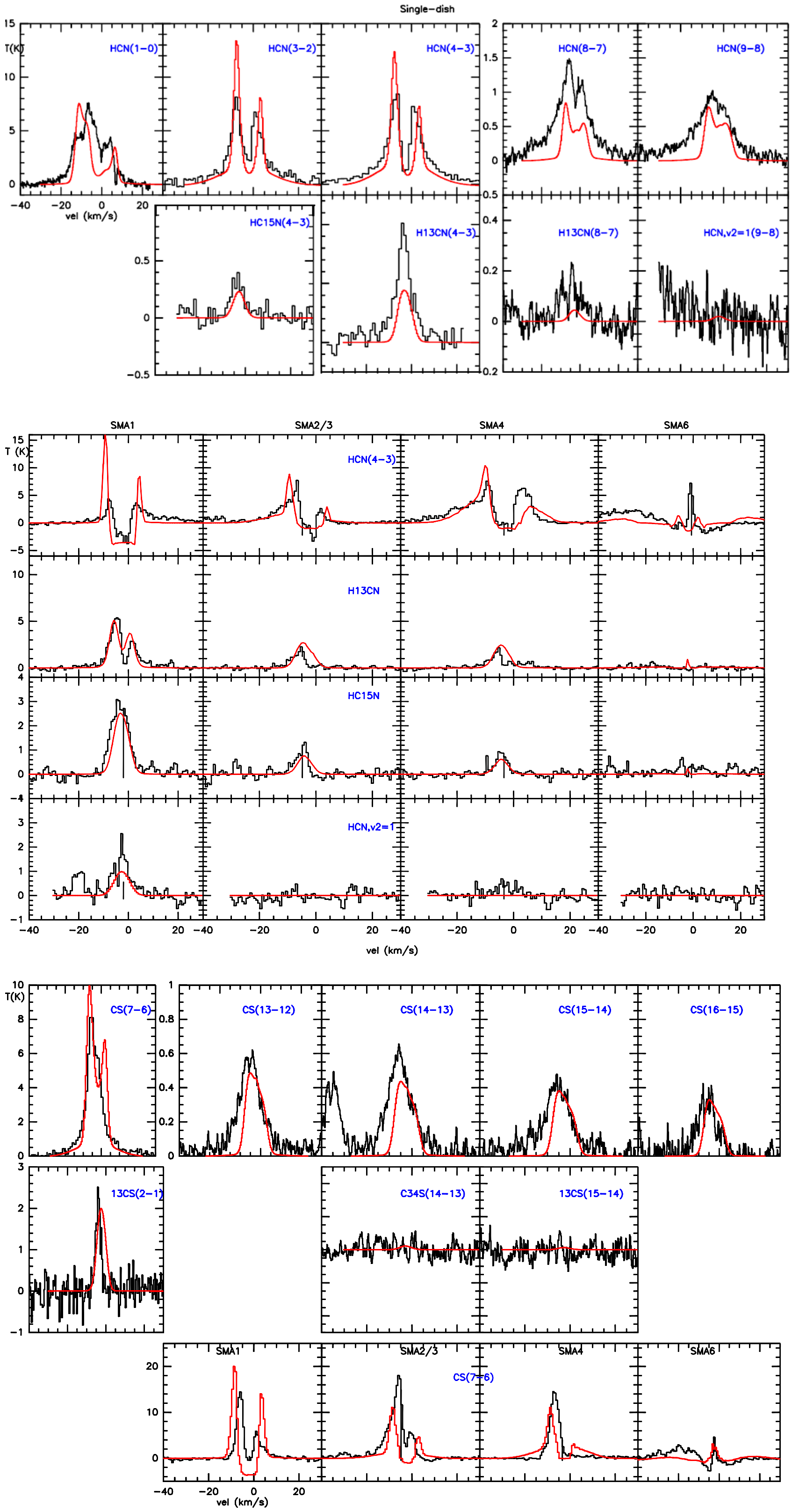

Figure 5.17.: NGC 6334I(N): Simulated spectra (red) overlaid with single-dish and interferometric observations (black). The velocity range is [−40,30] km/s in each case and vertical lines in the SMA spectra denote the central radial velocity of a core.

Table 5.4.: Best model parameters of the protostellar clusters NGC 6334I and IN

Core	x, y, z (1E3 au)	L ($L_\odot$)	m_* ($M_\odot$)	$n_{\max}$ (1/cm^3)	R (1E3 au)	N_{H_2} (1/cm^2)	Mass ($M_\odot$)	X(HCN) ^{a}	X(CS) ^{a}	AF
ISMA1	0, 0, 4.0	3.0E4	17.6	3.0E7	1.8	1.9E24	31	7E-10;3.5E-8	1E-10;1.4E-7	0.6
ISMA2	5.6, −3.1, −3.0	3.0E4	17.6	1.4E7	1.8	8.9E23	14	"	"	1.7
ISMA3	−0.5, −7.6, −7.0	3.3E3	8.5	1.0E5^d	2.5	-	0.06	"	"	0.01
ISMA4	6.6, −9.7, 60.0	1.9E4	14.9	2.0E7	1.0	1.0E23	3.5	"	"	0.01
$\mathrm{I}^{c}_{\mathrm{clump}}$	0, 0, 0	1.8E5	500	2.8E5	17.0	7.1E23	243	"	"	1.5
INSMA1	−6.5, 4.4, −15	1.6E4	14.1	2.4E7	1.4	1.2E24	12	2.5E-8;2.5E-8	4E-8;4E-8	0.7
INSMA2	0, 0.9, 10	1.7E3	7.0	1.6E7	0.8	4.5E23	1.4	"	"	0.2
INSMA3	−2.5, −3.0, 10	-	-	3.0E7	1.3	1.4E24	12	"	"	0.2
INSMA4	4.6, −4.3, 15	1.0E3	6.0	1.2E7	1.5	6.4E23	7	"	"	0.2
INSMA5	1.4, −1.2, 8.2	-	-	1.2E7	1.4	5.9E23	6	"	"	0.01
INSMA6	6.6, −18.5, 20	1.9E3	7.3	6.4E7	0.8	1.8E24	6	"	"	0.01
$\mathrm{IN}_{\mathrm{clump}}$	0, 0, 0	-	-	6.0E5	17.0	3.6E23	520	"	"	1.0

	x y z (1E3 au)	OA (degr.)	IA (degr.)	PA (degr.)	h (au)	n (1/cm^3)	T (K)	Mass ($M_\odot$)	AF
OutflowI1	0, 0, 4.0	20	45	40	51	5E4	100	14	1.0
OutflowI2	−8.5, −8.5, −40	15	45	−35	40	5E4	100	3.7	1.0
OutflowIN1	−6.5, 4.4, −15	15	45	25	34	5E4	130	2.2	1.0
OutflowIN6	6.6, −18.5, 20	25	70	43	15	5E4	70	0.6	1.0

The columns denote: (1) name of the core/outflow, (2) coordinates, (3) luminosity, (4) stellar mass, (5) maximum density, (6) radius, (7) column density, (8) integrated total mass, fractional abundance of HCN (9) and CS (10) and the abundance factor (11). (a) two values give the relative abundance below and above the jump temperature of 50 K. (c) luminosities and masses refer to the star cluster. (d) electron density. For the outflows, OA refers to the half-opening angle, IA to the inclination angle, PA to the position angle and h to the length of a cone.

5.7. Discussion

5.7.1. Comparison with previous models

A model of NGC 6334I was presented by van der Tak et al. (2000) based on continuum and line observations. The radial velocity was derived as $v = (-7.4 \pm 0.2)$ km/s and line width as $\Delta v = (5.3 \pm 0.3)$ km/s. The best fit for the model, with a density assumption of $n(r) = n_0(r/r_0)^{-\alpha}$, is n_0=6E4 1/cm^3, $\alpha = 2$ and r_0=43E3 au. A total mass of $M(< r_0)$=382 M$_\odot$, virial mass of $M_{\rm vir}$=725 M$_\odot$ and average temperature of $\overline{T} = 35$ K was derived. The column density in CO is N(CO)=1.7E20 1/cm^2 and relative abundance of CS X=1.2E-8.

The source I is part of several cluster-forming regions studied in Rolffs (2011) and was modeled with the 1D radiative transfer code `RATRAN`. The highest angular resolution of their APEX observations is 7″, hence the internal structure could not be resolved. It was concluded that a multiplicity of heating sources and a more complex velocity field are necessary to match the models more closely to the observations. They derived similar abundances of HCN of X=4E-10 and X=4E-8 below and above 50 K, a line width of 5 km/s, and an infall velocity of -1 km/s that is 10% of the free-fall velocity (assuming a mass >1000 M$_\odot$). The model for I proves also that a pure free-fall would overestimate the asymmetry in the lines. It is noticed that the blue asymmetry in their highest-frequency lines, HCN (9–8) and HCO$^+$ (10–9), is overestimated. Additionally, the intensities of the high-J HCN lines and the self-absorption are overestimated from their model, which was explained by the lack of clumpiness.

Another 1D radiative transfer model, including kinematics and based on the same HIFI data, is presented by Morales Ortiz et al. (2014). They derive a cosmic ray ionization rate of 0.8–2.0E-16 1/s and find a redshift asymmetry in the optically thick lines of HCO$^+$, C^{17}O and C^{18}O. These lines most likely trace the larger scales and less dense gas such as from the envelope. The redshift is interpreted by an expansion motion of the inner part of the clump. In their model, this inner part or envelope has a radius of r_1=7.6E3 au and radial velocity of $v_1 = -7.5$ km/s, whereas the outer envelope has a radius of r_2=34E3 au, a velocity of $v_2 = -6.0$ km/s, and a density of (1.0 ± 0.8)E5 1/cm^3. Therefore, their outer envelope is identical to the model here in velocity and density. The resulting mean velocity of all lines is $\langle v_{\rm LSR} \rangle = -7.3$ km/s, which corresponds to the velocity of ISMA2. Therefore, the velocity of the inner envelope is identical with ISMA2, and the observed asymmetry in the line profiles stems likely from the different motions of ISMA1, ISMA2 and the clump. The model and observations here suggest that the infall motion has indeed been reduced in the inner center, but no indications are found for an expansion motion in the higher-J lines of HCN and CS. That these lines are good tracers of expansion is demonstrated by Rolffs (2011), where in the massive star-forming region SgrB2(M) a reversal of the infall has been observed because of stellar feedback.

The thermal pressure from the hot ionized gas of the UCHII region could be responsible for the counteraction of the infall motion in I. Morales Ortiz et al. (2014) calculate the thermal pressure to $P_{\rm t}/{\rm k_B}$=1.6E9 K/cm^3 and use this value as an explanation for the proposed expanding envelope. Using the gravitational energy of the clump and assuming spherical symmetry, the gravitational pressure at a radius R is

$$P_{\rm G} = \frac{F}{A} = \frac{-\nabla(E)}{A} = -\nabla\left(\frac{-3{\rm G}M^2}{5R}\right) \times \frac{1}{4\pi R^2} = \frac{3{\rm G}M^2}{20\pi R^4}\,. \tag{5.12}$$

By using the values M=150 $M_{\odot}$ at r=34E3 au, a value of P_G/k_B=1.5E9 K/cm^3 is derived that is comparable to the thermal pressure mentioned above. Considering that in the energy balance additional supporting forces are present such as the kinetic gas pressure, turbulence and radiation pressure, the pressure of the UCHII region is sufficient to attenuate the infall motion of the clump. Because only spherical accretion is considered here, the UCHII region is not in the gravitational center and observations are more sensitive to the front half of the source, it is still possible that the cores accrete gas from the nearby main filament westward.

Several limitations are found in the models in the description of the clusters. The self-absorption in some lines of HCN is overestimated, whereas both clusters I and IN are embedded in a large filament, where most likely additional gas layers and foreground clumps are present. The simple model for the outflows with a constant temperature and density is sufficient to reproduce the emission in HCN and CS, but not in CO. Additional components might be necessary to explain in particular the high velocity emission up to −80 km/s and the hot compact emission visible in the high-J CO lines. Furthermore, a constant dust opacity is used for one source, but the composition of icy dust grain mantles are likely to change locally with time, temperature and density.

5.7.2. Discussion on accretion rates

The calculated infall and outflow mass rates are given in table 5.5. The calculated mass entrainment rates of the outflows are in the range ≈1E-3–1E-4 $M_{\odot}$/yr. These rates are a little bit higher but of the same order of magnitude as the one derived in Leurini et al. (2006) for source I, and are lower in IN compared to values from Megeath and Tieftrunk (1999) for the red wing. The derived rates are typical for molecular outflows in high-mass star-forming regions, because the median mass loss rate is 9.1E-4 $M_{\odot}$/yr (Sánchez-Monge et al., 2013b). However, they cannot exceed the infall rate, as their outflow rate is coupled to the inflow rate with an efficiency factor f by $M_{\rm out} = f\ M_{\rm in}$. Probably the assumption of a homogenous cone with a constant density and a maximum outflow rate is overestimating the rate and gives therefore rather an upper limit.

The infall velocity $v_{\rm inf}$ of the clump is 0.7 km/s at R=17E3 au in IN and the maximum infall velocity in I at R=34E3 au reaches 2.0 km/s. Using eq. 5.6, the rates are 1.7E-3 $M_{\odot}$/yr for I and 1.2E-3 $M_{\odot}$/yr for IN. The mass flow rate of the main filament can be derived by using eq. 4.12. By using an average velocity gradient of 2 km/s/pc (see 3), a mass length density of 833 $M_{\odot}$/pc and an inclination angle of α=45°, the mass flow rate is $\dot{M}_{\rm fil}$=1.7E-3 $M_{\odot}$/yr. The similar magnitude compared to the infall rates of the clusters supports the idea that the filament is feeding the clusters through accretion and provides a gas mass reservoir for them. The fraction fr in table 5.5 is defined as the ratio of the sum of the accretion rates in a cluster, according to the three models, over the kinematically derived accretion rate of the whole clump: $fr = \Sigma \dot{M}_i / \dot{M}_{\rm K}$.

Table 5.5.: Derived velocities and mass flow rates in the protostellar clusters NGC 6334I and I(N)

Core	v_{LSR} (km/s)	Δv (km/s)	M_{ff} ($M_\odot$)	M_{rot} ($M_\odot$)	v_{max} (km/s)	$\dot{M}_K$ ($M_\odot$/yr)	σ (km/s)	$\dot{M}_T$ ($M_\odot$/yr)	v_{rel} (km/s)	R_{BH} (au)	$\dot{M}_{BH}$ ($M_\odot$/yr)	R_{tid} (au)	$\dot{M}_{ca}$ ($M_\odot$/yr)
ISMA1	−5.0	4.2	-	8	-	-	1.9	1.7E-4	1.5	1.2E4	1.6E-3	6.9E3	4.6E-4
ISMA2	−7.5	4.2	-	8	-	-	1.4	4.6E-4	1.0	2.4E4	4.2E-3	6.6E3	2.8E-4
I_{clump}	−6.5	4.2	[0,100]	-	-	1.7E-3	-	-	-	-	-	-	-
Fraction fr	-	-	-	-	-		-	0.37	-	-	3.4	-	0.44
Outflow I1	−5.0	34	-	-	±20	1.2E-3	-	-	-	-	-	-	-
Outflow I2	−6.5	34	-	-	±20	3.8E-4	-	-	-	-	-	-	-
INSMA1	−2.0	5.8	-	8	-	-	2.1	2.2E-4	0.2	7.3E4	5.0E-2	5.3E3	8.8E-5
INSMA2	−4.0	5.8	-	-	-	-	1.6	1.1E-4	2.0	2.9E3	2.8E-4	4.0E3	5.1E-4
INSMA4	−4.0	5.8	-	-	-	-	2.1	3.6E-5	2.0	2.5E3	2.1E-4	3.7E3	4.5E-4
INSMA6	−2.0	1.8	-	-	-	-	1.0	4.7E-4	0.2	3.8E4	1.3E-2	4.1E3	5.4E-5
IN_{clump}	−2.2	4.6	9	-	-	1.2E-3	-	-	-	-	-	-	-
Fraction fr	-	-	-	-	-		-	0.70	-	-	53.1	-	0.92
Outflow IN1	−2.0	23	-	-	±5	2.1E-4	-	-	-	-	-	-	-
Outflow IN6	−2.0	35	-	-	±15	1.2E-4	-	-	-	-	-	-	-

Cells with no information are marked with "-". The columns denote: (1) name of the object, (2) radial velocity, (3) line width used in the model, (4) effective free-fall mass, (5) effective Keplerian mass (6) outflow velocity, (7) mass entrainment rate of the outflow or infall rate of the clump, (8) velocity dispersion from table 5.3, (9) turbulent accretion rate, (10) relative velocity, (11) Bondi-Hoyle radius, (12) Bondi-Hoyle accretion rate, (13) tidal-lobe radius and (14) competitive accretion model rate.

By comparing the values of the three models, it is found that the Bondi-Hoyle model overestimates highly the accretion rates in IN, because the sum of the core rates cannot be bigger than the clump's rate because of the principle of mass conservation. As expected, the values for $\dot{M}_\mathrm{T}$ and $\dot{M}_\mathrm{ca}$ are fr<1, because the census of all cores contained in the clusters is not complete but limited to the most massive ones owing to the receiver's sensitivity. Despite the different underlying assumptions, for source I the fractions fr from $\dot{M}_\mathrm{T}$ and $\dot{M}_\mathrm{ca}$ are similar, and the derived mean accretion rates of all cores by using the model of Bonnell et al. (2001) is $\langle\dot{M}_\mathrm{ca}\rangle$ = (3.1 ± 0.8)E-4 $\mathrm{M}_\odot$/yr and close to the one of $\langle\dot{M}_\mathrm{T}\rangle$ = (2.5 ± 0.8)E-4 $\mathrm{M}_\odot$/yr by using the eq. in Krumholz et al. (2005).

The statistical timescales of the evolution of massive stars is ≈1E5 yr (Russeil et al., 2012; Gerner, 2014), and by assuming a constant accretion rate of ≈1E-4 $\mathrm{M}_\odot$/yr it follows that a massive core can gather ≈10 $\mathrm{M}_\odot$ during its lifetime. The assumption here is that the accretion rates and the feedback are constant in time. Simulations by Peters et al. (2010) demonstrate that in the center the accretion rates are not spherically symmetric and the UCHII region expansion motions are episodic in time. This is corroborated by observations where an episodic outflow motion is detected in the gas.

5.7.3. General remarks

In the source IN, Megeath and Tieftrunk (1999) detected a blue and red wing of an outflow and interpreted the direction of the outflow to be in the northwest to southeast direction. A correction is proposed of the orientation of the outflow axis reported by Megeath and Tieftrunk (1999). The blue wing is part of SM2 and not of IN, whereas the red wing is part of IN. SM2 fragments into several cores (Hunter et al., 2014), and INSMA18 is a HMC in SM2 that might be the driving source for this outflow. In the source I, the outflow approximately perpendicular to the main one (outflowI2) is to faint to be visible in the APEX data. A red lobe is detected southeast of I and is also reported by McCutcheon et al. (2000). Considering the position angle of the blue lobe of outflowI2, the red lobe can thus be associated with outflowI2.

Because outflows produce shocked gas, their impact on the ISM can be seen in H_2 knots. The emission maps at 2.12 μm of NGC 6334I, measured with the Infrared Spectrometer And Array Camera (ISAAC) of the Very Large Telescope (VLT), revealed five H_2 knots (denoted by $\alpha, \beta, \gamma, \delta, \epsilon$; Seifahrt et al., 2008). While the H_2 knots α and β are produced by outflowI1, the H_2 knots γ and ϵ coincide with the detection of the blue and red wing of outflowI2. The H_2 knot δ is probably produced by the blue wing of outflowI1, because the position agrees with the alignment of the ammonia emission at this location (Seifahrt et al., 2008, fig. 6).

The standard deviation of the radial velocities of the cores in the clusters of $\langle v_\mathrm{LSR}\rangle$=1.8 km/s is similar to the average velocity dispersion of the cores $\overline{\sigma}$ =1.6 km/s for I, and is smaller for IN with $\langle v_\mathrm{LSR}\rangle$=1.6 km/s and $\overline{\sigma}$ =2.0 km/s. Similar values for a bigger sample of cores ($\langle v_\mathrm{LSR}\rangle$=1.43 km/s and $\overline{\sigma}$ =2.24 km/s) are derived in source IN by Hunter et al. (2014). From the virial theorem, the dynamical mass is derived as

$$M_\mathrm{dyn} = 3\langle v_\mathrm{LSR}^2\rangle R/\mathrm{G}. \tag{5.13}$$

As is shown by them for the source IN, the calculated dynamical mass is M_dyn = (5.2 ± 3.3)E2 $\mathrm{M}_\odot$ (assuming D=1.7 kpc). This is similar to the dust mass derived from observations (sect. 5.1) and the model of M_tot=564 $\mathrm{M}_\odot$. For source I, only two line-emitting cores are found presently that prevents to derive significant values. By calculating a variance of $\langle v_{\mathrm{LSR}}^2 \rangle$ = (3.1 ± 1.4) km/s for I and an effective radius of 17″, which is the fitted source size and half of the effective radius of IN, the dynamical mass is $M_{\mathrm{dyn}} \approx (3.0 \pm 1.4)$E2 $\mathrm{M}_\odot$. This dynamical mass is again in agreement with the model of M_{tot}=292 $\mathrm{M}_\odot$. Thus, both protostellar clusters are likely to be in a virial equilibrium. In both cluster, the most massive cores (ISMA1, INSMA1) are not found in the center of the cluster, but at the northeastern edge, therefore no mass segregation has occurred yet.

In summary, based on the luminosity and mass of the clusters, it is possible to distinguish their evolutionary stages according to the evolutionary tracks for young massive stellar objects by Molinari et al. (2008). While the younger source IN is in an "accelerating accretion phase", source I has converted most of its gas mass into stellar mass and is now in an "envelope clean-up phase". This classification is corroborated by the different infall motions in both clusters.

The overall infall motion of the clumps is super-sonic and a fraction of the free-fall velocity, in accordance with observations of other HMC sources (Rolffs, 2011). The 1D velocity dispersion derived from the line widths is similar to the standard deviation of the radial velocities of the cores, ≈1–2 km/s. It is concluded that the outer parts of the clumps hinder the direct determination of the infall velocities of the embedded protostellar cores in the center. Similar results are presented by Liu et al. (2013) for the source G10.6-0.4 (observed in the HCN (3–2) transition with SMA), where the cores are embedded in a flattened, rotating disk-like structure. The systematic velocities and the absorption dip of the western cores are red-shifted, whereas the velocities and absorption of the eastern cores are blueshifted, leading to the conclusion that the clump is in an overall collapse and imprints its signatures onto the cores.

An alternative way to determine the kinematics in the closest vicinity of massive protostars (and to derive infall and outflow rates directly) is to utilize molecular maser emission, as described by Goddi et al. (2011).

6. Molecular line survey of hot molecular cores in NGC 6334I and I(N)

6.1. Introduction

The chemical richness of the ISM is visible in spectral line surveys of HMCs. Most of these lines are identified as transitions from COMs, such as CH_3OH. While chap. 5 focuses on the optically thick lines of HCN, HCO^+, CS and CO in the massive protostellar cluster NGC 6334I and I(N), the remaining lines of the spectra are analyzed here. Most of these lines, especially from COMs, originate from the dense center of the core, where the LTE conditions are well approximated such that no sophisticated radiative transfer modeling is necessary. Especially the optically thin, high-energy excited lines, such as vibrationally excited HCN (ν_1=1), trace the most inner part of the core. Although the bandwidth of 8 GHz in the SMA observations is limited, the spectra of the identified cores in the clusters I and IN show a diversity and sensitivity which is good enough to derive some principal properties. Submm line surveys enable to determine reliably the temperature and column density of molecules unambiguously by many lines (Schilke et al., 1999), and enable to find possibly new chemical species.

6.2. Spectral observations

The massive clump IN was added to the CHESS program, and the HSO observing log is given in Table. 6.1. The single-pointing observation was focused on the coordinates $\alpha = 17^h20^m55.18^s$, $\delta = -35°45'03.9''$, which corresponds to the position of the core INSMA1. The core INSMA6 lies at the edge of the HSO beam. Because of the HSO beam size of $\approx 30''$, the single HMCs identified in the SMA observations are not resolved. Thus, the emission of all the cores contribute to the measured intensity in the HIFI spectrum. The core INSMA1 has the brightest line and continuum emission in IN, therefore it is expected that the HIFI spectrum is dominated by this source. Fig. 6.2 presents an overview of the spectrum from 626–801 GHz, which is in comparison to I (see Zernickel et al., 2012) less rich in lines. The continuum slightly increases from 1.5 to 2 K. Fig. 6.1 displays the spectra of the different HMCs from the SMA observations in the lower sideband (LSB) and upper sideband (USB) at a resolution of $\approx 2''$. The number of lines increases from top to bottom, and some optically thick lines have in addition emission from molecular outflows.

Table 6.1.: HSO observing log of NGC 6334I(N).

Band	Freq. range (GHz)	Beam size ($''$)	Date	Obs. time (h)	rms (K)
2a	626–726	31.9	13.09.2011	2.2	0.06
2b	714–801	28.5	13.09.2011	2.0	0.07–0.14

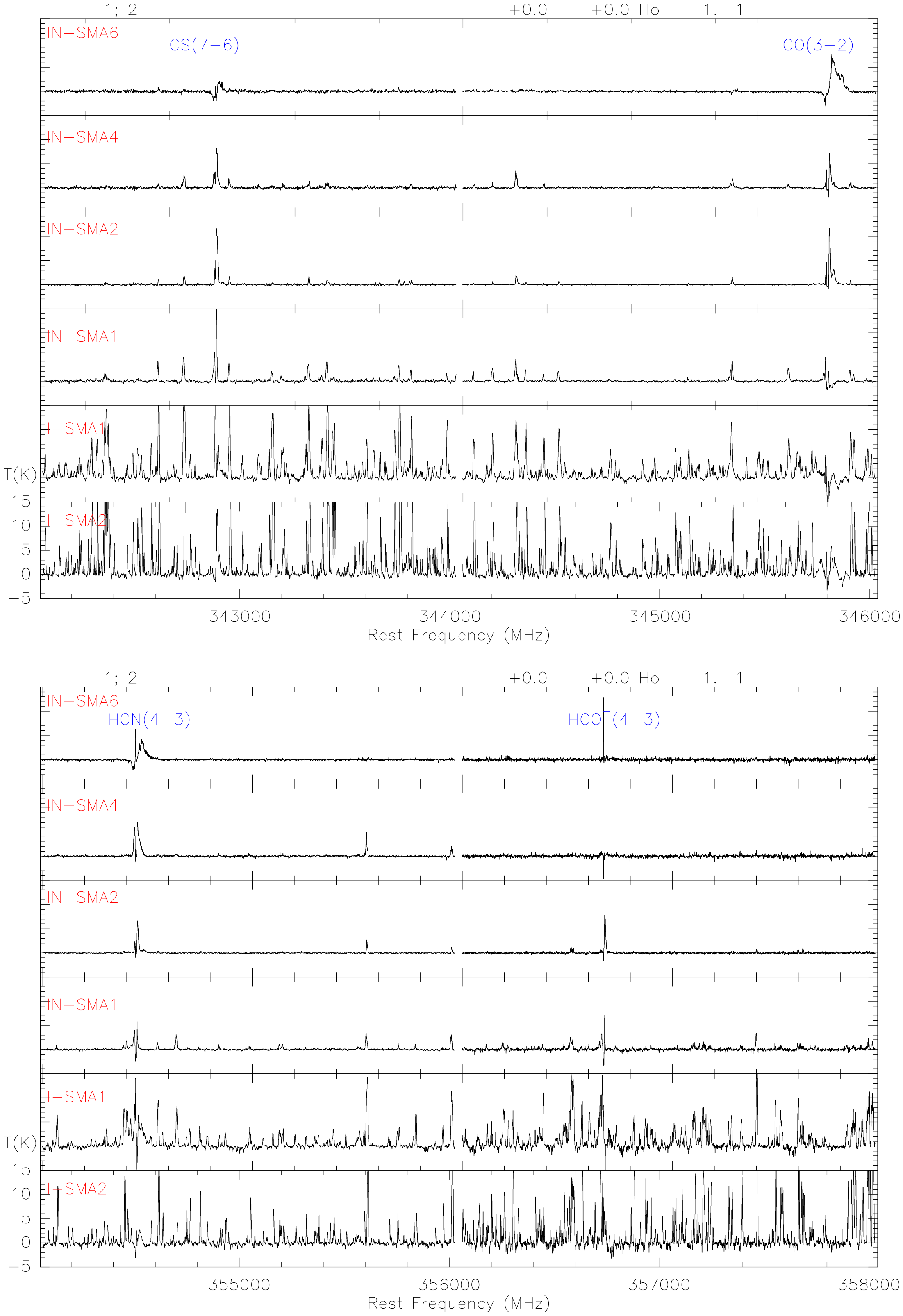

Figure 6.1.: LSB (top) and USB (bottom) SMA spectra toward the protostellar cores in NGC6334 I and I(N). The four most intense spectral lines are denoted in IN-SMA6.

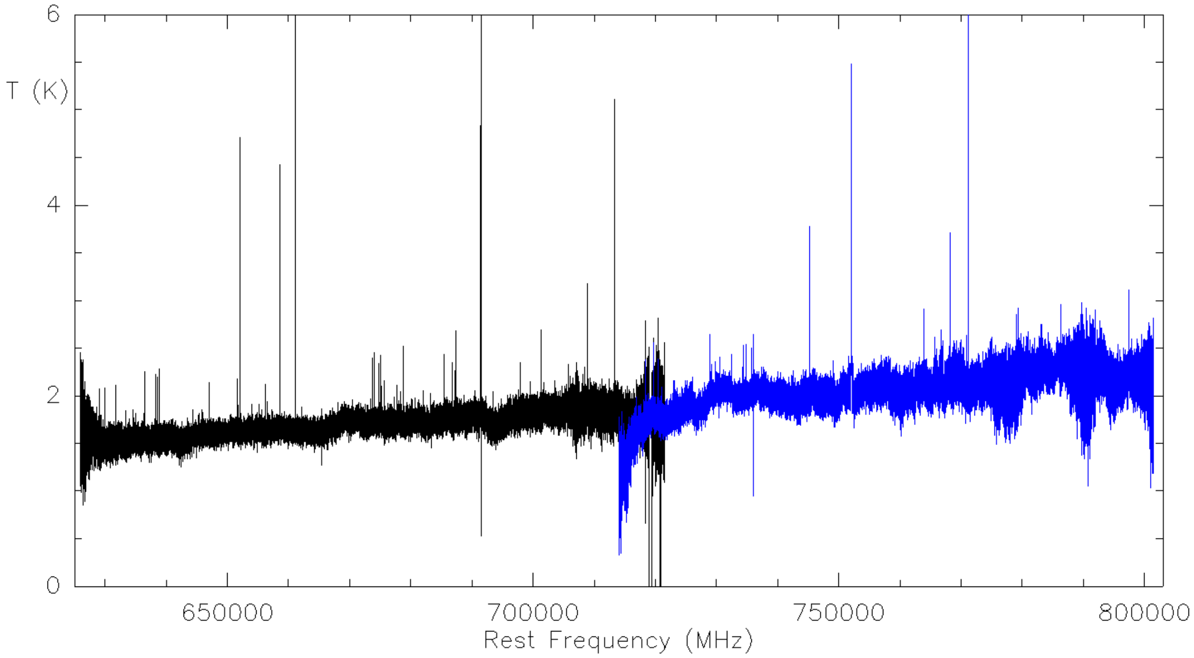

Figure 6.2.: The HIFI spectrum of NGC 6334I(N). Band 2a is colored in black and band 2b in blue, where the overlap is at 720 GHz.

6.3. Analysis: line identification and modeling

Because the center of HMCs is very dense (n=1E7 1/cm^3), the critical density of many transitions is reached and LTE is a good approximation, see fig. 5.9(c). The program `myXCLASS` is used in combination with `MAGIX` to analyze the spectra. This was done with the older `GILDAS` version of `myXCLASS`, and repeated with the newer `CASA` version. The line parameters are taken from the CDMS and JPL catalogs in the old version, and from VAMDC in the new version. One benefit of the VAMDC entries is that the partition function Z is calculated for more temperatures (~100) than in the catalogs mentioned above (~10), which makes thus the temperature derivation more reliable. Other values of $Z(T)$ are interpolated by a continuous polynomial function.

As described in Zernickel et al. (2012), the spectra are modeled by using the detection equation and several parameters:

- the source size Θ to take the beam dilution into account,
- the excitation temperature $T_{\rm ex}$ of the chemical species,
- its total column density N,
- and the line width Δv and radial velocity $v_{\rm LSR}$.

The line profile function is always a Gaussian. The same isotopologue ratios are used as mentioned in chap. 5. For the case of OCS, H_2CO and CH_3CN, only their isotopologues (^{13}C or ^{34}S) are detected in the SMA bands. However, in the following all species are denoted by their main isotopologue. For the clump IN, a dust emissivity index of β = 1.4 is adopted and a dust opacity of $\kappa_{1.3\rm mm}$ = 0.42 cm^2/g. The total hydrogen column density is $N(H_2)$=6.5E24 1/cm^2, which is derived from the average hydrogen density of the model given in table 5.4 and a source size of 10″. The beam size is given by the diameter of the telescope inside `myXCLASS`, and thus an effective diameter of 103 m is used for the synthesized beam of 2.1″ of the SMA observations.

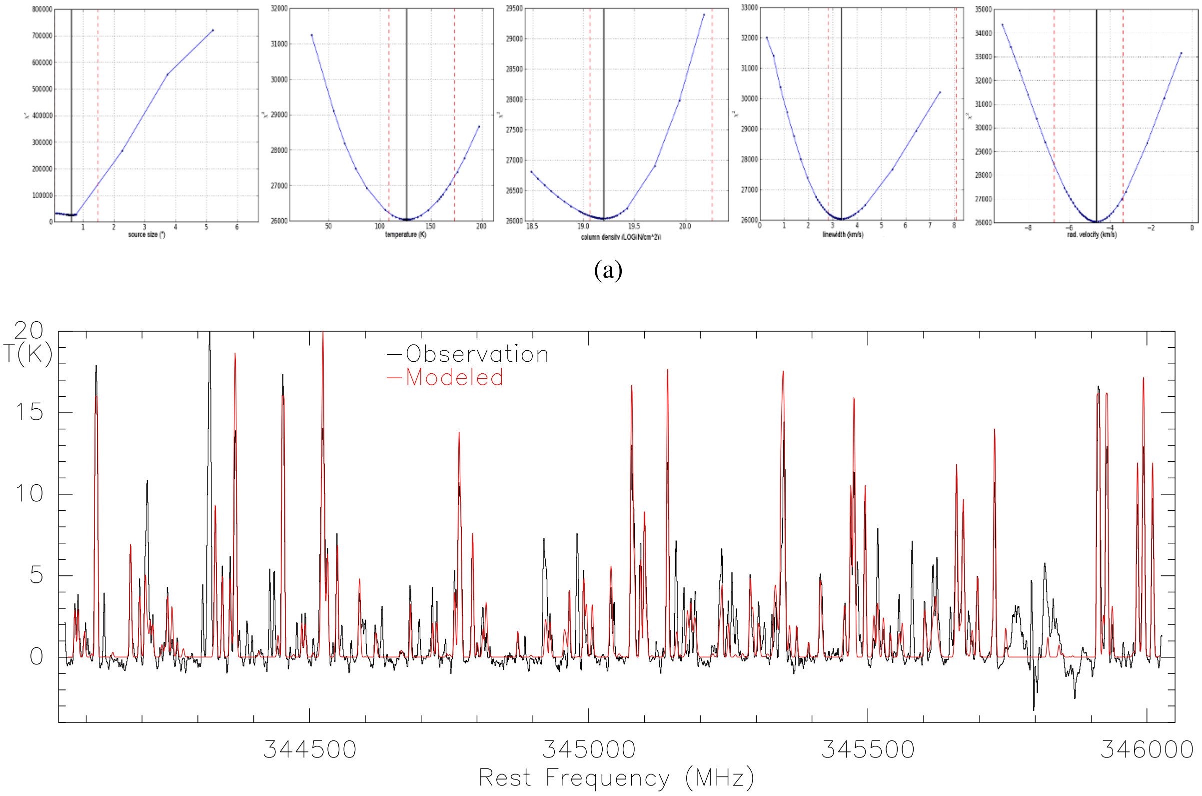

(a)

(b)

Figure 6.3.: (a) χ^2 values of methanol in ISMA1. The black line marks the minimum and red line the error ranges for each parameter. (b) A selection of the modeled spectrum in LTE in comparison to the observed spectrum in ISMA2.

As can be seen in fig. 6.2, the baseline is not always flat and is affected by sinusoidal features. For the fitting of one molecule, it was therefore decided to extract all the spectral lines of it in a narrow window, to fit and subtract a baseline of polynomial order ≤ 5, and to extracted these parts. Because the sources I and IN have a projected distance of $\approx$1 pc, it can be assumed that the chemical composition is not much different and mainly a result of evolutionary stage differences. Therefore, a template is used for the line identification from previous results obtained for source I by Zernickel et al. (2012). In some cases it is necessary to add additional components to improve the fit for one molecule. This component in the LOS is for example a different velocity component, an outflow, or emission from a less optically thick region (envelope + core). If the source size θ is difficult to estimate from the fitting procedure because of degeneracies, the source size is derived from integrated line emission maps, which is typically 2–4″.

The optimization with `MAGIX` is done by using a chain of three fit algorithms: the genetic, the Levenberg-Marquardt and the interval nested-sampling algorithm. The first one is used to explore the χ^2 landscape globally within a given range, the second one is a local optimizer to get the best values at the minimum, and the third one is used for the error estimation. The advantage of the usage of global fit algorithms (to the disadvantage of many calls) is that they can find several local minima and therefore avoid to get stuck in one local minimum. The uncertainty usually scales inversely with the number of lines of a molecule, and is given for the 3σ interval (i.e., for a confidence interval of 99.7%, where σ is the standard deviation). If lines are heavily blended, the SNR is low, or the fit results are bad, the parameters are adjusted manually (in this case no error is listed). Because the entries for Acetone (CH_3CH_3CO) are currently still missing in the VAMDC, they are not included in the new version and the values from older fits are reported. Fig. 6.3(b) illustrates an example of the simulated spectra fitted to the observed one in ISMA2, wheres Fig. 6.3(a) shows the χ^2 landscape of the five parameters of methanol in ISMA1. As can be seen, the source size is not determinable for small values, and for strong asymmetric shapes or to large boundaries one limit of the error is overestimated. In these cases the smaller error is reported.

6.4. Results

6.4.1. HIFI spectrum

In the HIFI spectrum, almost all lines could be identified. Only several weak emission and absorption lines remain unidentified. By using a detection threshold of 5×rms, no unidentified line remains. This is in contrast to the SMA spectra of the cores ISMA1 and ISMA2, where about 10–20% of all lines are unidentified. A total of 15 molecules with their isotopologues are identified in the HIFI spectrum of IN, where the best fit parameters for each molecule and component are given in table 6.2. The average source velocity is (-4.1 ± 0.1) km/s and average line width (4.4 ± 0.3) km/s. Additional to the Gaussian profile, the following molecules have broader emission at higher velocities which can be attributed to outflow motions: CO, HCN, SO and H_2O. As described in chap. 5, the asymmetric line profiles in HCN and CS are due to infall motions. The most optically thick lines of CH_3OH, H_2S and CO show self-absorption. The lower relative abundance of HCN and CS of 2E-9 in comparison to the values of chap. 5 are most likely a result of the high optical depths. The fitting of CO lines includes the isotopologues ^{13}CO, $C^{18}O$ and $C^{17}O$. For HCO^+ and $H^{13}CO^+$, only the transition J=8–7 is detected so that the temperature is uncertain. The same is true for H_2O, where only the line J=2(1,1)–2(0,2) is detected.

6.4.2. SMA spectra

The best fit parameters for each molecule in the SMA spectra are given in table 6.3 and 6.4. Missing values in a cell mean either that this molecule is not detected, or that it is blended with other species so that no meaningful value can be derived. Because INSMA6 shows no line emission except of CO, CS, HCN and HCO^+ (which are also contaminated by outflow emission), this core is not included. A visualization of these numbers as histograms are shown in fig. 6.4 and fig. 6.5. In general, the cores in IN have lower total column densities than the ones in I. The temperatures are about 100 K, which are typically for HMCs. Although the emission is weak in INSMA4 and INSMA2, they both reach temperatures above 100 K. The weak line emission is therefore not due to lower temperatures but due to lower column densities. Similar to the HIFI spectrum, some methanol lines show self-absorption toward the core INSMA1. The source sizes, except of H_2CO, are mostly smaller or equal to the beam size $\Theta \leq \Theta_B$, which is in

Table 6.2.: Best fit results for the HIFI spectrum of NGC 6334I(N)

Species	Θ	T	N	$\frac{N}{N(H_2)}$	Δv	v_{LSR}	Notes
	($''$)	(K)	(1/cm^2)		(km/s)	(km/s)	
CH_3OH	1.4(1.7)	77(15)	5(4)E17	8E-8	5.5(1.0)	-3.7(1.0)	c1,opt. thick
CH_3OH	2.5(3.0)	52(15)	7(6)E16	1E-8	2.1(8)	-4.2(1.0)	c2
N_2H^+	ext	39(1)	1.6(1)E13	2E-12	3.4(3)	-4.1(2)	opt. thin
SO	*7.0	65(21)	3(8)E15	5E-10	14(2)	-6(1)	opt. thin
H_2CO	3.7(1.7)	77(12)	4(2)E15	6E-10	5.6(9)	-3.6(8)	
HCO^+	ext.	22(8)	1(2)E15	2E-10	5(1)	-4(1)	$H^{13}CO^+$
NO	ext.	74(16)	3.1(7)E14	5E-11	4.7(1.0)	-5.3(8)	
CN	ext.	24(9)	1.7(8)E13	3E-12	2(1)	-4(2)	opt. thin
H_2S	ext.	48(12)	5(10)E14	7E-11	6(1)	-4(1)	c1
H_2S	ext.	9(5)	2(4)E15	3E-10	4(1)	-4(1)	c2,absorp.
H_2O	5(4)	2.4(2)E2	3(5)E16	4E-9	10(1)	-3.5(8)	c1
H_2O	7(6)	1.1(2)E2	2(5)E16	3E-9	38(6)	-6.0(9)	c2,outflow
H_2Cl^+	ext.	11(6)	5(2)E13	8E-12	3(1.5)	-1.5(1.5)	absorp.
CO	ext.	52(11)	1.0(4)E19	2E-6	5(1)	-4(1)	+isotop.
HNC	ext.	48(13)	1.1(3)E12	1E-13	2.8(9)	-4(1)	opt. thin
CH_3OCH_3	1.6(3)	42(5)	1.6(5)E17	2E-8	4.8(7)	-4.0(7)	
CS	5.3(2)	69(13)	2(4)E16	2E-9	9(3)	-4(1)	opt. thick
HCN	5.3(3)	36(15)	1.3(3)E16	2E-9	11(1)	-5.1(7)	$+H^{13}CN$

Asterisks denote fixed vales, "ext." denotes extended emission and c1/c2 the two component. The corresponding symmetric errors of the last digit are given in brackets. The columns denote: source size Θ, excitation temperature T, column density N, line width Δv, and radial velocity v_{LSR}.

agreement with the radius of r<2000 au or $r<1''$ in the HMC model (fig. 5.9(b)), supposing that the emission comes from a region $T \geq 100$ K.

The distribution of the line and continuum fluxes, together with the kinematic properties, are listed in fig. 6.4. These mean values are derived from table 6.3 and 6.4. The line-to-continuum flux ratios in fig. 6.4(a) demonstrate that there is no general trend or correlation between the line emission luminosity and dust continuum emission, which therefore indicates that the chemical abundances do not increase linearly. The core ISMA2 has the highest line-to-continuum ratio with over 50%. The kinematic information in fig. 6.4(b) are used and discussed in chap. 5 for the radiative transfer modeling. The average line width is ca. 5 km/s and therefore all these cores must undergo a super-sonic or turbulent accretion scenario. The only exception is the core INSMA6, which has a narrow line width of only 1.6 km/s or two velocity channels, but drives an outflow with a broad line width of 62 km/s.

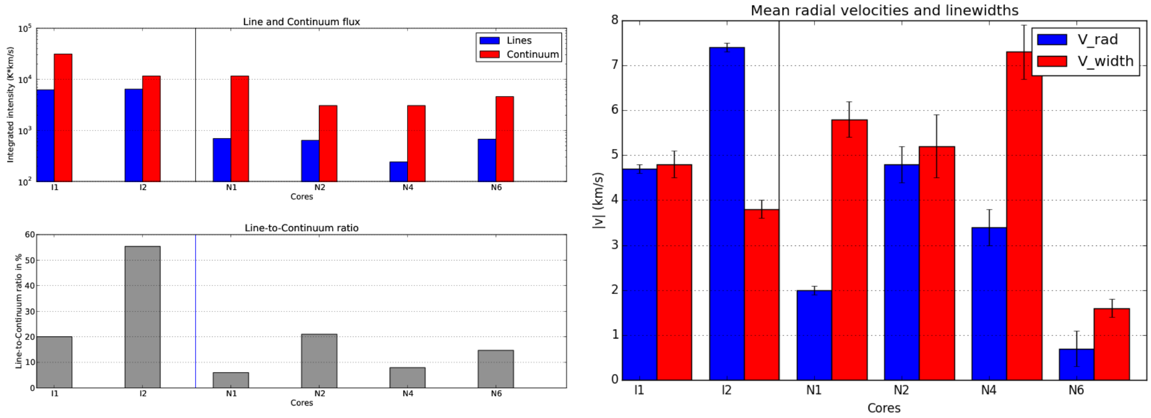

(a)

(b)

Figure 6.4.: (a) The line and continuum emission of cores in NGC 6334I and I(N), and their ration. (b) Central radial velocities and line widths of the cores. The error bars show the dispersion of the different molecules.

Table 6.3.: Best fit results for cores in NGC 6334I

Molecule	ISMA1					ISMA2				
	Θ	T	N	Δv	v	Θ	T	N	Δv	v
	($''$)	(K)	(1/cm^2)	(km/s)	(km/s)	($''$)	(K)	(1/cm^2)	(km/s)	(km/s)
CH_3OH	0.7(8)	126(32)	1.6(5)E19	3.4(5)	-5(2)	1(1)	118(16)	2.1(4)E19	3(1)	-8(1)
CH_3OCH_3	1(1)	109(24)	6.3(7)E17	4(1)	-5(1)	1.2(8)	120(27)	1.8(1)E17	5(2)	-8(1)
CH_3OCHO	1(1)	104(25)	6.8(8)E17	4(1)	-5(1)	1(1)	110(20)	8(3)E17	3(1)	-7(1)
H_2CS	1(1)	113(32)	5(2)E16	5(2)	-5(2)	2(1)	121(30)	1.2(2)E16	4(1)	-8(1)
H_2CO	ext.	161(40)	2.6(9)E16	6(1)	-5(1)	ext.	80(52)	2.3(8)E16	5(2)	-7(1)
SO_2	0.8(5)	105(13)	4(1)E16	6(1)	-4(1)	1(1)	194(27)	5(2)E17	3(1)	-7(1)
HC_3N	2	67(25)	6.0(1)E15	8(2)	-5(2)	2	37(6)	7(10)E16	9(2)	-9(2)
CH_3CHO	2	253(51)	5(2)E15	5(1)	-5(2)	2	100(34)	2(1)E15	6(2)	-8(2)
C_2H_5OH	0.4(2)	116(31)	2(1)E17	4(1)	-4(1)	1(1)	87(29)	6(2)E16	3(1)	-8(1)
H_2CCO	2	206(32)	7(3)E15	6(2)	-5(2)	2	180(31)	5(1)E15	4(1)	-8(1)
C_2H_5CN	0.6(5)	158(29)	1.9(8)E16	8(1)	-5(1)					
CH_3CN	2	154(26)	3.4(7)E16	5(1)	-5(1)	2	100(33)	1.2(7)E16	3(1)	-7(2)
CH_3CH_3CO	2.1	93	8.30E15	4	-4.9	2.1	125	1.6E16	3.8	-7
OCS	2.5	50	2.10E18	4.9	-4.9	2.5	52	1.2E18	3.8	-7.4
NH_2CHO	2(2)	254(55)	5(5)E15	9(3)	-3(2)	1(1)	305(45)	3(1)E16	3(1)	-9(2)
C_2H_4O	1.1	45	7.70E15	4.1	-5	1.2	64	1.2E16	3.4	-7.3
HCOOH	2	250(10)	2(1)E16	7(1)	-8(1)	2	50(22)	4.1(3)E16	4(1)	-8(2)
HCNO						2	122(40)	2.0(8)E13	1(1)	-7(2)
SiO						2	155(33)	2.1(1)E14	1.6(9)	-4(2)
$(CH_2OH)_2$	1	150	2E16	4.3	-4.9	6(3)	140(37)	5.8(7)E15	4(1)	-8(2)
CH_3NH_2	2	166(24)	1.8(9)E16	8(3)	-2(1)					

Table 6.4.: Best fit results for cores in NGC 6334I(N)

Molecule	INSMA1					INSMA2					INSMA4				
	Θ	T	N	Δv	v	Θ	T	N	Δv	v	Θ	T	N	Δv	v
	(″)	(K)	(1/cm^2)	(km/s)	(km/s)	(″)	(K)	(1/cm^2)	(km/s)	(km/s)	(″)	(K)	(1/cm^2)	(km/s)	(km/s)
CH_3CHO						ext.	31(13)	8(4)E14	4(2)	-4(2)					
CH_3OH	0.4(1)	115(30)	1.5(4)E18	4(1)	-2(2)	0.5(5)	52(17)	5(3)E17	4(1)	-4(1)	0.3(1)	125(24)	7(1)E17	5.5(9)	-3.5(1.0)
CH_3OCH_3	2	78(29)	1(1)E16	5(2)	-3(2)	0.3(3)	72(25)	2(2)E17	3(1)	-4(1)	2	77(29)	2.1(7)E15	6.1(1.5)	-2.9(1.4)
CH_3OCHO	2(2)	130(30)	1.0(3)E16	6(1)	-2(1)	2	250(50)	3(2)E15	5(1)	-4(2)	2	119(23)	2(1)E15	9(2)	-4(1)
H_2CS	0.8(8)	100(30)	1.2(6)E16	5(1)	-2(1)	2	70(26)	8(2)E14	6(2)	-5(2)	2	67(14)	1.1(3)E15	8(1)	-3(1)
H_2CO	ext.	153(24)	9(2)E15	6(1)	-2(1)	ext.	40(20)	2(1)E15	5(2)	-3(1)	ext.	70(12)	1.4(3)E15	4(1)	-5(1)
SO	3(3)	270(50)	1.7(5)E15	7(1)	-3(1)	2	100	5(2)E14	8(2)	-6(2)	2.1(9)	127(77)	1.3(5)E15	8(2)	-4(1)
C_2H_5OH	2	164(54)	2(2)E14	3(2)	-4(2)	2	64(30)	5(2)E14	4(1)	-4(2)					
SO_2	2	125(38)	9(2)E14	9(2)	-3(1)						2	132(29)	9(4)E14	9(2)	-2(2)
HC_3N	2	113(30)	5(3)E14	9(1)	-2(2)						2	36(15)	8(8)E15	9(2)	-3(2)
H_2CCO	4(4)	160(100)	6(3)E14	6(1)	-1(1)										
C_2H_5CN	2	104(34)	7(3)E14	5(1)	-2(1)										
CH_3CN	2(2)	99(26)	5(2)E15	7(2)	-2(2)										
CH_3CH_3CO	2.1	103	1.3E15	6	-2										
OCS	2	65(25)	8(5)E16	3(1)	-2(1)										

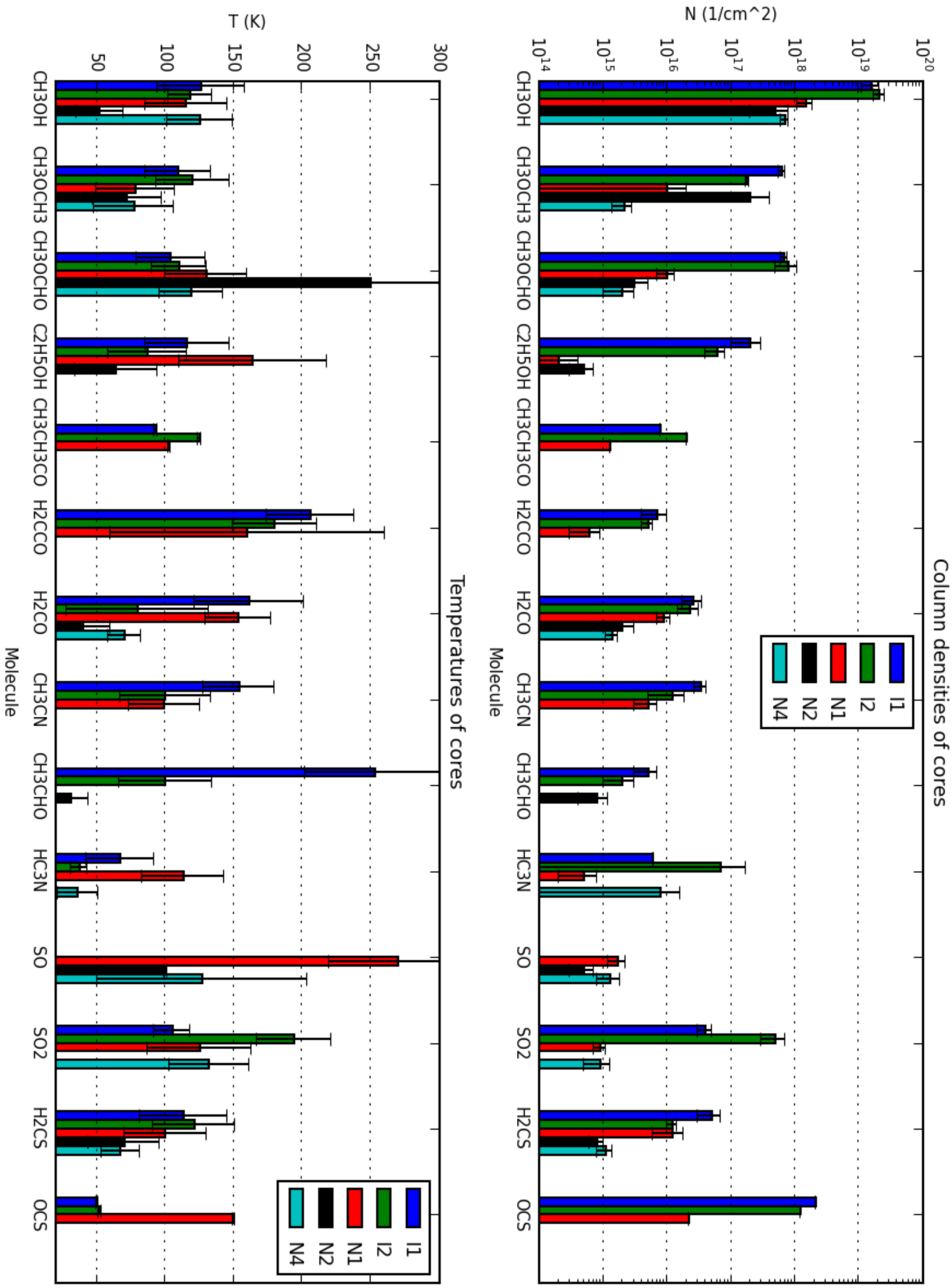

Figure 6.5.: Column densities (top) and temperatures (bottom) of different molecules for each core. The values are taken from the tables 6.3 and 6.4.

It was noticed that the radial velocity of COMs and other molecules are not always the same but vary for some cores. Because of opacity, temperature and velocity gradients in the cores, this is to some extend not surprising. The highest variation is presented in fig. 6.6 for the core ISMA2, where the Pearson correlation coefficient is R=0.4 between the radial velocity and temperature for all molecules. A similar trend was checked for the upper energy level of single lines of SO_2 in dependence of the velocity, which is because of blended lines and a smaller number less significant and not shown here. In general, the velocity increases from −8 km/s at 40 K to −7 km/s at 200 K. There are several possibilities for the explanation of this relation. Assuming a collapsing core with an asymmetric blueshifted infall profile, where the profile is not well resolved, the peak of the profile should be skewed in velocities when tracing the emission from the inner center at different opacities. However, this relation is not reproducible and in agreement with the model, because only a shift between the density and temperature peak can reproduce fig. 6.6. Another explanation is therefore a further fragmentation of core ISMA2 into a multiple system such as a binary with different physical properties, or a rotating inclined torus. Indeed, sub-arcsecond observations of the nearby core ISMA1 with VLA at cm wavelengths reveal a further substructure (Hunter et al., 2013) .

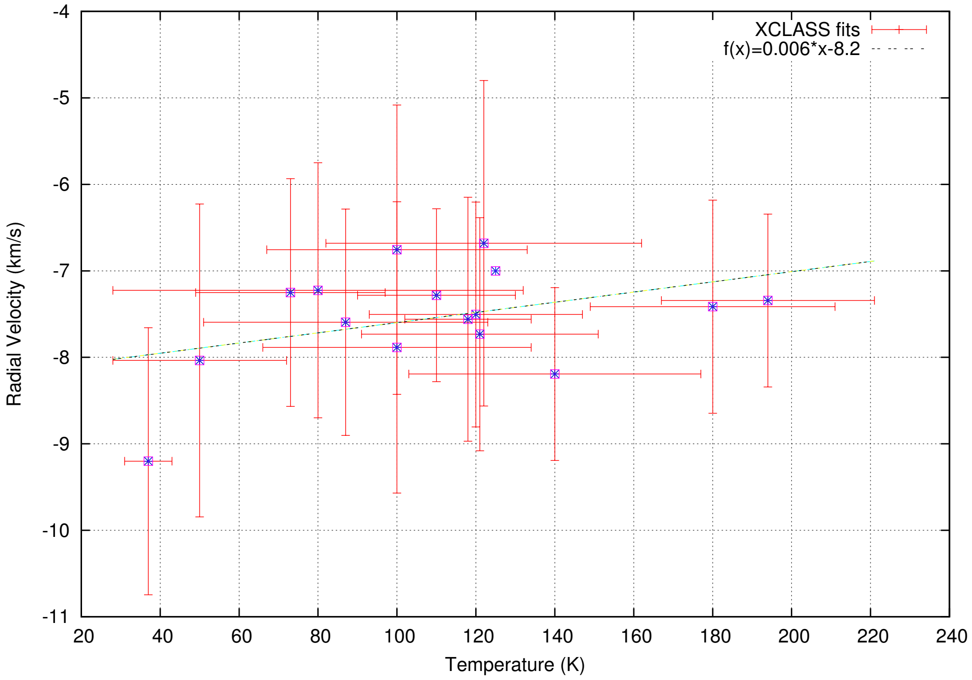

Figure 6.6.: The temperature-velocity relation in the core ISMA2 for all molecular tracer. A best linear fit to the data points is shown for comparison.

6.5. Discussion

A single-dish line survey of the source I is presented by McCutcheon et al. (2000) in table 2 in the frequency range 334–348 GHz, which overlapps with the range of the SMA observations in the LSB. All their line identifications are confirmed here, except of C_2H_3CN which is blended with CH_3OH, and more species are detected here owing to the lower beam dilution.

Zernickel et al. (2012) pointed out that there is a chemical differentiation between the cores ISMA1 and ISMA2, where more oxygen-bearing species arise or show dominant emission in ISMA2 and more nitrogen-bearing species in ISMA1. The results in the band 350 GHz confirm this trend partly: the species HCOOH, NH_2CHO, and C_2H_4O have either a higher temperature T or column density N (or both) in ISMA2 than in the neighboring core, whereas C_2H_5CN and CH_3NH_2 is only detected in ISMA1. In the case of the cores in I(N), it is noticeable that acetaldehyde (CH_3CHO) is detected in the fainter HMC INSMA2, but not in INSMA1.

As the source size could not always be determined well, there is some scatter in the values. For optically thin lines, the source size and column density can be degenerated. The relative abundance ratio is therefore calculated by multiplying the area given by the source size Θ with the column density to give the total number of molecules, $N_{\text{tot}} = \pi\Theta^2(\text{cm}^2)\times N(1/\text{cm}^2)$. The source size for species with extended emission such as H_2CO is set to 4″(twice the beam size).

The results here are compared with results from observations of Bisschop et al. (2007) and from chemical models of HMCs by Choudhury et al. (2015) in fig. 6.7. To reduce the uncertainty in the molecular hydrogen column density (which is more difficult to obtain) and therefore relative abundances of other molecules to it by $X(Y) = N(Y)/N(\text{H}_2)$, the ratios relative to CH_3OH are used, where then $N(\text{H}_2)$ cancels out. The calculation of the fractions has still the underlying assumption that the molecules are emitted from the same region in the LOS. It is noticeably that ISMA1 and ISMA2 have similar ratios (within the error bars) in CH_3OCHO, C_2H_5OH ,CH_3CH_3CO, and H_2CO. The same is true for the cores in IN considering CH_3OCHO and H_2CO. Furthermore, the similar ratios for cores within I and IN indicate that they are related to each other, either by an evolutionary age or chemically by the formation out of the same gas content. All the cores in IN fall into the ranges given by Bisschop et al. (2007), whereas the ratios of the HMCs in I are in general below. The ranges given by Choudhury et al. (2015, table 7), which are derived from astrochemical models of a HMC at ages of 8–1E5 yr, are in agreement with CH_3OCH_3 in ISMA1 and in CH_3OCHO with ISMA1 and ISMA2, whereas the abundance of C_2H_5OH is slightly underpredicted.

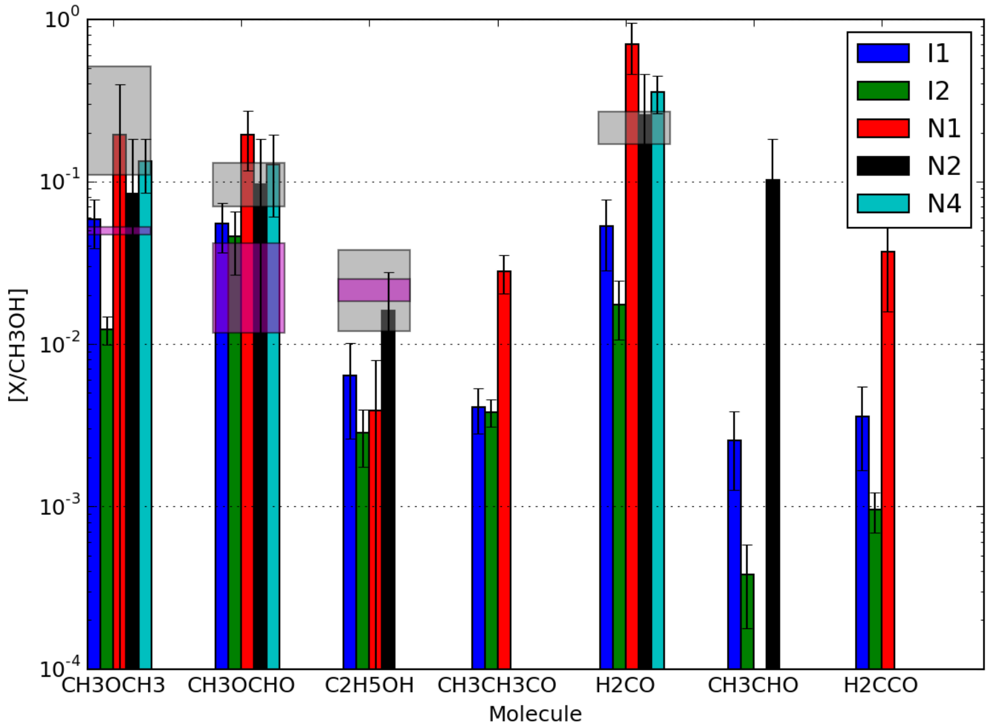

Figure 6.7.: The abundance ratios of COMs relative to CH_3OH for different cores in I and IN. The boxes in gray denote ranges given by Bisschop et al. (2007), and in magenta by Choudhury et al. (2015).

7. Discussion

7.1. Conclusion

In the following, the main results are discussed concisely and by chapter, and possible extensions of the work are outlined.

1. The dynamics of the main filament is explained by a collapsing motion. A comparison with MHD simulations could explain under which different conditions filaments form and collapse. The initial parameters should be set similar as in NGC 6334, i.e., a large gas mass reservoir of 1E5 $M_\odot$, a strong homogeneous magnetic field and possibly already evolved HII regions at the boundaries. From an evolutionary point of view, it is still difficult to distinguish if the HII regions triggered a further cycle of star formation or if they are a natural previous consequence of the star formation activity in the GMC and are disrupting the remaining gas. Synthetic observations of MHD simulations, also in velocity space by using a particular molecular line tracer, will make a direct comparison with observations easier.

2. The molecular line observations of NGC 6334 in the isotopologues of CO allowed the first time studying kinematically the whole region at a good angular resolution and to complement previous observations in continuum and other tracers (which often mapped this region only partly). The PVD demonstrates that there is a large velocity coherent structure over the whole cloud of 60 pc, extending to the more evolved giant HII region NGC 6357. The motions on small scales of 1 pc are complex and dominated by turbulence, which demand therefore preferentially for a statistical analysis. A closer inspection at the vicinity of the various clumps in this region is laborious, and therefore requires an automatic routine. As is shown by depicting one IRDC or filament in detail, a higher sample of several filaments will allow drawing better statistical conclusions. As stated by Tackenberg (2013), massive star-forming regions must be replenished by gas from their environment. Some accretion flows were observed by him as velocity gradients, and are also found in this work. Homogenous gas mass flows, as a result of the accretion of diffuse gas onto filaments, are found only partly and mainly in the cold eastern part of NGC 6334. The interpretation of some velocity gradients is ambiguous, as they can be produced also by rotation or outflow motion besides of gravitational attraction. One reason for this circumstance is that NGC 6334 is in an already evolved stage, so that younger sources similar to HMPO might be a better target. Furthermore, different historical impacts such as HII regions or collisions make it difficult to trace a gas particle from scales of the GMC down to a HMC. A consistency over all scales, at least for the cluster NGC 6334I(N), is only found in the alignment of the magnetic field.

Planck Collaboration (2015) presented for a sample of nearby molecular clouds a study between the orientation of B_z and the density structures in $N(\mathrm{H})$, where a systematic change with $N(\mathrm{H})$ is found from parallel alignment at the lowest to perpendicular alignment at the highest column densities. The change occurs at $\log_{10}(N(\mathrm{H})/\mathrm{cm}^2) \approx 21.7$. The fact that most of the dense gas in these clouds are orientated perpendicular to the magnetic field suggests that these clouds have formed by material accumulation and gravitational collapse along the magnetic field lines, and implies that their turbulence is trans- or sub-Alfvénic and anisotropic. Colliding flows or gas compression by shocks in a magnetized ISM along the field lines lead to massive clouds, which will later on loose the information about the inflows because the magnetic field redistributes the kinetic energy (Heitsch et al., 2009). All these trends fit into the case of

NGC 6334, where the connection to the velocity information shows that a preferential number of velocity gradients is aligned parallel to the magnetic field. Observations of the more diffuse gas in ^{12}CO or other tracers of this region would be necessary to confirm these results further.

3. The SMA observations revealed that different line opacities are needed to fully trace all structures of the clumps in the LOS. The combination with the additional single-dish observations at different scales are beneficial to restrict the parameter ranges. The 3D modeling gives a better understanding of the source structure, but the vast amount of parameters must be selected carefully. Both radiative transfer codes demand a high computational power. The new published version of `LIME` in 2014 with the capabilities of parallelization was therefore a high benefit and accelerated the fitting progress, i.e., the comparison of an ensemble of simulations with the observations. The determination of the infall velocity and mass accretion rates at the most inner center is still very difficult from an observational point of view. Because the envelope dominates the absorption dip in the interferometric observations, it was not possible to verify or differentiate between the two theories monolithic collapse and competitive accretion. One possible solution is the usage of masers, but it is not clear what is their physical origin (boundaries of HII regions, disks, outflows?), and therefore what part of the cloud they are tracing. An improvement of the model could be achieved by relating it to astrochemical calculations. The relative abundances of molecules in dependence of temperature and radius might not be a step function, but more continuously varying (see for example Bruderer et al., 2009). By combining the radiative transfer calculations with astrochemical codes, such as `SAPTARSY` (Choudhury et al., 2015), it will be possible to study the spatio-temporal evolution of molecular abundances and compare it with spectra of HMCs. In general, the static model could be improved by comparing it with different physical realizations from the literature and implementing more time-dependent dynamics, such as outflows or shocking events, while taking into account mass and energy conservation.

4. A comparison with other massive star-forming regions, such as SgrB2, W43, or Orion-KL, could reveal if the results obtained for NGC 6334 are unique or universal. The disadvantage is that other sources are more far away (except of Orion), which make a direct comparison more difficult. Another aspect that can be studied this way is the role and impact of the environment, as it is known that the Galactic center has extreme conditions.

7.2. Outlook

Like in many other fields, the research in astronomy was propelled by the progress of technology and instruments. The extreme amount and exponential increase of data volumes, e.g., from large surveys acquired by future instruments, MHD computer simulations and multi-dimensional radiative transfer models, make it necessary to go to the limit of the present computational power. It is therefore necessary to parallelize available codes, to explore the capabilities of graphic processing units and to develop intelligent algorithms to exploit the data. Therefore, astrophysics is together with other sciences at the front line of big data science.

Different surveys are on their way or are being accomplished at the moment: THOR (The HI/OH/Recombination line survey of the Milky Way), THRUMMS (Three-mm Ultimate Mopra Milky Way Survey) in the J=1–0 transition of ^{12}CO, ^{13}CO and C^{18}O, SEDIGISM (Structure, Excitation, and Dynamics of the Inner Galactic Interstellar Medium) with APEX covering the ^{13}CO (J=2–1) line, CHaMP (The Galactic Census of High and Medium-mass Protostars) with the NANTEN telescope with a similar frequency coverage as THRUMMS, and CLASSy

(CARMA Large Area Star Formation Survey, Storm et al. 2014) targeting the Perseus and Serpens molecular clouds. Similar to the goals of CLASSy, the famous nearby star-forming region Orion-KL is mapped with the CARMA interferometer in ^{13}CO, together with the Nobeyama 45m radio telescope, to study filaments at high-angular resolutions and to see if or how these filaments fragment into fibers and strings of cores or not.

Several new generation telescopes are on their way to be completed or to be built in the next couple of years, namely SKA, CCAT, SOFIA and ALMA. SKA (Square Kilometer Array) is a planned radio interferometer with an effective collecting area of 1 km^2 and a max. baseline of 3000 km (Carilli and Rawlings, 2004). In the context of star formation, SKA will improve the study of the HI line, of ionized gas in HII regions, of radio jets by using radio recombination lines and masers, of the magnetic field through Zeeman measurements, and of the star formation history in the early universe. CCAT (Cerro Chajnantor Atacama Telescope) will be a 25 m single-dish telescope (Woody et al., 2012). With a high surface accuracy of rms$\leq$ 10 μm, it is designed especially for the wavelengths 200–2200 μm to explore lines in the THz window.

The Stratospheric Observatory For Infrared Astronomy (SOFIA, Young et al., 2012) is an airplane telescope with a 2.5 m dish on-board and a successor of the Kuiper Airborne Observatory (KAO, operated from 1974–1995). Is is destined to observe in the THz regime with lines such as high-J CO lines, CII at 158 μm or OI at 63 μm. The instrument UPGREAT (upgrade of the German Receiver for Astronomy at THz Frequencies) is a multi-pixel high-spectral resolution heterodyne receiver which will enable to conduct OFT-maps efficiently. Together with CI and CO, the additional CII information allows deriving the carbon mass content in a cloud in the different states of matter (molecular, atomic, ionized) and to study how filaments form and gain in mass. This was executed by Beuther et al. (2014) for a sample of IRDC, which probably formed by converging gas flows. A similar attempt will be done in Orion-KL with a sample of filaments, where the CO lines will be complemented by maps in CII and CI (at 492 GHz) from successful proposals for SOFIA and APEX, respectively.

The full capabilities of ALMA will be completed in the next years, and at the end the highest resolution will be $\approx$0.01$''$ at submm wavelengths with a max. baseline of 16 km. In context of massive star formation, ALMA is capable to observe the fragmentation of massive clusters and distant galaxies. The resolution will be high enough (<200 au) to detect discs around massive stars or not. If they exist the same way as in low-mass stars, and at what sizes and timescales, is still debated. With the unprecedented capabilities of ALMA, high-angular and high-spectral resolution observations of protostellar clusters will provide extended insights into massive star-formation. With its high sensitivity, it will be possible to detect low-mass cluster members down to <1 M$_\odot$. The young cluster NGC 6334I(N) is well suited for this purpose, because it is shown by Hunter et al. (2014) that it contains at least 20 cores. Fig. 7.1 presents simulated ALMA observations of the cluster NGC 6334I(N), in comparison to SMA observations with similar outputs as in this work (chap. 5). Both have an integration time of 2 h and a bandwidth of 2 GHz at 350 GHz. The final noise in the deconvolved image is 66 mJy/beam with SMA and 1 mJy/beam with ALMA (in the configurations C34-7+C34-3+ACA). This improvement by two order of magnitudes in sensitivity would improve the census of cores and a derivation of the CMF, which was made by Rodón (2009) for other massive protoclusters.

ALMA will also push the frontiers for astrochemical detections. As the emission of COMs in HMCs stem from a very small region, single-dishes lack the resolution. Recently, the branched alkyl molecule iso-propyl cyanide (i-C_3H_7CN) was found by Belloche et al. (2014) in SgrB2

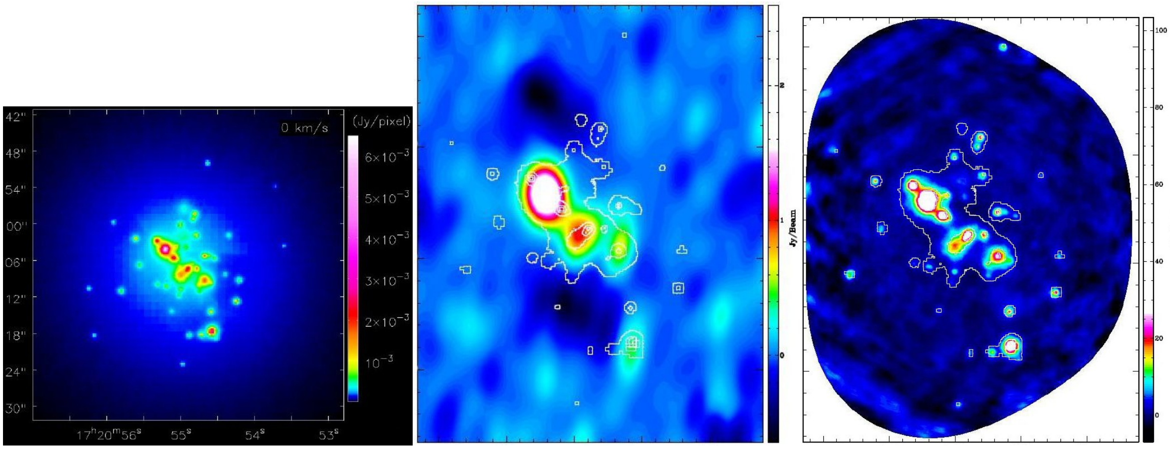

(a) Model (b) SMA obs. (c) ALMA obs.

Figure 7.1.: ALMA simulated continuum observations of NGC 6334I(N) at 350 GHz. The model (a) is observed with SMA (b) and with ALMA (c). The white contours of the model are overlaid for comparison.

with ALMA, which makes the presence of amino aids, the building blocks for life, more likely. Thus, spectral line surveys as described in chap. 6 will provide one possibility for new detections of chemical species.

From a scientific point of view, the gravo-turbulent paradigm of star formation becomes more and more accepted, because it can explain many aspects of the IMF. However, the Jeans criterion demands for overcoming at least three barriers to set in gravitational collapse: the kinetic energy (or thermal pressure), the angular momentum and the magnetic flux. Theoretically, many questions remain open in the field of (massive) star formation. At a conference in 2014, the following points were discussed and remain open:

1. What is the origin of the ISM turbulence: shocks, super-sonic motions?
2. What is the original shape of the IMF, and what is the relation to the CMF?
3. How are molecular clouds formed: by converging flows, or cloud-cloud collisions which lead to cluster formation?
4. Why is the star formation efficiency so low: is it because of outflows, feedback, photodissociation?
5. Is star formation a slow or a fast process, and what environments affect the timescale?
6. What is the role of the magnetic field: could it channel the gas flows?

Bibliography

Publications with more than 10 authors are abbreviated with et al.

André, P., Men'shchikov, A., Bontemps, S., et al. (2010). From filamentary clouds to prestellar cores to the stellar IMF: Initial highlights from the Herschel Gould Belt Survey. *A&A*, 518:L102.

André, P. and Montmerle, T. (1994). From T Tauri stars to protostars: Circumstellar material and young stellar objects in the rho Ophiuchi cloud. *ApJ*, 420:837–862.

Arce, H. G., Shepherd, D., Gueth, F., Lee, C.-F., Bachiller, R., Rosen, A., and Beuther, H. (2007). Molecular Outflows in Low- and High-Mass Star-forming Regions. *Protostars and Planets V*, pages 245–260.

Arzoumanian, D., André, P., Didelon, P., et al. (2011). Characterizing interstellar filaments with Herschel in IC 5146. *A&A*, 529:L6.

Batchelor, R. A., Robinson, B. J., and McCulloch, M. G. (1984). HCO(+) in NGC 6334. *Proceedings of the Astronomical Society of Australia*, 5:363–367.

Bec, J. and Khanin, K. (2007). Burgers turbulence. *Physics Reports*, 447:1–66.

Belloche, A., Garrod, R. T., Müller, H. S. P., and Menten, K. M. (2014). Detection of a branched alkyl molecule in the interstellar medium: iso-propyl cyanide. *Science*, 345:1584–1587.

Beuther, H., Ragan, S. E., Ossenkopf, V., et al. (2014). Carbon in different phases ([CII], [CI], and CO) in infrared dark clouds: Cloud formation signatures and carbon gas fractions. *A&A*, 571:A53.

Beuther, H., Thorwirth, S., Zhang, Q., Hunter, T. R., Megeath, S. T., Walsh, A. J., and Menten, K. M. (2005). High Spatial Resolution Observations of NH_3 and CH_3OH toward the Massive Twin Cores NGC 6334I and NGC 6334I(N). *ApJ*, 627:834–844.

Beuther, H., Walsh, A. J., Thorwirth, S., Zhang, Q., Hunter, T. R., Megeath, S. T., and Menten, K. M. (2007). Hot ammonia in NGC 6334I & I(N). *A&A*, 466:989–998.

Beuther, H., Walsh, A. J., Thorwirth, S., Zhang, Q., Hunter, T. R., Megeath, S. T., and Menten, K. M. (2008). ATCA 3 mm observations of NGC 6334I and I(N): dense cores, outflows, and an UCH II region. *A&A*, 481:169–181.

Bisschop, S. E., Jørgensen, J. K., van Dishoeck, E. F., and de Wachter, E. B. M. (2007). Testing grain-surface chemistry in massive hot-core regions. *A&A*, 465:913–929.

Bjorkman, J. E. and Wood, K. (2001). Radiative Equilibrium and Temperature Correction in Monte Carlo Radiation Transfer. *ApJ*, 554:615–623.

Blasi, P. (2014). Recent Results in Cosmic Ray Physics and Their Interpretation. *Brazilian Journal of Physics*, 44:426–440.

Bondi, H. and Hoyle, F. (1944). On the mechanism of accretion by stars. *MNRAS*, 104:273.

Bonnell, I. A. and Bate, M. R. (2002). Accretion in stellar clusters and the collisional formation of massive stars. *MNRAS*, 336:659–669.

Bonnell, I. A., Bate, M. R., Clarke, C. J., et al. (2001). Competitive accretion in embedded stellar clusters. *MNRAS*, 323:785–794.

Bonnell, I. A., Dobbs, C. L., Robitaille, T. P., and Pringle, J. E. (2006). Spiral shocks, triggering of star formation and the velocity dispersion in giant molecular clouds. *MNRAS*, 365:37–45.

Boreiko, R. T. and Betz, A. L. (1995). Ionized Carbon in NGC 6334. *ApJ*, 454:307.

Brinch, C., Crapsi, A., Hogerheijde, M. R., et al. (2007). Structure and dynamics of the class I young stellar object L1489 IRS. *A&A*, 461:1037–1047.

Brinch, C. and Hogerheijde, M. R. (2010). LIME - a flexible, non-LTE line excitation and radiation transfer method for millimeter and far-infrared wavelengths. *A&A*, 523:A25.

Brogan, C. L., Hunter, T. R., Cyganowski, C. J., Indebetouw, R., Beuther, H., Menten, K. M., and Thorwirth, S. (2009). Digging Into NGC 6334 I(N): Multiwavelength Imaging of a Massive Protostellar Cluster. *ApJ*, 707:1–23.

Brown, R. L., Wild, W., and Cunningham, C. (2004). ALMA - the Atacama large millimeter array. *Advances in Space Research*, 34:555–559.

Bruderer, S., Doty, S. D., and Benz, A. O. (2009). Chemical Modeling of Young Stellar Objects. I. Method and Benchmarks. *The Astrophysical Journal Supplement*, 183:179–196.

Brunt, C. M. and Heyer, M. H. (2002). Interstellar Turbulence. II. Energy Spectra of Molecular Regions in the Outer Galaxy. *ApJ*, 566:289–301.

Brunt, C. M. and Kerton, C. R. (2002). Molecular Cloud Distances via Principal Component Analysis. *ApJ*, 567:L41–L44.

Burkert, A. and Hartmann, L. (2004). Collapse and Fragmentation in Finite Sheets. *ApJ*, 616:288–300.

Burkhart, B., Lazarian, A., Goodman, A., and Rosolowsky, E. (2013). Hierarchical Structure of Magnetohydrodynamic Turbulence in Position-position-velocity Space. *ApJ*, 770:141.

Camps, P., Baes, M., and Saftly, W. (2013). Using 3D Voronoi grids in radiative transfer simulations. *A&A*, 560:A35.

Cappa, C. E., Barbá, R., Duronea, N. U., Vasquez, J., Arnal, E. M., Goss, W. M., and Fernández Lajús, E. (2011). A multifrequency study of the active star-forming complex NGC 6357 - I. Interstellar structures linked to the open cluster Pis 24. *MNRAS*, 415:2844–2858.

Caproni, A., Abraham, Z., and Vilas-Boas, J. W. S. (2000). Study of the ammonia emission in the NGC 6334 region. *A&A*, 361:685–694.

Carilli, C. L. and Rawlings, S. (2004). Motivation, key science projects, standards and assumptions. *New Astronomy Reviews*, 48:979–984.

Carlhoff, P. (2014). *Molecular Cloud Structure in the Star-forming Region W43*. Dissertation, Universität zu Köln.

Ceccarelli, C., Bacmann, A., Boogert, A., et al. (2010). Herschel spectral surveys of star-forming regions. Overview of the 555-636 GHz range. *A&A*, 521:L22.

Chabrier, G. (2003). Galactic Stellar and Substellar Initial Mass Function. *PASP*, 115:763–795.

Chandrasekhar, S. and Fermi, E. (1953). Magnetic Fields in Spiral Arms. *ApJ*, 118:113.

Chibueze, J. O., Omodaka, T., Handa, T., Imai, H., et al. (2014). Astrometry and Spatio-kinematics of H_2O Masers in the Massive Star-forming Region NGC 6334I(North) with VERA. *ApJ*, 784:114.

Chira, R.-A., Smith, R. J., Klessen, R. S., Stutz, A. M., and Shetty, R. (2014). Line profiles of cores within clusters - III. What is the most reliable tracer of core collapse in dense clusters? *MNRAS*, 444:874–886.

Choudhury, R., Schilke, P., Stéphan, G., Bergin, E., Möller, T., Schmiedeke, A., and Zernickel, A. (2015). Evolution of complex organic molecules in hot molecular cores. Synthetic spectra at (sub-)mm wavebands. *A&A*, 575:A68.

Churchwell, E., Babler, B. L., Meade, M. R., et al. (2009). The Spitzer/GLIMPSE Surveys: A New View of the Milky Way. *PASP*, 121:213–230.

Crutcher, R. M. (2012). Magnetic Fields in Molecular Clouds. *ARAA*, 50:29–63.

Cyganowski, C. J., Brogan, C. L., Hunter, T. R., and Churchwell, E. (2009). A Class I and Class II CH_3OH Maser Survey of EGOs from the GLIMPSE Survey. *ApJ*, 702:1615–1647.

Dame, T. M., Hartmann, D., and Thaddeus, P. (2001). The Milky Way in Molecular Clouds: A New Complete CO Survey. *ApJ*, 547:792–813.

De Buizer, J. M., Radomski, J. T., Piña, R. K., and Telesco, C. M. (2002). Mid-Infrared Imaging of NGC 6334 I. *ApJ*, 580:305–316.

de Graauw, T., Helmich, F. P., Phillips, T. G., et al. (2010). The Herschel-Heterodyne Instrument for the Far-Infrared (HIFI). *A&A*, 518:L6.

de Pree, C. G., Rodriguez, L. F., Dickel, H. R., and Goss, W. M. (1995). Rotation and Outflow in Compact H II Regions: VLA Observations of the Molecular and Ionized Gas in NGC 6334A and NGC 6334F. *ApJ*, 447:220.

Di Francesco, J., Johnstone, D., Kirk, H., MacKenzie, T., and Ledwosinska, E. (2008). The SCUBA Legacy Catalogues: Submillimeter-Continuum Objects Detected by SCUBA. *The Astrophysical Journal Supplement Series*, 175:277–295.

Dickel, H. R., Dickel, J. R., and Wilson, W. J. (1977). The detailed structure of CO in molecular cloud complexes. I - NGC 6334. *ApJ*, 217:56–67.

Dotson, J. L., Vaillancourt, J. E., Kirby, L., Dowell, C. D., Hildebrand, R. H., and Davidson, J. A. (2010). 350 μm Polarimetry from the Caltech Submillimeter Observatory. *The Astrophysical Journal Supplement*, 186:406–426.

Draine, B. T. (2003). Interstellar Dust Grains. *ARAA*, 41:241–289.

Dumouchel, F., Faure, A., and Lique, F. (2010). The rotational excitation of HCN and HNC by He: temperature dependence of the collisional rate coefficients. *MNRAS*, 406:2488–2492.

Evans, II, N. J. (1999). Physical Conditions in Regions of Star Formation. *ARAA*, 37:311–362.

Federrath, C. and Klessen, R. S. (2012). The Star Formation Rate of Turbulent Magnetized Clouds: Comparing Theory, Simulations, and Observations. *ApJ*, 761:156.

Federrath, C. and Klessen, R. S. (2013). On the Star Formation Efficiency of Turbulent Magnetized Clouds. *ApJ*, 763:51.

Feigelson, E. D., Martin, A. L., McNeill, C. J., Broos, P. S., and Garmire, G. P. (2009). Stellar Clusters in the NGC 6334 Star-Forming Complex. *The Astronomical Journal*, 138:227–239.

Flower, D. R. (1999). Rotational excitation of HCO^+ by H_2. *MNRAS*, 305:651–653.

Foster, J. B., Jackson, J. M., Barnes, P. J., et al. (2011). The Millimeter Astronomy Legacy Team 90 GHz (MALT90) Pilot Survey. *The Astrophysical Journal Supplement*, 197:25.

Furuya, R. S., Kitamura, Y., and Shinnaga, H. (2014). A Dynamically Collapsing Core and a Precursor of a Core in a Filament Supported by Turbulent and Magnetic Pressures. *ApJ*, 793:94.

Garrod, R. T., Weaver, S. L. W., and Herbst, E. (2008). Complex Chemistry in Star-forming Regions: An Expanded Gas-Grain Warm-up Chemical Model. *ApJ*, 682:283–302.

Gerner, T. (2014). *Chemical characterization of the early evolutionary phases of high-mass star-forming regions*. Dissertation, Ruprecht-Karls-Universität Heidelberg.

Gezari, D. Y. (1982). The remarkable 400 micron source NGC 6334/I/North/. *ApJ*, 259:L29–L33.

Godard, B., Falgarone, E., Gerin, M., Hily-Blant, P., and de Luca, M. (2010). Molecular absorption lines toward star-forming regions: a comparative study of HCO^+, HNC, HCN, and CN. *A&A*, 520:A20.

Goddi, C., Moscadelli, L., and Sanna, A. (2011). Infall and outflow within 400 AU from a high-mass protostar. 3D velocity fields from methanol and water masers in AFLG 5142. *A&A*, 535:L8.

Gómez, G. C. and Vázquez-Semadeni, E. (2014). Filaments in Simulations of Molecular Cloud Formation. *ApJ*, 791:124.

Gooch, R. (1996). Karma: a Visualization Test-Bed. In Jacoby, G. H. and Barnes, J., editors, *Astronomical Data Analysis Software and Systems V*, volume 101 of *ASP Conference Series*, page 80.

Goodman, A. A., Benson, P. J., Fuller, G. A., and Myers, P. C. (1993). Dense cores in dark clouds. VIII - Velocity gradients. *ApJ*, 406:528–547.

Goodman, A. A., Rosolowsky, E. W., Borkin, M. A., Foster, J. B., Halle, M., Kauffmann, J., and Pineda, J. E. (2009). A role for self-gravity at multiple length scales in the process of star formation. *Nature*, 457:63–66.

Grenier, I. A., Casandjian, J.-M., and Terrier, R. (2005). Unveiling Extensive Clouds of Dark Gas in the Solar Neighborhood. *Science*, 307:1292–1295.

Güsten, R., Nyman, L. Å., Schilke, P., Menten, K., Cesarsky, C., and Booth, R. (2006). The Atacama Pathfinder EXperiment (APEX) - a new submillimeter facility for southern skies -. *A&A*, 454:L13–L16.

Hacar, A., Tafalla, M., Kauffmann, J., and Kovács, A. (2013). Cores, filaments, and bundles: hierarchical core formation in the L1495/B213 Taurus region. *A&A*, 554:A55.

Heitsch, F. (2013). Gravitational Infall onto Molecular Filaments. *ApJ*, 769:115.

Heitsch, F., Stone, J. M., and Hartmann, L. W. (2009). Effects of Magnetic Field Strength and Orientation on Molecular Cloud Formation. *ApJ*, 695:248–258.

Hennebelle, P., Banerjee, R., Vázquez-Semadeni, E., Klessen, R. S., and Audit, E. (2008). From the warm magnetized atomic medium to molecular clouds. *A&A*, 486:L43–L46.

Henshaw, J. D., Caselli, P., Fontani, F., Jiménez-Serra, I., and Tan, J. C. (2014). The dynamical properties of dense filaments in the infrared dark cloud G035.39-00.33. *MNRAS*, 440:2860–2881.

Ho, P. T. P., Moran, J. M., and Lo, K. Y. (2004). The Submillimeter Array. *ApJ*, 616:L1–L6.

Högbom, J. A. (1974). Aperture Synthesis with a Non-Regular Distribution of Interferometer Baselines. *Astronomy and Astrophysics Supplement*, 15:417.

Hogerheijde, M. R. and van der Tak, F. F. S. (2000). An accelerated Monte Carlo method to solve two-dimensional radiative transfer and molecular excitation. *A&A*, 362:697–710.

Hosokawa, T. and Omukai, K. (2009). Evolution of Massive Protostars with High Accretion Rates. *ApJ*, 691:823–846.

Houde, M., Bastien, P., Dotson, J. L., Dowell, C. D., Hildebrand, R. H., Peng, R., Phillips, T. G., Vaillancourt, J. E., and Yoshida, H. (2002). On the Measurement of the Magnitude and Orientation of the Magnetic Field in Molecular Clouds. *ApJ*, 569:803–814.

Hull, C. L. H., Plambeck, R. L., Kwon, W., et al. (2014). TADPOL: A 1.3 mm Survey of Dust Polarization in Star-forming Cores and Regions. *The Astrophysical Journal Supplement*, 213:13.

Hunter, T., Brogan, C., Cyganowski, C., Young, K., Menten, K., Indebetouw, R., Chandler, C., and Beuther, H. (2013). Evolutionary diversity in a massive protocluster: Subarcsecond (600 AU) imaging of NGC6334I from 6 cm to 0.8 mm. In *Protostars and Planets VI Posters*, page 34.

Hunter, T. R., Brogan, C. L., Cyganowski, C. J., and Young, K. H. (2014). Subarcsecond Imaging of the NGC 6334 I(N) Protocluster: Two Dozen Compact Sources and a Massive Disk Candidate. *ApJ*, 788:187.

Hunter, T. R., Brogan, C. L., Megeath, S. T., Menten, K. M., Beuther, H., and Thorwirth, S. (2006). Millimeter Multiplicity in NGC 6334 I and I(N). *ApJ*, 649:888–893.

Hurley, J. R., Pols, O. R., and Tout, C. A. (2000). Comprehensive analytic formulae for stellar evolution as a function of mass and metallicity. *MNRAS*, 315:543–569.

Indriolo, N. and McCall, B. J. (2012). Investigating the Cosmic-Ray Ionization Rate in the Galactic Diffuse Interstellar Medium through Observations of H_3^+. *ApJ*, 745:91.

Inoue, T. and Fukui, Y. (2013). Formation of Massive Molecular Cloud Cores by Cloud-Cloud Collision. *ApJ*, 774:L31.

Jackson, J. M., Finn, S. C., Chambers, E. T., Rathborne, J. M., and Simon, R. (2010). The ”Nessie” Nebula: Cluster Formation in a Filamentary Infrared Dark Cloud. *ApJ*, 719:L185–L189.

Jackson, J. M. and Kraemer, K. E. (1999). Photodissociation Regions and H II Regions in NGC 6334. *ApJ*, 512:260–270.

Jeans, J. H. (1902). The Stability of a Spherical Nebula. *Royal Society of London Philosophical Transactions Series A*, 199:1–53.

Kauffmann, J., Pillai, T., and Goldsmith, P. F. (2013). Low Virial Parameters in Molecular Clouds: Implications for High-mass Star Formation and Magnetic Fields. *ApJ*, 779:185.

Kennicutt, R. C. and Evans, N. J. (2012). Star Formation in the Milky Way and Nearby Galaxies. *ARAA*, 50:531–608.

Kirk, H., Myers, P. C., Bourke, T. L., Gutermuth, R. A., Hedden, A., and Wilson, G. W. (2013). Filamentary Accretion Flows in the Embedded Serpens South Protocluster. *ApJ*, 766:115.

Klein, B., Hochgürtel, S., Krämer, I., Bell, A., Meyer, K., and Güsten, R. (2012). High-resolution wide-band fast Fourier transform spectrometers. *A&A*, 542:L3.

Klessen, R. S. and Glover, S. C. O. (2014). Physical Processes in the Interstellar Medium. *ArXiv e-prints*.

Kolmogorov, A. (1941). The Local Structure of Turbulence in Incompressible Viscous Fluid for Very Large Reynolds' Numbers. *Akademiia Nauk SSSR Doklady*, 30:301–305.

Kraemer, K. E. and Jackson, J. M. (1999). Molecular Gas in the NGC 6334 Star Formation Region. *The Astrophysical Journal Supplement Series*, 124:439–463.

Kraemer, K. E., Jackson, J. M., Lane, A. P., and Paglione, T. A. D. (2000). Properties of the Photodissociated Gas in NGC 6334. *ApJ*, 542:946–956.

Kraemer, K. E., Jackson, J. M., Paglione, T. A. D., and Bolatto, A. D. (1997). A 2000 $M_\odot$ Rotating Molecular Disk around NGC 6334A. *ApJ*, 478:614–623.

Kramer, C., Stutzki, J., Rohrig, R., and Corneliussen, U. (1998). Clump mass spectra of molecular clouds. *A&A*, 329:249–264.

Kritsuk, A. G., Lee, C. T., and Norman, M. L. (2013). A supersonic turbulence origin of Larson's laws. *MNRAS*, 436:3247–3261.

Kroupa, P. (2001). On the variation of the initial mass function. *MNRAS*, 322:231–246.

Krumholz, M. R. and McKee, C. F. (2008). A minimum column density of $1\mathrm{gcm}^{-2}$ for massive star formation. *Nature*, 451:1082–1084.

Krumholz, M. R., McKee, C. F., and Klein, R. I. (2005). The formation of stars by gravitational collapse rather than competitive accretion. *Nature*, 438:332–334.

Kuiper, R., Klahr, H., Beuther, H., and Henning, T. (2010). Circumventing the Radiation Pressure Barrier in the Formation of Massive Stars via Disk Accretion. *ApJ*, 722:1556–1576.

Kuiper, T. B. H., Peters, III, W. L., Forster, J. R., et al. (1995). Ammonia Observations of NGC 6334 I(N). *ApJ*, 446:692.

Küpper, A. H. W., Maschberger, T., Kroupa, P., et al. (2011). Mass segregation and fractal substructure in young massive clusters - I. The McLuster code and method calibration. *MNRAS*, 417:2300–2317.

Kurtz, S., Cesaroni, R., Churchwell, E., Hofner, P., and Walmsley, C. M. (2000). Hot Molecular Cores and the Earliest Phases of High-Mass Star Formation. *Protostars and Planets IV*, pages 299–326.

Kwok, S. (2007). *Physics and Chemistry of the Interstellar Medium*. University Science Books, Sausalito, US-CA.

Lada, C. J. (1987). Star formation - From OB associations to protostars. In Peimbert, M. and Jugaku, J., editors, *Star Forming Regions*, volume 115 of *IAU Symposium*, pages 1–17.

Larson, R. B. (1981). Turbulence and star formation in molecular clouds. *MNRAS*, 194:809–826.

Larson, R. B. (1985). Cloud fragmentation and stellar masses. *MNRAS*, 214:379–398.

Lazarian, A. (2007). Tracing magnetic fields with aligned grains. *Journal of Quantitative Spectroscopy & Radiative Transfer*, 106:225–256.

Leurini, S., Schilke, P., Parise, B., Wyrowski, F., Güsten, R., and Philipp, S. (2006). The high velocity outflow in NGC 6334 I. *A&A*, 454:L83–L86.

Li, H., Griffin, G. S., Krejny, M., Novak, G., Loewenstein, R. F., Newcomb, M. G., Calisse, P. G., and Chuss, D. T. (2006). Results of SPARO 2003: Mapping Magnetic Fields in Giant Molecular Clouds. *ApJ*, 648:340–354.

Li, H.-b., Fang, M., Henning, T., and Kainulainen, J. (2013). The link between magnetic fields and filamentary clouds: bimodal cloud orientations in the Gould Belt. *MNRAS*, 436:3707–3719.

Liu, T., Wu, Y., Liu, S.-Y., Qin, S.-L., Su, Y.-N., Chen, H.-R., and Ren, Z. (2011). Infall and Outflow Motions in the High-mass Star-forming Complex G9.62+0.19. *ApJ*, 730:102.

Liu, T., Wu, Y., Wu, J., Qin, S.-L., and Zhang, H. (2013). Competitive accretion in the protocluster G10.6-0.4? *MNRAS*, 436:1335–1342.

Loughran, L., McBreen, B., Fazio, G. G., Rengarajan, T. N., Maxson, C. W., Serio, S., Sciortino, S., and Ray, T. P. (1986). Multiband far-infrared observations of the NGC 6334 complex. *ApJ*, 303:629–637.

Luzum, B., Capitaine, N., Fienga, A., et al. (2011). The IAU 2009 system of astronomical constants: the report of the IAU working group on numerical standards for Fundamental Astronomy. *Celestial Mechanics and Dynamical Astronomy*, 110:293–304.

Mangum, J. G., Emerson, D. T., and Greisen, E. W. (2007). The On The Fly imaging technique. *A&A*, 474:679–687.

Masunaga, H. and Inutsuka, S.-i. (2000). A Radiation Hydrodynamic Model for Protostellar Collapse. II. The Second Collapse and the Birth of a Protostar. *ApJ*, 531:350–365.

Matthews, H. E., McCutcheon, W. H., Kirk, H., White, G. J., and Cohen, M. (2008). The Distribution and Properties of Cold Dust in NGC 6334. *The Astronomical Journal*, 136:2083–2101.

McClure-Griffiths, N. M., Dickey, J. M., Gaensler, B. M., Green, A. J., Haverkorn, M., and Strasser, S. (2005). The Southern Galactic Plane Survey: H I Observations and Analysis. *The Astrophysical Journal Supplement Series*, 158:178–187.

McCutcheon, W. H., Sandell, G., Matthews, H. E., Kuiper, T. B. H., Sutton, E. C., Danchi, W. C., and Sato, T. (2000). Star formation in NGC 6334 I and I(N). *MNRAS*, 316:152–164.

McKee, C. F. and Ostriker, E. C. (2007). Theory of Star Formation. *ARAA*, 45:565–687.

McKee, C. F. and Tan, J. C. (2003). The Formation of Massive Stars from Turbulent Cores. *ApJ*, 585:850–871.

Megeath, S. T. and Tieftrunk, A. R. (1999). The Detection of Outflows in the Infrared-quiet Molecular Core NGC 6334/I(North). *ApJ*, 526:L113–L116.

Mohr, P. J., Taylor, B. N., and Newell, D. B. (2012). CODATA recommended values of the fundamental physical constants: 2010. *Reviews of Modern Physics*, 84:1527–1605.

Molinari, S., Pezzuto, S., Cesaroni, R., Brand, J., Faustini, F., and Testi, L. (2008). The evolution of the spectral energy distribution in massive young stellar objects. *A&A*, 481:345–365.

Molinari, S., Swinyard, B., Bally, J., et al. (2010). Clouds, filaments, and protostars: The Herschel Hi-GAL Milky Way. *A&A*, 518:L100.

Möller, T., Bernst, I., Panoglou, D., Muders, D., Ossenkopf, V., Röllig, M., and Schilke, P. (2013). Modeling and Analysis Generic Interface for eXternal numerical codes (MAGIX). *A&A*, 549:A21.

Morales Ortiz, J. L., Ceccarelli, C., Lis, D. C., Olmi, L., Plume, R., and Schilke, P. (2014). Ionization toward the high-mass star-forming region NGC 6334 I. *A&A*, 563:A127.

Muñoz, D. J., Mardones, D., Garay, G., Rebolledo, D., Brooks, K., and Bontemps, S. (2007). Massive Clumps in the NGC 6334 Star-forming Region. *ApJ*, 668:906–917.

Müller, H. S. P., Schlöder, F., Stutzki, J., and Winnewisser, G. (2005). The Cologne Database for Molecular Spectroscopy, CDMS: a useful tool for astronomers and spectroscopists. *Journal of Molecular Structure*, 742:215–227.

Murray, N. (2011). Star Formation Efficiencies and Lifetimes of Giant Molecular Clouds in the Milky Way. *ApJ*, 729:133.

Myers, P. C. (2012). Mass and Luminosity Evolution of Young Stellar Objects. *ApJ*, 752:9.

Nagasawa, M. (1987). Gravitational Instability of the Isothermal Gas Cylinder with an Axial magnetic Field. *Progress of Theoretical Physics*, 77:635–652.

Neckel, T. (1978). UBV, VRI and H-beta observations of stars in the H II regions NGC 6334 and NGC 6357. *A&A*, 69:51–56.

Norris, R. P., Byleveld, S. E., Diamond, P. J., et al. (1998). Methanol Masers as Tracers of Circumstellar Disks. *ApJ*, 508:275–285.

Novak, G., Dotson, J. L., and Li, H. (2009). Dispersion of Observed Position Angles of Submillimeter Polarization in Molecular Clouds. *ApJ*, 695:1362–1369.

Ossenkopf, V. (2002). Molecular line emission from turbulent clouds. *A&A*, 391:295–315.

Ossenkopf, V. (2009). Optimization of mapping modes for heterodyne instruments. *A&A*, 495:677–690.

Ossenkopf, V. and Henning, T. (1994). Dust opacities for protostellar cores. *A&A*, 291:943–959.

Ossenkopf, V., Krips, M., and Stutzki, J. (2008). Structure analysis of interstellar clouds. II. Applying the Δ-variance method to interstellar turbulence. *A&A*, 485:719–727.

Ostriker, J. (1964). The Equilibrium of Polytropic and Isothermal Cylinders. *ApJ*, 140:1056.

Padoan, P. and Nordlund, Å. (2002). The Stellar Initial Mass Function from Turbulent Fragmentation. *ApJ*, 576:870–879.

Padovani, M., Jørgensen, J. K., Bertoldi, F., et al. (2011). Adaptable Radiative Transfer Innovations for Submillimeter Telescopes (ARTIST). In *Computational Star Formation*, volume 270 of *IAU Symposium*, pages 451–454.

Panopoulou, G. V., Tassis, K., Goldsmith, P. F., and Heyer, M. H. (2014). ^{13}CO filaments in the Taurus molecular cloud. *MNRAS*, 444:2507–2524.

Parker, Q. A., Phillipps, S., Pierce, M. J., et al. (2005). The AAO/UKST SuperCOSMOS Hα survey. *MNRAS*, 362:689–710.

Peretto, N., Fuller, G. A., André, P., et al. (2014). SDC13 infrared dark clouds: Longitudinally collapsing filaments? *A&A*, 561:A83.

Persi, P. and Tapia, M. (2010). Multifrequency behaviour of high mass star forming regions: The case of NGC 6334. *Memorie della Societa Astronomica Italiana*, 81:171.

Peters, T., Banerjee, R., Klessen, R. S., Mac Low, M.-M., Galván-Madrid, R., and Keto, E. R. (2010). H II Regions: Witnesses to Massive Star Formation. *ApJ*, 711:1017–1028.

Pickett, H. M., Poynter, R. L., Cohen, E. A., Delitsky, M. L., Pearson, J. C., and Müller, H. S. P. (1998). Submillimeter, millimeter and microwave spectral line catalog. *Journal of Quantitative Spectroscopy and Radiative Transfer*, 60:883–890.

Pilbratt, G. L., Riedinger, J. R., Passvogel, T., et al. (2010). Herschel Space Observatory. An ESA facility for far-infrared and submillimetre astronomy. *A&A*, 518:L1.

Planck Collaboration (2015). Planck intermediate results. XXXV. Probing the role of the magnetic field in the formation of structure in molecular clouds. *ArXiv e-prints*.

Pon, A., Johnstone, D., and Heitsch, F. (2011). Modes of Star Formation in Finite Molecular Clouds. *ApJ*, 740:88.

Pon, A., Toalá, J. A., Johnstone, D., Vázquez-Semadeni, E., Heitsch, F., and Gómez, G. C. (2012). Aspect Ratio Dependence of the Free-fall Time for Non-spherical Symmetries. *ApJ*, 756:145.

Purcell, C. (2006). *What's in the brew? A study of the molecular environment of methanol masers and UCHII regions.* Dissertation, University of New South Wales.

Rixon, G., Dubernet, M. L., Piskunov, N., et al. (2011). VAMDC – The Virtual Atomic and Molecular Data Centre. In Bernotas, A., Karazija, R., and Rudzikas, Z., editors, *American Institute of Physics Conference Series*, volume 1344, pages 107–115.

Robitaille, T. P., Tollerud, E. J., Greenfield, P., et al. (2013). Astropy: A community Python package for astronomy. *A&A*, 558:A33.

Rodón, J. (2009). *The Fragmentation of Massive Star-Forming Regions.* Dissertation, Ruprecht-Karls-Universität Heidelberg.

Rodriguez, L. F., Canto, J., and Moran, J. M. (1982). Radio sources in NGC 6334. *ApJ*, 255:103–110.

Rolffs, R. (2011). *Structure of Hot Molecular Cores.* Dissertation, Universität zu Köln.

Roman-Duval, J., Jackson, J. M., Heyer, M., Johnson, A., Rathborne, J., Shah, R., and Simon, R. (2009). Kinematic Distances to Molecular Clouds Identified in the Galactic Ring Survey. *ApJ*, 699:1153–1170.

Rosolowsky, E. W., Pineda, J. E., Kauffmann, J., and Goodman, A. A. (2008). Structural Analysis of Molecular Clouds: Dendrograms. *ApJ*, 679:1338–1351.

Russeil, D., Schneider, N., Anderson, L. D., et al. (2013). The Herschel view of the massive star-forming region NGC 6334. *A&A*, 554:A42.

Russeil, D., Zavagno, A., Adami, C., Anderson, L. D., Bontemps, S., Motte, F., Rodon, J. A., Schneider, N., Ilmane, A., and Murphy, K. J. (2012). Statistical study of OB stars in NGC 6334 and NGC 6357. *A&A*, 538:A142.

Russeil, D., Zavagno, A., Motte, F., Schneider, N., Bontemps, S., and Walsh, A. J. (2010). The earliest phases of high-mass star formation: the NGC 6334-NGC 6357 complex. *A&A*, 515:A55.

Rybicki, G. B. and Hummer, D. G. (1991). An accelerated lambda iteration method for multilevel radiative transfer. I - Non-overlapping lines with background continuum. *A&A*, 245:171–181.

Salpeter, E. E. (1955). The Luminosity Function and Stellar Evolution. *ApJ*, 121:161.

Sánchez-Monge, Á., Cesaroni, R., Beltrán, M. T., et al. (2013a). A candidate circumbinary Keplerian disk in G35.20-0.74 N: A study with ALMA. *A&A*, 552:L10.

Sánchez-Monge, Á., López-Sepulcre, A., Cesaroni, R., Walmsley, C. M., Codella, C., Beltrán, M. T., Pestalozzi, M., and Molinari, S. (2013b). Evolution and excitation conditions of outflows in high-mass star-forming regions. *A&A*, 557:A94.

Sandell, G. (2000). (Sub)mm continuum mapping of NGC 6334 I & I(N). A cobweb of filaments and protostars. *A&A*, 358:242–256.

Sarma, A. P., Troland, T. H., Roberts, D. A., and Crutcher, R. M. (2000). VLA OH and H I Zeeman Observations of the NGC 6334 Complex. *ApJ*, 533:271–280.

Sarrasin, E., Abdallah, D. B., Wernli, M., Faure, A., Cernicharo, J., and Lique, F. (2010). The rotational excitation of HCN and HNC by He: new insights on the HCN/HNC abundance ratio in molecular clouds. *MNRAS*, 404:518–526.

Sault, R. J., Teuben, P. J., and Wright, M. C. H. (1995). A Retrospective View of MIRIAD. In *Astronomical Data Analysis Software and Systems IV*, volume 77, page 433.

Schilke, P., Phillips, T. G., and Mehringer, D. M. (1999). Submillimeter Line Surveys. In Ossenkopf, V., Stutzki, J., and Winnewisser, G., editors, *The Physics and Chemistry of the Interstellar Medium*, page 330.

Schilke, P., Walmsley, C. M., Pineau des Forets, G., and Flower, D. R. (1997). SiO production in interstellar shocks. *A&A*, 321:293–304.

Schneider, N., Csengeri, T., Bontemps, S., Motte, F., Simon, R., Hennebelle, P., Federrath, C., and Klessen, R. (2010). Dynamic star formation in the massive DR21 filament. *A&A*, 520:A49.

Schneider, N., Ossenkopf, V., Csengeri, T., Klessen, R. S., Federrath, C., Tremblin, P., Girichidis, P., Bontemps, S., and André, P. (2015). Understanding star formation in molecular clouds. I. Effects of line-of-sight contamination on the column density structure. *A&A*, 575:A79.

Schöier, F. L., van der Tak, F. F. S., van Dishoeck, E. F., and Black, J. H. (2005). An atomic and molecular database for analysis of submillimetre line observations. *A&A*, 432:369–379.

Schuller, F., Menten, K. M., Contreras, Y., et al. (2009). ATLASGAL - The APEX telescope large area survey of the galaxy at 870 μm. *A&A*, 504:415–427.

Seifahrt, A., Thorwirth, S., Beuther, H., Leurini, S., Brogan, C. L., Hunter, T. R., Menten, K. M., and Stecklum, B. (2008). Synergy of multi-frequency studies from observations of NGC 6334I. *Journal of Physics Conference Series*, 131(1):012030.

Shu, F. H., Adams, F. C., and Lizano, S. (1987). Star formation in molecular clouds - Observation and theory. *ARAA*, 25:23–81.

Smith, R. J., Longmore, S., and Bonnell, I. (2009). The simultaneous formation of massive stars and stellar clusters. *MNRAS*, 400:1775–1784.

Sobolev, V. V. (1957). The Diffusion of Lα Radiation in Nebulae and Stellar Envelopes. *Soviet Astronomy*, 1:678.

Stahler, S. W. and Palla, F. (2005). *The Formation of Stars*. Wiley-VCH.

Steinacker, J., Baes, M., and Gordon, K. D. (2013). Three-Dimensional Dust Radiative Transfer*. *ARAA*, 51:63–104.

Storm, S., Mundy, L. G., Fernández-López, M., et al. (2014). CARMA Large Area Star Formation Survey: Project Overview with Analysis of Dense Gas Structure and Kinematics in Barnard 1. *ApJ*, 794:165.

Tackenberg, J. (2013). *Early stages of high-mass star formation*. Dissertation, Ruprecht-Karls-Universität Heidelberg.

Tan, J. C., Beltrán, M. T., Caselli, P., Fontani, F., Fuente, A., Krumholz, M. R., McKee, C. F., and Stolte, A. (2014). Massive Star Formation. *Protostars and Planets VI*, pages 149–172.

Tapia, M., Persi, P., and Roth, M. (1996). The embedded stellar population in northern NGC 6334. *A&A*, 316:102–110.

Tielens, A. G. G. M. (2005). *The Physics and Chemistry of the Interstellar Medium*. Cambridge University Press, Cambridge, UK.

Tigé, J. (2014). *Les premières phases d'évolution des étoiles massives dans NGC 6334 et NGC 6357 révélées par le sondage Herschel-HOBYS*. Dissertation, LAM, Aix-Marseille University.

Toalá, J. A., Vázquez-Semadeni, E., and Gómez, G. C. (2012). The Free-fall Time of Finite Sheets and Filaments. *ApJ*, 744:190.

Tobin, J. J., Hartmann, L., Bergin, E., Chiang, H.-F., Looney, L. W., Chandler, C. J., Maret, S., and Heitsch, F. (2012). Complex Structure in Class 0 Protostellar Envelopes. III. Velocity Gradients in Non-axisymmetric Envelopes, Infall, or Rotation? *ApJ*, 748:16.

Vaillancourt, J. E. (2011). Observations of Polarized Dust Emission at Far-infrared through Millimeter Wavelengths. In *Astronomical Polarimetry 2008: Science from Small to Large Telescopes*, volume 449 of *ASP Conference Series*, page 169.

Vallée, J. P. (2008). New Velocimetry and Revised Cartography of the Spiral Arms in the Milky Way - A Consistent Symbiosis. *The Astronomical Journal*, 135:1301–1310.

van der Tak, F. F. S., van Dishoeck, E. F., Evans, II, N. J., and Blake, G. A. (2000). Structure and Evolution of the Envelopes of Deeply Embedded Massive Young Stars. *ApJ*, 537:283–303.

van Dishoeck, E. F. and Blake, G. A. (1998). Chemical Evolution of Star-Forming Regions. *ARAA*, 36:317–368.

van Zadelhoff, G.-J., Dullemond, C. P., van der Tak, F. F. S., et al. (2002). Numerical methods for non-LTE line radiative transfer: Performance and convergence characteristics. *A&A*, 395:373–384.

Vassilev, V., Meledin, D., Lapkin, I., et al. (2008). A Swedish heterodyne facility instrument for the APEX telescope. *A&A*, 490:1157–1163.

Veach, T. J., Groppi, C. E., and Hedden, A. (2013). Vibrationally Excited HCN around AFGL 2591: A Probe of Protostellar Structure. *ApJ*, 765:L34.

Wang, K.-S., Bourke, T. L., Hogerheijde, M. R., van der Tak, F. F. S., Benz, A. O., Megeath, S. T., and Wilson, T. L. (2013). Dense molecular cocoons in the massive protocluster W3 IRS5: a test case for models of massive star formation. *A&A*, 558:A69.

Ward-Thompson, D. and Buckley, H. D. (2001). Modelling submillimetre spectra of the protostellar infall candidates NGC 1333-IRAS 2 and Serpens SMM4. *MNRAS*, 327:955–983.

Willis, S., Marengo, M., Allen, L., Fazio, G. G., Smith, H. A., and Carey, S. (2013). A Wide-field near- and Mid-infrared Census of Young Stars in NGC 6334. *ApJ*, 778:96.

Wilson, T. L., Rohlfs, K., and Hüttemeister, S. (2009). *Tools of Radio Astronomy*. Springer-Verlag.

Woody, D., Padin, S., Chauvin, E., et al. (2012). The CCAT 25m diameter submillimeter-wave telescope. In *Society of Photo-Optical Instrumentation Engineers (SPIE) Conference Series*, volume 8444 of *SPIE Conference Series*, page 2.

Wu, Y. W., Sato, M., Reid, M. J., et al. (2014). Trigonometric parallaxes of star-forming regions in the Sagittarius spiral arm. *A&A*, 566:A17.

Young, E. T., Becklin, E. E., Marcum, P. M., et al. (2012). Early Science with SOFIA, the Stratospheric Observatory For Infrared Astronomy. *ApJ*, 749:L17.

Zernickel, A., Schilke, P., Schmiedeke, A., et al. (2012). Molecular line survey of the high-mass star-forming region NGC 6334I with Herschel/HIFI and the Submillimeter Array. *A&A*, 546:A87.

Zernickel, A., Schilke, P., and Smith, R. J. (2013). The global velocity field of the filament in NGC 6334. *A&A*, 554:L2.

Zhang, Q., Qiu, K., Girart, J. M., et al. (2014). Magnetic Fields and Massive Star Formation. *ApJ*, 792:116.

Zheng, X.-W. (1989). VLBI measurement of OH masers in NGC 6334 F. *Chinese Journal of Space Science*, 9:87–95.

Zinnecker, H. and Yorke, H. W. (2007). Toward Understanding Massive Star Formation. *ARAA*, 45:481–563.

Appendix

List of Figures

List of Tables

A. List of abbreviations

Table A.1.: List of chemical species

C_2H_4O	Ethylene oxide	H_2O	Water
C_2H_5CN	Ethyl cyanide	H_2S	Hydrogen sulfide
C_2H_5OH	Ethanol	H_3^+	Trihydrogen cation
$(CH_2OH)_2$	Ethylene glycol	HC_3N	Cyanoacetylene
CH_3CH_3CO	Acetone	HCN	Hydrogen cyanide
CH_3CHO	Acetaldehyde	HCNO	Fulminic acid
CH_3CN	Methyl cyanide	HCO^+	Oxomethylium
CH_3NH_2	Methylamine	HCOOH	Formic acid
CH_3OCH_3	Dimethyl ether	HI	Atomic hydrogen
CH_3OCHO	Methyl formate	HII	Ionized hydrogen
CH_3OH	Methanol	HNC	Hydrogen isocyanide
CN	Cyanide radical	N_2H^+	Diazenylium
CO	Carbon monoxide	NH_2CHO	Formamide
CS	Carbon monosulphide	NO	Nitrogen oxide
H_2	Molecular hydrogen	OCS	Carbonyl sulfide
H_2CCO	Ketene	OH	Hydroxyl radical
H_2Cl^+	Chloronium	SiO	Silicon monoxide
H_2CO	Formaldehyde	SO	Sulphur monoxide
H_2CS	Thioformaldehyde	SO_2	Sulphur dioxide

Table A.2.: List of acronyms

A&A	Astronomy and Astrophysics	`LIME`	Line Modeling Engine
ATLASGAL	APEX Telescope Large Area Survey of the Galaxy	LOS	Line-of-sight
ALMA	Atacama Large Millimeter/submillimeter Array	LTE	Local thermodynamic equilibrium
APEX	Atacama Pathfinder Experiment	`MAGIX`	Modeling and Analysis Generic Interface for eXternal numerical codes
ApJ	The Astrophysical Journal	MALT90	Millimetre Astronomy Legacy Team 90 GHz
ARAA	Annual Review of Astronomy and Astrophysics	MHD	Magnetohydrodynamic
CDMS	Cologne Database for Molecular Spectroscopy	`MIRIAD`	Multichannel Image Reconstruction, Image Analysis and Display
CHESS	Chemical HErschel Surveys of Star forming regions	*MNRAS*	Monthly Notices of the Royal Astronomical Society
`CLASS`	Continuum and Line Analysis Single-dish Software	NGC	New General Catalogue of Nebulae and Clusters of Stars
COM	Complex organic molecule	OTF	On-the-fly
FWHM	Full width at half maximum	*PASP*	Publications of the Astronomical Society of the Pacific
`GILDAS`	Grenoble Image and Line Data Analysis Software	PDF	Probability distribution function
GLIMPSE	Galactic Legacy Infrared Mid-Plane Survey Extraordinaire	PDR	Photodissociation/photon-dominated region
GMC	Giant molecular cloud	PVD	Position-velocity diagram
HIFI	Heterodyne Instrument for the Far Infrared	PWV	Precipitable water vapor
`HIPE`	Herschel Interactive Processing Environment	SED	Spectral energy distribution
HMC	Hot molecular core	SMA	Submillimeter Array
HSO	Herschel Space Observatory	SNR	Signal-to-noise ratio
IMF/CMF	Initial/Core mass function	SOFIA	Stratospheric Observatory For Infrared Astronomy
IRAM	Institut de Radioastronomie Millimétrique	UCHII	Ultra compact HII
IRDC	Infrared dark cloud	URL	Uniform resource locator
ISM	Interstellar medium	YSO	Young stellar object
LAMDA	Leiden Atomic and Molecular Database	ZAMS	Zero age main sequence

B. List of astrophysical units and physical constants

Table B.1.: Astrophysical units and physical constants.
References: Mohr et al. (2012); Luzum et al. (2011).

Symbol	Value (uncertainty)	unit	Explanation
c	2.99 792 458E+8	m/s	speed of light in vacuum
k_B	1.380 6488(13)E-23	J/K	Boltzmann constant
h	6.626 069 57(29)E-34	Js	Planck constant
N_A	6.022 141 29(27)E+23	1/mol	Avogadro constant
m_u	1.660 538 921(73)E-27	kg	atomic mass constant
m_h	1.007 825 032 07(10)	m_u	hydrogen atom mass
G	6.673 84(80)E-11	$m^3/kg/s^2$	gravitational constant
e	1.602 176 565(35)E-19	C	elementary charge
$''$	1/60	$'$ (arcmin)	arcsecond
	1/3600	° (degree)	
	4.8481368...E-6	rad	
yr	365.25	d	Julian year
	3.15576E+7	s	
Jy	1E-26	$W/Hz/m^2$	Jansky flux
au	1.495 978 707E+11	m	astronomical unit
pc	1 au/tan(1$''$)≈206265	au	parsec
	3.0856776...E+16	m	
$M_\odot$	1.9884(2)E+30	kg	solar mass
$R_\odot$	6.9551E+8	m	solar radius
$L_\odot$	3.845E+26	W	solar luminosity

C. Acknowledgment

- This work was carried out within the Collaborative Research Centre 956 "Conditions and Impact of Star Formation - Astrophysics, Instrumentation and Laboratory Research", subproject "A6: High-Mass Star formation", funded by the Deutsche Forschungsgemeinschaft (DFG).
- This research has made use of NASA's Astrophysics Data System.
- Herschel is an ESA space observatory with science instruments provided by European-led Principal Investigator consortia and with important participation from NASA.
- This publication is based on data acquired with the Atacama Pathfinder Experiment (APEX). APEX is a collaboration between the Max-Planck-Institut fur Radioastronomie, the European Southern Observatory, and the Onsala Space Observatory.
- The Submillimeter Array is a joint project between the Smithsonian Astrophysical Observatory and the Academia Sinica Institute of Astronomy and Astrophysics and is funded by the Smithsonian Institution and the Academia Sinica.

The following people collaborated with me and contributed, more or less, to this work: Peter Schilke by supervision; Rainer Rolffs by previous work on radiative transfer models; Thomas Möller by `MAGIX` and `myXCLASS@CASA`; Sheng-Li Qin by his SMA expertise; Rumpa Choudhury in relation to astrochemistry; Álvaro Sánchez-Monge by his expertise in HMSF, observations and data reduction; Fanyi Meng by exploring dendrograms; Darek Lis by discussion of science related to NGC 6334; Rowan Smith in relation to theoretical background and simulations; Martin Emprechtinger and Ronan Higgins by HIFI data reduction; Arnaud Belloche and Friedrich Wyrowski by support with APEX.

Table C.1.: Software used throughout this work

XEphem	Fv	HIPE
Karma	GILDAS	LIME
MIRIAD	RADMC-3D	Starlink
mcluster	CASA	ParaView
MAGIX	LaTeX	myXCLASS
OpenOffice	GIMP	gnuplot
Maple	QFitsView	SAOImage DS9
Python Packages:	NumPy, SciPy	matplotlib
Astropy	APLpy	astrodendro

D. List of publications and scientific activities

List of publications as main author and co-author:

- 2010 Sabha, N., Witzel, G., Eckart, A., Buchholz, R. M., Bremer, M., Gießübel, R., Garcia-Marin, M., Kunneriath, D., Muzic, K., Schödel, R., Straubmeier, C., Zamaninasab, M., and Zernickel, A. (2010). The extreme luminosity states of Sagittarius A*. *A&A*, 512:A2.
- 2012 Zernickel, A., Schilke, P., Schmiedeke, A., Lis, D. C., Brogan, C. L., Ceccarelli, C., Comito, C., Emprechtinger, M., Hunter, T. R., and Möller, T. (2012). Molecular line survey of the high-mass star-forming region NGC 6334I with Herschel/HIFI and the Submillimeter Array. *A&A*, 546:A87.
- 2013 Zernickel, A., Schilke, P., and Smith, R. J. (2013). The global velocity field of the filament in NGC 6334. *A&A*, 554:L2.
- 2014 Choudhury, R., Schilke, P., Stéphan, G., Bergin, E. A., Möller, T., Schmiedeke, A., and Zernickel, A. (2015). Evolution of Complex Organic Molecules in Hot Molecular Cores. *A&A*, 575:A68.

Scientific activities in the framework of the SFB 956 (2012-2014):

- SFB 956 retreat 5.2012 (2013/2014), Wermelskirchen
- ALMA community days/workshop 5.2012, Bonn
- 8th IRAM interferometry school 10.2012, Grenoble, France
- CHESS meeting 11.2012, Alcala de Henares, Spain
- SFB 956 students retreat 10.2013, Noordwijk, Netherlands
- SFB 956 soft skills workshop "Communication & Presentation" 2.2014, Cologne
- SFB 956 evaluation 7.2014, Cologne
- IRAM 30m observations 10.2014, Sierra Nevada, Spain
- Star formation conference 11.2014, Noordwijk, Netherlands

Table D.1.: Proposals written for NGC 6334 as principal investigator

Telescope	Purpose	Year	Rating
APEX	HCN, HCO^+	2012	B
APEX	^{13}CO	2013	B
APEX	CI	2014	C
SOFIA, Cycle 3	CII, OI	2014	B-
ALMA, Cycle 1	HCN, diff. cores	2012	C
ALMA, Cycle 2	HCN, diff. cores	2013	C
ALMA, Cycle 2	HCN, cluster IN	2013	C

E. Declaration of authorship (Selbständigkeitserklärung)

Erklärung nach §4 Abs. 1 Nr. 9 der Promotionsordnung der Mathematisch-Naturwissenschaftlichen Fakultät der Universität zu Köln

Ich versichere, dass ich die von mir vorgelegte Dissertation selbständig angefertigt, die benutzten Quellen und Hilfsmittel vollständig angegeben und die Stellen der Arbeit – einschließlich Tabellen, Karten und Abbildungen –, die anderen Werken im Wortlaut oder dem Sinn nach entnommen sind, in jedem Einzelfall als Entlehnung kenntlich gemacht habe; dass diese Dissertation noch keiner anderen Fakultät oder Universität zur Prüfung vorgelegen hat; dass sie – abgesehen von auf Seite 143 angegebenen Teilpublikationen – noch nicht veröffentlicht worden ist, sowie, dass ich eine solche Veröffentlichung vor Abschluss des Promotionsverfahrens nicht vornehmen werde. Die Bestimmungen der Promotionsordnung sind mir bekannt. Die von mir vorgelegte Dissertation ist von Prof. Dr. Peter Schilke am I. Physikalischen Institut betreut worden.

Köln, den

Unterschrift